TEMPORAL AND FREQUENCY CHARACTERISTICS OF DISTRIBUTED FEEDBACK DYE LASERS

Michael E. Lusty

A Thesis Submitted for the Degree of PhD
at the
University of St Andrews

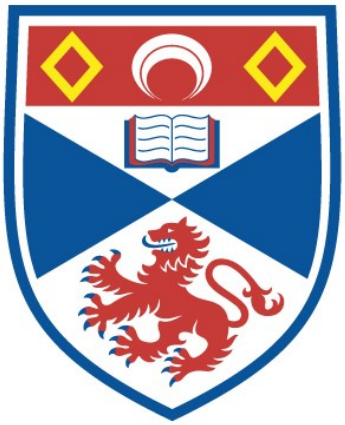

1989

Temporal and Frequency Characteristics of Distributed Feedback Dye Lasers.

A thesis presented by Michael E. Lusty B.Sc. M.Sc. to the University of St. Andrews in application for the degree of Doctor of Philosophy.

Declaration

I, Michael Edward Lusty, hereby certify that this thesis has been composed by myself, that it is a record of my own work, and that it has not been accepted in partial or complete fulfilment of any other degree or professional qualification.

Signed , Date 5th June 1989

I was admitted to the Faculty of Science of the University of St. Andrews under Ordinance General No 12 on the 1 st October 1985 and as candidate for the degree of Ph.D. on 1 st April 1986

Signed Date 5th June 1989

I hereby certify that Michael Edward Lusty has fulfilled the conditions of the Resolution and Regulations appropriate to the degree of Ph.D.

Signature of Supervisor Date 5 June 1989

Copyright

Acknowledgements

I would like to thank my supervisor Dr Malcolm H. Dunn for all his encouragement, help and support, which he gave so freely both during the research and in the writing of this thesis.

Many thanks also extend to all of the other members of staff within the department and especially those of the electrical and mechanical workshops and the teaching laboratories.

Thanks to the staff of the University Computer Laboratory and in particular Dr John R. Ball.

I am grateful to Professor Wilson Sibbett for the loan of the streak camera and to Dave Walker for assistance in using it.

The other 'PG's' also deserve thanks for help, making an enthusiastic and productive working environment, and in seeing me through the rough times. Colleagues worthy of a special mention are Messrs (correct at time of press) Andy Finch and Simon Wenden.

There are some people who must be acknowledged for helping to make my time at St. Andrews such an enjoyable one. Firstly, all of the above who I regard as friends as well as colleagues. Some of the people I will never forget include Araz Ali, Nina Donnelly, Ian Ferguson and Mohammed Nasban who, by extending their friendship, have given me a new outlook on life.

Many thanks also to all the staff of David Russell Hall. Truth be told, they deserve a medal, not thanks, for putting up with me for over four years!

The above list is by no means exhaustive and many others have helped. To all those people, I have forgotten to mention, many thanks.

I sincerely thank all of my family for their unending support and encouragement throughout my education. I am very proud of them as they are proud of me. In appreciation, it is to them, and especially the memory of my mother, that I dedicate this thesis.

Abstract

Previous studies of distributed feedback dye lasers (DFDL's) have identified that the linewidth of the device scales, to a first approximation, with the level of pumping employed. A more recent development is that the DFDL can be used to produce single ultrashort pulses. To produce such pulses the main requirement is that the laser is operated close to its threshold. An apparent contradiction exists here since, by lowering the pump power to achieve narrow linewidth operation, the near threshold region must be avoided since pulsing operation acts to increase the linewidth (to at least the Fourier transform of the pulse duration).

This thesis further investigates the mechanisms which contribute to the temporal and linewidth properties of the laser. It is identified that by judicious choice of operating conditions a regime exists where the DFDL may be operated with a linewidth approaching that of the transform limit for the nanosecond pulse durations involved.

After introducing the different types of distributed feedback lasers the thesis first reviews previously understood DFDL behaviour. Different DFDL geometries are considered with a view to their particular temporal and linewidth properties. A strategy for the development of a narrow linewidth DFDL is presented.

The experimental laser system is described detailing the operation and characteristics of the frequency doubled Q switched Nd:YAG pump laser and the two different DFDL geometries. A high resolution computer aided interferometry (CAIN) system is described which provided single shot linewidth measurements. This system was used extensively in the experiments reported.

DFDL linewidth is seen to depend on the thermo-optical properties of the dye's host solvent and as such a full characterization of commonly used solvents is presented.

The temporal behaviour of the laser is considered theoretically with the aid of a coupled rate equation model which describes the interplay between the population inversion and the cavity photon flux. The model is used to predict short (picosecond) and smooth (nanosecond) pulse operation of the laser.

Finally, a description of and the results obtained from various experimental investigations into the DFDL are presented. Temporal analysis, using a streak camera,

revealed that, as expected, under certain circumstances multiple pulsing of picosecond duration could occur. Different conditions however, lead to narrow linewidth (~100 MHz) operation. A description of the two operating regimes is presented and these are related to the particular parameters involved e.g. the grating length or the level of pumping employed.

Contents

Chapter I–An introduction.

Chapter I

1.1 Introduction to the Distributed Feedback Laser.

1.1.1 The tunable dye laser.

A tunable laser has four requirements:

1) A broad bandwidth active medium.

2) Some means of pumping or supplying energy to the active medium.

3) Some form of feedback mechanism, so as to sustain oscillation.

4) Wavelength or frequency selective elements so as to produce a narrow linewidth of radiation, important for many applications.

The organic dye laser is an important category of tunable lasers. The active medium (denoted as (1) in the above list) consists of an organic dye, such as one of the rhodamine series, contained in a host solvent. The operation of a dye laser can be considered with reference to figure (1) which is a schematic diagram of the Eigenstates of a typical dye molecule. Energy is supplied to the dye, in a process normally referred to as pumping (requirement (2) above), either from flashlamps or by another laser. On absorbing a pump photon, the molecule is excited into a rotational–vibrational state contained within the first excited electronic state (S_1). This is followed by a rapid (~1 picosecond) decay to the potential energy minimum of the S_1 state in a process known as thermalisation. This relaxation is rapid because the large dye molecule experiences greater than 10^{12} collisions/second with the solvent molecules. The energy from this nonradiative decay is transferred into the kinetic energy of the solvent. Relaxation of the molecule to the ground (G) state can occur via one of three routes; stimulated emission, spontaneous emission (also known as fluorescence) or nonradiative decay. Through the process of stimulated emission the dye can produce optical gain at certain wavelengths. Spontaneous emission typically occurs with a lifetime of the order of 1 to 5 nanoseconds. Nonradiative decay mainly occurs directly from the lowest excited singlet state (S_1) to the ground state (G). The molecule can also decay nonradiatively to the lowest electronic state of a system of triplet states (T_1). For optimal lasing efficiency it is desirable that stimulated emission dominates over fluorescence and nonradiative decay. Once the molecule is in its ground state thermalisation rapidly returns the molecule to its potential energy minimum. As will be seen in the next section, in conventional lasers the feedback (requirement (3)) is

provided by means of two (or more) carefully aligned mirrors. The frequency selection (requirement (4)) becomes increasingly complex according to the frequency selectivity required, using prisms or diffraction gratings for coarse and interferometric methods for fine tuning. The important developments in the realisation of tunable narrow linewidth dye laser sources are now traced.

Early dye lasers, such as those of Sorokin and Lankard [1], Schafer, Schmidt and Marth [2] and McFarland [3] employed only the basic elements necessary for laser action. Two plane mirrors formed the resonators of these lasers. Coarse wavelength tuning was achieved by varying the laser dye acting as the active medium. Less coarse tuning of the spectrally broad pulse could be provided by control of features such as dye concentration, dye solvent and cavity length. The output produced from these early dye lasers could have a spectral width of up to tens of nanometers. An important development to the pulsed dye laser was made by Soffer and McFarland [4] when a diffraction grating was substituted for one of the resonator mirrors to introduce wavelength dependent feedback. The diffraction grating employed was used in the Littrow arrangement where light of a particular wavelength (i.e. that wavelength satisfying the grating equation) is reflected back exactly along its own path into the laser cavity. Spectral narrowing of the output is achieved because those wavelengths not satisfying the grating equation are not reflected back into the cavity for further amplification. The authors of [4] obtained spectral narrowing from 6 to 0.06 nm and a continuous tuning range of 45 nm for the device. Since, the resolution of a diffraction is directly proportional to the number of lines illuminated, the incorporation of an intracavity telescope to expand the beam to fill all of the diffraction grating resulted in a decreasing of the linewidth of pulsed dye lasers still further. This was used by Hansch [5] in developing a narrow linewidth dye laser for high resolution spectroscopy. Hansch also incorporated an interferometric frequency selective device, namely a Fabry–Perot etalon into the cavity for further linewidth reduction. Combining these two features, the Hansch style geometry became the standard approach in the construction of pulsed tunable narrow linewidth dye lasers. Figure (2) is a schematic diagram for the Hansch style resonator. More recently the diffraction grating has been used at grazing incidence which, when combined with an additional mirror

improves the frequency resolution of the grating. This modification, which reduced the bandwidth by a factor of 3 over that of the Hansch resonator was first demonstrated by Gallagher et al. [6]. By reduction of the cavity length of a grazing incidence grating geometry to approximately 5 cm, Littman [7] produced a tunable dye laser which, when pumped with a Nd:YAG laser, produced a time averaged linewidth of < 150 MHz. The reduction in cavity length increases the number of round trips and passes through the frequency selective element.

The resonator geometries described above represent what, for the purposes of this thesis, will be termed conventional geometries. Other novel geometries have been developed which fulfil the four requirements of a tunable line-narrowed laser source. One such geometry is the distributed feedback dye laser, the properties of which are the subject matter of this thesis. Another interesting geometry is that of the modeless, variable bandwidth laser of Ewart [8]. The operation of the laser can be considered with reference to figure (3). Light which originates as spontaneous emission from the central gain region experiences a number of trips (typically 4) through the cavity. During each pass the light receives amplification and is line-narrowed as the light passes through the gain region and frequency selective device. The frequency selective device is a 1800 lines mm^{-1} holographic diffraction grating used at grazing incidence. Wavelength tuning is accomplished by the rotation of the prism used in conjunction with the diffraction grating. The bandwidth of the device is determined by the setting of the grating. Simultaneous rotation of the grating and prism varies the number of lines of the grating illuminated hence altering its resolution. Using four passes through the system the linewidth of the device has been lowered to approximately 6 GHz although, significantly, the time averaged bandwidth of the device was quoted in [8] as around 10 GHz.

The distributed feedback laser is now considered.

1.1.2 The Distributed Feedback Laser.

The distributed feedback laser (DFB) is distinguished from other types of laser by the use of a novel method of combining feedback (3) and frequency selection (4). Rather than having a mirror at each end of the active medium the DFB laser has a spatial modulation

of the refractive index and/or gain along some or all of the length of the active medium. For reasons that will become apparent shortly certain wavelengths can be 'reflected' from the modulated region. Because of certain similarities with the diffraction grating the modulated region in DFB lasers is often referred to as a grating region. The analysis of these types of optical Bragg structures is identical to that of Bragg diffraction of X-rays from crystal planes. Light of wavelength λ is diffracted at an angle θ from a grating which has a period Λ when the Bragg condition is satisfied, i.e.,

$$2\Lambda \mathrm{Sin}\ \theta = n\lambda \qquad (1.1)$$

where n is an integer. As can be seen from (1), light which is at normal incidence (θ=90°, sinθ=1) to the grating planes experiences back reflection when its wavelength is equal to twice the grating period, i.e.,

$$\lambda = 2\Lambda \qquad (1.2)$$

The light with a wavelength at or near to the Bragg wavelength, travelling perpendicular to the modulations in the medium, will therefore be backscattered in the opposite direction to its original direction of propagation. Figure (4) is a simplified illustration of the growth of two waves inside a gain medium containing a Bragg structure, and is obtained using a coupled wave theory which is outlined later [9]. The waves are represented as vectors and are labelled as R and S, representing waves travelling to the right and left respectively. As each wave travels through the Bragg grating, it receives a portion of the oppositely travelling wave through the coherent backscattering. If the feedback has a frequency that is within the gain region of the active medium then both waves will increase enabling laser oscillation to occur. Distributed feedback refers to the fact that, as has been described, the feedback is distributed throughout the gain length. Lumped feedback would best describe the type of feedback in conventional lasers. Spectral selection occurs due to the wavelength sensitivity of the Bragg effect.

To date, several types of DFB lasers have been demonstrated. These include DFB dye lasers (DFDLs) which are the subject of this thesis. Other types of DFB laser include the semi-conductor and gas DFB lasers which are briefly considered in section 1.1.4.

1.1.3 The Distributed Feedback Dye Laser of Kogelnik and Shank.

The first distributed feedback dye laser (DFDL) was demonstrated by Kogelnik and Shank [10]. Figure (5) is a schematic diagram of the laser. The interference pattern produced by the overlapping of two coherent beams obtained from a He-Cd laser was recorded onto a dichromated gelatin film. After exposure the gelatin film was developed causing a refractive index variation between the exposed and unexposed regions. The porous developed gelatin was then soaked in a solution of the laser dye rhodamine 6G. A spatially modulated region, or Bragg grating, of the type outlined above was therefore created in the gain medium. The ultra-violet light from a nitrogen laser provided the pumping of the structure. Pump powers greater than 1 MW cm^{-2} resulted in laser output at a wavelength of 630 nm. The linewidth of this first DFDL was less than 0.05 nm. Under similar conditions a uniform film of gelatin lased with a linewidth of 5 nm, centred around 590 nm. The incorporation of a distributed feedback structure into the dye medium therefore resulted in a 100 times reduction in the laser linewidth.

Before further considering the DFDL it is interesting to consider some other types of DFB laser. Semiconductor and gas distributed feedback lasers are now briefly considered.

1.1.4 Other Types of DFB Laser.

In the first semiconductor DFB laser Nakamura et al. [11] etched the top surface of a GaAs wafer to form a grating of spacing d ~ 0.35 μm. Gain was provided by optically pumping the wafer using a Q-switched ruby laser at a wavelength of λ = 694 nm. Third order (n=3) Bragg reflection from the grating provided the feedback at the laser frequency of ~ 830 nm. The linewidth of the device was of the order of 2 nm which compares with a spontaneous emission bandwidth of ~18 nm when used with a similar GaAs wafer with no corrugated region. Within a short space of time semiconductor DFB lasers had developed into self contained electrically pumped diode lasers [12]. The feedback for these lasers was produced by a corrugated interface between the active GaAs layer and a p-type $Ga_{1-x}Al_xAs$ layer. Similar to the laser described in [11] these lasers used 3rd order Bragg scattering. The linewidth of this device was less than 0.03 nm whilst operating at a wavelength of λ = 811 nm. More recently semi-conductor diode lasers have been

demonstrated operating in the wavelength region of 1.5 μm using InGaAsP/InP [13]. This spectral region is of particular interest to optical fibre communication systems since the transmission of single mode silicon fibres is at a maximum (0.2 dB/km loss) around this wavelength. Fibre optic transmission systems employing such lasers are now available commercially (from STC, BT&D and Plessey) which offer high speed data transmission at greater than 2.4 Gbits/s for distances exceeding 60 km.

Using a rectangular metallic waveguide with mechanically milled corrugations with a period of 248 μm Affolter and Kneubull [14] obtained the operation of a DFB gas laser using the gas CH_3F. Pumping the medium was done optically using a grating tuned single mode CO_2 laser (λ = 10.6 μm). The spectral linewidth of the device was at the transform limit of ~ 22 MHz for the 50 ns output pulse. Research continues into DFB gas lasers with much interest concentrating on the possibility of providing line-narrowed output from a CO_2 laser.

Having introduced the DFB laser and its variations, a review of some of the most significant DFDL developments which predate this work is now presented.

1.2 The Distributed Feedback Dye Laser.

1.2.1 Introduction.

Since 1971, and the first DFDL of Kogelnik and Shank, the laser has developed in many important respects. this section presents a review of the physical and theoretical developments of the DFDL which predate this thesis. Physical changes are described first. Developments in previous theoretical descriptions of the laser are then considered. As will be seen in the review, the models which best fit the observed behaviour of the laser are;

i) a rate equation model developed by Bor which describes the laser's temporal behaviour in the near threshold region, and,

ii) an experimentally derived model developed by McIntyre and Dunn which describes the linewidth behaviour of the laser when operating substantially above threshold.

As can be seen however, these theories are limited to specific areas of DFDL operation and the need for a further theoretical and experimental investigations into the behaviour of the laser then becomes apparent.

The developments of the DFDL are now traced.

1.2.2 Developments of the DFDL Geometry.

i) The Shank style DFDL.

The first DFDL, demonstrated by Kogelnik and Shank [9], had the disadvantage that the laser wavelength was pre-determined by the recorded grating period. Within a period of three months of this first demonstration Shank, Bjorkholm and Kogelnik [15] reported a tunable DFDL. When the ability to tune the laser is added, the DFDL the laser fulfills all four of the requirements listed above for a tunable narrow linewidth laser. The structure of the Shank laser is shown on figure (6) and is very simple. The second harmonic light from a single mode ruby laser is split into two using a beam splitter and is then recombined inside the dye cell containing the dye rhodamine 6G. Here, the coherent beams interfere to produce a gain and refractive index Bragg grating along the pumped length of dye, the period Λ of which is given by,

$$\Lambda = \frac{n_s \lambda_p}{2 \text{ Sin } \theta} \tag{1.3}$$

where n_s is the solvent refractive index, λ_p the pump laser wavelength and θ is the half angle of intersection of the two pump beams. From (2) and (3) it can be seen that the wavelength of the Shank DFDL is given by,

$$\lambda_d = \frac{n_s \lambda_p}{\text{Sin } \theta} \tag{1.4}$$

Thus the DFDL contains all of the four functions necessary for a tunable narrow linewidth laser, within a single element, namely the pumped gain medium.

Tuning of the laser may be achieved by altering any of the three parameters on the right hand side of equation (4). Since most DFDL systems use a fixed frequency pump laser eg. ruby [15] Nitrogen [16] or frequency doubled Nd:YAG the dye laser wavelength is most easily tuned by altering the angle of intersection of the two pump beams or by

varying the refractive index of the dye solvent. By changing θ Shank et al. achieved a tuning range of 64 nm in the dye rhodamine 6G. A similar tuning range was also observed by varying the refractive index of the solvent from 1.33 to 1.55 by proportionate mixing of methanol and benzyl alcohol. This method of providing tuning by the dynamic production of the grating in the active medium became the standard approach in subsequent DFDL geometries.

One limitation to the Shank style DFDL is that for a given pump laser the minimum output wavelength is given by the product of n_s and λ_p. In a slight modification to the Shank design Bakos [17] mounted an isosceles prism in front of the dye cell enabling a DFDL to be pumped by a laser whose wavelength is close to that of the DFDL. A labelled schematic diagram for the prism coupled DFDL is shown on figure (7). Expression (7) is now no longer valid and is replaced by,

$$\lambda_d = \frac{n_s \lambda_p}{n_p \, \mathrm{Sin}\,[\phi + \mathrm{Sin}^{-1}(\frac{\mathrm{Sin}\,\theta}{n_p})]} \qquad (1.5)$$

where n_p is the refractive index of the prism, ϕ is the base angle of the prism and θ is the angle of incidence of the pump beam on the entrance face of the prism. This type of geometry was employed in the majority of experiments performed in this laboratory where, using a frequency doubled Q-switched Nd:YAG laser ($\lambda_p = 532$ nm) we have operated our DFDL in the wavelength range 580–680 nm.

ii) The Bor style geometry.

By replacing the beam splitter of the Shank style DFDL with a diffraction grating Bor [16] demonstrated a DFDL where the DFDL linewidth is decoupled from the effects of pump laser linewidth and spatial incoherence. This allowed Bor to produce a DFDL which when pumped (near threshold) by a partially coherent N_2 laser, produced pulses of duration around 100 picoseconds with a near transform limited linewidth of around 0.05 Å.

The DFDL geometry used by Bor is essentially the same as that of Shank with the exception that the pump beam is divided into two using a diffraction grating. Figure 8(a)

is a schematic diagram of the Bor style DFDL geometry. The diffraction grating splits the pump beam into the +1 and -1 orders at an angle determined by the grating equation,

$$\text{Sin } \alpha = \lambda_p \, e \tag{1.6}$$

where e is the grating constant (=1/ number of lines per metre). The two identical pump beams are, after reflection from the mirrors, then recombined inside the dye cell producing a dynamic grating region of distributed feedback similar to that of the Shank style DFDL. Assuming that the two mirrors are perpendicular to both the dye cell and diffraction grating the wavelength of the laser is therefore given by,

$$\lambda_d = \frac{n_s \lambda_p}{\text{Sin } \alpha} \tag{1.7}$$

Combining (6) and (7) the output wavelength of the Bor style DFDL is given by,

$$\lambda_d = \frac{n_s}{e} \tag{1.8}$$

It is therefore seen that the DFDL output wavelength is independent of the pump laser wavelength. Achromatism was the term used by Bor to describe this de–coupling of the pump and DFDL wavelengths. The geometry has another important property in that, to a first approximation, for each point on the dye cell the interfering beams have been diffracted from the same point on the grating. This property, along with the achromatism, relaxes some of the constraints on the spatial coherence and linewidth on the pump laser and as such allowed Bor to pump his DFDL with a N_2 laser.

Tuning of the laser while still retaining the desirable achromatic properties of the device is achieved by varying the refractive index of the dye solvent. In his first report of the geometry Bor [16] demonstrated a tuning range of over 80 nm (employing three laser dyes) using this method. Tuning can also be employed by tilting the two beam steering mirrors, however, in doing so, the structure loses its achromatic properties. Achromatic properties are also lost if a prism is mounted on the front face of the dye cell.

A more careful analysis of the Bor style structure shows that the requirements on the pump laser are not completely removed by employing a diffraction grating. The position of the plane of interference caused by the intersection of the two beams is a function of

wavelength. This condition is completely relaxed in a two diffraction grating geometry demonstrated by Szatmari and Racz [18]. The geometry for which the authors claim a complete relaxation of wavelength and spatial coherence is illustrated schematically on figure 8(b).

1.2.3 DFB theory – Linewidth and Temporal Behaviour.

Before considering further DFDL developments and experimental investigations, it is interesting to consider some of the previous theoretical predictions made about the laser.

Within the first report of distributed feedback laser action, Kogelnik and Shank presented a coupled mode analysis of the laser which formed the basis for much of the theoretical work to follow. A detailed account of the theory can be found in [9] to which the reader is referred (see also Yariv [19] section 13.6). The periodic modulation of the medium is modelled as a combination of modulation in the refractive index n or the gain a as,

$$n(z) = n + n_1 \text{ Cos } kz$$
$$a(z) = a + a_1 \text{ Cos } kz \qquad (1.9)$$

where z is measured along the optic axis, a and n are the average values of gain and refractive index, a_1 and n_1 are the modulation amplitudes of the gain and refractive index, and k is the Bragg wavenumber ($2\pi/\Lambda$). The coupled mode picture assumes that the field E in the device is of the form,

$$E = R(z)\, e^{-ikz/2} + S(z)\, e^{ikz/2} \qquad (1.10)$$

consisting of two counter-running waves with complex amplitudes R and S representing waves travelling to the right and left respectively. As indicated in figure (4) the two waves grow in the presence of gain and, due to the spatial modulation of the medium, couple energy into each other. Using this analysis the authors derived expressions for the threshold and spectral bandwidth of the output of the DFB laser. The main limitations of the model are (i) the model is time independent, and (ii) it is a linear theory, the model can therefore only predict steady state solutions at laser threshold. Within these limitations two important conclusions were obtained with regard to the predicted spectral output. The

first is the existence of resonance 'modes' separated in frequency by c/2nL ie the same as in a usual two mirror laser cavity with length L. A distinction became apparent depending on the type of coupling used in modelling. When gain coupling was assumed there is a resonance at exactly the Bragg frequency, whereas if refractive index coupling is assumed then the modes are situated symmetrically about the Bragg frequency. An estimation of the linewidth of the device is obtained by evaluating the wavelength offset $\Delta\lambda$ required to reduce the coupling to half its maximum value and is shown to be,

$$\frac{\Delta\lambda}{\lambda} = \frac{a}{K_0} \tag{1.11}$$

where a is the gain per unit length in the medium and K_0 is the propagation constant at the laser wavelength.

More elaborate theories of DFB laser action have since appeared in an attempt to describe more fully the operation of these lasers. The effect of saturation was included by Hill and Watanabe [20] although spatial hole burning and dispersion in the active medium were neglected. Sargent et al. [21] treated the DFB semiclassicially by describing the electromagnetic field classically while treating the active medium according to the laws of quantum mechanics. This approach allowed Sargent's model of the DFB laser to include spatial hole burning and atomic linewidth in the analysis. Duling [22] added time dependence to the semiclassical theory to account for field propagation within the DFB laser cavity. Despite these and other attempts to describe the DFDL little headway has been achieved in the interchange of theory and experiment. For example, the modes of a DFB laser predicted by the coupled wave model have never been observed.

With regards to the temporal form of the laser, a simple rate equation model, first developed by Bor [23] was successful in predicting the temporal profile of the laser. This model consists of a pair of coupled rate equations which describe the interplay between the cavity photon flux and the atomic inversion. Bor restricted his attention to near threshold in his interest in the production of single ultrashort pulses. This model is re-investigated later in Chapter V to explore its validity outside the near threshold region.

A review of experimental investigations into the processes contributing to both the linewidth and temporal form of the DFDL now follows.

1.2.4 Linewidth Behaviour of DFDLs.

This section draws together some general conclusions about DFDL linewidth from several sources including including investigations in our own laboratory [24,25]. It will be seen that DFDL linewidth depends on:

(a) properties of the pump laser (e.g. linewidth, coherence, beam divergence etc), and,

(b) the level of pumping of the DFDL, through thermal and dispersive effects on refractive index which are seen to depend on choice of dye parameters used in the DFDL's active medium (i.e. laser dye and type of solvent used).

These are now considered in turn along with the transient behaviour of DFDL wavelength and linewidth saturation.

(a) Pump laser parameters

(i) Pump laser linewidth

Several authors, including the original report of Shank [15], have reported that the linewidth of the DFDL scales with the linewidth of the pump laser. However, as yet no quantative measurements have appeared in the literature. An estimate of the effect of how a pump laser, with linewidth $\Delta\lambda_p$, can contribute to the linewidth of the DFDL may be obtained by differentiating equation (4) to obtain,

$$\Delta\lambda_d = \frac{n_s}{\text{Sin } \theta}\Delta\lambda_p \qquad (1.12)$$

Alternatively, if the laser is used with a front mounted prism equation (8) can be used to give,

$$\Delta\lambda_d = \frac{n_s}{n_p \text{ Sin } [\phi + \text{Sin}^{-1}(\frac{\text{Sin } \theta}{n_p})]}\Delta\lambda_p \qquad (1.13)$$

Therefore if the laser is operating in the wavelength range of 600 to 650 nm then the minimum expected linewidth is around 1.2 times $\Delta\lambda_p$. In the majority of our DFDL research reported before this thesis our Nd:YAG laser was operated with a conventional Q switch. The linewidth of the laser was measured as approximately 3 GHz (0.03 Å) representing oscillation over 20 longitudinal modes. Thus if all other (often more

dominant) linewidth effects can be neglected the minimum DFDL linewidth using the pump laser in this configuration is approximately 3.5 GHz.

(ii) Pump laser coherence

As can be seen from figure (6) that pump beam which is transmitted by the beam splitter undergoes one less reflection than that beam which is reflected. The consequence of this is that the interference pattern in the dye cell is formed by the wavefront interfering with the mirror image of itself. This places a restriction on the wavefront coherence of the pump beam if a high visibility grating is to be produced.It will be seen later that a high grating visibility contributes to increased spectral selectivity of the DFDL. Bakos [26] observed an increase in DFDL linewidth by a factor of seven when using a ruby laser with poor spatial coherence over that when using a high quality ruby laser pump source. Shank [15] in his DFDL used a TEM_{00} SLM ruby laser hence ensuring maximum fringe visibility. Vashchuk [27] demonstrated a special splitting prism enabling the formation of a high visibility grating when derived from a laser of poor spatial coherence.

(iii)Pump laser divergence

The influence of pump beam divergence on the DFDL linewidth may be estimated by differentiating equations (5) and (6) with respect to θ to obtain,

$$\Delta\lambda_d = -\frac{\lambda_d \cos\theta}{\sin^2\theta}\Delta\theta \qquad (1.14)$$

or,

$$\Delta\lambda_d = -\frac{\lambda_d \cos\theta}{\tan\left[\phi + \mathrm{Sin}^{-1}\left(\frac{\mathrm{Sin}\,\theta}{n_p}\right)\right]\sqrt{(n^2 - \sin^2\theta)}}\Delta\theta \qquad (1.15)$$

for the basic Shank and prism coupled Shank style geometries respectively. The effect was considered and verified experimentally in this laboratory (see for example [24,25]) by varying the effective divergence of the Nd:YAG laser used in the pumping of our DFDL. The beam from the pump laser was passed through two 20 cm (nominal) focal length lenses which were spaced by approximately 40 cm (see figure 9(a)). The divergence was altered by moving one of the lenses with respect to the other and the resulting linewidth measured (see figure 9(b)). This experiment showed that the linewidth

of the DFDL is dependent on the divergence, coming to a minimum for a separation between the lenses (41.2 cm) corresponding to the beam waist formed by the lens combination falling in the dye cell when the divergence of the pump beams in the cell is a minimum.

(b) Power dependence of linewidth.

Although the DFDL demonstrates a dependence of linewidth on the pump laser parameters considered above, the effects cannot account for the power dependence of linewidth which has been reported by several DFDL experimenters. Shank [15] found that the linewidth of his device was very small at threshold, ~ 0.001 nm (1 GHz), but this increased to 0.05 nm when the pump power was five to fourteen times threshold. This was confirmed by Bakos [26] who found that the linewidth increased from 0.013 nm to 0.4 nm at high pump powers. The work in this laboratory with our DFDL has shown that, before the onset of linewidth saturation at pump powers greater than ~ 20 mJ, the DFDL linewidth scales with the level of pumping employed. Saturation of linewidth is considered in a following section. Two refractive index effects were identified which enable the pump power dependence of DFDL linewidth to be explained. These effects are:

(i) a time dependent refractive index for the solvent due to thermal effects, and

(ii) a time dependent contribution to the refractive index of the active medium due to the dispersion associated with the optical gain.

Substituting the time dependent refractive index, $n_s(t)$ into equation (4) the time dependence of the output wavelength λ_d is written as,

$$\lambda_d(t) = \frac{n_s(t)\,\lambda_p}{\mathrm{Sin}\ \theta} \tag{1.16}$$

Thus the effect of a changing refractive index during the course of the pump pulse is therefore to produce a dynamic sweeping (or chirp) of the DFDL wavelength. On integrating over the whole pulse the sweep is observed as a contribution to linewidth which is given by,

$$\Delta\lambda_d = \frac{\lambda_p}{\mathrm{Sin}\ \theta}\Delta n_s \tag{1.17}$$

or,

$$\Delta\lambda_d = \frac{\lambda_p}{n_p \, \mathrm{Sin}\,[\phi + \mathrm{Sin}^{-1}(\frac{\mathrm{Sin}\,\theta}{n_p})]} \Delta n_s \qquad (1.18)$$

for the basic Shank and prism coupled Shank style geometries respectively. The thermal and dispersive contributions to the linewidth are now considered separately.

(i) Thermal effects in dye laser solvents.

Heating effects are inherent in the absorption and emission of optical radiation in a dye molecule. Localised heating changes the density of the solvent hence causing a change in the solvent refractive index. The refractive index change in the pumped region of the dye, of volume V, due to heating is given by,

$$\Delta n_S = \frac{AE}{\rho V s} \frac{dn_s}{dT} \qquad (1.19)$$

where E is the pumping energy (per pulse). The other parameters are properties of the solvent used; ρ is the density, s the specific heat capacity, A the fraction of photon energy converted to heat and dn_s/dT is the rate of change of refractive index with temperature.

The mechanism by which thermal effects contribute to the linewidth is that, during a pumping pulse, the temperature of the active volume increases, thus reducing the refractive index (for negative dn_s/dT) with a consequent reduction in the DFDL wavelength. On integrating over the whole pulse, this sweep in DFDL wavelength is seen as a contribution to the linewidth, given by,

$$\Delta\lambda_d = \frac{\lambda_d AE}{\rho V s n_s} \frac{dn_s}{dT} \qquad (1.20)$$

Equation (20) assumes that during the course of the pump pulse there is sufficient time to reach thermal equilibrium. However, for the timescales involved (tens of nanoseconds) for most DFDLs this assumption is probably not valid. General conclusions can be made however and these have been validated experimentally. In this laboratory we have observed a linewidth dependence on solvent dn/dT. When the laser was operated using methanol as the dye solvent a larger linewidth was recorded over that when using water. Methanol has a high dn/dT ($-47\times10^{-5}\ K^{-1}$) whereas water has a low dn/dT ($-8\times10^{-5}\ K^{-1}$). It would seem plausible that by reducing the pump power and using a larger active

volume that thermal effects can be reduced. However, a more careful analysis of these effects is needed, and this forms part of the contribution of this thesis.

(ii) Dispersive effects on active medium refractive index.

In the previous section the pump power dependence of DFDL linewidth has been related to thermal effects in the dye solvent. McIntyre and Dunn were the first authors to report that the DFDL linewidth was also dependent on its operating wavelength. While operating the Nd:YAG pumped DFDL at high pump powers while using rhodamine B dissolved in water, it was observed that the linewidth increased from 0.15 Å to 0.4 Å when operated at the wavelengths of 580 nm and 600 nm respectively. The incorporation of a dispersive contribution to the refractive index of the active medium was sited by McIntyre and Dunn as an explanation of the dependence of the linewidth on wavelength. As will be seen later dispersive effects further explain the pump power dependence of DFDL linewidth.

The refractive index of a medium varies rapidly with frequency for frequencies close to an atomic or molecular resonance of the medium. More particularly, if a resonance has a Lorentzian profile, with a halfwidth $\Delta\nu$ say, the dispersion resulting from the resonance has the functional dependence on frequency,

$$n(\nu) = 1 + \frac{c(\nu - \nu_o)\, a(\nu)}{2\,\pi\,\nu\,\Delta\nu} \qquad (1.21)$$

where c is the speed of light, ν_o is the resonant frequency and $a(\nu)$ is the frequency dependent gain of the medium, and depends on the relative populations in the upper and lower states of the resonance and also the transition cross-section (if a is negative then the medium exhibits absorption and the more usual condition of anomalous dispersion applies).

A consequence of this dispersion is that the refractive index of the active medium is dependent on the upper and lower state populations, and also on wavelength. In the case of a DFDL this can result in an oscillation frequency which is dependent on the intracavity laser radiation intensity. Moreover, since this intensity changes during the course of a pulse, i.e. increases and then decreases, it is to be expected that the oscillation frequency

will also undergo an "excursion" during the pulse, and if the output is integrated over the length of the pulse, this excursion will be interpreted as a linewidth.

Dispersion in a dye laser active medium is more complicated than implied above; for instead of having a single Lorentzian gain profile, the (fluorescent) emission resonance is Stokes-shifted with respect to the absorption resonance (see figure 10(a)) for the emission and absorption spectra of rhodamine B), and so the resulting dispersion curve has two frequency-dependent components, one arising from absorption and the other from emission. In addition, the absorption and emission spectra do not have Lorentzian profiles and so the exact form of the dispersion relation given in equation (21) does not hold; numerical methods now being necessary to determine dispersion curves. However, certain general conclusions regarding the form of the dispersion profile may be deduced from the absorption/gain profile using the Kramers-Kronig relations without knowing the exact gain profile [28]; namely the dispersion is always zero where the frequency derivative of the gain or absorption is zero and the dispersion reaches a peak when the gain or absorption is changing fastest with frequency. Since these general relations exist between gain/absorption and dispersion, it is appropriate to represent the absorption and emission spectra of the dye molecule by a reasonable, analytic approximation (e.g. Lorentzian) and expect the resulting dispersion curve to show the correct general behaviour. Such an approximation allows the functional dependence of the dye dispersion to be examined with respect to relative populations and DFDL wavelength without recourse to an extensive numerical solution to the Kramers-Kronig relations, but gives only an estimate of the magnitude of such effects.

Using this Lorentzian approximation, the refractive index of a dye solution may be written as the sum of refractive indices,

$$n(\nu) = n_s - \frac{c(\nu_e - \nu)\, N_1\, \sigma_e(\nu)}{2\,\pi\,\nu\,\Delta\nu_e} + \frac{c(\nu_a - \nu)\,(N-N_1)\,\sigma_a(\nu)}{2\,\pi\,\nu\,\Delta\nu_a} \qquad (1.22)$$

where n_s is the bulk refractive index of the solvent, ν_e is the frequency of the fluorescent emission peak, $\Delta\nu_e$ is the halfwidth of fluorescent emission, ν_a is the frequency of maximum absorption, and $\Delta\nu_a$ is the halfwidth of absorption. The density of dye

molecules is N and the population in the upper, S_1, state is N_1. The frequency dependent emission and absorption cross-sections are σ_e and σ_a respectively. These are approximated here by Lorentzian profiles with the above halfwidths and appropriate magnitudes. In figure 10(a) the measured absorption and emission cross sections for rhodamine B are plotted. Lorentzian approximations for this data are plotted in part (b) of the figure. The second term on the right hand side of (22) represents dispersion due to gain and the third term represents dispersion due to ground state absorption. Dispersion due to triplet absorption has been ignored because the 10 ns pulse is too short to allow the growth of a significant triplet state population.

As can be seen from equation (22), the dispersive contributions to the refractive index are dependent on the excited state population, N_1, and also the frequency of the DFDL radiation hence indicating its power and wavelength dependence.

The mechanism through which the dispersion affects the linewidth of the DFDL is that, during a pumping pulse, the upper level population, N_1, grows from zero to a maximum and then falls back to zero again, while the ground state population, N_0, suffers a dip during the pulse. As this happens, the refractive index of the medium, given by equation (22) undergoes an excursion, the instantaneous refractive index being determined by N_1 and N_0. Any change in the refractive index of the DFDL results in a change in the oscillating wavelength, and so the time averaged linewidth appears to be broadened. This incorporation of a dispersive contribution in the DFDL linewidth can therefore explain the dependence of the linewidth on both pump energy and laser wavelength.

Figure 11(a) shows the dispersive contribution to the refractive index as a function of relative excitation (N_1/N_0) for various wavelengths for the dye rhodamine B. The wavelength dependence of equation (22) is illustrated more clearly on figure 11(b). This figure indicates a maximum contribution by dispersion to the time averaged linewidth at around 600 mm, and this is exactly what is observed (see Table 1). Interestingly, around 558 nm the dispersive contribution to the refractive index is zero, i.e. the refractive index is decoupled from (N_1/N_0). This occurs when the dispersive contribution from emission is equal and opposite to that of absorption, the linewidth then being determined only by

the three previously mentioned processes. Unfortunately at this wavelength for this dye absorption exceeds emission so laser oscillation cannot occur.

Thus the dispersive model of line broadening has been used to explain the observed dependence of linewidth on both pump power and operating wavelength. Moreover, as is considered next, it successfully predicts the temporal behaviour of the DFDL wavelength during the course of a pumping pulse.

Transient behaviour of the DFDL wavelength.

An important distinction exists in the time evolution of the thermal and dispersive components which contribute to the DFDL linewidth. The dispersive component is seen to sweep (or chirp) the frequency of the laser in two directions. Operating on the high wavelength side of the gain profile the laser down chirps reaching a maximum value at the peak of the pumping pulse before returning to its original value in the latter part of the pulse. The direction of the frequency chirp is reversed when operating at a lower wavelength side of the gain curve. The magnitude of the effect is dependent on the laser wavelength and, before the onset of saturation (see next section) scales directly with the level of pumping. However, since the temperature of the solvent contained within the active volume has insufficient time to reach thermal equilibrium with its surroundings the frequency chirp produced is in the downward direction only (downward because the dn/dTs of all solvents are negative).

In investigating the transient behaviour of the DFDL wavelength these two components were observed directly. A full explanation of the method used is given in [24] which is included as an appendix to the thesis. Using the dye rhodamine B the two way frequency chirp associated with dispersion was, as expected, observed to be dependent on wavelength. A larger two way chirp was recorded for 600 nm than for 580 nm which is just as expected considering the wavelength dependence of equation (22) (see also figure 11). The one way chirp associated with thermal effects was seen to be dependent on solvent dn/dT. The transient behaviour of the DFDL further supports the evidence for the existence of a dynamic thermal and dispersive contributions to its linewidth.

Linewidth saturation.

As was stated above the linewidth of the DFDL scales with the level of pumping employed until reaching a saturation value. The nature and origin of linewidth saturation is now discussed. In the linear region of moderate levels of pumping (5–20 mJ), the dominant processes determining linewidth are thermal and dispersive contributions to refractive index. Pumping the DFDL with energies less than approximately 20 mJ it was found that the linewidth scaled linearly with pump energy. For pump energies greater than 20 mJ the linewidth remained constant. Figure (12) illustrates linewidth behaviour for pump energies around this saturation value. The saturation of linewidth can be explained with reference to figure (13) which plots the measured amplified spontaneous emission (ASE) as a function of pump power. As can be seen from the figure the ASE, similar to to linewidth, also saturates around 20 mJ. This behaviour suggests that the saturated gain above 20 mJ is independent of pumping energy, i.e. the maximum upper state population, N_1, is independent of pumping energy. Below 20 mJ, the saturated gain (as shown by the ASE behaviour) increases with pumping power, implying that the maximum value of N_1 also increases with increased pumping. Thus, since N_1 behaves in this manner, so must the dispersive component, i.e. it increases with pumping energy up to about 20 mJ and then remains constant. As a result, the laser is expected to sweep during an increasingly shorter fraction of the pulse duration for energies above 20mJ, i.e. the laser frequency is constant at a frequency corresponding to the saturated gain for an increasingly longer fraction of the pulse. For a time averaged spectrum, this is interpreted as a decrease in contribution to the linewidth due to dispersion. Since thermal effects continue to contribute increasingly with pumping power the two effects now offset one another. The observed independence of linewidth on pump power for pump powers above 20 mJ (see figure 12) is consistent with this behaviour.

Summary of linewidth effects.

In this section the linewidth behaviour of the DFDL has been explained. The linewidth is seen to depend on two factors:

1) the properties of the pump laser (linewidth, divergence, etc.)

2) the level of pumping employed (through thermal and dispersive effects on refractive index).

Effect (1) mainly contributes to the linewidth by affecting the properties of the induced grating. For example, the coherence and linewidth of the pump beam determine the visibility and periodicity respectively of the grating which, in turn determine its spectral selectivity.

The power dependence of linewidth (effect 2) derives from thermal and dispersive contributions to refractive index which chirps the DFDL wavelength during the course of the pulse. When time averaged the chirping is interpreted as the device linewidth. As will be seen later (section 1.3), where the development of a narrow linewidth DFDL is discussed, these factors are of considerable importance.

1.2.5 Temporal Behaviour of the DFDL.

In the period between 1971, when the DFDL was first demonstrated, and 1980 the DFDL was assumed to have a temporal behaviour which followed the pump laser pulse. In previous studies studies in this laboratory our time domain experiments (temporal resolution ~ 1.3 nanosecond) have been in agreement with this conclusion. Shank et al. [15] in their paper state that "The dye–laser pulse followed closely the smooth second harmonic pump pulse shape which had a duration of approximately 10 nsec". They continue in the next sentence to say, "However, the dye–laser pulse was not smooth and showed a slight superimposed structure". These two sentences were quoted by Bor when in [29] he reviewed the previous two years work on ultrashort pulse generation in DFDLs. By operating a N_2 pumped DFDL close to its threshold Bor produced a DFDL capable of generating single picosecond duration pulses. This worked has continued as an active area of DFDL research until the present day. To date (March 1989) the shortest reported directly generated pulse obtained from a DFDL is 320 fs [30].

Bor [29,30] presented a coupled rate equation model describing the interplay between the population inversion and the photon flux inside the laser 'cavity'. In the region near threshold for the device two operating regimes were identified using the model. Before considering the dynamics of the laser action it is important to draw an important

distinction between the DFDL and a conventional Fabry–Perot cavity laser. In a Fabry–Perot laser the cavity decay time is a constant, depending mainly on mirror reflectivity. In contrast the decay time of a distributed feedback laser is a function of the modulation providing feedback. In particular, as will be developed in chapter 5, the feedback, (or cavity Q) of the DFDL is proportional to the square of the gain of the laser. The dynamics of the laser action are now considered.

In the early stages of pumping the population inversion and gain of the laser increase. As a consequence of the increased gain the cavity Q increases for the reason described above. Below threshold the cavity gain is exceeded by its loss. As the pumping continues laser threshold is reached and surpassed, the gain now exceeding the loss. The DFDL pulse now develops but in doing so stimulated emission causes a depletion of the population inversion which, in turn, lowers the cavity Q causing termination of the laser action. An important consequence of this switching process termed 'self Q-switching' is that the emitted DFDL pulse can be significantly shorter than that of the pump pulse. In the first regime identified by Bor the laser is operated sufficiently close to (around twice) threshold to allow only a single pulse to develop. By pumping above this level Bor identified a second regime where multiple pulsing of the laser occurs. The dynamics of the laser action is essentially the same as that of single pulse production with the exception that, as a consequence of increased pumping the gain can recover to again exceed the loss causing the generation of another short duration pulse. Pumping at levels much above threshold (i.e. greater than five times threshold) has not been reported by Bor nor has he considered this regime using the rate equation model.

1.2.6 Summary.

In this section aspects of the DFDL have been explored. An emphasis has been placed on the factors contributing to the temporal and linewidth behaviour of the DFDL. When reviewing the DFDL literature two regimes of operating the DFDL become apparent. Near threshold operation, leading to the production of short pulses is the first regime. In the second regime the laser is operating typically more than five times that of the threshold

value. Here the linewidth of the DFDL has been seen to depend on two main factors, namely:

1) the properties of the pump laser (linewidth, coherence, divergence etc.) and,

2) the level of the pumping employed (through thermal and dispersive on refractive index).

These factors have been considered in full and estimates of the magnitudes of the effect of these parameters has been given. When considering the power dependence of linewidth two power dependent parameters were discussed; a thermally and a dispersively derived dynamic sweep of refractive index which when time averaged contribute to the linewidth of the device.

However, in previous literature, no apparent connection exists between the two regimes. This suggests the need for a further investigation into the operation of the laser. Such an investigation forms the subject matter of this thesis an outline of which is presented in the next section.

1.3 Temporal and Frequency Characteristics of Distributed Feedback Dye Lasers: Thesis Review.

In the previous two sections an introduction to the DFB laser is followed by a review of the processes affecting the linewidth and temporal behaviour of the DFDL. From this review two, seemingly distinct, operating regions of the DFDL have been identified. These are:

1) a near threshold region where self Q switching can lead to picosecond pulsing, and,

2) a well above threshold region where three processes were identified as contributing to the linewidth, namely:

(i) Pump laser parameters (linewidth, coherence, divergence etc.),

(ii) a time dependent refractive index for the solvent due to thermal effects, and

(iii) a time dependent contribution to the refractive index of the active medium due to the dispersion associated with the optical gain.

Processes (ii) and (iii) together identify a general trend scaling the linewidth with the level of pumping employed and are the more dominant processes at moderate levels of pumping.

However, it has become apparent that, thus far, no general model exists which provides a description of the DFDL. Having seen that two, seemingly unconnected regimes exist in the experimentally observed behaviour of the laser, it is reasonable to ask if it is possible to reconcile the two in a such a model which provides a general description of distributed feedback dye laser action. Such a description should be consistent with all of the previously modes of operation e.g. in the production of ultrashort or narrow linewidth pulses. This apparent lack of understanding has stimulated this further experimental and theoretical investigation into the properties of the DFDL. This thesis presents the results of these further investigations. It will be seen that our experimental laser system could be configured for either short duration or narrow linewidth pulses. In the light of these investigations we present a new model which comprehensively describes the behaviour of the laser and is in good agreement with previous experimental observations.This model should further aid the understanding of the DFDL.

A significant development of this investigation was the production of a DFDL which can operate at or near to its transform limited linewidth of 100 MHz for the 10 nanosecond duration pulse under a much less restrictive range of operating conditions than previously reported, namely 580 to 680 nm using a variety of laser dyes. Such operation was obtained by the following strategy:

1) Identifying, both theoretically and experimentally, pulsing regimes so as to avoid them,

2) Reducing pump laser effects to a minimum by employing a narrow linewidth, highly coherent, low divergence pump laser, and

3) Operating the laser at reduced pump powers while minimising, as far as practicable, thermal effects by the use of low dn/dT solvents and restricting oscillation to wavelength regions of low dispersion.

The remainder of this thesis considers the experimental and theoretical investigations into DFDL behaviour.

Chapter 2 contains details of the design and construction of the experimental DFDL system. The geometries of Shank [15] and Bor [16] are considered. In addition the modifications to the Nd:YAG pump laser enabling the production of TEM_{00} single longitudinal mode pulses are described.

To facilitate linewidth measurements a computer aided interferometer (CAIN) system was constructed. Chapter 3 contains a full account of the device which was used for the majority of the linewidth measurement in later experiments. This self contained system allows single shot measurements down to 100 MHz level which is approximately the transform limit for the 10 ns DFDL pulses. The system consists of a non degenerate 1.5 GHz free spectral range interferometer and an image grabbing system which is made up from a CCD camera, a video framestore and a computer.

Chapter 4 contains an account of the heating mechanisms inside the dye medium and presents the results from an investigation into the thermo-optical properties of dye laser solvents. These properties are of considerable importance when assessing the thermally derived refractive index sweeps contributing to linewidth. The method of assessment is discussed together with a characterisation of a wide range of dye laser solvents.

Chapter 5 further investigates the coupled rate equation model of Bor. In addition to the near threshold region investigated by Bor, operation well above threshold is considered, conditions appropriate to our line narrowed DFDL. The equations are solved numerically using a fourth order Runge–Kutta method. A variety of parameters are explored in addition to that of increased pumping including the effect of reduced visibility of fringes, grating length etc.

Chapter 6 comprises the main body of experimental work performed on the DFDL under the new pumping conditions (reduced power, line-narrowed pump laser etc.). A full interferometric investigation into the linewidth properties of the DFDL under a range of operating conditions is presented. In addition to this linewidth investigation results are presented where simultaneous linewidth using the CAIN system and temporal measurements using a streak camera were made. The motivation for this investigation was to ascertain if the pulse envelope contained a large number of picosecond pulses as has been

suggested by Bor [31], or if single narrow linewidth pulses may be produced by pumping well above threshold.

A conclusion to the thesis forms the last chapter. In the conclusion a new model is presented which links the various operating regimes. The model considers both ultrashort pulse and nanosecond pulse generation. The linewidth of the laser can also be predicted depending upon the particular operating circumstances.

The thesis also includes four appendices.

The first is a paper written by I.A McIntyre and myself under the supervision of M.H.Dunn which describes the processes determining the DFDL linewidth. The paper was published in the Journal of Modern Optics.

The second appendix is a paper written by myself and M.H.Dunn which reports on an investigation into the thermo–optical properties of dye laser solvents. This paper was published in the journal of Applied Physics B.

The third appendix contains details of the operation of the CAIN system and includes a listing of the computer software.

The fourth and final appendix contains a listing of the FORTRAN program used in the solution of the coupled differential rate equations describing the temporal behaviour of the DFDL. The algorithm employed was a fourth-order Runge–Kutta method.

Wavelength λ_d (nm)	Linewidth at 5°C (Å)	Linewidth at 22°C (Å)
580	0.15	0.22
590	0.22	0.32
600	0.4	0.6

Table (1). Previously reported DFDL linewidth at different operating wavelengths and two temperatures (1.5 mJ pumping, water/Decon solvent).

Chapter I References

[1] P. Sorokin and J. Lankard: "Stimulated emission observed from an organic dye, chloroaluminum phtalocyanine" IBM J. of Res and Dev **10**, 162 (1966).

[2] F.Schafer, W. Schmidt and J.Volze: "Organic dye solution laser" Appl. Phys Lett **9**,306 (1966).

[3] B.B. McFarland: Appl. Phys Lett **10**, 208 (1966).

[4] B.Soffer and B.B. McFarland: Appl. Phys Lett **10**, 266 (1966).

[5] T.W. Hansch: "Repetitively pulsed tunable dye laser for high resolution spectroscopy" Appl. Optics, **11**,895 (1972).

[6] T. Gallagher, R. Kachru and F. Gounand: "Simple linewidth – reducing modification for a Hansch dye laser" Appl. Optics, **21**, 895 (1972).

[7] M.Littman: "Single mode pulsed tunable dye laser" Appl. Optics, **23**, 4465 (1972).

[8] P.Ewart: "A modeless variable bandwidth, tunable dye laser": Optics Commun. **55**, 124 (1985).

[9] H.Kogelnik and C.V.Shank: "Coupled Wave Theory of Distributed Feedback Lasers" J. Appl. Phys **43**,5,p2327 (1972).

[10] H.Kogelnik and C.V.Shank: "Stimulated Emission in a Periodic Structure" Appl. Phys. Lett. **18**,4,p152 (1971).

[11] M.Nakamura, A. Yariv, H.W. Yen, S.Soneth and H.L. Garvin: "Optically pumped GaAs surface laser with corrugation feedback" Appl. Phys. Lett **22**,10,515 (1972).

[12] M.Nakamura, K. Aiki, J Umeda, A.Yariv, H.W.Yen and T. Morikawa: "GaAs-$Ga_{1-x}Al_xAs$ double-hetrostructure distributed feedback diode laser" Appl.Phys.Lett **25**, 4887 (1972).

[13] K. Satai, K. Utaki, S. Akita and Y. Matsashime: "1.5 μm range InGsAsP / InP DFB lasers", IEEE J. Quantum Electron, QE-**18**, 1272 (1982).

[14] E.Affolter and F. Kneubuhl: "Far-Infrared distributed feedback gas laser",

IEEE J. Quantum Electron, QE-**17**, 115 (1981).

[15] C.V.Shank, J.E.Bjorkholm and H.Kogelnik: "Tunable Distributed Feedback Dye laser" Appl. Phys. Lett. **18**, 9, p395 (1971).

[16] Zs Bor: "A novel pumping arrangement for tunable simple picosecond pulse generation with a N_2 laser pumped DFDL" Optics Commun. **29**,103 (1979).

[17] J.Bakos, Z Fuessy, Z Sorlei and J. Szigeti: "DFDL of wavelength tunable from 747 nm to 840 nm" Phys Lett **50A**, 227 (1974).

[18] Szatmari and Racz: "Novel achromatic DFDL for subpicosecond operation" Appl. Phys B **43**, 173 (1987).

[19] A.Yariv: *Optical Electronics* Third Edition, Holt, Rinehart and Winston (1985).

[20] K.Hill and A.Watanabe: "Envelope gain saturation in DFB lasers" Appl. Optics **14**, 950 (1975).

[21] M.Sargent III, W. Swantner and J.Thomas: "Theory of a distributed feedback laser" IEEE J.Quantum Electron QE–**16**, 465 (1980).

[22] I.Durling III and M.Raymer: "Time dependent semiclassical theory of gain coupled DFB lasers" IEEE J.Quantum Electron QE–**20**, 1202 (1984).

[23] Z.Bor: "Tunable picosecond pulse generation by a N_2 laser pumped self Q switched DFDL" IEEE J Quantum Electron. QE-16, 517 (1980).

[24] I.McIntyre: Ph.D. Thesis "Dye lasers with induced Bragg gratings" University of St.Andrews (1985).

[25] I.McIntyre, M.E.Lusty and M.H.Dunn:"Linewidth determining processes in DFDLs" J.Mod.Optics 35, 325 (1988).

[26] J.Bakos, Z.Sorlei:"High power DFB laser tunable in the 7426Å to 10500 Å range"Optics Commun. **22**, 258 (1977).

[27] V.Vashchuck, E.Zabello and E. Tikhonov:"New dye laser systems with dynamic distributed feedback" Sov.J.Quantam Electron, **8**,859 (1978).

[28] R.Loudon: *The Quantum Theory of Light*, Oxford Univ. Press (1973).

[29] Z.Bor, A.Muller, B.Racz and F.Schafer: "Ultrashort pulse generation by DFDLs" Appl. Phys B **27**, 9 (1987).

[30] S. Szatmari and B. Racz: "Generation of 320 fs pulses with a DFDL" Appl. Phys B, **43**, p93 (1987).

[31] Zs. Bor: Private Communication 1984.

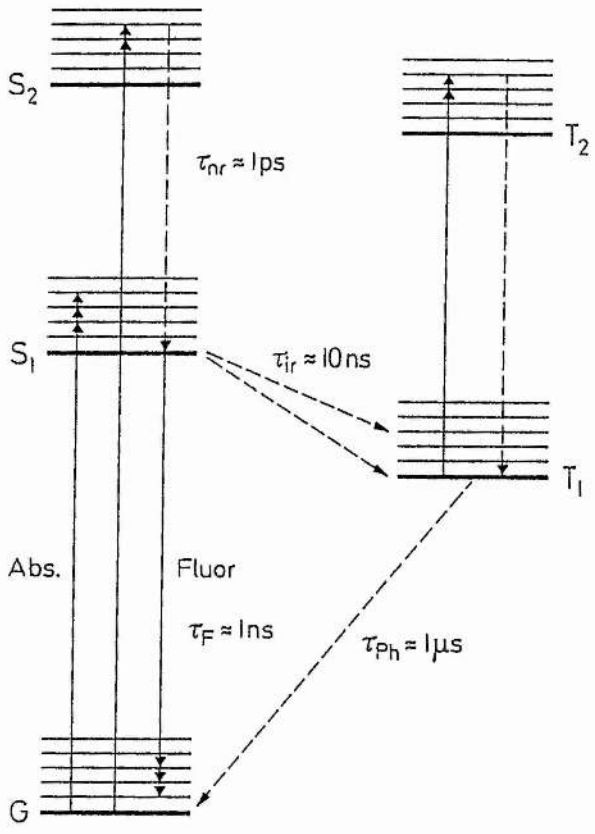

Figure 1. Eigenstates of a typical dye molecule with radiative (solid lines) and non-radiative (broken lines) transitions.

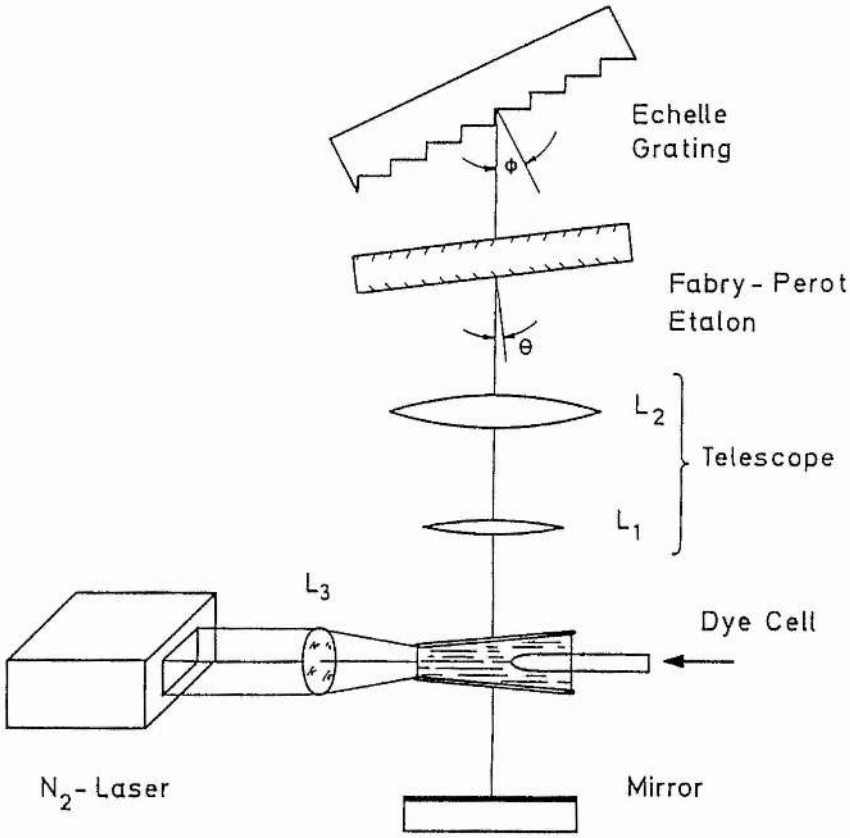

Figure 2. The tunable line–narrowed dye laser of Hansch [5]. Coarse tuning is achieved by rotation of the diffraction grating while fine tuning is schieved using the Fabry–Perot etalon.

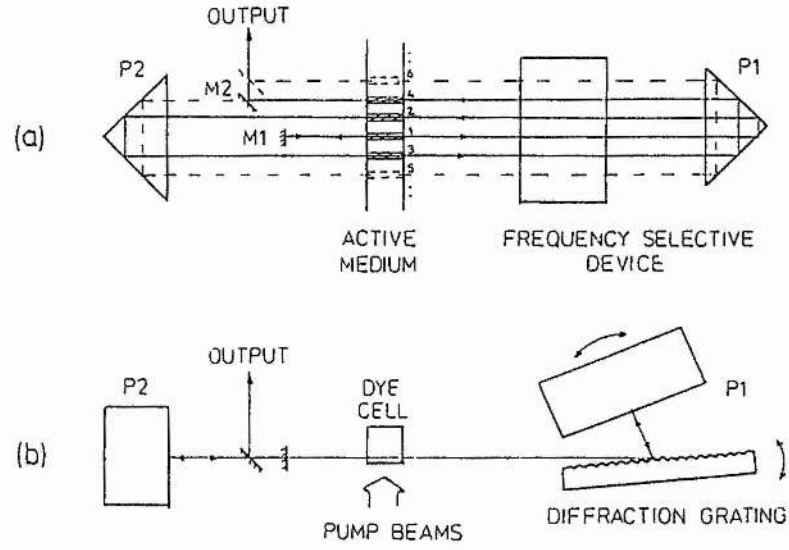

Figure 3. The modeless dye laser of Ewart [8]. (a) Shows the basic geometry of the system while (b) shows the system in plan view. Tuning is achieved by rotation of P1.

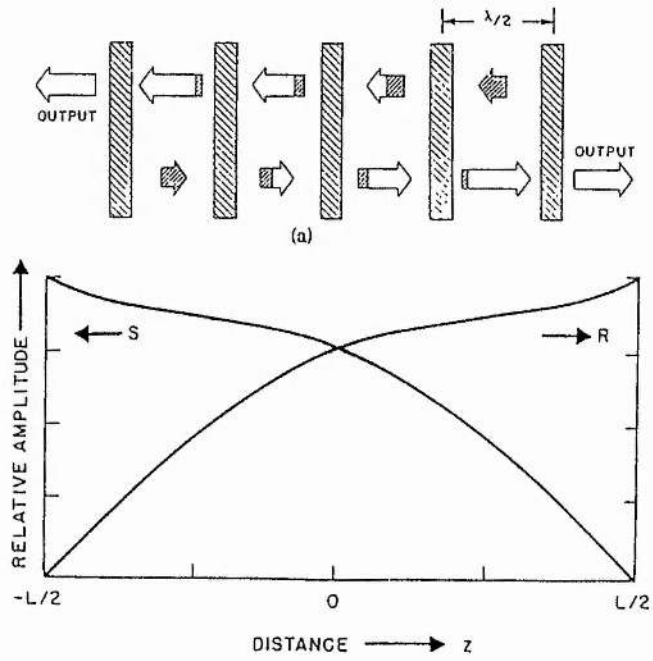

Figure 4. (a) Illustration demonstrating laser oscillation in a periodic structure. (b) Plot of the amplitudes of left (S) and right (R) verses distance. (Obtained from the coupled wave analysis of [9]).

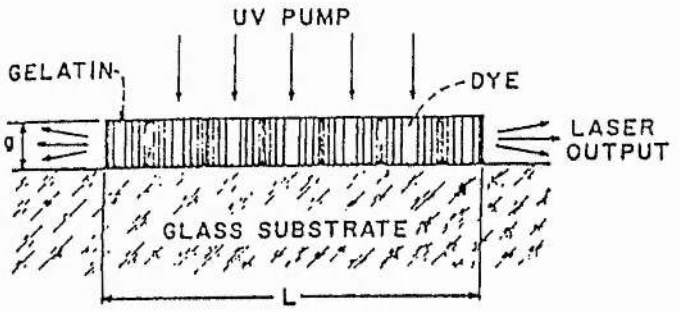

Figure 5. Cross section of the first distributed feedback dye laser of Kogelnik and Shank [10]. The gain region modulation was provided by exposure to two overlapping beams obtained from a He–Cd laser. The structure was transversely pumped by an N_2 laser. Using a modulation period of approximately 300 nm and the dye rhodamine 6G laser action at approximately 630 nm resulted. The linewidth of the device was less than 0.5 Å.

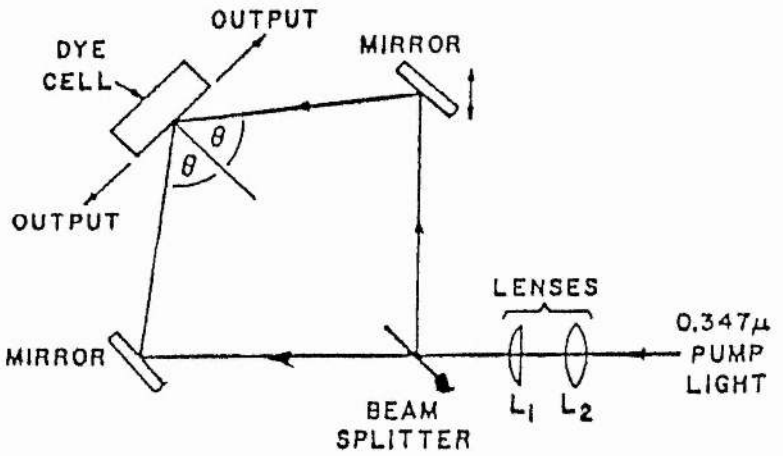

Figure 6. Schematic diagram of the experimental setup of the first Shank style DFDL [15].

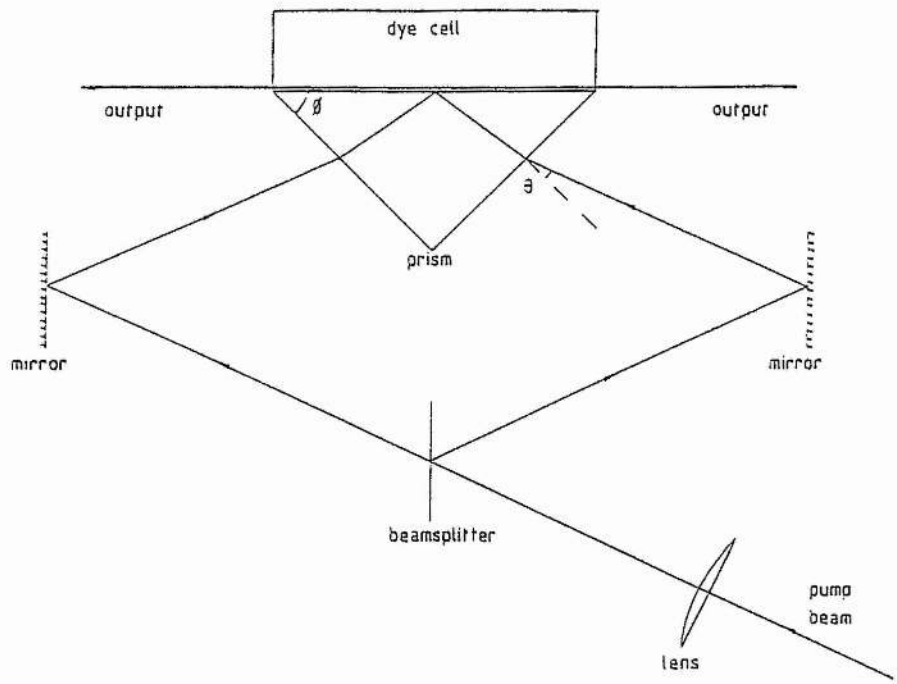

Figure 7. Prism coupled DFDL geometry showing the angle of incidence on the prism θ and the prism base angle ϕ.

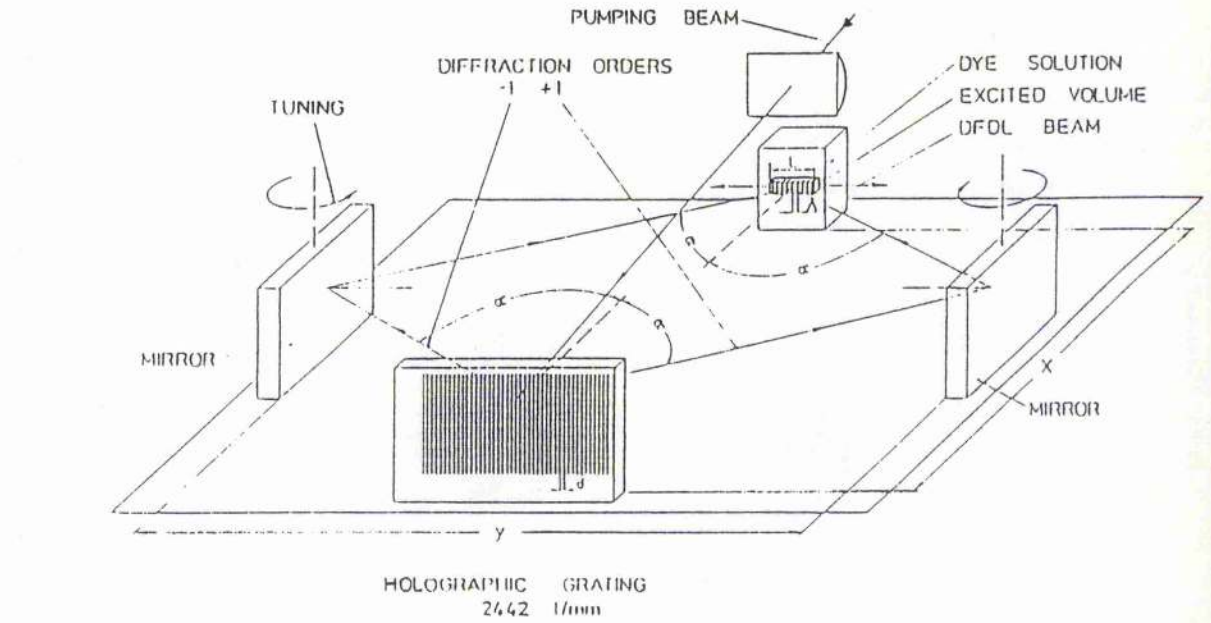

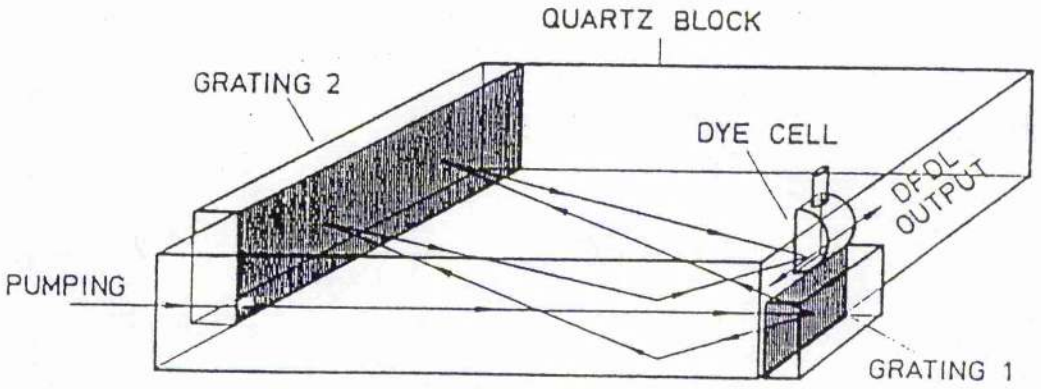

Figure 8. The DFDL geometries of (a) Bor and (b) Szatmari and Racz. In the Bor geometry a single diffraction acts as a beam splitter whereas that of the Szatmari and Racz employs two gratings.

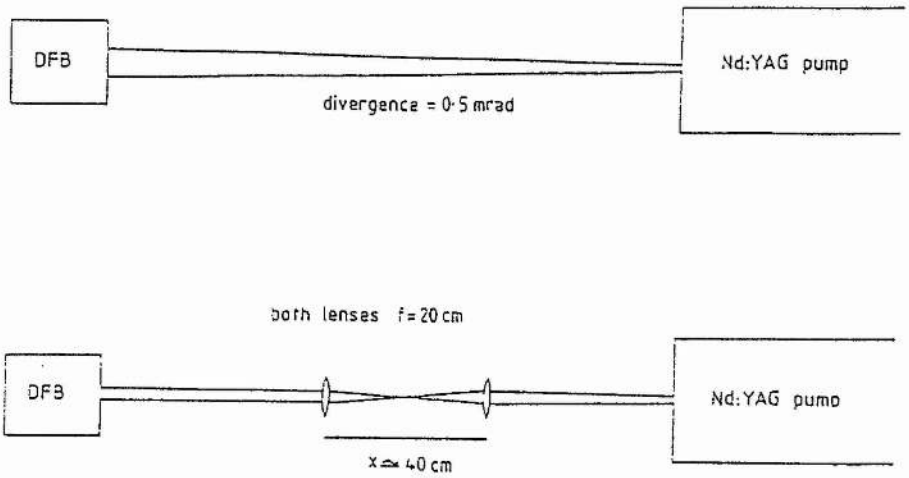

Figure 9. (a) Arrangement used to vary the divergence of the pump beam of the DFDL. (b) The dependence of the DFDL linewidth on lens seperation (and hence divergence of the pump beam).

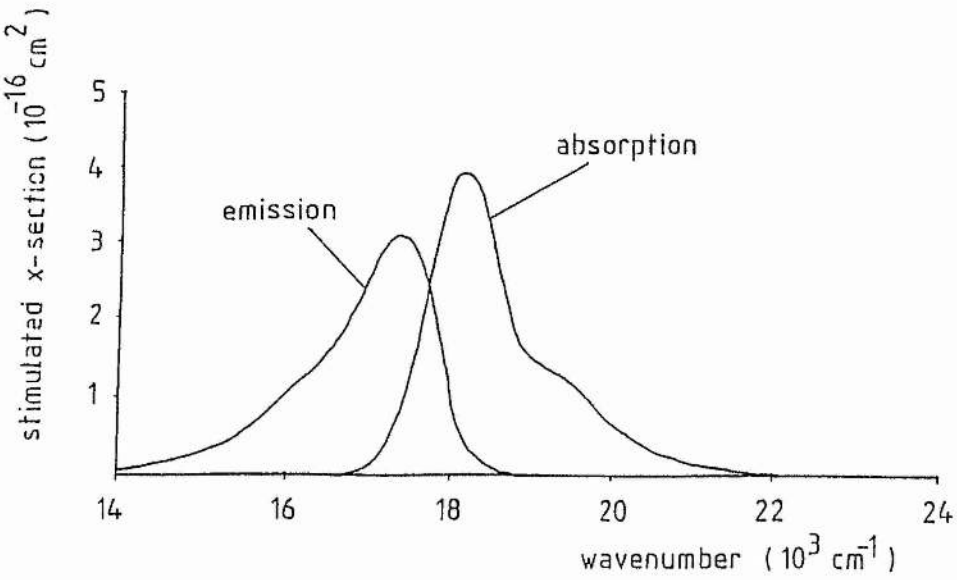

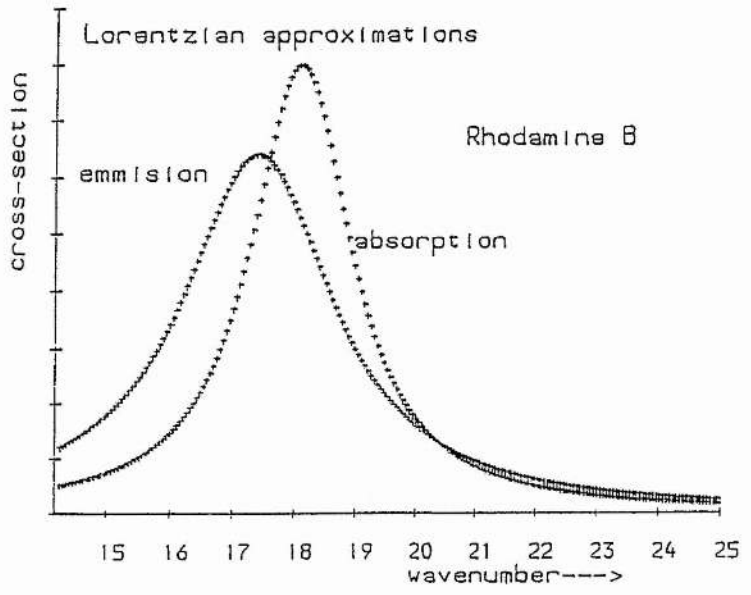

Figure 10. (a) Measured and (b) Lorentzian approximations to the absorption and fluorescence cross-sections of rhodamine B.

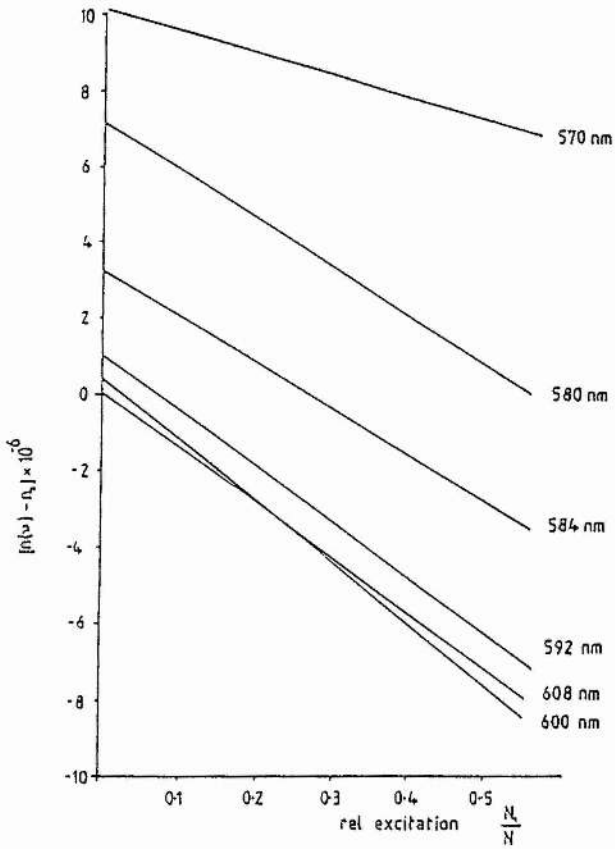

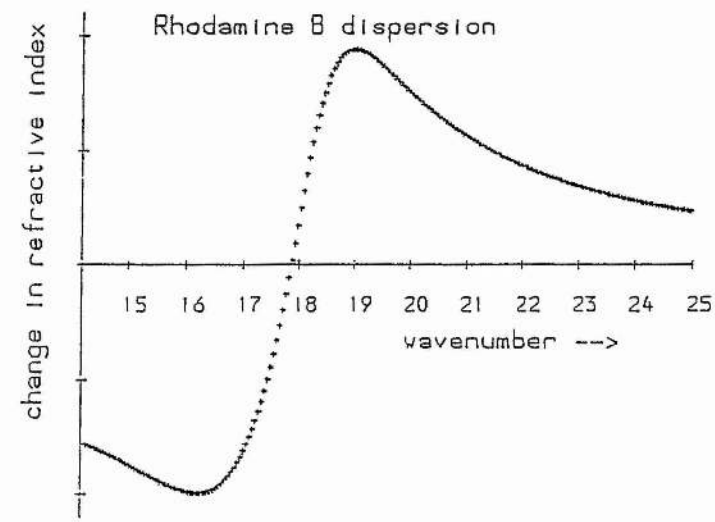

Figure 11. (a) Dispersive contribution to the refractive index, calculated using equation (22) for rhodamine B. (b) Normalised wavelength dependence of the dispersive contribution to refractive index.

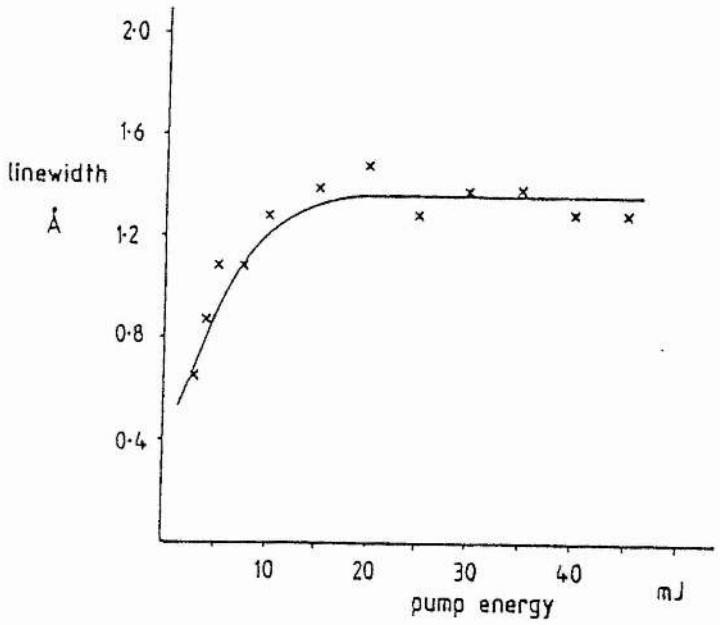

Figure 12. Linewidth of the DFDL as a function of the pumping energy (mJ). Similar to the observed ASE behaviour the linewidth saturates under conditions of a high level of pumping.

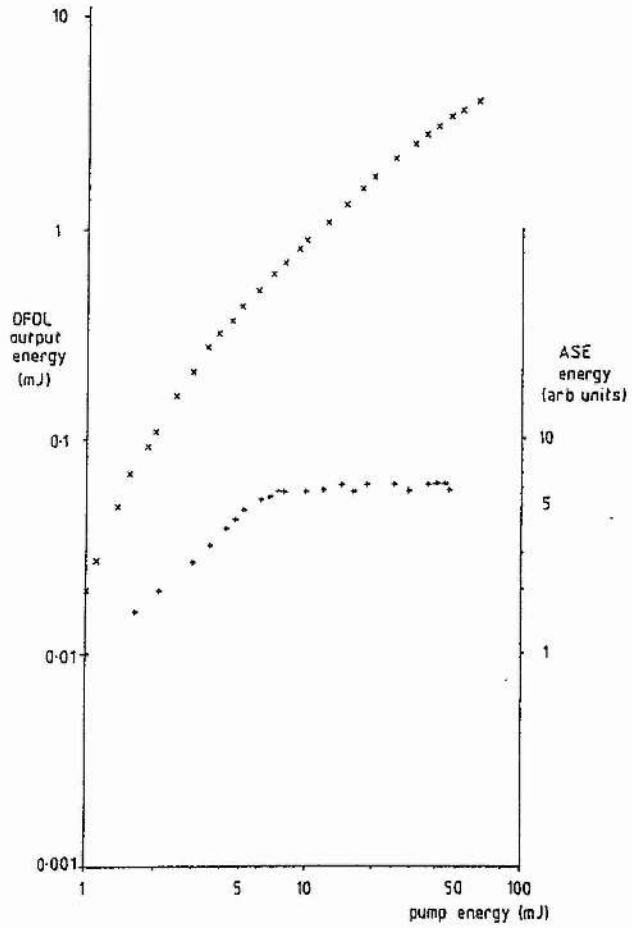

Figure 13. Energy (arbitary units) of amplified spontaneous emission (ASE) in the presence of DFB laser action. Note that at a high level of pumping the ASE saturates.

Chapter II–The experimental laser system.

2.1 Introduction.

In contrast to Chapter I where the concept of the DFDL is described, this chapter presents specific details of the Nd:YAG laser and distributed feedback dye laser systems. The Nd:YAG laser used for the pumping of the DFDL was a modified version of the commercially available Quantel YG 480. Since, as will become apparent later, the parameters of the pump laser have a major influence on the operation of the DFDL, a description of the construction and operation of the pump laser is included. In considering the DFDL specific details of the apparatus used in the construction are presented, together with a brief outline of its performance.

Sections 2.2 and 2.3 consider the Nd:YAG and the dye lasers respectively.

2.2 The Nd:YAG pump laser.

2.2.1 Introduction.

The frequency doubled, Q switched Nd:YAG laser used for the pumping of the DFDL was a modified version of the commercially available Quantel YG480 [1].

Two resonator configurations were available for the laser, the choice of which being determined by the conflicting interests of pulse energy, beam quality and linewidth. To obtain the highest pulse energies an unstable resonator, incorporating an intracavity telescope was employed. This configuration, denoted as the 'standard' configuration by the manufacturers, maximizes the available Nd:YAG rod volume. In the alternative configuration, denoted as 'TEM_{00}' by the manufacturers, a stable resonator is employed, which together with aperturing of the Nd:YAG rod and the incorporation of a solid (L = 10 mm) intracavity etalon ensures operation on the lowest order transverse electro-magnetic mode (TEM_{00}). In the unaltered TEM_{00} configuration the linewidth was measured as approximately 1.5 GHz (as compared with ~ 3 GHz using the unstable resonator). Since the laser cavity length is 1.05 m even the lower linewidth figure represents oscillation over approximately 10 longitudinal modes.

In Chapter I, where a strategy for the development of a narrow linewidth DFDL is presented, it is identified that the pump laser should have a narrow linewidth combined with high temporal and spatial coherence. For this reason the laser was operated in a

modified form, namely with slow Q switching which limited oscillation to a single longitudinal mode (SLM) using the technique of slow Q switching [2–4]. The laser was modified in the laboratory by Andritsakis and Dunn [4]. In this slow Q switched mode, the laser produced SLM, temporally smooth pulses of duration ~ 12 nanoseconds (FWHM). The pulse energy at the second harmonic wavelength of 532 nm was in the region of 0.5 to 1.0 mJ.

The operation of the unmodified Nd:YAG laser is now explained and is followed by details of the operation and action of the slow Q switch.

2.2.2 The standard Quantel YG480.

Introduction.

Figure (1) is a schematic diagram of the layout of the basic laser. The laser consists of two parallel arms, the main laser cavity and the switch-out arm. Following the labelling of figure (1), the laser cavity can be considered as consisting of five main components:

(1) A pumping chamber.

(2) Two highly reflecting end mirrors.

(3) A Pockels cell.

(4) Two quarter wave plates.

(5) A Glan Taylor polariser.

The 3 components of the switch-out arm are the following:

(6) TIR steering prism.

(7) Quarter wave plate.

(8) Second harmonic generator.

The eight components are now considered in turn.

The pumping chamber contains the Nd:YAG rod. The yttrium aluminium garnet $Y_3Al_5O_{12}$ (YAG) crystal is doped at a concentration of 1% with Nd^{3+} ions, has length 115 mm and diameter 7 mm. The rod faces are cut at an angle of 2° from the transversal plane and are anti-reflection coated for the laser wavelength of $\lambda = 1.06$ μm. Providing the pumping for the rod are two close proximity xenon flashlamps. The remainder of the pumping chamber is filled with a resin of magnesium oxide which acts as a diffuser.

The cavity mirrors are positioned at either end of the 1.05 m long cavity. They are of dielectric construction and have a maximum reflectivity at a wavelength of $\lambda = 1.064$ μm. As was outlined above the laser cavity can be operated in one of two geometries which utilize either an unstable or stable resonator. The unstable resonator uses a plane and a divergent mirror (radius of curvature = -3m), whereas the stable resonator uses a plane and a convergent mirror (radius of curvature = 5m). A full description of the two resonator geometries can be found in a later section.

The Pockels cell is an electro-optical component which, in conjunction with the quarter wave plates allows the switching of the cavity Q. The cell is fitted with a KDP crystal orientated such that at zero field the crystal does not affect the polarization of light passing through it. On the application of the suitable voltage (4.2 kV) the cell behaves as a quarter wave plate.

Two quarter wave plates are included in the cavity which are labelled as Q_1 and Q_2 on figure (1). Most of the light to the left of the Glan-Taylor prism is coupled out of the cavity after a double pass through Q_1. Rotation of Q_1 controls the value for the high Q state. Q_2 operates in conjunction with the Pockels cell to allow the switching of the cavity Q in a manner which is described below.

A Glan-Taylor (GT) polariser consists of two prisms separated by a small air gap. The two prisms are constructed of a birefringent material, such as calcite or quartz. Each prism is cut so that the ordinary and extraordinary rays passing through the prism confronts an angle which exceeds the critical angle for one of the rays but not for the other. The second prism is provided to redirect the refracted ray to its original direction of propagation. The GT employed is positioned such that it transmits vertically polarized light while deflecting horizontally polarized light out of the cavity. The polariser is anti-reflection coated on all four faces.

The first component of the output arm of the laser is a steering prism of quartz construction. The output beam from the GT is reflected down the output arm of the laser towards the second harmonic generator after internal reflection from the rear face of the prism. The infrared output beam passes through a quarter wave plate before passing into the second harmonic generator. The wave plate has its optic axis orientated at 45° to the

incident polarization and therefore circularly polarized light is produced after the single pass through it.

The second harmonic generator is the final component in the switch-out arm of the laser. The nonlinear material used is a 12 x 12 x 30 mm parallelepiped crystal of deuteriated potassium dihydrogen phosphate (KD^*P). The crystal employs type II phase matching and is angle tuned. The frequency doubled output is plane polarized at a wavelength of λ = 532 nm. The crystal is surrounded by index matching fluid and hermetically sealed in a cell. The cell windows are AR coated for the laser fundamental wavelength of $\lambda = 1.064$ μm.

Action of the laser Q switch.

The technique of Q-switching is an established way of obtaining intense short bursts of radiation from lasers. The laser cavity quality factor Q is lowered by some means during the pumping of the lasers active medium so that the population inversion can build up to a very high value without the laser oscillating. The laser cannot oscillate when the cavity is in this low Q state because the gain of the laser is well below the loss. When the inversion reaches its peak the Q of the laser cavity is switched from a low to a high value. The gain in the laser medium is now well above threshold and a rapid build-up of laser action results. Since, at the high intensities produced the population inversion (and hence the gain) is quickly depleted, Q-switched pulses tend to be shorter than the duration of the radiation providing the pumping. Since this method uses the active medium to provide energy storage, Q-switching is most profitably used in those active medium with relatively long lived excited state lifetimes.

Operation of the Quantel Q-switch.

The action of the Q-switch is as follows. Normally no voltage is applied to the Pockels cell. As was explained above, when no voltage is present on the cell it has no effect on light passing through it. Horizontally polarized light from the gain medium is coupled out of the cavity by the Glan Taylor (GT) prism. Vertically polarized light, which passes through the GT polariser, is rotated though 90° by the double pass through the quarter wave plate which is labelled as Q_2 on figure 1. Since this horizontally polarized light is

now coupled out of the cavity the cavity is completely lossy i.e. it is in its low Q state. When the appropriate voltage is applied to the Pockels cell, so that it acts as a quarter wave plate, vertically polarized light, after a round trip through the cell and the passive quarter wave plate, then retains its vertical polarization and therefore remains inside the cavity. Q_2 is orientated so that most of the light passing through it is subsequently reflected out of the cavity by the Glan Taylor prism leaving a small proportion (5%) to recirculate through the cavity for further amplification.

Resonator configurations.

As was stated previously the laser can be operated with one of two resonator configurations. Figure 2(a) is a schematic diagram of the 'standard' geometry. The basic resonator structure is formed by using a diverging (R = -3m) and a plane mirror. The cavity also contains a diverging telescope and two 6mm diameter aperture in order to make maximum use of the Nd:YAG rod volume. The diverging telescope also serves to compensate for self focussing in the thermally distorted Nd:YAG rod and can be adjusted to minimize the output beam divergence. A converging telescope is situated in the output arm of the laser which reduces the beam size for efficient second harmonic generation. Using the laser in this configuration resulted in the production of pulses of energies of around 330 and 110 mJ at the wavelengths of λ = 1.064 μm and 532 nm respectively.

Figure 2(b) is a schematic diagram of the 'TEM_{00}' geometry. In this geometry the laser uses a converging mirror (R = 5m) in conjunction with a plane mirror. In transferring from an unstable to a stable resonator geometry, where less of the Nd:YAG rod is used leads to a sizable decrease in available pump power. The cavity mode diameter is reduced over that of the standard configuration by the use of two apertures which have diameters of 2.1 and 1.9 mm. A 10 mm etalon was included in the cavity which resulted in the production of pulses of energies of around 20 and 1.5 mJ at the wavelengths of λ = 1.064 μm and 532 nm respectively, with linewidths of around 1.5 GHz at 532 nm.

2.2.3 The modified Quantel YG480.

The laser used to pump the DFDL in most of the experiments described in later chapters of this thesis was a modified version of the Quantel YG480. In particular, a slow Q

switch was developed which allowed the production of SLM pulses. In the following, the technique of slow Q-switching is firstly discussed together with details of the modification made to the laser.

Slow Q-switching [2,3] is a technique which allows the reliable production of single longitudinal mode pulses in pulsed Nd:YAG lasers. In normal, or active Q switching, the cavity Q is switched from a low to a high Q at some predetermined time when the gain of the medium is greatest. On switching the Q a large number of modes experience gain and contribute to the output of the laser pulse. For the short pulse duration of ~ 12 ns there is insufficient competition between modes to allow any favoured mode to dominate. In slow Q-switching the cavity Q starts off at some intermediate Q which, when the gain of the active medium is near its maximum value, can just support laser oscillation. When the laser oscillation occurs in this situation, i.e. without the action of the cavity Q-switch, the laser is said to be free-running. When the laser is free running the output is seen to consist of a damped train of microsecond duration pulses called relaxation oscillations. The physical mechanism leading to such relaxation oscillations is an interplay between the light flux (or photon density) in the resonator and the population inversion of the active medium. An increase in light flux decreases the population inversion due to the increased rate of stimulated emission transitions. As a consequence the laser gain is reduced which in turn tends to decrease the intracavity intensity. These relaxation oscillation pulses have durations which are much longer than those of Q-switched pulses. The linewidth of the relaxation oscillation pulses tends to be narrower than those of Q-switched pulses for a number of reasons. Firstly the gain of the medium only just exceeds the cavity loss when the laser is free running, and, as such, a much reduced number of cavity modes experience gain. Because of the increased pulse duration the pulse undergos a large number of cavity round trips. This improves the selectivity of any frequency devices present in the cavity. Finally the increased pulse duration leads to increased competition between modes. Thus the established relaxation oscillations present in the laser when it is free running in the intermediate Q state can be considerably line-narrowed over that of a normal Q switched pulse. If the technique is employed to its full then the result can be the establishment of a pulse with oscillation on one cavity mode. This mode is coupled out of

the cavity where it is detected. The signal from the detector then initiates the switching of the Q to a high value. On switching to a high Q a large number of modes experience gain. However that mode forming the pre-lase pulse grows much more strongly than other modes which must establish their oscillation from a noise level so that single mode oscillation is maintained throughout the Q-switched pulse. This slow Q switching technique was applied to the Quantel Nd:YAG laser resulting in reliable production SLM operation. Details of the modification to the Quantel laser are now presented.

The laser used the TEM_{00} resonator configuration (see section 3.2.2). As explained above the principle of slow Q switching is to initially set the cavity Q at an intermediate value, detect laser oscillation when it occurs and thereafter switch the cavity Q on the established mode. Increasing the cavity Q is achieved in practice by a small rotation of Q_2 hence allowing some of the light within the cavity to recirculate within it. As the flashlamps pump the YAG rod and the gain increases until the gain just equals the loss and the laser begins to oscillate. Relaxation oscillations occur in this situation with a period of around 1–5 μs. Most of the modulated output of the laser is coupled out of the cavity via the GT prism. This light is then used to initiate the switching of the cavity Q to a high value. A small (5 x 7 mm) prism was placed on the face opposite of the GT from which the high power output is taken. The output from this prism was then reflected onto a photodiode (Hamamatsu PIN S1188 [5]). Once detected the optical pulse initiates the operation of the feedback by applying the appropriate high voltage to the Pockels cell, hence switching the cavity Q to a high value. The feedback circuit consists of the PIN photodiode, a logic circuit, and the standard 'fast switching circuit' which provides the HT to the Pockels cell. The logic circuit was designed and constructed in the Departments electronics workshop by J.Wade. Full details, including a circuit diagram can be found in [4]. In essence the logic circuit takes the output of the photodiode and converts it into a signal which is suitable for the Quantel's standard switching circuit. In order to avoid spurious signals occurring due to the large amounts of electrical noise which occurs when the flashlamps fire the logic circuit is first primed by a signal from the laser which is present to initiate the firing of the flashlamps. The logic circuit only accepts signals from the photodiode at a preset time after the firing of the flashlamps.

It was found [4] that by reducing the rate of switching of the Pockel's cell, SLM operation was encouraged. To this end a simple LCR (inductive, capacative and resistive) damper was incorporated into the fast switching circuit.

Specifications of the modified Nd:YAG laser.

The specifications of the modified Nd:YAG laser are now discussed. As has been stated above, the modified laser provided pulses of duration ~ 12 nanoseconds (FWHM) with a pulse energy of between 0.5 and 1.0 mJ at a wavelength of 532 nm. Examples of the temporal form of pulses produced by the laser are shown on figures 3(a) and 3(b). Evaluation of the frequency spectrum of the Q-switched pulse is now considered. For reasons that will shortly become apparent, in order to ascertain that SLM operation has been attained, measurements must be carried out simultaneously in both the frequency and time domains. Temporal pulse measurements were obtained using a 275 MHz oscilloscope and fast (~ 30 GHz) photodiode giving an overall risetime of 1.3 nano-seconds. A description of the pulse measurement system may be found in chapter VI. As can be seen by the figures the pulses may be smooth or show mode beating. As will be seen below the smooth pulses represent operation of the laser on a single longitudinal mode. The laser linewidth was measured as less than 300 MHz at (λ = 532 nm) by using the 1.5 GHz free spectral range confocal interferometer which is described in chapter III of this thesis. However, the figure of 300 MHz represents an upper estimate of the laser linewidth since its represents the finesse of the interferometer at 532 nm. Since the intermode spacing of the laser is approximately 150 MHz this linewidth could represent oscillation on two adjacent modes. In this case the temporal profile of the laser can be used to establish the frequency spectrum of the pulse. If two adjacent modes are oscillating a beat wave between them is produced. The beat period is equal to the reciprocal of the intermode spacing, which for the 1.05 m cavity length, is around 6 ns. The temporal form of the optical pulse can therefore be used to obtain information about the pulse linewidth. Two modes oscillating with relative intensities I_1 and I_2, with difference frequency will have a temporal form which is given by,

$$I(t) = F(t) [I_1 + I_2 + 2 \sqrt{(I_1 I_2)} \cos(\omega t)] \qquad (2.1)$$

where F(t) describes a smooth pulse that is modulated by the (cosinusoidal) beat frequency term [6]. Figures (4 a–d) plot the function described by equation (1). In (4a) the ratio of the intensities is 10:1 while in the (4b) the ratio is 100:1. The modulation of the pulse is proportion to the ratio of field amplitudes, i.e. in the case of 10:1 ratio of intensities the modulation is $\sqrt{10}$:1. These represent the temporal behaviour of the output at the fundamental wavelength of 1.06 μm. Figures (4c) and (4d) again represent the temporal behaviour of the 10:1 and 100:1 ratio of intensities. These figures represent temporal behaviour of the intensities after second harmonic generation. As the second harmonic generation efficiency is proportional to the square of the input power the effect in the time domain is to square the modulation of the pulse. The increased sharpness in the temporal domain can be explained in the frequency domain using a simple Fourier analysis. The two frequencies components (with frequency f_1 and f_2 will, after second harmonic generation (or any nonlinear process) produce frequencies at $2f_1$, $2f_2$ and also the sum frequency $f_1 + f_2$. As can be seen from the figures a mode beating may be observed in the second harmonic pulse even when the ratio of the intensities in the fundamental is 100:1. Since all pulse measurements were measured at the second harmonic wavelength of 532 nm it may be concluded that the output pulses of the type illustrated on figure 3 (a) represent oscillation on a single longitudinal mode.

On passing through the frequency doubler, the radiation is reflected off two dichroic mirrors to separate the second harmonic from the fundamental. the 532 nm component then makes three round trips through a delay line consisting of two 75 mm multi–layer dielectric coated plane mirrors separated by approximately 1.5 m. The purpose of the delay line is to allow higher order modes to diffract out. Divergence increases the beam size from 7 to 14 mm before being incident on the dye cell apparatus which is now considered.

2.3 The distributed feedback dye laser.

2.3.1 Introduction.

This section describes the apparatus used in the operation of both the Shank and the Bor style DFDL geometries. The geometries described were those used in the experiments

described in later chapters. The essential features of both designs are outlined in Chapter I where it is seen that the only difference between the two geometries lies in the method of splitting the pump beam before producing the feedback grating. As has been described previously in the Shank system a beam splitter is used whereas, in the Bor system a diffraction grating is employed. All other components of the system are common to both designs. The components of the two geometries are first described and this is followed by details of the operation of the devices. Schematic diagrams of the Shank and the Bor structures can be found in chapter one (figures 5 and 6).

2.3.2 The DFDL components.

The components of the dye laser systems consist of the following apparatus; cylindrical lens, a beam splitting element (beam splitter or diffraction grating), two beam steering mirrors, a coupling prism and a dye cell. These components are now described.

The cylindrical lens used was a Melles Griot high precision cylindrical lens with a 30 cm focal length (01 LQC 008) [7]. Using this lens in conjunction with the Nd:YAG laser a diffraction limited focus of approximately 30 μm was theoretically possible, although, in practice the focussing was relaxed to produce a pumped region of between 100μm to 200μm. The lens was held in an Oriel 3 axis mount (no. 2510) [8]. Using the Shank geometry the rotation angle around the beam propagation direction was the most critical adjustment. As will be seen later in chapter VI, rotation of the lens could be used to vary the degree of overlap between the two pump beams.

When the DFDL was used in the Shank configuration, a 50% beam splitter (obtained from CVI [9]) was mounted in a NRC beamsplitter mount (MM–2A). When used in the Bor configuration a 1200 lines per mm square sinsuiodal holographic diffraction grating diffracted the incident pump beam into the +1 and -1 diffraction orders at an angle of ~ 39° from the grating normal. A sinusoidal grating was employed since this grating only diffracts energy into the first orders hence obtaining high efficiency (approximately 30% into each order [10]). The grating was obtained from Optometrics Ltd.

The beam steering mirrors were 2.54 cm diameter multi-layer dielectric coated mirrors obtained from CVI optics (item no Y2-10-30), specially designed for high reflectivity at an angle of incidence of 30°. These were held in standard Ealing beam-steering mounts.

The quartz dye cell used was a flowing type (Lambda Physik FL42/2). The inside diameter of the cell was marginally larger then the induced grating length. The cell was tilted to 10° from the vertical to prevent parasatic lasing between the two end faces. For some experiments cooling of the dye was necessary (see chapter IV where the thermo-optical properties of commonly used dye laser solvents are investigated). To allow this, the dye was circulated using a Coherent model 460 dye circulator and, by insertion of the dye filter assembly into a refrigerated bath of water/ethylene glycol, cooling of the solvents down to -2°C was possible.

A 45°quartz prism (see Chapter I) was mounted on the entrance face of the dye cell using the silicon oil 'Baysilicon M1000' as index matching fluid.

With the exception of the cylindrical lens, all components were mounted on Ealing minibenches. Two parallel arms were used, the beam-splitting and steering assembly were mounted on a 500 mm minibench while a 200 mm minibench supported the dye cell. Figure 7 is a scale drawing of the minibench DFDL system.

2.3.3 Basic experimental DFDL details.

When characterizing a laser the parameters of interest include the threshold of operation, the energy efficiency, the physical characteristics of the output beam, the tuning range and factors about the lasers temporal and linewidth behaviour. These first four parameters are now briefly considered, the other two form a substantial part of the subject matter of other chapters of the thesis.

As a dye laser the output parameters are, to a large extent, determined by the properties of the dye used as the laser's gain medium. As an example the operating wavelength of the laser must lie within the dyes gain bandwidth which is obviously dependent upon the type of dye used. As will be seen later, five laser dyes were employed in the efficient operation of the laser in the wavelength range of 580–680 nm. For a particular dye the efficiency is wavelength dependent, maximum efficiency being obtained when the laser is

operated in the region of maximum gain. In order to present a reasonable indication of the laser's performance under typical operating conditions, the remainder of the data presented in this section refers to that dye which was most commonly used; rhodamine B.

Using rhodamine B the threshold for distributed feedback lasing required a pump energy of about 0.1 mJ (10 kW). For a pump energy of 10 mJ the efficiency of the DFDL was around 18%. The measured beam divergence of the output beam from the dye laser was 11 mrad by 17 mrad. Using the dye the device could be tuned over the range of 580–630 nm. Figure (8) is a plot of the operating wavelength of the laser plotted as a function of the angle of incidence of the pump beams on the prism (obtained using equation (5) of Chapter I). Figure (9) shows the experimentally obtained tuning range of the laser using rhodamine B. Tuning over some 10 nm was possible by rotation of the beam steering mirrors only, but outwith this range it was found necessary also to translate the mirrors. As will be seen in later chapters, the temporal and linewidth behaviour is dependent on a variety of parameters such as pump power, the length and visibility of the feedback grating, and the dye/solvent combination used. These factors form the subject matter of the remainder of this thesis.

2.4 Summary and conclusion.

In this chapter the lasers used in the experiments of later chapters have been described. The Nd:YAG laser used for pumping of the DFDL was used in a modified form which utilises the technique of slow Q switching to provide SLM pulses of between 0.5 and 1.0 mJ with a duration of around 12 nanoseconds (λ = 532 nm). The DFDL was used in both the configurations of Shank and Bor. Basic experimental details of the DFDL were presented i.e. the tuning range, threshold power efficiency etc. These are further considered later, together with a complete description of the temporal and linewidth properties of the laser .

Chapter II References

[1] Quantel SA: 17, avenue de l'Atlantique, Orsay, France.

[2] Y. Park and B. Byer: Optics Commun., **37**, 6,(1981).

[3] A. Berry, D. Hanna and C. Sawyers: Optics Commun., **40**, 6,(1981).

[4] A. Andritsakis: M.Sc. Thesis University of St Andrews, (1985).

[5] Hamamatsu UK distributor: Hakuto International (UK) Ltd, Leigh on Sea, England.

[6] W. Fountain and M.Bass: IEEE J. QE-18,432,(1981).

[7] Melles Griot: Optics Guide 4, 1 Fredrick St, Aldershot, England.

[8] Oriel Scientific Ltd, 1 Mole Business Park, Leatherhead, England.

[9] CVI, UK distributor: Optilas Ltd, 14 Cochran Cl. Milton Keynes, England.

[10] Optometrics Ltd. Cross Green Approach, Leeds, England.

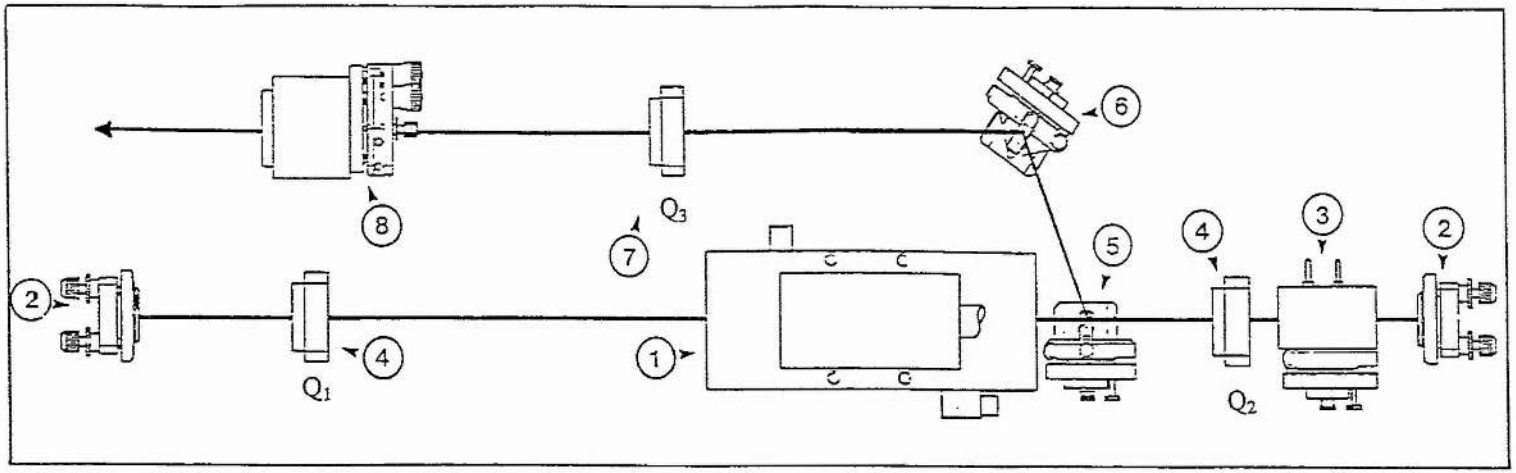

Figure 1) Schematic diagram of the cavity layout of the Quantel Nd:YAG laser. The labelled components are the following:

(1) Pumping Chamber
(2) End mirrors
(3) Pockel's cell
(4) Quarter wave plates Q_1 and Q_2
(5) GT polariser
(6) TIR steering prism
(7) Quarter wave plate Q_3
(8) Second harmonic generator

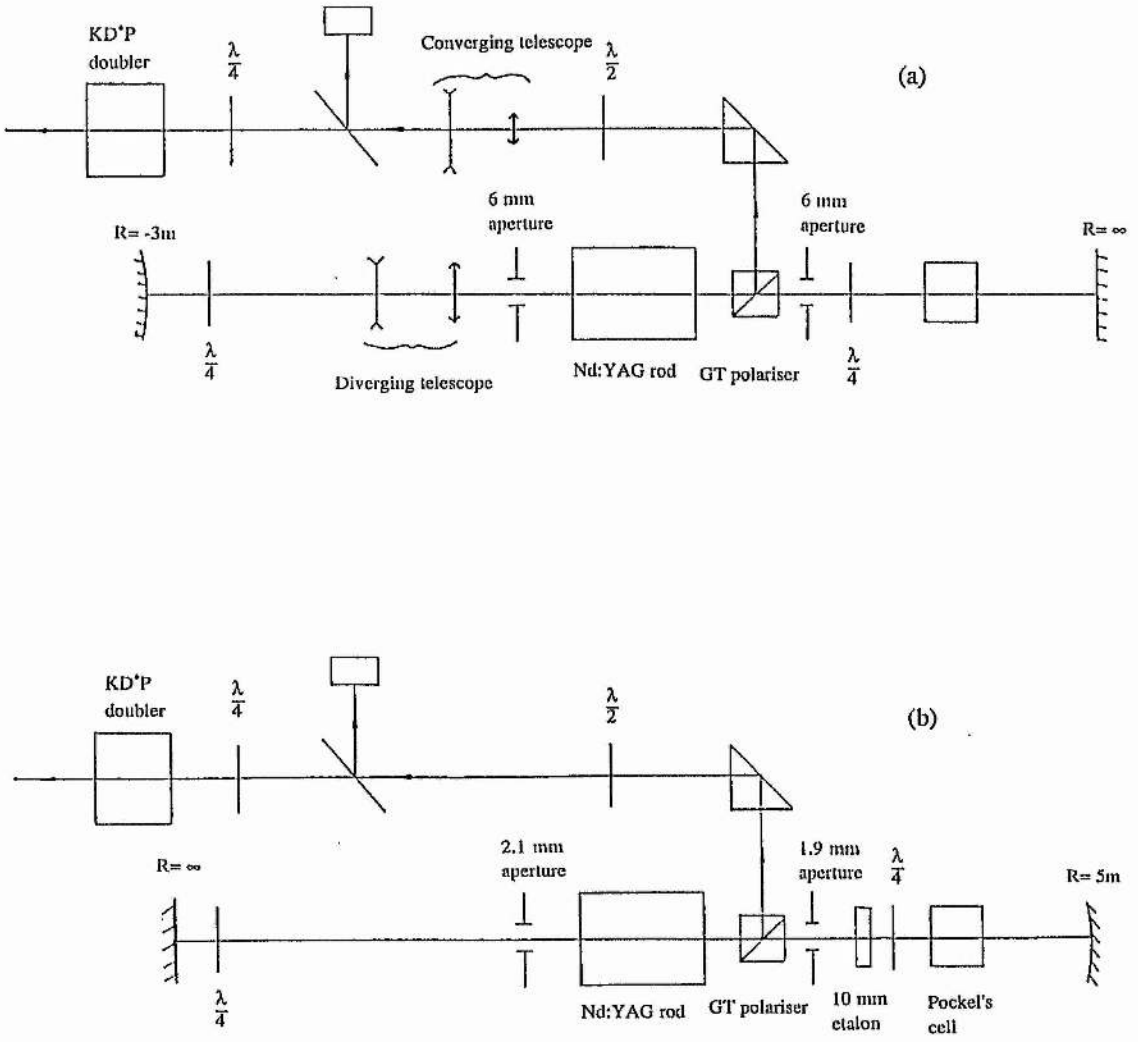

Figure 2. (a) Schematic diagram of the cavity layout of the 'standard' Quantel Nd:YAG laser. By employing an unstable resonator and an intracavity telescope to use all of the available Nd:YAG rod, this geometry maximises the output pulse energy. Pulse energies of ~330 mJ and 110 mJ are available using this mode at the wavelengths of $\lambda = 1.064$ μm and 532 nm respectively. (b) Schematic diagram of the cavity layout of the 'TEM_{00}' Quantel Nd:YAG laser. This geometry employs a stable resonator to achieve laser action on the lowest order transverse mode. The laser has a lower linewidth in this geometry, at the expense of lower pulse energy (70 mJ and 20 mJ spec power at $\lambda = 1.064$ μm and 532 nm respectively).

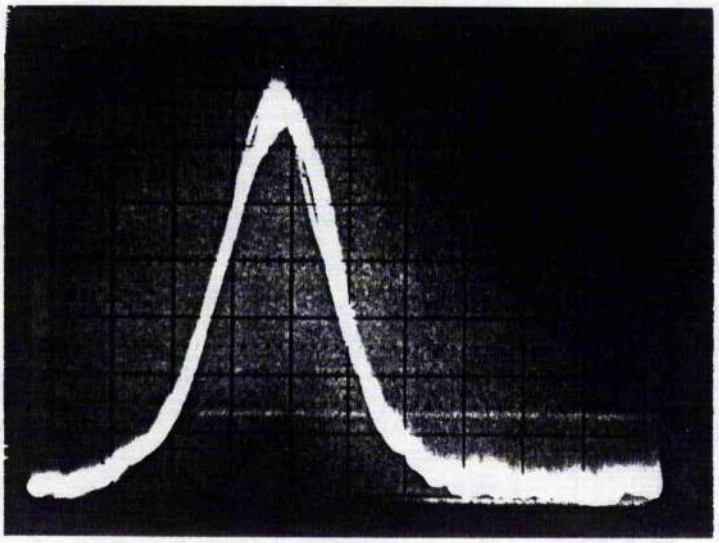

1 div = 5 ns

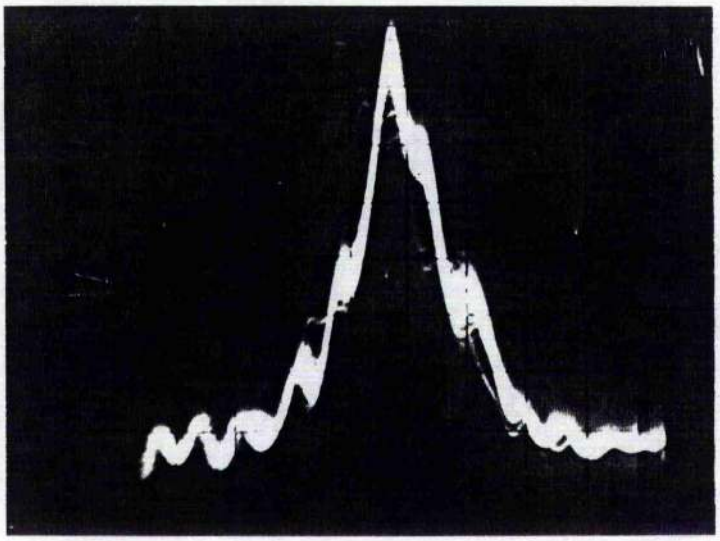

Figure 3. Two examples of the temporal pulse profiles of the Nd:YAG laser (λ = 532 nm). Both traces represent approximately 10 shots. In the upper trace the smoothness of the pulse profile indicates (when combined with interferometric measurements) that the laser is operating on a single longitudinal mode. In the lower trace more than one longitudinal mode is oscillating superimposing a 5 ns beat onto the pulse.

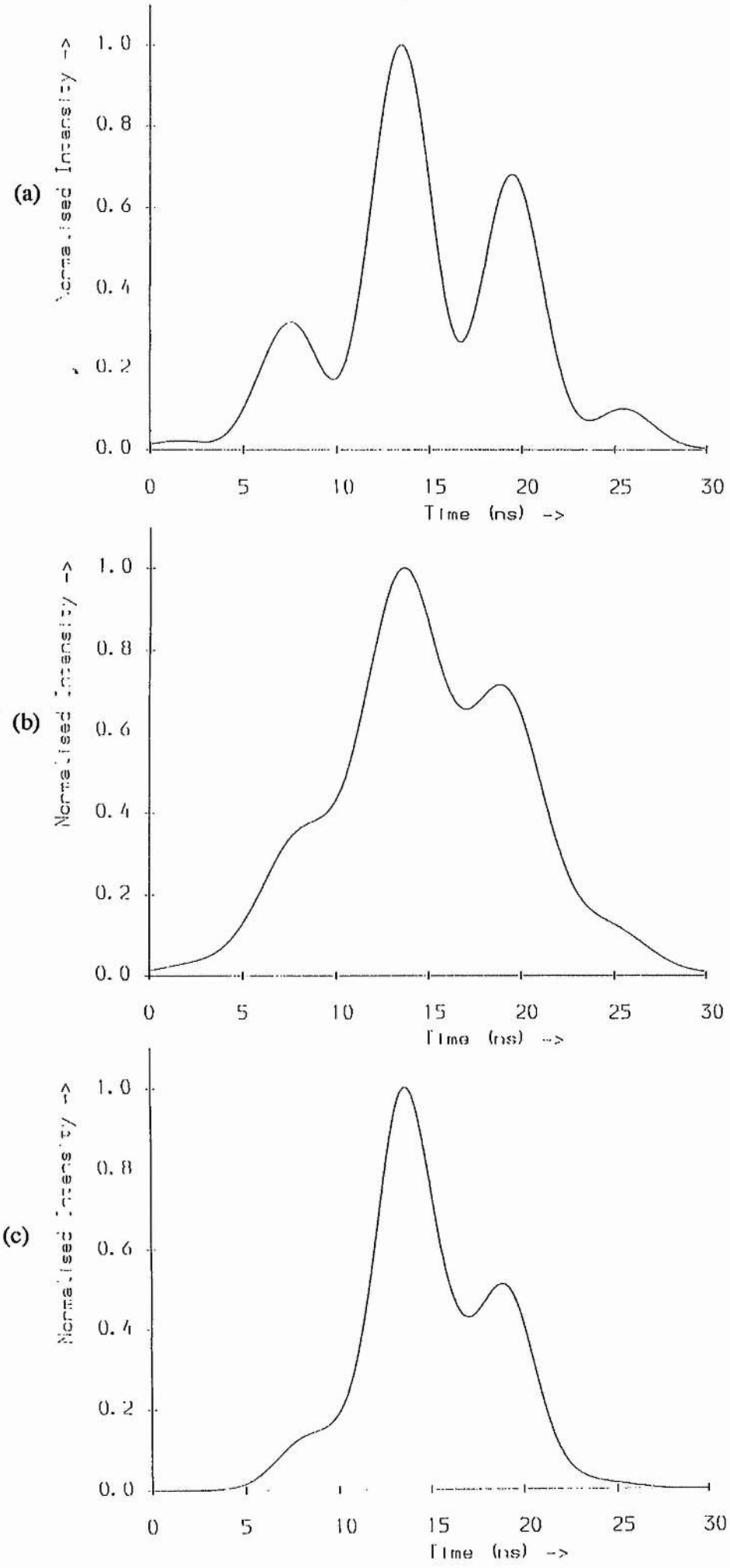
(a)
Normalised Intensity ->
1.0
0.8
0.6
0.4
0.2
0.0
0
5
10
15
20
25
30
Time (ns) ->
(b)
Normalised Intensity ->
1.0
0.8
0.6
0.4
0.2
0.0
0
5
10
15
20
25
30
Time (ns) ->
(c)
Normalised Intensity ->
1.0
0.8
0.6
0.4
0.2
0.0
0
5
10
15
20
25
30
Time (ns) ->

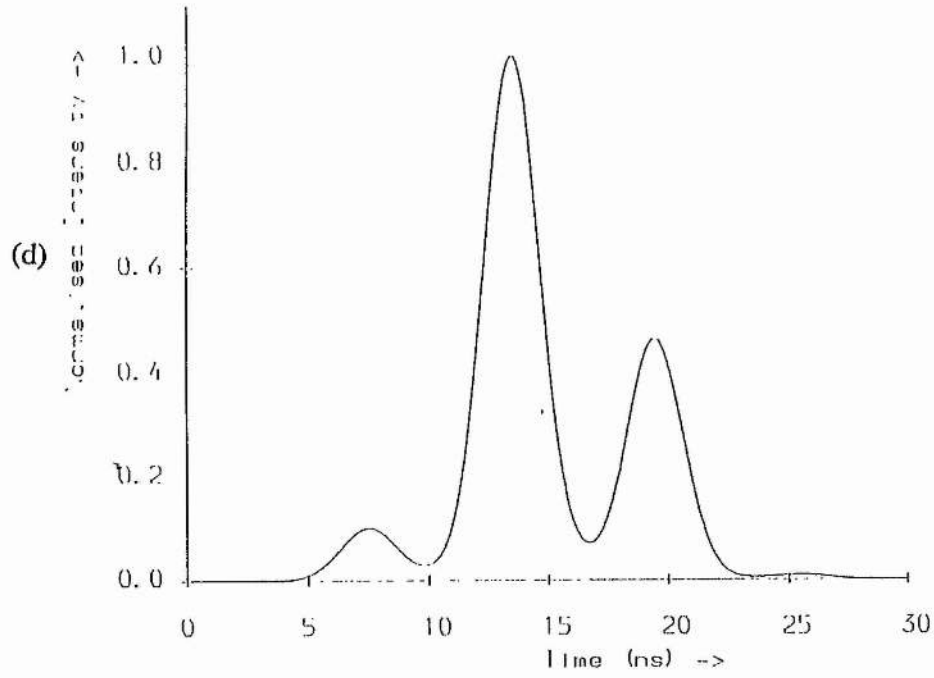

Figure 4. Examples of the beating produced by two adjacent cavity modes as predicted by equation (1). Figures (a) to (d) represent the following:

(a) 10:1 intensity ratio between the modes, signal at fundamental wavelength,

(b) 100:1 intensity ratio between the modes, signal at fundamental wavelength,

(c) 10:1 intensity ratio between the modes, signal at second harmonic wavelength,

(d) 100:1 intensity ratio between the modes, signal at second harmonic wavelength.

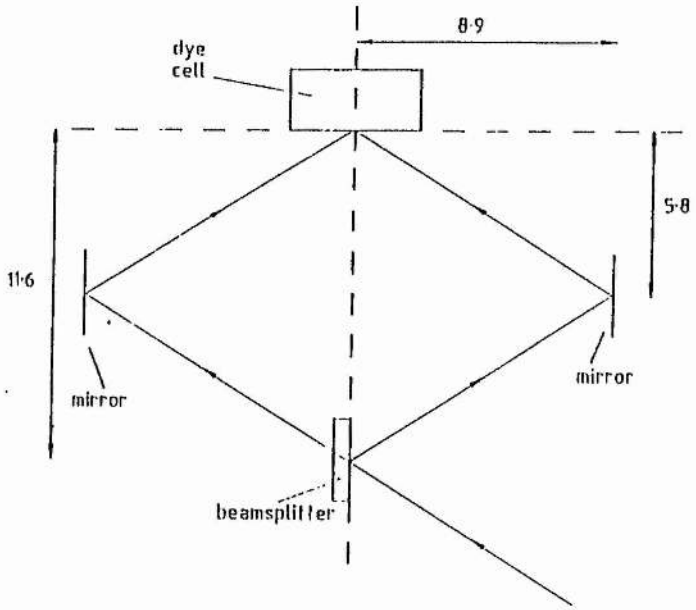

Figure 5. Scale drawing of Shank style DFDL tuned to 580 nm. All dimensions are in cm.

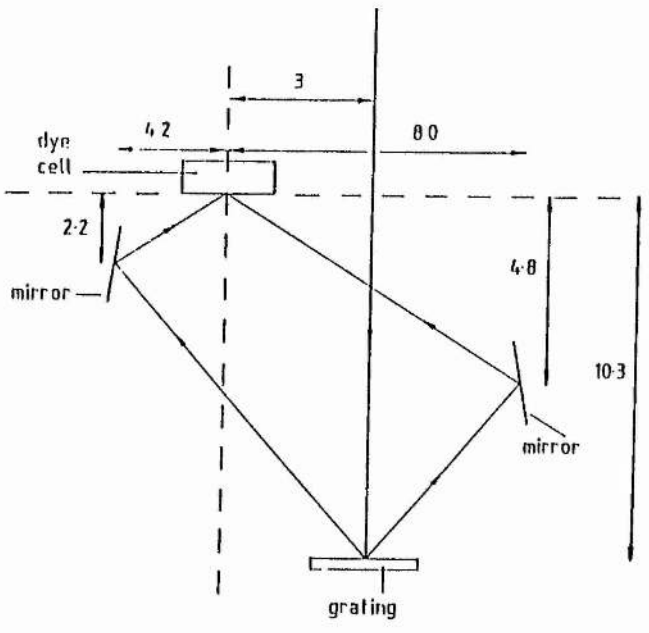

Figure 6. Scale drawing of Bor style DFDL tuned to 590 nm. All dimensions are in cm.

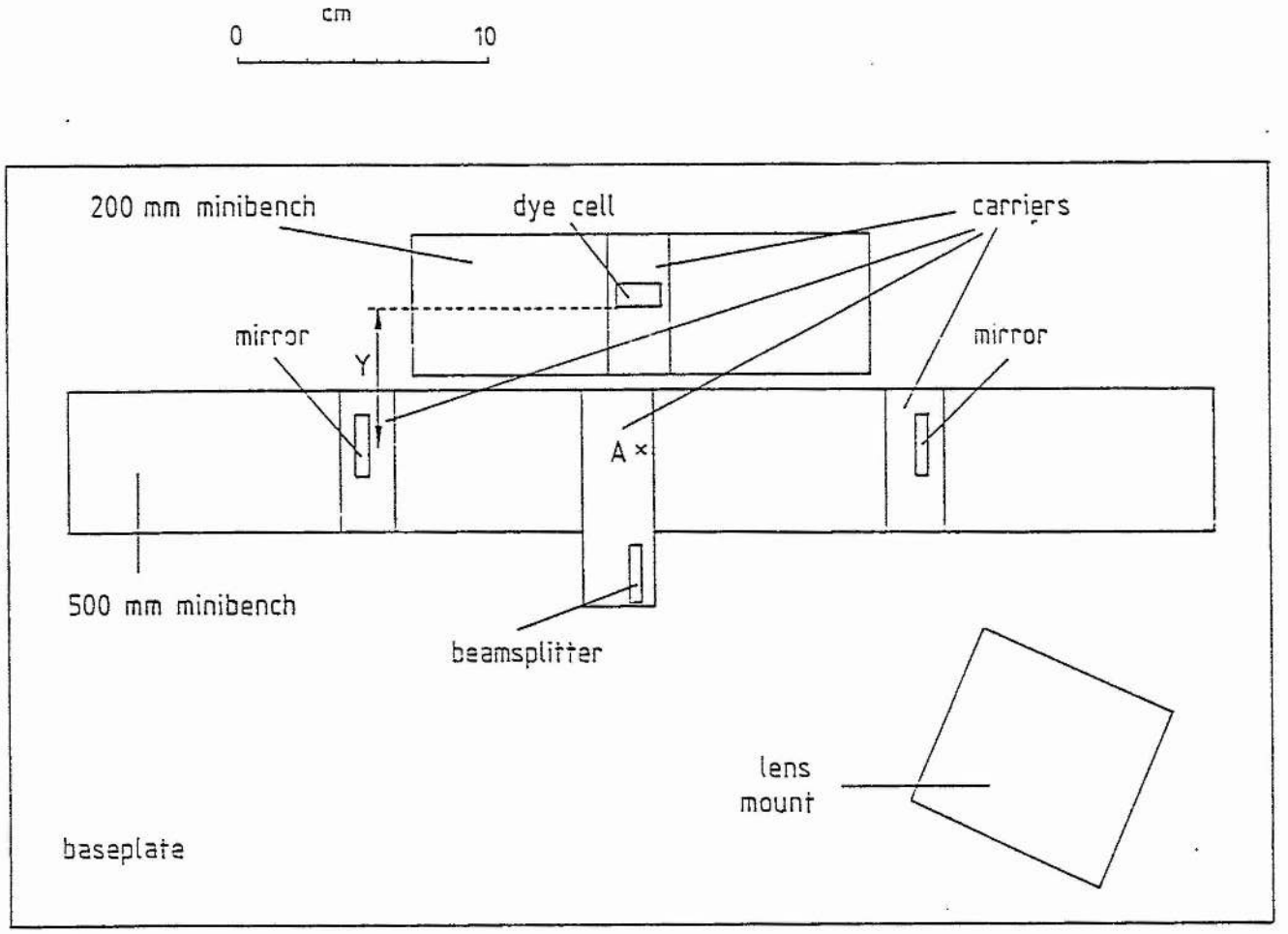

Figure 7. Scale drawing of minibench dye laser system. The holders for the mirrors, beamsplitter and dye cell have been omitted for clarity.

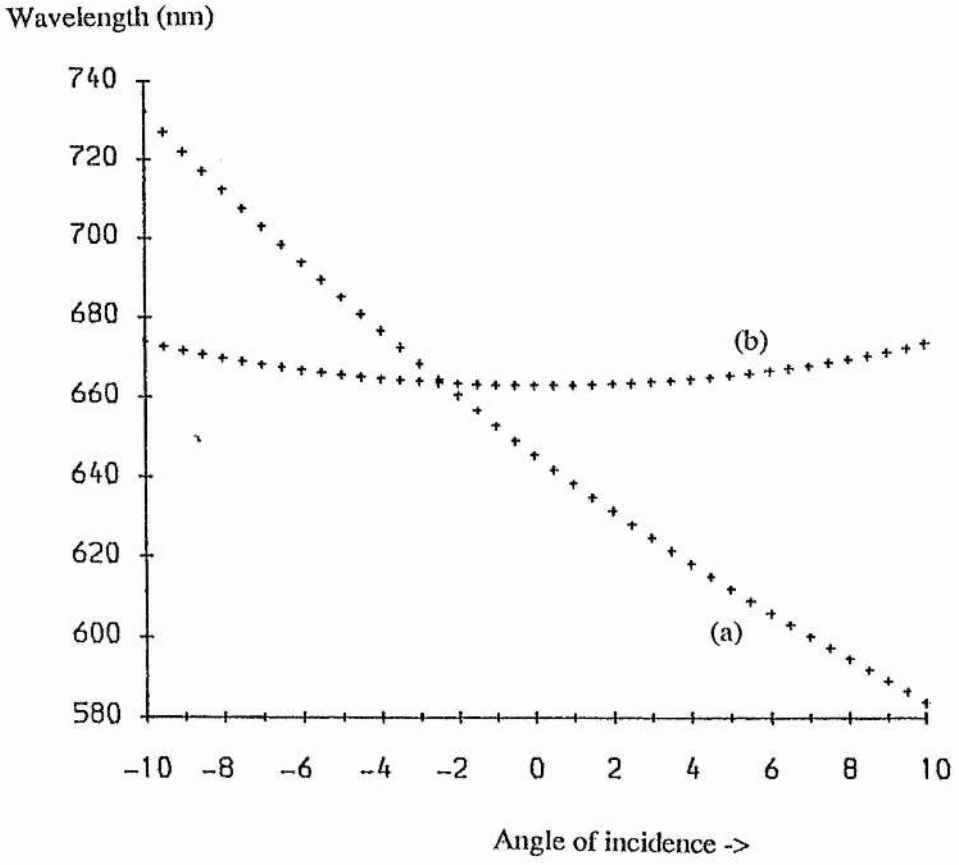

Figure 8. Operating wavelengths of (a) Shank and (b) Bor style DFDL geometries (1200 lines mm^{-1} grating) plotted as a function the of angle of incidence of the pump beam onto the face of the prism coupled DFDL (ϕ=45°).

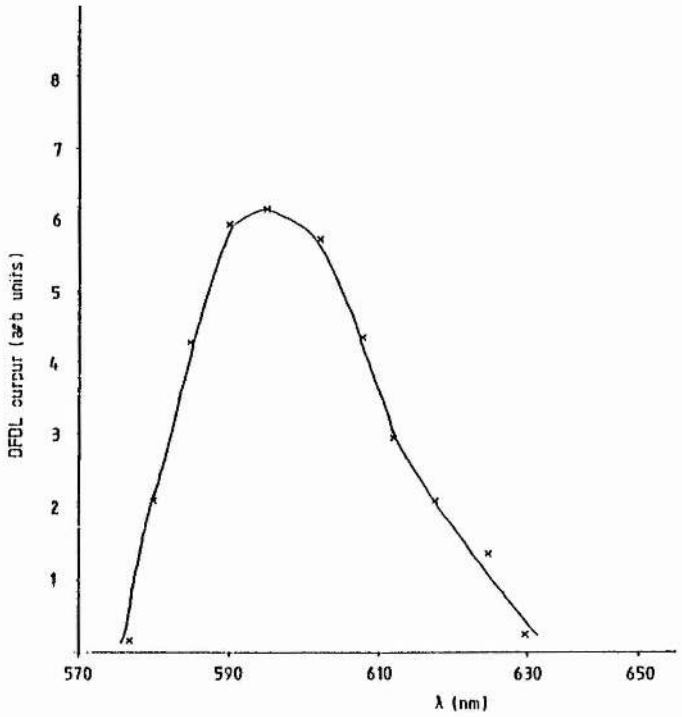

Figure 9. Experimentally observed tuning range when using the dye rhodamine B.

Chapter III–Computer aided interferometer.

3.1 Introduction.

In order to facilitate linewidth measurements at a level approaching the transform limit (around 50 MHz for a 10 ns pulse) of the DFB dye laser an interferometric measurement system had to be constructed. Furthermore the investigation of the lasers shot-to-shot frequency stability (as discussed in chapter II) necessitated that the interferometer had the capability to measure linewidth on a single shot basis. A full description of the system developed is given in this chapter.

A common method of linewidth measurement at this level of resolution uses a Fabry-Perot interferometer. This chapter describes the design, construction and use of an automated interferometric system used to provide single shot measurements of linewidth. The system developed used a non-degenerate confocal interferometer the output of which was coupled, using a projection lens system, to produce an image on the array of a CCD camera. The video output of the CCD camera was then digitised and stored in a video framestore before being read into a computer memory. The computer program could then display directly the intensity/position of the interference pattern and hence linewidth may be determined. An acronym for this computer assisted interferometry is CAIN. It was the use of the video framestore which allowed the system to make single shot measurements since it stored the image and allows subsequent video display or analysis by computer.

In section 2 of this chapter the design and construction considerations for this CAIN system are described detailing the interferometer, the CCD camera, the video framestore and the computer hard/software. Section 3 contains some results of the CAIN system as illustrated with a cw He-Ne laser, the Quantel Nd:YAG laser and the DFDL, where it will be seen that the single shot CAIN system can perform favourably with that of a scanning interferometer.

3.2 Design of CAIN.

CAIN element	Design Considerations
Interferometer	Type, FSR, finesse, wavelength range, etendue
Camera	CCD sensor, 1D vs 2D, responsivity, resolution
Framestore	Analog/Digital bit accuracy
Computer	Speed, memory, input/output ability, data storage

Table (1). Design considerations for each of the CAIN elements.

The table above shows a summary of some of the design considerations involved in the construction of the CAIN system. Each element is now described.

3.2.1 Interferometer.

i) Introduction to the Fabry-Perot interferometer.

As stated in the introduction an interferometric measurement device had to be constructed in order to facilitate linewidth measurements at the 100 MHz level. A common method for such measurements uses the Fabry-Perot interferometer, which is named after its inventors Charles Fabry and Alfred Perot. The plane parallel interferometer (FPP) is the simplest Fabry-Perot interferometer and consists of two highly (but not totally) reflecting plane mirrors aligned parallel to a high precision. A schematic diagram for the FPP is shown on figure (1). The FPP mirrors are separated by a distance L and have intensity reflectivity R. The medium between the two mirrors has refractive index n. As only a small proportion of the light incident onto each mirror is transmitted the light undergos multiple reflection through the interferometer. The path difference between adjacent emerging beams, attributable to one additional round trip, causes a phase difference ϕ, which is given by,

$$\phi = \frac{4\pi}{\lambda} n L \cos\theta \qquad (3.1)$$

where λ is the free space wavelength and θ the internal angle of incidence of the incident light. The spatially dependent output of the interferometer depends on the phase difference between adjacent beams. Unity transmission or resonance occurs when emerging beams are completely in phase i.e.,

$$\phi = 2\,m\,\pi \tag{3.2}$$

where m is an integer. From (1) and (2) it can be seen that a limiting case exists when the (m+1) th order overlaps with the m th order. This limiting case is known as the free spectral range and is given by,

$$\Delta\lambda_{FSR} = \frac{\lambda^2}{2nL} \tag{3.3}$$

More commonly (3) is expressed in terms of frequency, hence obtaining the familiar expression,

$$\Delta\nu_{FSR} = \frac{c}{2nL} \tag{3.4}$$

The transmission characteristics of the FPP will be further developed later but meanwhile equations (1) and (2) can be used to the illustrate the two main modes of operation of the interferometer which are:

(a) Central Spot Scanning.

(b) Entire Fringe Observation.

The choice of method in which to use the interferometer depends on the application. Both modes normally seek to measure the frequency spread, or linewidth, of a source. In both cases a finite $\Delta\nu$ leads to a broadening of the fringe as (2) is satisfied for a range of angles. These are considered in turn below.

(a) Central Spot Scanning.

By illuminating the interferometer with a plane wave at a fixed angle to the interferometer axis (generally $\theta = 0°$) the interferometer resonance wavelength may be scanned by varying L, maximum transmission occurring when equation (2) is satisfied. Figure 2(a) shows how this is realized in practice. The source S is placed in the front focal plane of a lens. The collimated beam passes through the interferometer and, after emerging from the interferometer, the fringes are examined in the focal plane of a second

lens. If the interferometer is on resonance all of the incident light (ie neglecting mirror absorption) passes through the interferometer and is incident on the detector. By scanning the interferometer length the transmission changes until, as the interferometer moves off resonance, the resonance condition is again satisfied when the interferometer length has changed by $\lambda/2$ corresponding to a scan of one free spectral range. In this mode the interferometer essentially behaves as a band-pass filter. Successive frequency components are sampled sequentially as the resonance frequency is altered. This mode is also known as sequential spectrometry for this reason [1]. Since ϕ varies linearly with frequency as L is scanned the interferometer output has linear dispersion. The length can be varied in practice by attaching one mirror to a piece of piezo-electric material or to a magnetic drive similar to a loudspeaker. The change in transmission is measured using a linear detector such as a photodiode.

Scanning may also be accomplished by placing the entire instrument in a vacuum chamber and slowly altering the pressure. This changes the optical thickness, nL, of the gas between the plates since n varies very nearly in proportion to the density or pressure of the gas.

The main advantage of the scanning method is that output is linear in both frequency (linear dispersion) and in intensity through the use of a linear detector. Interpretation of the fringe pattern produced is therefore more simple. Since only the central fringe is utilized in scanning mode this represents a limitation on the radial throughput (or etendue) of the interferometer. Resolution may be traded off against light collection efficiency by increasing the detector aperture size. A disadvantage of this method is that it requires that the pulse length must be greater than the scan time if single shot measurements are to be made. This method is not used for the single shot linewidth measurement of nanosecond time-scale pulses since, on these time-scales, it is not practicable to produce a linear movement of the interferometer mirrors. However, if the pulse to pulse frequency stability of the source is less than the single pulse laser linewidth, the scanning interferometer may be used with a pulsed source. By slowly scanning the interferometer it is possible to sample successive frequency components of successive pulses and assemble a frequency spectrum of the source. However, if the pulse to pulse frequency jitter is

greater than the linewidth then it is the jitter which is recorded using the scanning method. Hence, single shot measurements, despite the disadvantages of non-linearity in fringe position with frequency, are best made using the multiplex approach, which has the advantage that the entire frequency spectrum is sampled during one shot. This mode is discussed in the next section.

In summary therefore the scanning method fixes θ of equation (1) and the interferometer transmission is thereafter altered by scanning L or n. Linear dispersion is the main advantage of the method.

(b) Multiplex spectrometry mode.

Fellgett [1] gave the name multiplex spectrometry to this mode of interferometry where all frequencies are used and observed simultaneously. The multiplex method has advantages in transient or pulsed conditions and, as identified by Fellgett [2], has increased interferometer throughput. Figure 2(b) shows a schematic diagram of the operation of interferometer when used in multiplex mode. The value of L is fixed and the interferometer illuminated with a diverging beam so as to provide a range of incident angles. A given wavelength will be transmitted at several values of θ, when equation (2) is satisfied. Another wavelength will be transmitted at other values of θ. Multiplex refers to the fact that all wavelengths contribute to the output simultaneously. However unlike the scanning interferometer this method has the disadvantage of non-linearity of the fringe position with frequency (nonlinear dispersion). The interference fringes produced appear at infinity and can be projected onto a screen using a lens by placing a screen in the rear focal plane of the lens. Conventionally the image was recorded by projecting the fringes onto photographic film. This method of recording has the disadvantage of non-linearity since the response of a photographic film is logarithmic This, combined with nonlinear dispersion makes interpretation of the fringes more difficult. Recently, CCD's have become readily available, and their use in place of photographic film offers a number of major advantages. The most significant of these are their sensitivity, response linearity, compatibility with digital storage, and, unlike photographic film, they are completely

reusable. These parameters are discussed in section 2.3 when a comparison is made between solid state sensors and photographic film.

The multiplex method has been shown [1,2] to represent an advantage over the scanning method under low light level illumination. All of the spectral bandwidth of interest is observed for the whole of the duration of the experiment whereas in the scanning mode spectral components are sampled for short periods which sum to give the total time of the experiment. If M spectral elements in the range $\Delta\nu$ are to be measured in time T then in the scanning mode each spectral element is sampled for a time T/M. If the signal integrates in proportion to T and the noise in proportion to $\sqrt{T}$, as it does in detector noise limited systems, then the sensitivity (proportional to the signal to noise ratio) is in direct proportion to $\sqrt{T}$, for the multiplex device, while in direct proportion to $\sqrt{T/M}$ for the scanning device. The gain in sensitivity in using the multiplex method is therefore $\sqrt{M}$. Relaxation of the incident beam collimation improves the light collection efficiency of the interferometer when used in this mode (i.e. resolution is traded for light collection efficiency).

As stated previously the shot-to-shot frequency stability problem associated with the Shank style DFDL geometry dictated the need for an interferometer with the capability to measure linewidth on a single shot basis. This constraint therefore points to the multiplex mode which was the mode used experimentally, together with a solid state image sensor.

ii) Introduction to the confocal interferometer.

A major limitation which is placed on the plane parallel interferometer occurs when the separation of the interferometer mirrors is greater than their diameter. At this separation diffraction loss becomes a dominant loss mechanism as the mirrors effectively aperture the beam on each reflection. Curvature of one or both mirrors decreases diffraction loss associated with aperturing by compensating the diffraction of the beam on each reflection with mirror curvature. The spherical confocal Fabry-Perot interferometer (FPS) is an interferometer which uses two spherical mirrors with equal radii separated by a distance equal to this radius of curvature and was first developed by Connes [3] and further described by Hercher [4]. There are a number of geometrical advantages associated with

this arrangement. Diffraction loss and the effects of mirror imperfections are minimised, and hence it can be used at larger mirror separations than an equivalent plane parallel Fabry-Perot interferometer. Light collection efficiency is also improved over that of the FPP and other types of interferometer since the interferometer can accommodate a greater range of incident illumination angles.

The Airy function, free spectral range, and finesse.

Although the derivations of the Airy function, free spectral range and finesse are well known for the case of a plane parallel interferometer these are outlined below while developing, in parallel, similar expressions for the confocal interferometer. Expressions for the FPP terms are listed on the left while those for the FPS are found on the right. The plane parallel interferometer mirrors have intensity reflectivity R, and separation L. For simplicity the medium between the mirrors has refractive index of one. The FPS has its two identical spherical mirrors separated by a distance equal to their common radius of curvature r. For confocal operation using the paraxial approximation each mirror images the other upon itself. In this idealised picture, which is shown schematically on figure 3(b), a ray entering the interferometer will be re-entrant after the first four reflections. This cycle repeats itself giving rise to an infinite number of coincident beams at this point.

The phase change ϕ, between two adjacent emerging beams (0,1,2,...n), is given by,

$$\phi = \frac{2\pi}{\lambda} 2\,L\,\mathrm{Cos}\,\theta \qquad\qquad \phi = \frac{2\pi}{\lambda} 4\,r \qquad (3.5)$$

The phase term for the FPS, as has be explained above, is independent of θ since in this paraxial approximation the ray path is independent of angle. If r_a is the amplitude reflectance of the reflecting plates, and t_a is the amplitude transmittance then the total field is,

$$E=E_0t_a^2(1+r_a^2e^{-i\phi}+r_a^4e^{-2i\phi}+\ ...) \qquad E=E_0t_a^2\,(1+r_a^4e^{-i\phi}+r_a^8e^{-2i\phi}\ +...) \qquad (3.6)$$

It should be noted that the equations for the FPS are the same as those of the FPP with the exception that the r_a term is replaced with r_a^2. These equations form simple geometric series, the sums of which are given by,

$$E = \frac{E_oT}{(1-Re^{-i\phi})} \qquad\qquad E = \frac{E_oT}{(1-R^2e^{-i\phi})} \qquad (3.7)$$

where T and R are the intensity transmittance and reflectance respectively of the interferometer plates. The transmitted intensity ($I=EE^*$) is obtained from (7) and is,

$$I=\left(\frac{T}{1-R}\right)^2 \frac{I_o}{1+\frac{4R}{(1-R)^2}\sin^2\frac{\phi}{2}} \qquad I=\left(\frac{T}{1-R^2}\right)^2 \frac{I_o}{1+\frac{4R^2}{(1-R^2)^2}\sin^2\frac{\phi}{2}} \quad (3.8)$$

where the angle ϕ is obtained from (5). Equation (8) is known as the Airy function and describes how the transmitted intensity I varies with wavelength and interferometer length. It is interesting to note that, as a consequence of the extra reflections involved during the double pass of the interferometer, is that in equation (4) the Airy function for the FPS may be obtained by replacing R with R^2 in the FPP expression. The free spectral range (FSR) of an interferometer, as defined in the previous section, is the frequency range, $\Delta\nu$, over which the interferometer accommodates and is given by,

$$(FSR)_{(FPP)}=\frac{c}{2L} \qquad (FSR)_{(FPS)}=\frac{c}{4r} \quad (3.9)$$

The minimum resolvable frequency of an interferometer is obtained from equation (8) when the second term contained in the denominator equals one and hence the transmission falls to one half maximum. The finesse of an interferometer is defined as the ratio of FSR divided by the minimum resolvable frequency and hence using (8) and (9) the finesse is given by,

$$\text{Finesse}_{(FPP)}=\frac{\pi\sqrt{R}}{(1-R)} \qquad \text{Finesse}_{(FPS)}=\frac{\pi R}{(1-R^2)} \quad (3.10)$$

FPP Finesse may be as high as 30 or 50 before other factors such as alignment or surface flatness of the mirrors begins to influence resolution. FPS finesse may be as high as 40 000 [5]. From equation (10) it can be seen that,for a given mirror reflectivity R, the finesse of the FPP is greater than that of the FPS by a factor $(1+R)/\sqrt{R} \sim 2$.

b) Non-degenerate confocal interferometer – Theory of operation.

As outlined above the FPS comprises two identical spherical mirrors separated by a distance at, or, as will be developed below, near to, their common radius of curvature. In all cases multiple beam interference pattern is produced in the vicinity of the central plane

of the interferometer. When the interferometer mirrors have exactly confocal separation the central fringe covers the entire output field of view. Developed below are equations describing the more general case to extend equations (8), and (9) which, following closely the derivation of Hercher [4], allows the analysis to be extended to include aberration, and the general case when the mirrors are not at confocal separation.

When the FPS is exactly confocal and, neglecting the effects of spherical aberration, an incident ray is re-entrant after two round trips of the interferometer. However, due to aberration a ray is in general not re-entrant but follows a path such as is shown in figure 3(b) causing it to intersect itself in the vicinity of a point P, located in the central plane of the FPS at a distance ρ from the axis. In this exactly confocal, or degenerate, condition the mirror axial mirror spacing is exactly r, the mirror radius, then the extra path difference Δ_0 between successive intersections at a point P is, [4],

$$\Delta_0 = \frac{\rho_1^2\,\rho_2^2\,\mathrm{Cos}\,2\theta}{r^3} + \text{higher order terms} \qquad (3.11)$$

where θ is the skew angle the ray makes relative to the axis, ρ_1 and ρ_2 are the distances from the axis at which the ray enters and departs from the interferometer.

The parameter ε is defined to include situations where the mirror spacing is a distance ε from r. Equation (11) can therefore be extended to include this general case and hence the path difference Δ, obtained from (11) is written as,

$$\Delta = \frac{\rho_1^2\,\rho_2^2\mathrm{Cos}\,2\theta}{r^3} + \frac{2\,\varepsilon\,(\rho_1^2+\rho_2^2)}{r} \qquad (3.12)$$

When ρ_1 is approximately equal to ρ_2 then close to the interferometer axis (θ~0) equation (12) may be written as,

$$\Delta(\rho) = \frac{\rho^4}{r^3} + \frac{4\,\varepsilon\,\rho^2}{r^2} \qquad (3.13)$$

where ρ is the height at which an entering ray crosses the central plane of the FPS. Referring to figure 3(a) and considering only beams transmitted at points 1 and 2 it is seen that two sets of rays are transmitted; those which have been reflected 4m times (type 1), and those which have been reflected 4m + 2 times (type 2). Following the above derivations, the equations describing the interference patterns produced in the central plane of the interferometer are given by,

Type 1: $$I_1(\rho,\lambda) = \left(\frac{T}{1-R^2}\right)^2 \frac{I_O}{1 + \frac{4R^2}{(1-R^2)^2}\,\mathrm{Sin}^2\,\frac{\phi(\rho,\lambda)}{2}} \qquad (3.14a)$$

or

Type 2: $$I_2(\rho,\lambda) = R^2 I_1(\rho,\lambda) \qquad (3.14b)$$

where the confocal phase term $\phi(\rho,\lambda)$, as given by (5), is,

$$\phi(\rho,\lambda) = \frac{2\pi}{\lambda}\,[\Delta(\rho) + 4(r + \varepsilon)] \qquad (3.15)$$

Equation (14) is most useful in describing the action of the FPS interferometer. Figure (4) shows the interference fringes as a function of ρ for two different values of ε (the departure from the confocal position) for a 5 cm FPS, with R=0.9 and λ = 633 nm. The upper and lower figure represent values of ε = 0.1 mm and ε = 0.2 mm respectively. As can be seen from the diagram as the interferometer mirrors are positioned further from confocal increasing numbers of fringes are located within a given diameter. From equation (8) it can be seen that fringe maxima occur when $\phi(\rho,\lambda) = 2m\pi$, and, using (13),

$$\frac{\rho^4}{r^3} + \frac{4\rho\pi^2}{r^2} = m\lambda \qquad (3.16)$$

where, m is an integer. Fringes produced are located in the central plane of the interferometer and have radii given by,

$$\rho_m = \sqrt{[\,-2\varepsilon r \pm \sqrt{(4\varepsilon^2 r^2 + m\lambda r^3)}\,]} \qquad (3.17)$$

For $\varepsilon > 0$, only one solution exists for ρ_m and in this case m is positive. When $\varepsilon < 0$, ρ_m has two solutions i.e. the same fringe may appear twice within a particular field of view. Figure 5 shows the fringe pattern in cross section, as obtained from (17), with ρ plotted against ε, again for r= 5cm and λ = 633 nm. As can be seen from figures (4) and (5) the location of fringes is nonlinear with position, however moving away from the confocal position leads to increased linearity.

In conclusion therefore it is seen that the confocal interferometer can be used in a multiplex mode in a manner similar to that described for the plane parallel interferometer.

As such the instrument is suitable for single shot measurements, such as were required in the experiments described elsewhere in this thesis. It should also be noted that the confocal interferometer is also well suited to use as a linear dispersion scanning interferometer in a manner described in the introductory section. In this case the interferometer is positioned at confocal separation in order to maximise the size of the centre fringe. The interferometer then behaves like a band pass filter allowing only the transmission of on resonance components. Scanning the length by $\lambda/4$ scans the interferometer through one free spectral range.

iv) Experimental Interferometer.

The interferometer used experimentally is described in this section. The interferometer mirrors, supplied by IC optical systems, have a diameter of 1/2" and a radius of curvature of 5cm, hence providing a free spectral range of 1.5 GHz. The zero focus mirrors used have the same radius of curvature on each face so as to avoid any focussing of the incoming wavefront (a planar–concave mirror would behave as a lens). The multi-layer dielectric reflective coatings were layered so as to produce a maximum reflectivity at $\lambda = 600$ nm. Using the interferometer in scanning mode with a three mode He-Ne laser the instrumental finesse was measured as approximately 15 at $\lambda = 633$ nm. Assuming that the finesse is determined purely by mirror reflectivity this finesse represents a mirror reflectivity of 90%. The finesse is expected to be greater than 15 for those wavelengths below 633 nm down to 600 nm where reflectivity is at a maximum. The mirrors are separated by two hollow cylindrical sections of type 5H piezo-electric ceramic material (PZT) obtained from Vernitron Limited, Southhampton (part number 16 - 16125). Each PZT section is 1" long, 1" outside diameter (OD) and has 1/8" thickness. The two sections were cemented together. It was found experimentally that a ramp voltage of ~150 V scans the interferometer through two free spectral ranges. The mechanical support for the interferometer is provided by a hollow cylindrical section of aluminium rod with OD and ID= 50 and 40 mm respectively.

When used in scanning mode the driving voltage to the PZT is obtained from an oscilloscope ramp generator from a modified oscilloscope. The output of the

interferometer is then incident onto a photodiode, the output of which was then displayed on the same oscilloscope as used to drive the PZT. In this configuration the oscilloscope trace, rather than plotting signal as a function of time, draws on the screen a trace of x against y.

In addition to piezo-electric mirror movement the mirror separation can also be varied using a fine pitch thread on one of the mirror mounts, thus enabling the positioning of the mirrors at separations other than confocal and the use of the interferometer in multiplex mode i.e. all fringes are observed simultaneously. Normally the mirrors were positioned so as to allow the viewing of around five fringes within a field of view of less than 1 cm diameter. As can be seen from figure (5) this condition represents a departure from confocal position of around 0.1 mm.

Some results obtained using the interferometer within the completed CAIN system are described in section 3 of this chapter.

3.2.2 Image relay and observation.

The fringes produced by the interferometer are located in a plane between its mirrors. A plane wave incident on the interferometer produces fringes located in the central plane while wavefront divergence, or convergence moves the fringes either away from or towards the central plane. Two methods were employed in the observation of the interferometer fringes; (a) a simple microscope and, (b) a single relay lens.

The microscope employed was manufactured by J. Swift, London and was part of a traveling measurement microscope apparatus. Since the microscope working distance (the physical distance between the front focal plane and the face of the objective lens was 4 cm, the fringes could be viewed through the interferometer mirror. The microscope was fitted with a X3 objective and a X9 eyepiece which provided a field of view of 7.5 mm. The microscope was mainly used for observation during the interferometer alignment. Recording was made possible by using the CCD camera which is described in the next section. The camera was fitted with a 25 mm f/1.4 lens, focussed to infinity, and positioned as closely as possible to the microscope eyepiece.

The second method of projecting the fringes from within the interferometer used a 50 mm f/1.8 Nikon camera lens, acting so as to relay the fringe pattern onto the CCD camera array. Since the sizes of the fringe pattern and of the CCD sensor were approximately equal the lens was used in a 2f–2f position, hence obtaining unity magnification. Changes in magnification, where necessary, were made by altering the position of the lens. This single lens method of fringe recording proved to be the superior of the two methods in fringe projection, in terms of throughput and ease of use, and was the method employed in the majority of the results to follow.

3.2.3 CCD camera.

(i) Comparison of image recording methods.

The two previous sections describe the origin and the projection of fringes from an interferometer onto the image plane of a camera in order to record the image. After the recording of this image linewidth measurement could be made.

Conventionally the fringe pattern, containing linewidth information, is recorded using photographic film. Recently CCD's have become readily available and their use in place of photographic film offers a number of advantages. These advantages are discussed in this section and include high sensitivity, response linearity, and compatibility with digital storage. Unlike photographic film these devices are completely reusable.

In photographic emulsions there is a trade-off between resolution and sensitivity. Emulsions are made more light sensitive by increasing the size the light sensitive material, normally silver halide grains. This increase in size however, has a detrimental effect on the resolution of the film. The spatial resolution is expressed in terms of the number of resolvable lines per millimetre. Tabulated below is a comparison of the EEV P8602 CCD sensor and two types of photographic film. Data for the film was obtained from [6]. The sensitivity has been expressed as the minimum energy density (pJ cm^{-2}) required to record an image using each of the various mediums.

As can be seen in table (2) the CCD offers advantages in both sensitivity and resolution over photographic film. The reason for the superior sensitivity is that CCD's have a quantum efficiency, the number of photo-electrons generated per incident photon, of

around 50% in the visible region. In comparison photographic films have a quantum efficiency which, at best in fast films, only approaches 1%. The voltage signal produced by CCD's has a highly linear dependence on applied illumination. A further advantage of such a video camera is that the output voltage may digitised and thereafter analysed by computer.

Medium	Minimum Illumination pJ cm^{-2}	Resolution lines mm^{-1}
CCD sensor	~100	50
Fast Silver Halide film	~500	50
Medium Silver Halide film	~10 000	150

Table (2). Comparison of sensitivity and resolution of CCD sensor and photographic film.

In summary CCD cameras are well suited to optical measurement systems for several reasons including:

(a) They have a linear signal response (in comparison to the log response of photographic films).

(b)They have a greater sensitivity than photographic film and hence offer greater resolution at low light levels.

(c) They have high signal-to-noise ratios.

(d) CCD pixel locations are accurate in position and size and hence are suitable for measurement systems.

Preliminary DFDL linewidth measurements were made using an EEV P4330 CCD video camera. An attempt was made to photograph the fringes using a 35 mm camera and medium speed (ASA 400) film but this proved difficult due to insufficient intensity. In the light of these investigations it was decided that a CCD camera would best suit the CAIN system. The considerations involved in the choice of a CCD sensor included; spatial resolution, sensitivity, dynamic range, choice of either a 1D (linear) or 2D (area) array,

and cost. In addition to an introduction into the operation of CCD's, these considerations are described below. With regard to cost it is interesting to note that the cost of CCD devices has fallen dramatically. The P4330 camera was purchased in 1987 at a cost of over £1500. A similar camera, with higher resolution and superior video circuitry, can now (April 1989) be purchased in modular form from Philips for £300 (CCD Monochrome imaging module 56474 H).

(ii) Charge-Coupled Device Image Sensors.

CCD's are a relatively new family of components using a silicon semiconductor substrate which permit the accumulation, storage and transfer of analog information in the form of charge packets. Introductions into the operation of CCD's can be found in manufacturers literature, see for example [7,8]. Both one and two dimensional CCD arrays are available. In general, two dimensional arrays are designed mainly as video cameras, while one dimensional arrays have a more specialized market. Due to a higher volume of production CCD video cameras are available with prices comparable with 1D arrays. As will be seen later the performance of two dimensional arrays is similar those of one dimension. There are however, advantages in using a two dimensional array in the CAIN system. The fringes produced by the interferometer are two dimensional and therefore only an area array can record the full image. Ease of use was a second, highly practical advantage, in having the full image available when using the sensor experimentally. When aligning the interferometer, projection lens and camera viewing of the full image was possible via a video monitor making the alignment a relatively straightforward process.

The CCD is essentially a silicon MOS-type integrated circuit the basic structure of which is illustrated schematically in figure (6). The silicon substrate is separated from an array of closely spaced semi-transparent polysilicon electrodes by a thin insulating oxide layer. Each electrode-oxide-silicon element behaves like a MOS-type capacitor. Light falling onto the array penetrates the electrode structure and generates electron-hole pairs in the underlying silicon substrate. The electrons then diffuse to the nearest biased electrode where they are collected as signal. The holes diffuse down into the substrate where they

are effectively lost. The quantity of charge collected is proportional to the local light intensity and the time allowed for collection (see later for experimental investigation of signal linearity). Signal information is therefore carried in the form of a quantity of electronic charge. This charge is localised beneath the electrodes with the highest applied potentials because the positive potential on an electrode (designated as V_G on figure 6) causes the underlying silicon to be in depletion and thus assume a positive potential which attracts the negatively charged electrons. It is for this reason that electrons are said to sit inside a 'potential well'. The active part of the device in which the charges are located is called the channel. This region is in turn bounded by electrically inactive p-type regions known as channel-stops.

Charge coupling is the technique by which charge can be transferred from under one electrode to the next. This is achieved by taking the voltage on an adjacent electrode to a high level and then reducing the voltage on the first, as illustrated in figure (7). Hence by sequentially pulsing the voltages on the electrodes between high and low levels, charge can be made to pass down a large number of electrodes with very little loss and without much superimposed noise. To achieve this the electrodes are connected in sequence to a set of three-phase drive pulses; ϕ_1, ϕ_2 and ϕ_3 as illustrated. These pulses (typically around 10 V amplitude) must be generated by external electronics (normally referred to as driver circuitry).

Most two dimensional image sensors use separate areas of collecting and storage of their images in a method known as frame transfer. In this type of sensor the array architecture is such that the electrodes are grouped into two sections; an upper image section and a lower, usually identical, storage section. A schematic diagram for such a frame transfer array is shown on figure (8). A further line readout section below the store is employed to transfer the charges in each line to the on-chip charge detection amplifier for video output. The drive pulses applied to the image, store and readout sections for device operation are designated Iϕ, Sϕ and Rϕ respectively. The direction of charge transfer under such operation is shown by arrows. At 50 Hz video frame-rates the time duration for both integration time for aquision of the image and the readout process is 20 ms. Frame transfer from image to storage sections can be considered as instantaneous

since this occurs in under 0.5 ms. Since the store and readout sections are made of the same photo-sensitive material as the image section it is important that these areas are shielded from incident illumination and, to this end, are normally masked by manufacturers.

Some CCD sensors, particularly those used for video camera applications, have a feature in the CCD array described as anti-blooming. Blooming is the phenomena by which an oversaturated bright area on the picture can streak over all, or part, of the frame. Anti-bloom sensors incorporate a series of channels in the array into which excess charge can flow if an element becomes saturated, in order to prevent charge spilling into an neighbouring element. However the physical space used for this masks some of the photo-sensitive surface and hence reduces the sensitivity of the array.

Having gained a knowledge of the workings of charge-coupled devices further investigation can be made into factors affecting their performance. To this end factors contributing to resolution, sensitivity and dynamic range are now considered.

Pixel size is the limiting factor in determining spatial resolution. Recently high resolution CCD's have become available commercially from Kodak and Polaroid and these have pixel sizes in the order of 6 to 7 μm, giving a resolution of between around 150 lines mm^{-1}. The Kodak *Megaplus* CCD camera, geared to the high resolution T.V. market, contains 1320 H x 1035 V pixels i.e. around four times the number of pixels found in todays standard devices. This level of resolution is at least comparable with standard types of photographic film, although holographic glass plates can have up to 2500 lines mm^{-1}.

Device sensitivity, and dynamic range are important properties in the assessment of image sensors. Sensitivity is a measure of how much signal is obtained from the device for a given input. Dynamic range gives a measure of the range of input signal with which the device may be used. In the case of image sensors the dynamic range enables the evaluation of the maximum and minimum illumination levels. Maximum illumination is determined as that illumination which corresponds to the saturation of the device. Minimum illumination is determined by noise parameters. Since the CCD is a relatively

new device, and no standard definitions exist for the parameters of sensitivity or dynamic range, these are considered below.

In expressing sensitivity Mullard choose V/μW cm^{-2}, EEV mA/W, while Texas Instruments and Thomson-CSF choose to measure the response in terms of V/μJ cm^{-2}. This makes the comparison of CCD's difficult. The latter unit seems a sensible choice in that the output voltage produced by the device is expressed in terms of the energy density of incident light. The units favoured by Mullard and EEV could easily be converted to V/μJ cm^{-2} by consideration of frame rate, array area etc. As an example consider the EEV P8602 sensor which has a peak signal of 300 nA when the output voltage is 200 mV . The responsivity of the sensor is 0.175 A $Watt^{-1}$ at 600 nm (manufacturers data). The saturation power can therefore be obtained by dividing the saturation current by the responsivity i.e.,

$$\text{Saturation power} = \frac{\text{Saturation current}}{\text{Responsivity}} = \frac{300 \times 10^{-9}}{0.175} = 1.71\ \mu W \qquad (3.18)$$

This power is deposited for the duration of the integration time t_i (the reciprocal of which is the frame rate) and thus the saturation energy can be obtained, hence,

$$\text{Saturation energy} = \frac{\text{Saturation power}}{\text{Frame rate}} = \frac{1.71 \times 10^{-6}}{50} = 3.43 \times 10^{-8}\ J \qquad (3.19)$$

Energy density is obtained knowing the CCD image area (0.544 cm^2), hence,

$$\text{Energy density} = \frac{\text{Saturation energy}}{\text{CCD area}} = \frac{3.43 \times 10^{-8}}{0.544} = 6.3 \times 10^{-8}\ J\ cm^{-2} \qquad (3.20)$$

This saturation energy density corresponds to a saturation voltage of 200 mV and hence the sensitivity may be obtained as,

$$\text{Sensitivity} = \frac{\text{Voltage output}}{\text{Incident energy density}} = \frac{0.2}{6.3 \times 10^{-8}} = 3.15\ V/\mu J\ cm^{-2} \qquad (3.21)$$

This figure of ~ 3 V/μJ cm^{-2} for the P8602 sensor is typical for CCD's, as can be seen on table 3 where four sensors are compared.

Knowing the sensitivity a device can be completely characterized if the saturation signal and dynamic range is known. This enables the evaluation of the maximum and minimum

illumination with which the device may be used. Maximum illumination is defined here as that illumination which just corresponds to saturation of the device. The upper level of illumination is set by the maximum charge handling capability of the sensor. Minimum illumination is defined as the minimum illumination which provides as useful output. At the lower level of illumination the device is limited by noise fluctuations in the output. As such manufactures, in general, define dynamic range as the ratio of saturation signal to the r.m.s. noise. Dynamic range is sometimes however quoted as the ratio of saturation signal to the peak-to-peak noise. Since the r.m.s. noise is typically around one-fifth that of peak-to-peak noise it is obvious of the need to compare like with like. The saturation illumination is obtained by dividing the saturation voltage by the array sensitivity. Both figures should be available form the manufacturers. Electrical noise determines the lowest level illumination with which a device may be used. There are four main noise sources in CCD's:

(a) Dark Current Noise.

(b) Reset Noise.

(c) Fixed Pattern Noise.

(d) Pre-Amplifier Noise.

Like any photo-detector the CCD is subject to dark current. The variation of dark current with temperature is given by,

$$I_D = A \exp - \frac{V_{BG}}{2kT/q} \qquad (3.22)$$

where A is a constant, V_{BG} is the bandgap of the material = 1.1 eV, and kT/q ~ 25 m eV at room temperature. This dark current has associated shot noise which, expressed in the number of electrons, is given by,

$$N_d = \left(\frac{I_D\, t_i}{e}\right)^{1/2} \qquad (3.23)$$

where t_i is the integration time between readouts. As can be seen from (23) dark current shot noise can be reduced by cooling. At video frame-rates this is not the dominant noise source so that only a small benefit in performance of the array can be achieved by cooling.

Some applications however, such as astronomy, require long exposures in order to integrate the charge generated by low intensity images. Equation (22) gives a value for the

dark current. This represents ~ 10^5 electrons per element per second at 300 K and as such the device would be saturated with charge in approximately three seconds. Therefore if the integration time of the sensor is be greater than around one-half a second then cooling must be employed. Cooling the array has the effect of reducing the thermal noise by a factor of two for every 7 °C. Cooling to liquid nitrogen temperatures reduces dark current to less than electron per element per hour.

Reset noise is basically the the variation in the amount of charge remaining in an element after frame transfer. This is a random variation in the residual charge at a pixel location after the readout phase. It is Johnson noise caused by the thermal motion of the electrons.

Noise in the pre-amplifier is essentially 1/f in character at low frequencies (below 100 kHz). However at video frequencies (8MHz) white noise is the dominant type of noise in the pre-amplifier.

The effect of these noise sources is that they determine the lower limit of illumination on the sensor. Typically the dynamic range of a CCD sensor is ~ 1500. For the EEV P8602 the maximum number of electrons accumulated per pixel is $3x10^5$. The noise sources discussed contribute to a r.m.s. variation of 200 electrons thus giving a dynamic range of 1500. Table (3) below shows a comparison of four sensors, in terms of minimum illumination required (when the response is at a level just equal to the noise) and dynamic range.

Manufacturer	Sensitivity	Illumination min pJ cm^{-2}	Illumination max pJ cm^{-2}	Dynamic Range	Pixel size µm
EEV (P8602)	3.15	43	64 500	1500	22x22
Mullard (NXA 1011)	3.0	89	133 000	1500	10x15.6
Thomson-CSF (TH 7801)	3.0	55	330 000	6000	13x13
Reticon (1024D)	2.3*	45	72 000	1600	18x18

Table (3) Comparison of CCD image sensors. The EEV and Mullard sensors are 2D arrays, while the Thomson and Reticon sensors are 1D arrays. Illumination is described in terms of optical energy density incident on the array. Dynamic range is defined as the ratio of the saturation signal to the r.m.s. noise.

It should be noted that the above considerations are for the image sensing array and not the overall system. For a camera system optomisation of parameters for a particular application occurs. For video camera applications the frame rate is the dominant factor. The dominant array noise sources at those rates are normally ascribed to reset, fixed pattern and pre-amplifier noise. As such cooling the array to reduce dark current shot noise has little effect. Processing the signal from the sensor into video format adds a further source of noise. The overall CCD camera performance is less than that of the array. The EEV photon camera has a specified dynamic range of >55 dB which compares to a 63 dB specification for the array. A CCD array packaged into a video camera therefore represents a compromise in terms of performance, ease of use and cost. If the full potential of the CCD is to be realised more sophisticated driver and processing circuit would be required. Experimental investigations into the above parameters for the camera system are discussed in the next section.

(iii) Experimental camera system.

In the light of the design considerations above the CCD camera chosen for experiments to follow was an EEV P46110 *photon* camera. This camera uses the same P8602 non anti-bloom CCD array as a P4330 camera used in preliminary investigations. The P8602 sensor contains 385x288 pixels of size 22x22 μm. The P46110 *photon* camera is equipped with lower noise video circuitry and hence has increased dynamic range over previous CCD cameras. In particular the *photon* camera incorporates a technique known as double correlation sampling. By sampling the output from a particular location twice, once after resetting and again after charge output, reset noise can be eliminated by taking the difference between the two levels.

An experimental investigation into CCD camera performance was undertaken. The parameters of particular interest were signal linearity, sensitivity and dynamic range. Two cameras were tested, serial numbers P864512 and P862837.

In the first of two experiments the linearity and relative responses of two cameras were compared. Light from a He-Ne laser was attenuated using neutral density (ND) filters and then incident directly onto the arrays of the CCD cameras. The voltage forming the output

of the camera was measured on a particular field line. To achieve this the composite video signal was stripped of its sync and blanking pulses using a video sync separator. The National Semiconductor Corporation LM1881, launched in 1987, is a single integrated circuit designed for this task. The video line selector circuit was exactly as described in the manufacturers literature [10]. The field line selected was the one with the highest peak voltage, therefore representing a slice through the centre of the He-Ne spot. This single line could then be displayed on an oscilloscope, the voltage/time representing intensity as a function of position. The incident intensity was varied by using a range of different ND filters, the voltage being recorded for each value of intensity.

Figure (9) shows the relation between voltage output and illumination for the two cameras tested. Both cameras are seen to have the desired linear response. The gradient of these graphs is a measure of the relative sensitivities of the two cameras. It is interesting to note that the sensitivities of the two cameras are significantly different. The sensitivity of the P862837 camera is over three times that of the P864512. However of the two cameras the P862837 had significantly less noise when measured at zero illumination and hence it has a higher dynamic range.

In the second experiment light from the He-Ne laser was attenuated using ND filters and a polariser. Rather than stripping the video frame of one line the complete frame was grabbed and computer analysed. The trace obtained was that of voltage as a function of position corresponding to intensity/position on the array. A typical trace is shown on figure (10). The software identified and labelled the maximum voltage V_{max} and also $V_{max} \times 1/e^2$, hence allowing the calculation of the beam spot size. In the experiment the intensity incident onto the CCD was varied by rotating the polariser. The transmission of the polariser is given by Malus's law as,

$$I = I_o \, Cos^2 (90-\theta) \qquad (3.23)$$

where θ is the angle measured from the extinction position.

In order to remain consistent with the previous section the illumination of the array is to be described in terms of energy density ($\mu J \, cm^{-2}$). In the experiment however the illumination is described in terns of incident power. To convert from the total power to energy density the following procedure was used:

The He-Ne laser beam has an intensity distribution which is assumed to have a Gaussian distribution, i.e. has the form,

$$I(r) = I_{max} \exp\left[\frac{2r^2}{\omega_o^2}\right] \qquad W\ m^{-2} \qquad (3.24)$$

The measured quantity is the total power which, using (24) can be expressed as,

$$\text{Total Power} = \int_0^\infty 2\ \pi\ r\ I_{max} \exp - \frac{2r^2}{\omega_o^2}\ dr$$

$$= 2\ \pi\ I_{max} \int_0^\infty r \exp - \frac{2r^2}{\omega_o^2}\ dr \qquad W\ m^{-2} \qquad (3.25)$$

Evaluating (25) allows the peak intensity I_{max} to be expressed in terms of the total power and beam spot size ω_o as,

$$I_{max} = \frac{2\ \text{Power}}{\pi\ \omega_o^2} \qquad W\ m^{-2} \qquad (3.26)$$

The spot size ω_o is defined as the radius of the beam when the intensity is $1/e^2$ times I_{max} and was measured as 0.50 mm. A value for I_{max} for the 4.1 mW He-Ne laser is therefore obtained as 10.4 kW m^{-2}. The power is deposited during the frame integration time (20 ms) and hence the illumination energy may be obtained. The beam was attenuated using ND filters and thus, knowing ω_o and the He-Ne beam power (4.1 mW) the illumination energy is written as,

$$\text{Illumination energy density} = \frac{I_{max}}{10^{ND}} \times\ t_i \times \frac{I_{out}}{I_{in}} \qquad J\ m^{-2}$$

$$= \frac{2.08 \times 10^4}{10^{ND}}\ \frac{I_{out}}{I_{in}} \qquad \mu J\ cm^{-2} \qquad (3.27)$$

Figure (11) shows the relation between voltage output and illumination for the camera. Energy density was obtained using (27). Two data sets are shown. Method 1 used only one ND filter and the polariser, method 2 used a range of ND filters and the polariser. As can be seen from the graph there is good agreement between the two sets. A least squares straight line fit was obtained for the data. The gradient of this line, which, by definition, is the overall sensitivity of the camera was ~ 30 V/μJ cm^{-2}. The y axis intercept is at 8 mV. and a least squares straight line fit was obtained in the linear region, below 0.7 V.

Dynamic range is obtained from this data. The intercept gives the value of noise i.e. that signal present for zero illumination. This represents an upper estimate of the peak-to-peak noise and hence may be reduced by a factor of five to obtain an estimate of the r.m.s. value [9]. A value of dynamic range is therefore obtained as,

$$\frac{\text{Saturation signal}}{\text{r.m.s. noise}} = \frac{0.7\ \text{V}}{8\ \text{mV}} \times 5 \sim 440 \sim 53\ \text{dB} \qquad (3.28)$$

The upper and lower ranges of illumination with which the cameras may be used was also obtained from the data. The upper limit is defined as that illumination which provides the maximum allowable video voltage of 0.7 V and hence is given by,

$$\text{Maximum Illumination} = \frac{0.7\ \text{V}}{\text{Sensitivity}} \sim 23\ 000\ \text{pJ cm}^{-2} \qquad (3.29)$$

From (28) and (29) the lower limit of illumination is obtained as ~ 50 pJ cm^{-2} . For the P8602 array values for the maximum and minimum illumination are quoted as 64 000 and 43 pJ cm^{-2} respectively. No data is available for the overall camera response. It is seen that the measured saturation figure of 23 000 pJ cm^{-2} is more than 2.5 times less than the quoted value. Since it is unlikely that the array is 2.5 times more responsive than the quoted figure (this would exceed a quantum efficiency of one) it is thought that the array and video amplifiers are mismatched. The maximum voltage allowed is 0.7 V and thereafter the voltage is clamped at this level. If the amplifier gain is too high then it is the video amplifier which 'saturates' when 0.7 V is reached. In this circumstance the camera saturates at a level lower than that of the array.

iv) CCD Summary.

In this section the basic principles of operation of charge coupled devices were explained. This knowledge is necessary in order to chose a sensor which meets a particular application. As has been discussed any CCD video camera compromises performance for cost and ease of use. However for the CAIN application the dynamic range of the camera far exceeds the digitising accuracy of the video framestore (1 part in 128). The EEV P46110 *photon* camera performed well in terms of cost, resolution and sensitivity. Further details into the operation of the camera within the CAIN system can be found in section 3.3.

3.2.4 Video framestore.

In order to capture the video output from the CCD camera a video framestore was constructed. This enabled the grabbing and storage of a single frame of video. The spatial resolution of the digitised video frame is 512 horizontal and 256 vertical lines per frame. The video voltage is digitised with 7 bit accuracy (8 bits displayed) giving a resolution of one part in 128. Figure (12) shows a schematic diagram of the framestore system. The framestore was constructed by J. Wade of the department's electronics workshop along the design lines of D.E.A. Clarke [11]. Printed circuit boards were obtained from Ipswich Electronics Ltd, Ipswich.

The reader is referred to the papers of Clarke for a detailed description of the device. On a basic level the operation of the framestore may be sub-divided into three areas. The analog video format input signal is first digitised using an A/D converter (Mullard PNA 7509 P). The digital information is then stored and thereafter re-converted to an analog video format for output (D/A converter Mullard PNA 7518). This process repeats at video frame-rates which therefore causes the store to be continuously updated. Interruption of the update signal causes the framestore to retain the current frame. However, output via the D/A converter still occurs from the store and so its current (stored) frame is continuously displayed on a video monitor. This stored frame could thereafter be read by a computer. The storage update can be derived either internally or externally. In the experimental system the update signal was continuous except when interrupted by a signal obtained from the Nd:YAG laser slow Q switch control. In this state the system is primed to store the next video frame arriving from the camera. Once stored the output is displayed on a monitor and the user given the choice of either reading the stored frame into the computer for display and analysis or further real-time updating. Further details of how the framestore was incorporated into the CAIN system can be found in section 3.3.

3.2.5 Computer system.

The function of the computer in the CAIN system was primarily to allow rapid measurement of the fringe pattern derived from the interferometer and stored in the framestore. The required result was a plot of intensity verses position of the

interferometer fringes so that linewidth could be determined. Two approaches could be considered:

(i) Using the framestore as the exclusive information store hence using the computer as a processor while addressing the information in the framestore during analysis, or,

(ii) Using the framestore as a short term information store and mapping the stored frame into computer memory, and thereafter performing image analysis directly from the computer memory.

The first method would have to be employed if the computer used had insufficient memory to store the image. A stored frame has 512x256 bytes (128 Kb) of information and hence is too large for microcomputers such as the popular BBC series. The disadvantage of this method is twofold in that:

(a) The framestore memory can only be addressed sequentially i.e. in a fashion similar to a rastor scan.

(b) The transfer of information from the framestore to the computer is relatively slow in comparison to operations occurring within the computer memory.

Thus it is advantageous to have a computer with at least 256 Kb of RAM (128 Kb for the stored frame and at least as much again for the program and system commands).

High processing speed is also an important consideration in any image processing application since even simple applications, such as averaging, spatial filtering or edge detection, require large amounts of computation.

In the light of these memory and processing speed considerations an Acorn Archimedes computer was chosen as the computer for this application. This, at the time of purchase, represented a significant step forward in microcomputer processing speed with the use of its 32 bit processor. The machine has 1Mb of RAM and therefore has ample memory for the storage of a 8 bit video frame. Ease of interfacing and the machines use of BBC BASIC added to the attractiveness of the machine.

The computer could be used with a variety of screen modes each with different screen resolution and number of colours available. Mode 15 out of the machines 20 screen modes was the mode normally used. This was the computers highest resolution mode and

it displays a total of 256 colours by mixing four tints of 64 base colours. The mode gave a resolution of 640 H x 256 V pixels. Since each colour was determined by a 8 bit number, and this is the type of number forming the output of the framestore, the mode was ideally suited to use with the framestore. Interrogation of the framestore memory at a particular location yields an 8 bit number, this number was then put straight into the screen memory in a location corresponding its location within the framestore. The image produced on the computer screen was therefore displayed in false colour. The assignment of colours within the computers colour pallet in this mode was not easily accessible and the false colour image not easily interpreted as it effectively ran in four cycles, corresponding to the value of tint, of the 64 base colours. To make the image more easy to interpret a small routine was written to convert from this 256 level colour image into a 16 (or 4 bit) grey level black and white image. In doing so however, intensity information was lost and hence for measurement purposes the full 8 bit image had to re-addressed from the framestore or disc.

The machine was fitted with two floppy disc drives, one of which used 3.5 inch discs with 800 Kb memory. The memory needed in order to save a complete screen of information containing the 640 H x 256 V pixels (of which the video picture accounts for 512 x 256 pixels) is 160 Kb and hence 4 frames could be stored on a single disc.

Details of the algorithm used for extraction of fringe information is given in the next section, and further details of how the computer was used within the CAIN system is given in section 3.3.

3.2.6 Algorithm for linewidth determination.

Two methods of obtaining intensity verses position plots from the stored information were investigated. The first takes a single horizontal slice of the pattern and simply sequentially samples the digital value of memory elements (the values of which is proportional to the voltage signal from the video picture at that position). This value is then plotted as a function of position across the line. An extension to the horizontal method is to average over more than one line, averaging adjacent vertical pixels. Sampling a larger number of pixels was carried out in order to average out random noise and local

intensity variations due in part to the interference between the type 1 and type 2 fringe patterns. This method is hereafter called a line scan average. It is obvious that this method is limited by fringe curvature and hence it can only be employed over a limited number of lines. Normally either five or ten lines were used in a line-scan average.

In order to use all the available information a circular scan method was developed, which exploits the circular symmetry of the fringe pattern. If the centre of the fringe pattern is known the all (x,y) points lie on a particular radius r when $x^2 + y^2 = r^2$. The program can therefore sample all points corresponding to this particular radius, hence averaging around the circle circumference. This averaging is repeated for increasing radii. This method was somewhat further complicated since elliptical fringes were produced when the rectangular T.V. picture with aspect ratio of 4:3 was mapped and displayed on a square (1:1) memory. The method can still be employed using the equation of an ellipse $x^2/a^2 + y^2/b^2 = 1$. As will be seen in the nest section this method represents a considerable improvement over the line-scan results. Results obtained from the single line, line-scan average, and elliptical averaging methods are given in the next section.

Full details, including a program listing, of the CAIN computer program are given in appendix III.

3.3 Results and Summary.

The CAIN system assembled therefore consisted of a non-degenerate confocal interferometer, a relay lens, a CCD camera, a video framestore and a computer. In operating the CAIN system the sequence of events was as follows. The CCD camera would be continuously clocking out pictures at 50 frames a second which, until the arrival of the firing of the Nd:YAG laser and thereafter the DFDL were blank. The start sequence was the control signal from the Nd:YAG laser slow Q switch control which activated the laser Q switch and, after input into the framestore interrupted the update signal. The framestore was then primed to store the next frame, which on the time-scales involved, was already incident on the CCD array. After CCD frame transfer this image formed the output of the next video picture and was therefore stored by the framestore. The stored image was thereafter displayed on a monitor or read into the computer for analysis. The

process was largely controlled by computer, for example the computer could over-ride the update signal. The system was normally operated with the laser firing at 1 Hz. This gave sufficient time for the operator to decide if the image was to form the input to the computer for analysis or to sample another frame.

A three mode He-Ne laser was used to test the system. A 10x expanded He-Ne beam was incident onto the interferometer. The fringes produced in the central plane of the interferometer were projected out of the interferometer onto the CCD camera array. The output from the camera was stored in the memory of the framestore and read into the memory of the computer.

Figure 13(a) shows the false colour image produced on the computer screen. The horizontal fringes are a result of the interference between type 1 and type 2 fringes (see section 2.1). Figure 14(a) shows the result of a single line-scan sample obtained by scanning across a single line of data. Figure 14(b) shows the result of averaging over 10 vertical lines. As can be seen from the figure the image is enhanced over that obtained using a single line as local variations are averaged out. Figure 15(a) shows the result of the elliptical averaging on the 3 mode He-Ne laser interferogram used above. As can be seen from the figure this represents a considerable improvement over the line-scan results. This compares well with the measured instrumental finesse of around 12 at 633 nm. Figure 15(b) shows a result obtained whilst using the system experimentally for DFDL analysis. The linewidth results to follow in subsequent chapters were obtained using the apparatus detailed in this chapter with both line-scan and elliptical algorithms employed.

Chapter III References

[1] P.B. Fellgett: Ph.D. Thesis, University of Cambridge, (1951).

[2] J. Chamberlain: *The principles of interferometric spectroscopy*, Wiley-Interscience Chichester (1979).

[3] P.Connes: Rev. Opt. 35, 37 (1956).

[4] M. Hercher: Appl. Opt 7, 951, (1968).

[5] The Newport Catalogue: No 100 (1988) Newport Corporation (USA).

[6] SPSE Handbook of Photographic Science and Engineering: W. Thomas Jr, Editor, Wiley -Interscience USA (1973).

[7] *CCD Imaging III*, EEV Chelmsford, May 1986 (UK).

[8] Charge Coupled Devices, Electron Tube Division, Thomson-CSF (France).

[9] Image Sensing Products Catalogue 1986, EG&G Reticon (USA).

[10] National Semiconductor Data Sheet TL / 4 / 9150 (1986).

[11] D.E.A. Clarke: Electronics and Wireless World, Nov 1986-March 1987 (Various articles).

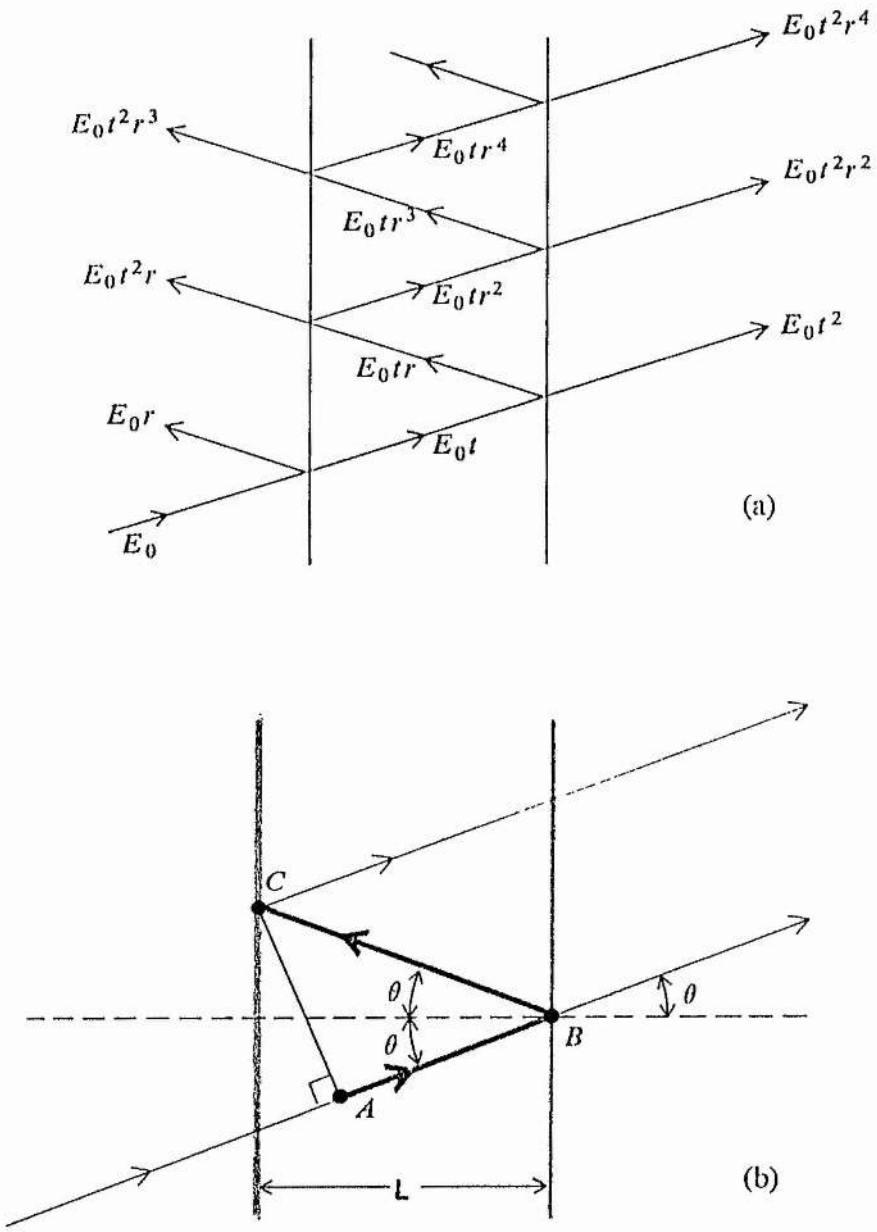

Figure 1. (a) Schematic representation of ray paths through a plane parallel Fabry-Perot interferometer (FPP). (b) Diagram showing the path difference between two successive rays after one additional round trip. The path difference δL is given by,

$$\delta L = AB+BC = L\,\frac{\text{Cos } 2\theta}{\text{Cos } \theta} + \frac{L}{\text{Cos } \theta} = L \text{ Cos } \theta\ .$$

The phase difference ϕ is given by,

$$\phi = \frac{2\pi(\delta L)n}{\lambda} = \frac{4\pi n L \text{ Cos } \theta}{\lambda}\ .$$

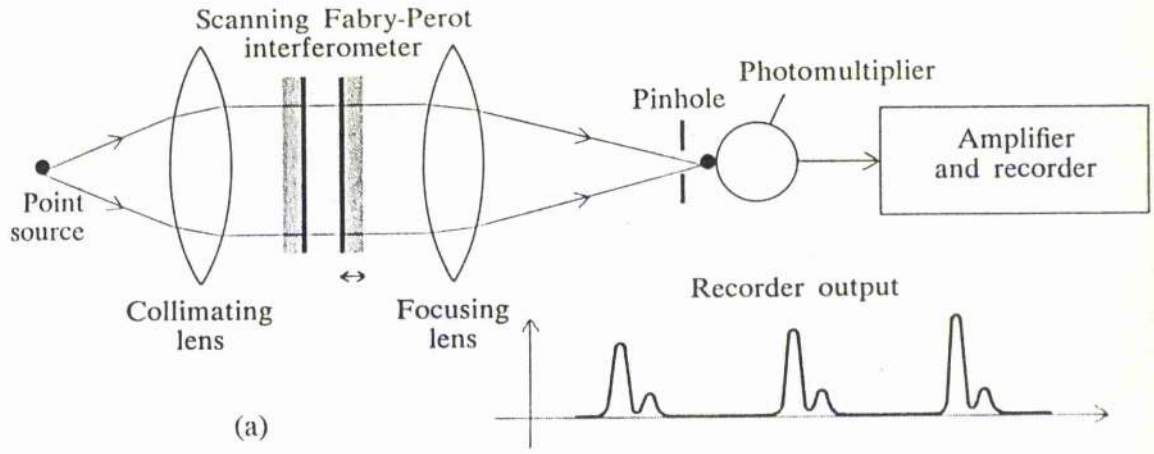

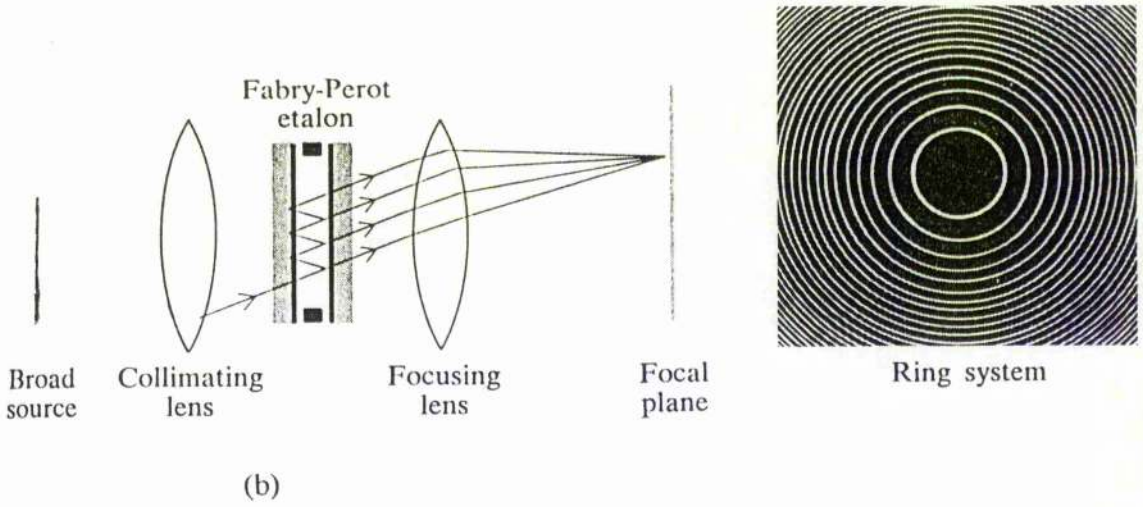

Figure 2. (a) Typical method used in central spot scanning. θ is fixed by collimating the input beam with a lens. L is varied using, for example piezo electric mirror mounts. The output is normally focussed onto a photodetector. (b) Typical experimental arrangement used in the multiplex mode. L is constant and a range of input angles produced by a diverging beam. Conventionally the fringes are recorded using photographic film although this latterly has been replaced with devices such CCD arrays.

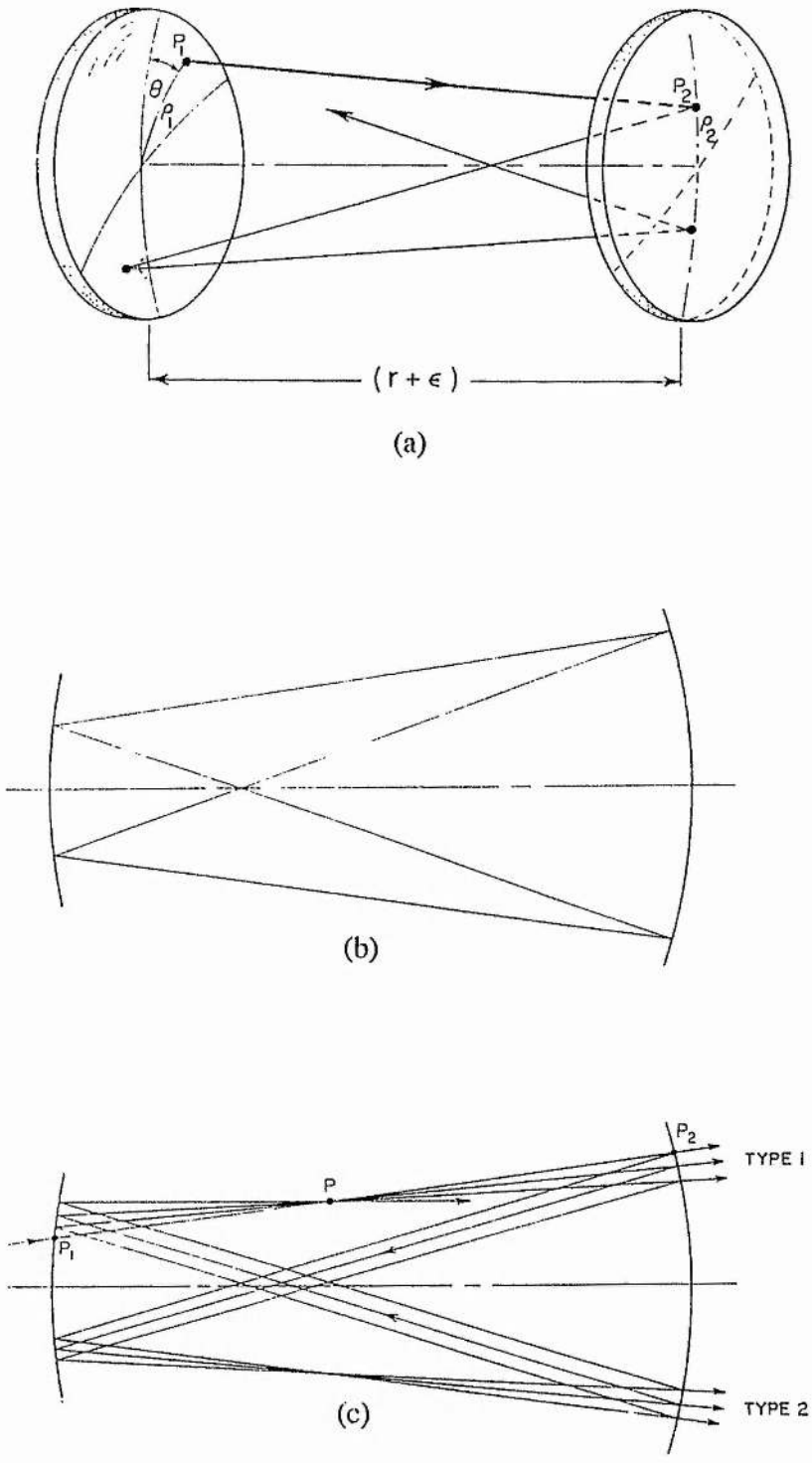

Figure 3. Spherical confocal interferometer (FPS) schematic after Hercher [4].

(a) General ray path through the interferometer.

(b) Ray path in the paraxial approximation.

(c) General case showing the intersection of rays at point P.

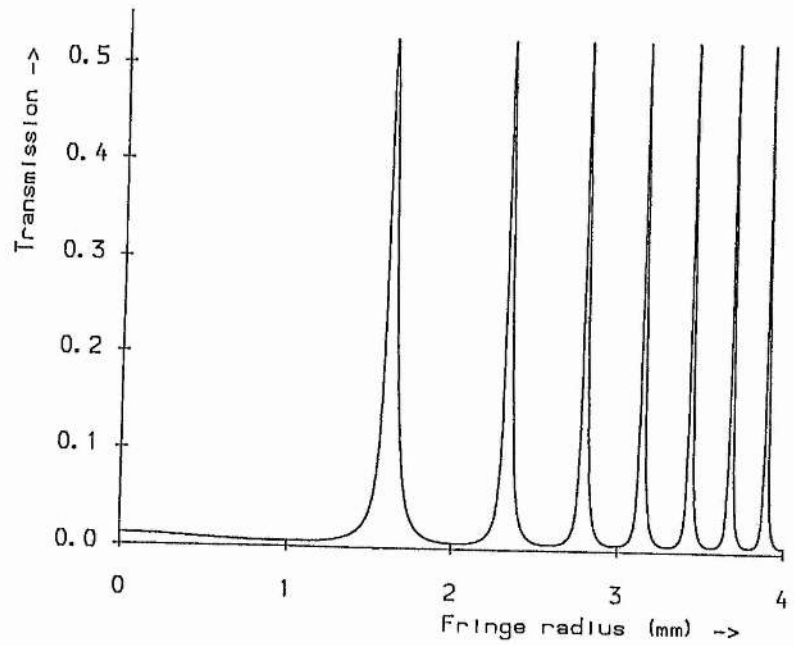

Figure 4. Interferometer fringe pattern in cross section. The upper and lower figures represent values of ε, the departure from confocal position, of 0.1 and 0.2 mm respectively.

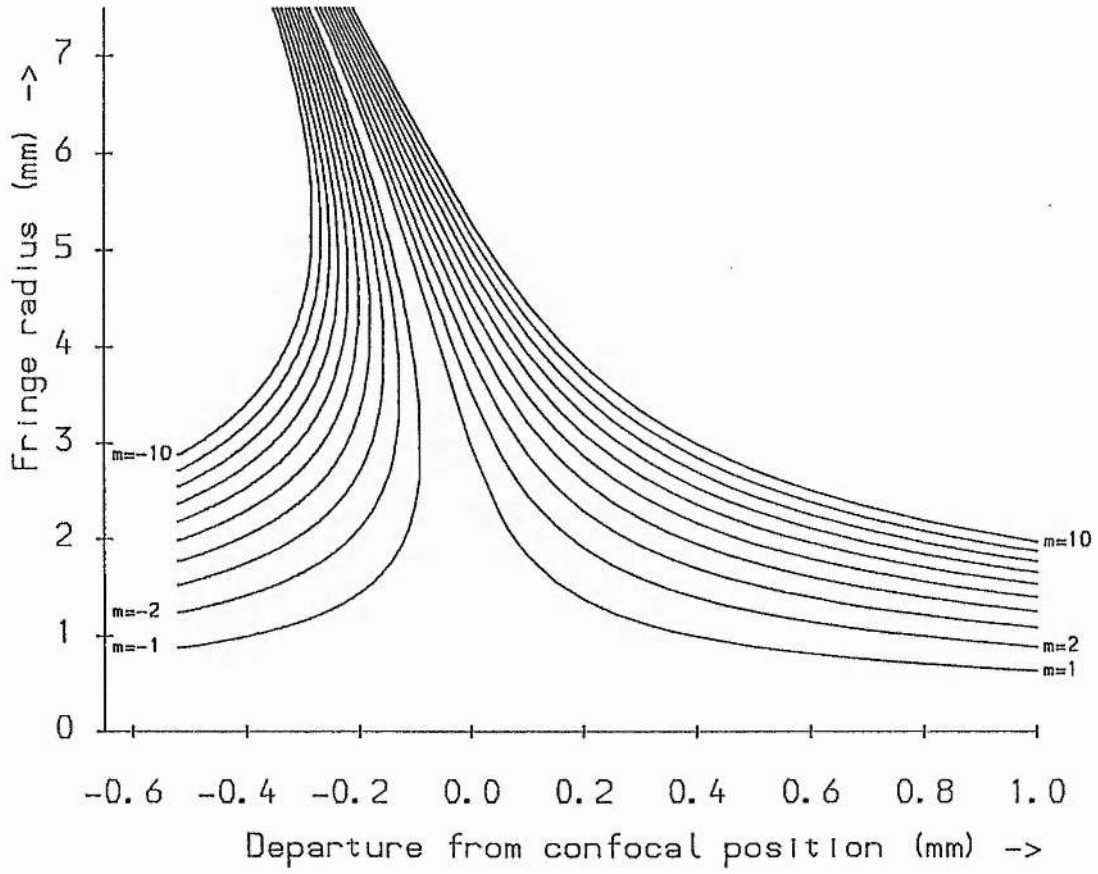

Figure 5. Near confocal FPS fringe patterns for r = 5 cm and λ = 633 nm.

See Equation 17.

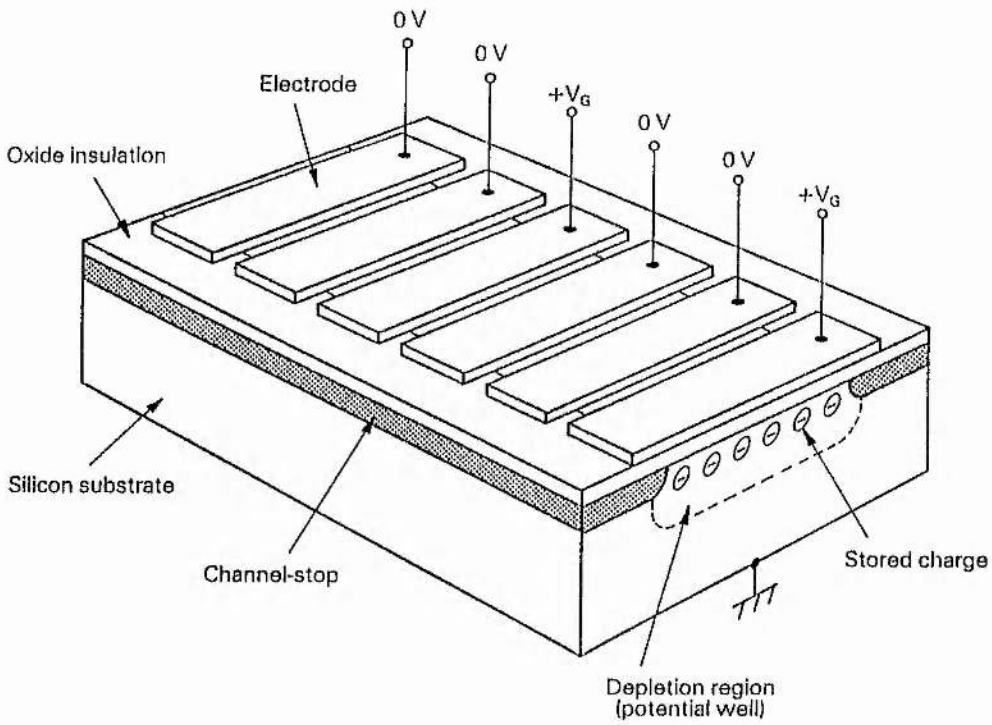

Figure 6. Basic structure of a charge coupled device array (obtained from [7]).

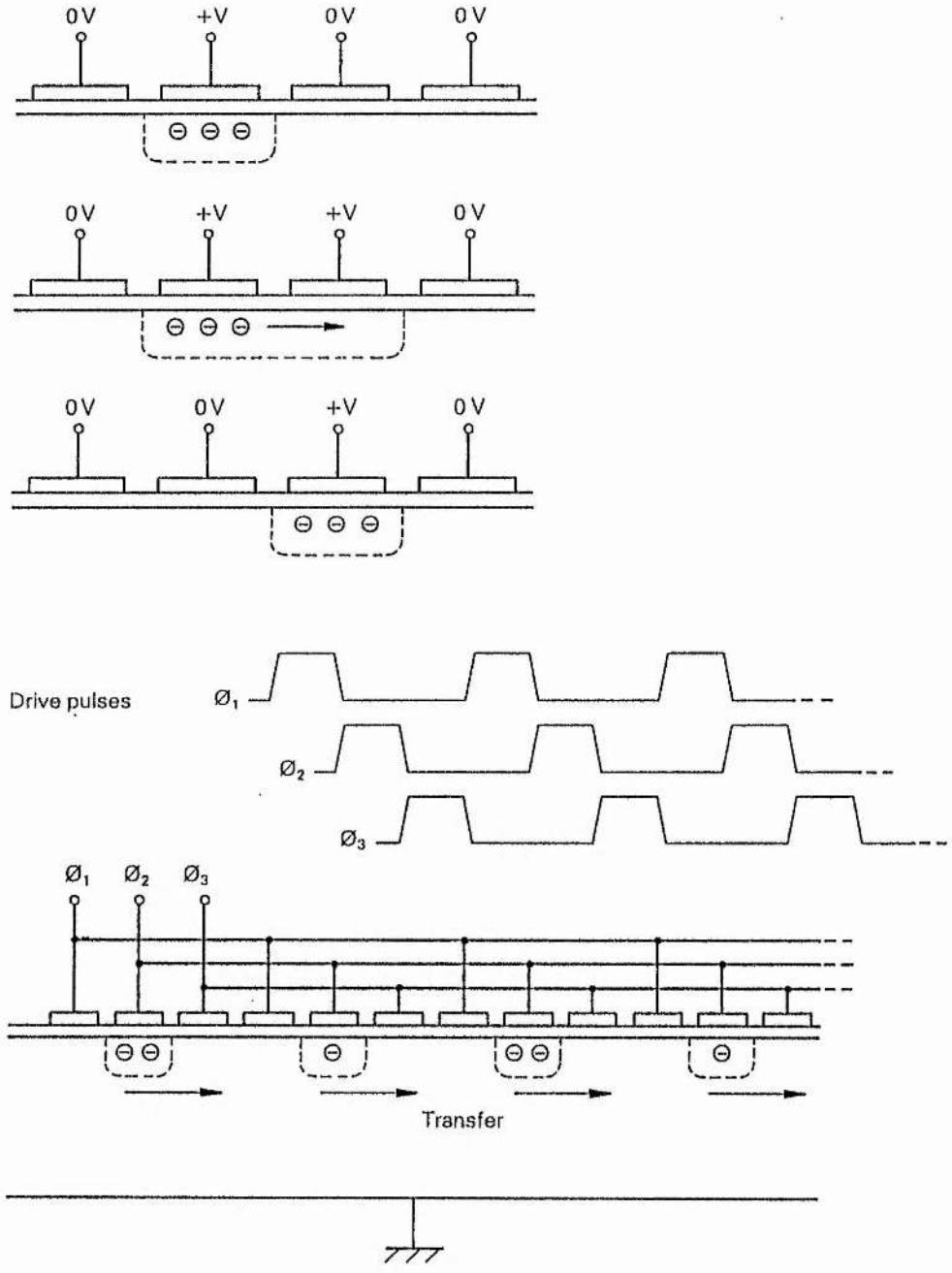

Figure 7. Schematic for the charge transfer mechanism in CCD's (after [7]). By sequentially pulsing the voltages on the electrodes, charge is made to pass from one electrode to another.

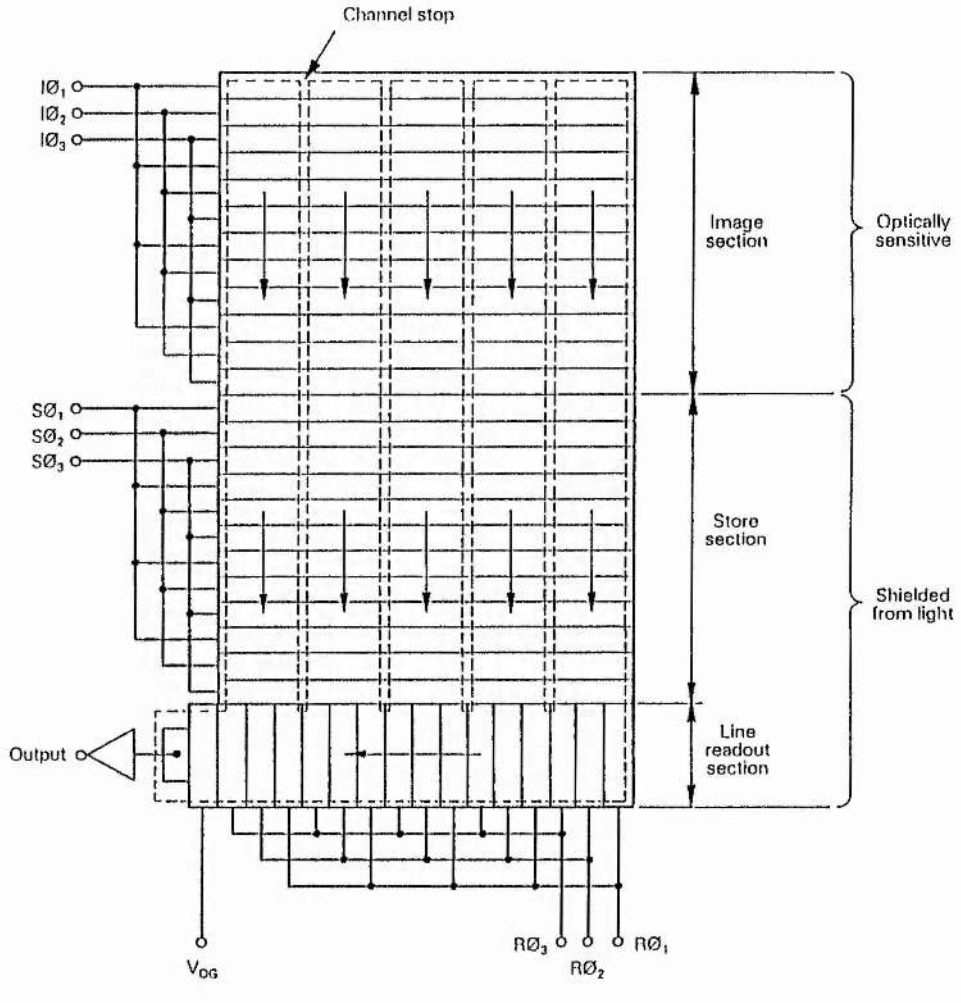

Figure 8. CCD frame transfer schematic (after [7]). The identical sections form two groups. The upper image section collects charge and, after frame transfer into the lower storage section, the image is then clocked out of the array via the line readout section.

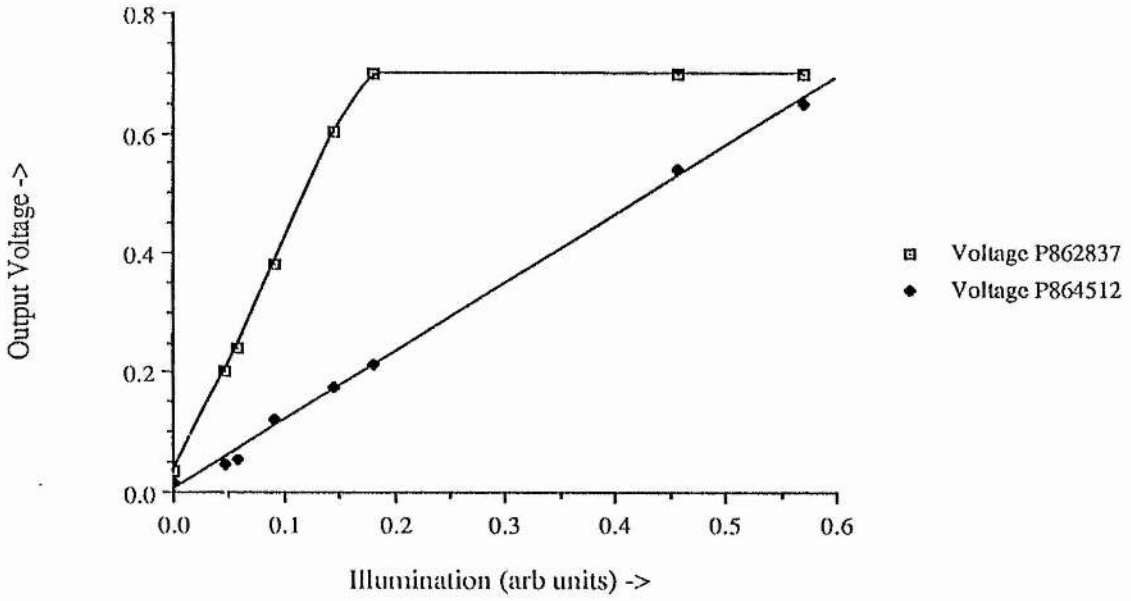

Figure 9. Voltage output as a function of illumination for the two CCD cameras. Both cameras have the desired linear response but the sensitivity of the two, supposedly identical cameras, varies by a factor of three.

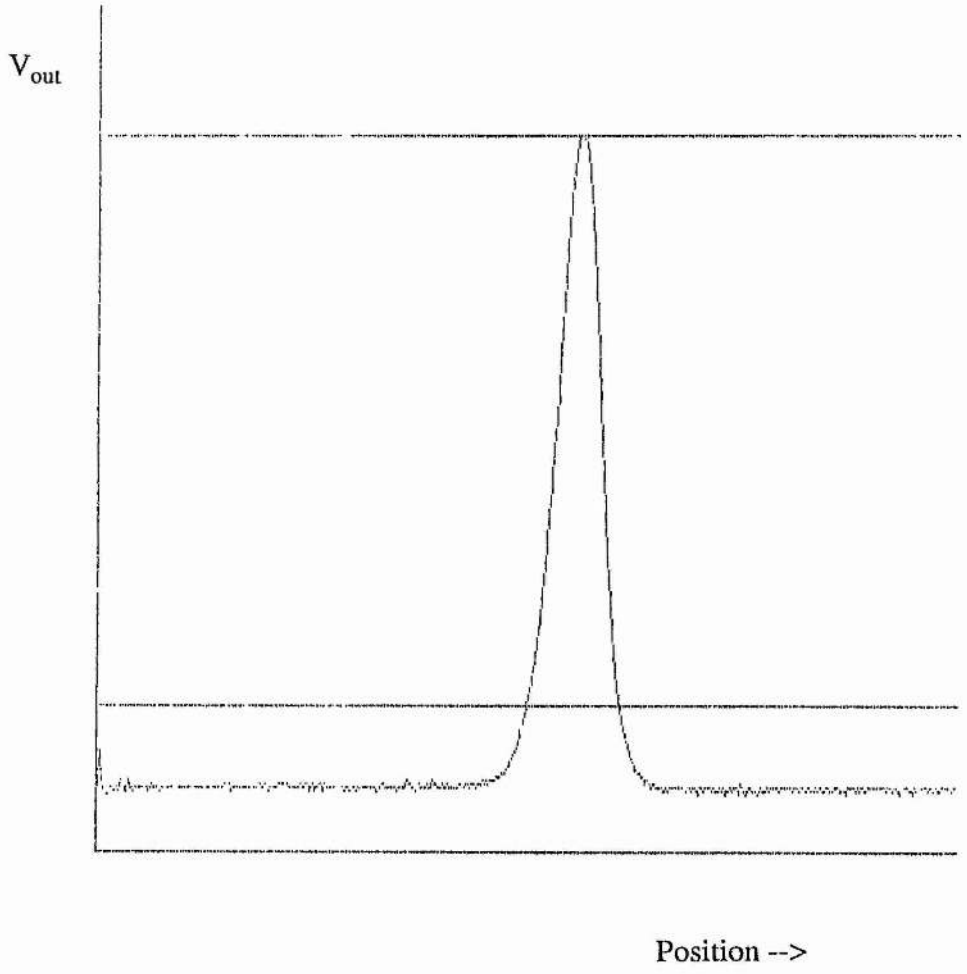

Figure 10. Plot of voltage against position obtained by illuminating the CCD array with an attenuated He–Ne beam. In addition to the maximum voltage V_{max}, V_{max} / e^2 is labelled to allow calculation of the beam spot size (0.5 mm).

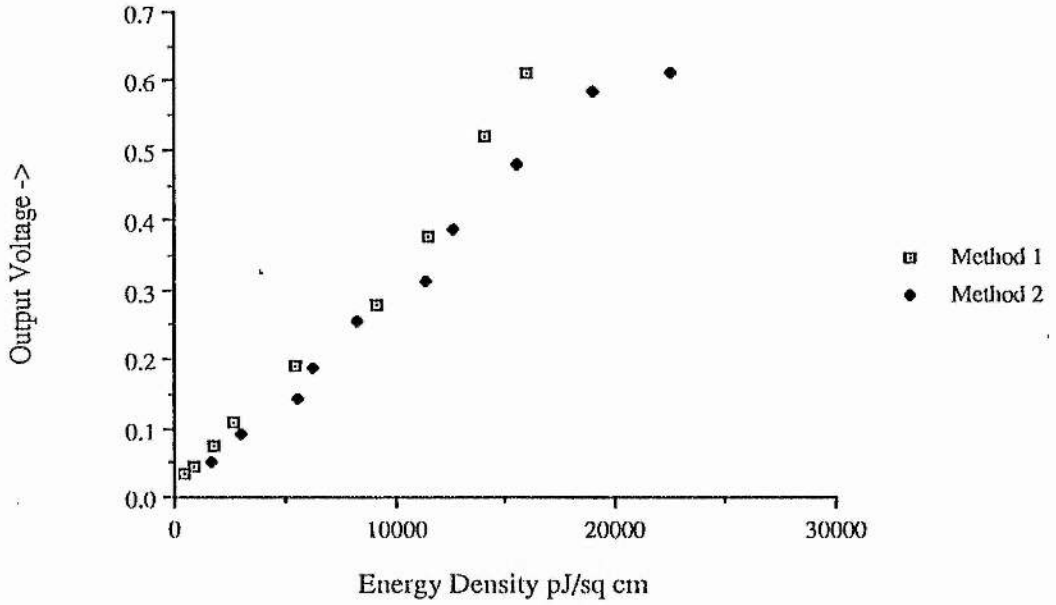

Figure 11. Voltage output as a function of illumination for the P864512 CCD camera. Illumination is defined in the absolute units of pJ cm^{-2}. Method 1 used a combination of ND filters and a polarizer, whereas method 2 used only one ND filter and a polarizer for attenuation of the He–Ne beam.

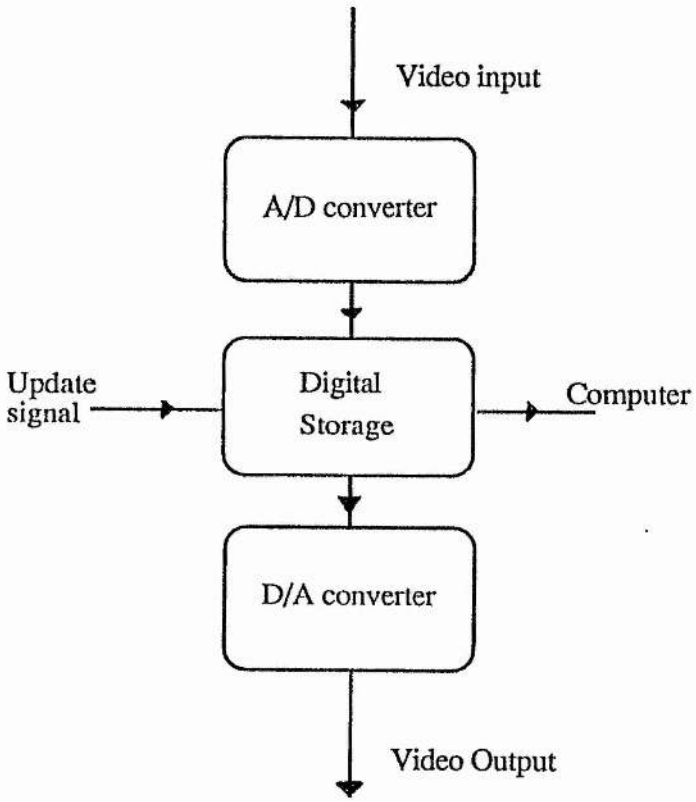

Figure 12. Schematic diagram illustrating the operation of the video framestore. The video signal is digitised, stored and then reconverted into analog video format. If the update signal is interrupted then the current (stored) frame forms the continuous output. This stored frame may then be displayed on a video monitor or be addressed and read by the computer.

Figure 13. False colour images produced by the computer. Two images are shown. 13(a) includes the ellipse used to obtain the eccentricity of the imaged fringed pattern. 13(b) is an example of a false colour image obtained when the DFDL was operating with a narrow linewidth.

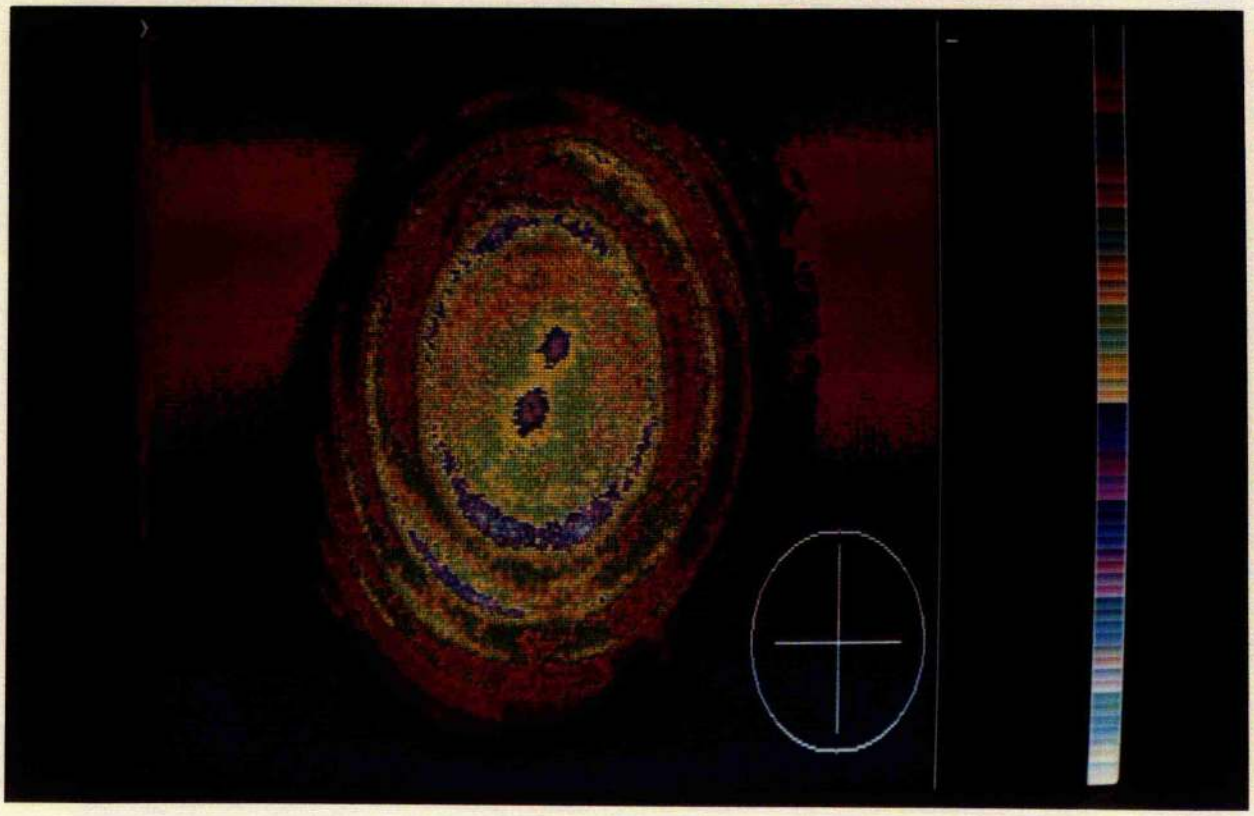

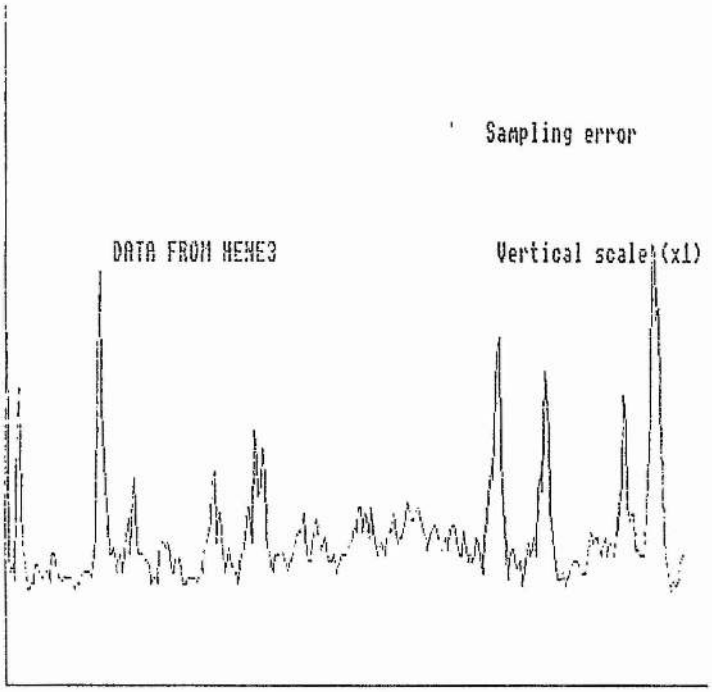

(a)

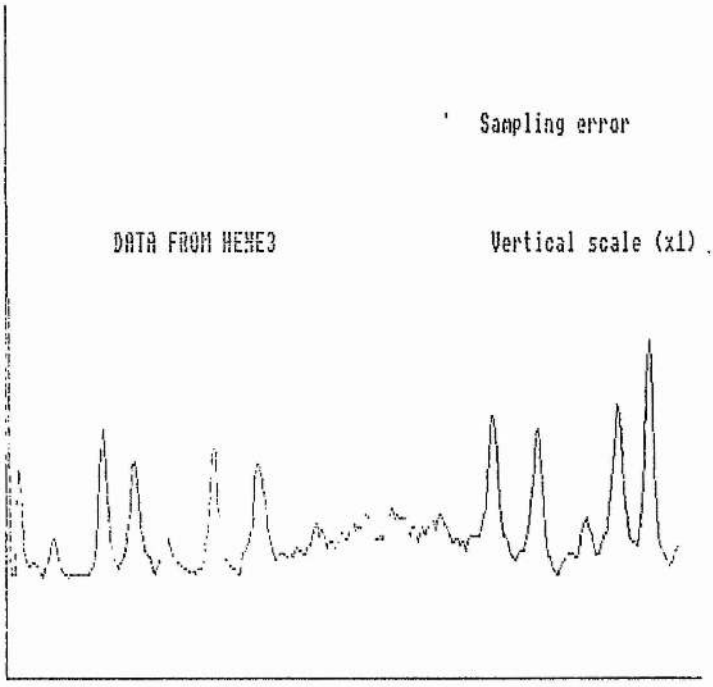

(b)

Figure 14. Examples of line-scan results.

(a) A single line of data sampled from an He–Ne interferogram.

(b) Averaging over 10 lines shows a reduction of the signal noise as more data points are employed.

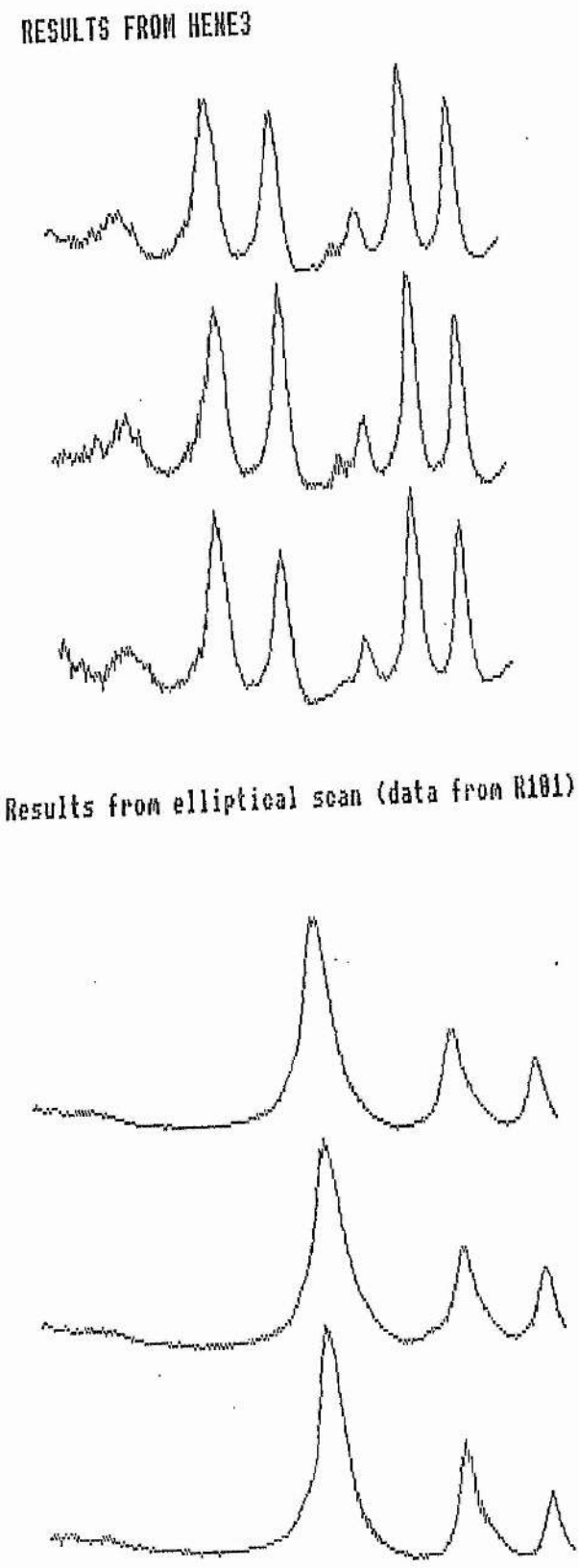

Figure 15. Examples of elliptical scan results.

(a) An elliptical average of the same picture used in the previous figure showing the mode structure of a He–Ne laser.

(b) This is an example of the elliptical scan when used in DFDL linewidth analysis.

Chapter IV–Thermo-optical properties of dye laser solvents.

4.1 Introduction.

In Chapter I it was shown that time dependent changes in the refractive index of the DFDL's active medium causes a chirp of the instantaneous wavelength of the laser. Over the period of the pulse this chirp is interpreted as the laser linewidth. The chirp was seen to be derived from two sources. In the first, dispersion, associated with the changes in the electronic population distribution of the dye molecule, changes the refractive index of the gain medium. The second chirp was seen to be a time dependent change in the dye host solvent refractive index, caused by a heating of the solvent during the pumping process.

This chapter is concerned with a full characterisation of the origin of thermal effects in dye lasers. The amount of heating is dependent upon the pump pulse energy, the overall efficiency of the dye, and on the thermo-optical properties of the dye solvent. These properties are considered for the majority of commonly used dye laser solvents. A general consideration of the importance of these properties to all types of dye laser is followed by a description of the experimental method used to measure changes in refractive index as small as 0.0002. A theoretical section considers how the refractive index of a liquid is related to its density and considers the effect of mixing different liquids. The results of the experimental investigation are then presented, subdividing the solvents into three groups: (i) organic solvents; (ii) water and water based solvents; and (iii) solvent mixtures. The chapter ends with a summary and conclusion.

4.2 Thermal effects in dye lasers.

A major limitation on achieving high power, spectrally narrow and spatially coherent radiation from dye lasers lies in the formation of refractive index gradients due to non-uniform heating by the pump radiation in the region of optical gain. As will be considered in the next section pump radiation is converted into heat in the dye solution by two processes; radiationless deactivation of molecules in excited states, the proportion of which determines the dyes fluorescence efficiency, and through Stokes shift since the emitted photons are less energetic than the absorbed photons.

In chapter I this thermal effect has been shown to be a major limiting factor in narrow linewidth operation of distributed feedback dye lasers (see also [1]). The effect is

however, by no means confined to DFDL's since in high power cw and pulsed dye lasers the formation of such refractive index gradients acts as a thermal lens with severe consequences for output power [2], cavity stability [3], spatial coherence [4] and minimum linewidth obtainable [5]. The quantity dn/dT, the rate at which solvent refractive index changes with temperature, is a most useful parameter in assessing a solvent thermo-optically. The technique employed for the investigation of the thermo-optical properties of dye laser solvents measures the wavelength tuning of the distributed feedback dye laser. In doing so solvent refractive index changes as small as 0.0002 may be determined. The technique hence allows precise measurement of refractive index dependence on temperature, (dn/dT), and therefore enables the thermo-optical properties of solvents used in dye lasers to be assessed. In addition to single component solvents, the thermo-optical properties of solvent mixtures and additives are reported in this chapter. Refractive index change with temperature, dn/dT, is related to solvent density change with temperature, dρ/dT, through molecular polarizability. These accurate values of dn/dT were first reported in [6] for a wide range of dye laser solvents, solvent mixtures and solvents with additives.

4.3 Origin of heating of dye solvent.

The origin of thermal effects in dye lasers is now considered. In the introduction to chapter I the mechanics of absorption and emission in an organic dye are described. It is seen that rapid thermalisation with a particular singlet state occurs as the molecules relax to the potential energy minimum for that state. The emitted photons are less energetic than the absorbed ones (Stokes shifted) and the excess energy is deposited as heat. The fraction of the incident pump radiation contributing to heat as a result of this energy difference is given by,

$$A_S = (1 - \frac{\lambda_p}{\lambda_d}) \qquad (4.1)$$

Although the effect can be minimised by pumping the laser at a wavelength close to the DFDL wavelength, λ_p and λ_d are constrained to lie within the absorption and fluorescence bands of the dye. Variation in the Stokes shift (the separation between absorption and fluorescence maxima) of different laser dyes can be large. For example rhodamine B has a

Stokes shift of around 30 nm [27] whereas laser dye DCM has a Stokes shift of around 165 nm [28]. A second means of contributing to the kinetic energy of the solvent is nonradiative decay between excited and lower energy states. The proportion of radiative transistions determines the fluorescence efficiency* of the dye. In an ideal laser dye the fluorescence efficiency would have the highest possible value, 100% (however, the fluorescence efficiency of a dye is never 100% as there is always a probability of nonradiative decay). The fluorescence efficiency varies from dye to dye and furthermore it can vary for a particular dye according to the solvent used or the temperature of the solvent. Drexhage in *Dye Lasers* [29] attributes this variation to the mobility of the molecules diethylamino groups and, as an example he compares rhodamine B and rhodamine 101. Rhodamine B has a fluorescence efficiency which varies from only a few percent at the temperature of boiling ethanol (78.5 °C) increasing to about 40% at 25°C until reaching 100% at lower temperatures. Cooling increases the efficiency as diethylamino groups are localised. In comparison in dyes where these groups rigidised (e.g. rhodamine 101) are characterised by high fluorescence efficiencies (virtually 100% for rhodamine 101) which is independent of temperature.

Combining the two heating mechanisms the overall fraction, A, of the incident pump energy operating in a dye with fluorescence efficiency, FE, is given by,

$$A = (1 - FE\frac{\lambda_p}{\lambda_d}) \qquad (4.2)$$

Typically about 25% of incident light is converted into heat, within a confined area.

---

* Confusion exists in the published literature about the naming of two processes contributing to the efficiency of the dye. In particular the fluorescence efficiency (i.e. the proportion of photons which decay radiatively) is referred to in a variety of ways e.g. quantum yield of fluorescence, quantum efficiency, fluorescence yield etc. It is suggested that the word quantum is inapplicable in this case and that fluorescence efficiency is more appropriate and should be adopted. Although not used here to aviod possible confusion the term quantum efficiency is suggested for describing the difference in energy between the absorbed and emitted photons.

4.4 Experimental Method.

The period of the interference pattern produced along the axis of the dye cell causing feedback is dependent only on the free space wavelength of the pump laser, λ_p, and the angle of intersection of the two pump beams, θ. This interference causes Bragg backscattering of radiation with a wavelength in the solvent equal to twice the grating period. As a result the free space wavelength at which the dye laser oscillates is given by,

$$\lambda_d = \frac{n_s \lambda_p}{\sin \theta} \qquad (4.3)$$

where n_s is the solvent refractive index at wavelength λ_d. As can be seen from equation (1), this wavelength can be tuned by altering n_s, λ_p, and θ. The pump laser was slow Q-switched to produce narrow linewidth (single longitudinal mode) pulses of duration 12 nsec and energy 1 mJ at a wavelength of λ_p=532 nm. In order to determine dn/dT for a solvent the change of lasing wavelength λ_d was measured, using a high resolution monochromator (Rank Hilger Monospek 1000) giving resolution down to 0.01 nm, as the dye solvent temperature was changed by using a refrigerator unit in the circulator system. Equation (1) was then used to deduce the associated change in refractive index. The DFDL wavelength was normally around 600 nm. DFDL linewidth and shot-to-shot fluctuation of DFDL wavelength were less than the resolution limit set by the monochromator. This technique was first demonstrated by McIntyre and Dunn [7]. In the tables of results to follow, where a numerical value of dn/dT is quoted for a particular temperature this represents a least squares fit over the range ± 2°C around that temperature. Since n is recorded every 0.5°C each fit utilizes nine data points. Errors quoted in brackets are the standard deviation of the fit to the data. Values of dn/dT are quoted for 20°C and 5°C representing room and cooled dye laser operation respectively.

4.5 Refractive index, polarizability and density.

The Lorentz-Lorenz formula [8] relates the mean polarizability α to the refractive index n and the number of molecules per unit volume N by,

$$\alpha = \frac{3}{4\pi N} \frac{n^2-1}{n^2+2} \qquad (4.4)$$

Using the molar refractivity A, which is essentially the total polarizability of a mole, equation (4) may be written as,

$$\frac{n^2-1}{n^2+2}=\frac{A}{W}\rho \qquad (4.5)$$

where W is the molecular weight and ρ the density.

For a mixture of liquids, the refractive index of the mixture is given by,

$$\frac{n_m^2-1}{n_m^2+2}=\left(\frac{A_1}{W_1}f_1+\frac{A_2}{W_2}f_2\right)\rho_m=\left(\frac{A}{W}\right)_m\rho_m \qquad (4.6)$$

where n_m and ρ_m represent the refractive index and density respectively of the mixture. A_1, A_2 and W_1, W_2 represent the molar refractivities and molecular weights of molecules type 1 and 2. f_1 and f_2 are the fractions, by mass, of molecules of type 1 and 2. Refractive index and density are functions of temperature (T), but molar refractivity is expected to be independent of temperature, so that,

$$\frac{n_m^2(T)-1}{n_m^2(T)+2}=\left(\frac{A}{W}\right)_m\rho_m(T) \qquad (4.7)$$

Hence, assuming that the refractivity of a liquid is constant, dn/dT may be estimated from the density, refractive index and dρ/dT, by differentiating equation (7) with respect to temperature to find,

$$\frac{dn_m}{dT}=\left(\frac{A}{W}\right)_m\frac{(n_m^2+2)^2}{6n_m}\frac{d\rho_m}{dT} \qquad (4.8)$$

However since,

$$\left[\frac{A}{W}\right]_m=\frac{1}{\rho_m}\frac{n_m^2-1}{n_m^2+2}$$

(8) may be expressed in terms of the macroscopic properties of density and refractive index.

4.6 Results.

Solvents for dissolving organic dyes may be divided into three main categories:

a) Simple organic solvents eg. methanol, ethanol, ethylene glycol, and mixtures of them.

b) Water based solvents e.g. pure water or water based solutions such as ammonyx LO.

Using a) and b) together yields a third class of dye laser solvent i.e.,

c) Mixtures of water based solvents and organic solvents eg. ethylene glycol/ ammonyx LO. The need for this class of solvent, as will become apparent shortly, is to combine good solubility of the laser dye with good thermo-optical characteristics.

a) Organic solvents.

The most commonly used dye laser solvents are contained in this class e.g. methanol, ethanol, ethylene glycol, benzyl alcohol and propylene carbonate. Figure 1 shows the variation of refractive index with temperature for ethylene glycol and methanol which are typical of this group. Since the dn/dT's of these organic solvents are, to within 10% independent of temperature, results are quoted as a straight line fit over the temperature range of 5–25°C. Results of all the organic solvents measured are found listed in Table 1, and show that the dn/dT's of these organic solvents are much higher than that of water. These liquids, unlike water, have a normal density/temperature behaviour i.e. their density decreases linearly, by expansion, with increasing temperature. In order to verify that the temperature dependence of refractive index is due solely to the temperature dependence of density, as implied by equation (7), figure 2(a) plots A as a function of temperature deduced from our measured values of n(T) and CRC tabulated values of density [8] for ethanol. The constancy of A with temperature verifies this assumption. Its value of 12.9 is close to that expected from the addition of generally accepted atomic refractivities [7,8], which gives 13.2.

b) Water based dyes.

Water based solvents are generally regarded as superior in their thermo-optical properties since $d\rho/dT$ and hence from equation (8) dn/dT is small in comparison with other liquids. Furthermore the density of water increases until 4°C, the temperature at which the density is at a maximum, i.e. $d\rho/dT$ equals zero. Thus for small changes in temperature around 4°C, dn/dT may be expected to be zero, although there is some doubt

about the exact temperature at which this occurs [9]. It is this particular property, exhibited only by water, that makes it the best solvent thermo-optically. Figure 3 shows the measured refractive index versus temperature profile for water and it can be seen that around 4°C there is no detectable change in refractive index with temperature. The molar refractivity A of water is plotted as a function of temperature on Figure 2(b) using our measured values of refractive index and CRC [8] values for density. As is the case of ethanol, the refractivity is constant, with A = 3.71. This compares very well with the tabulated values of 3.72 [7,8]. However dye lasers based on aqueous solutions exhibit low efficiencies. This is due to the association of dye molecules to produce dimers, whose absorption spectra lie in the absorption region of the lasing monomers and also frequently overlap their fluorescence band hence reducing the fluorescence efficiency. In organic solutions dimerization is slight and hence the efficiency is much improved. It is possible however to suppress this process of dimerization by the addition of organic compounds to water [10,11,12,13]. This class includes the two soaps ammonyx LO (lauryl dimethylamine oxide) [10,11], Triton-X100 [12], and the much simpler compound urea $CO(NH_2)_2$ [13], and indeed an increase in the efficiency of the DFDL was observed using these products. What has been misunderstood however is their effect on the temperature dependence of refractive index. To this end the effects of the addition of both ammonyx LO and urea have been characterised.

i) Ammonyx LO/Water Series.

The ratio of liquid ammonyx LO (30%, by mass lauryl dimethylamine oxide ($CH_3(CH_2)_{10}$-CH_2-$N(CH_3)_2$ --> O), 70% water) to water was varied in this experiment from 0 to 100% by volume and two features of refractive index measured, namely: a) bulk index (the refractive index at 20°C) for different proportions of ammonyx LO and water; and b) temperature dependence of refractive index dn/dT for particular mixes. Results to part (a) are given in Figure 4(a). These show that the measured bulk index is equal to the ratio by volume of ammonyx LO times its refractive index (n(20°C) = 1.380) plus the ratio by volume of water times its refractive index (n(20°C) = 1.333), as is to be anticipated on the basis of simple proportionality. Note that the solution was unable to

cooled to less than 8.2°C due to its high viscosity. Results to part (b) are given in Figure 3, for pure water, and Figure 5 for varying proportions of ammonyx LO. Since ammonyx LO is a commonly used solvent the refractive index/temperature relation is listed more fully in Table 2. The effect of the addition of lauryl dimethylamine oxide to water may be explained using equation (6). To determine the molar refractivity of the ammonyx LO active ingredient (lauryl dimethylamine oxide) equation (4) is solved using the following values: $n_m = 1.380$, $W_1 = 18$ g, $W_2 = 229$ g, $f_1 = 0.7$, $f_2 = 0.3$, $\rho_m = 0.96$ g cc^{-1} and $A_1 = 3.71$ to give A_2, the molar refractivity of the lauryl dimethylamine oxide molecule, as 74.1. This last figure may be checked by the usual procedure of the addition of the refractivites of the constituent atoms [7,8], which gives A = 72.63, in good agreement with our experimentally obtained value. Results are shown fully on Table 3. The molar refractivity A versus temperature was obtained using refractive index and density values which were experimentally obtained as a function of temperature for the mixture of 1:1 by volume of ammonyx LO:water. The density/temperature measurement for this mix showed that $d\rho/dT$ was always non zero. As was observed previously with ethanol and water, the molar refractivity of the mixture was independent of temperature, to greater than 1 part in 10^{+4} showing that the refractive index behaviour is due solely to the change in the density with temperature, the addition of ammonyx LO acting to suppress the agglomeration of water molecules which normally leads to a density minimum. Since the dn/dT of pure ammonyx LO is similar to that of a normal liquid (see Figure 5(d)), i.e. no flat portion in dn/dT,the addition of ammonyx LO will degrade the thermal properties of water in proportion to the amount added. On the basis of these results, the commonly used proportions of 1.5 to 4% ammonyx LO [11,14] produce only a slight degradation in the thermal properties.

However the use of ammonyx LO at much higher concentrations has been reported, e.g. 18% [15] or 20% [16] have been used, and indeed 100% ammonyx LO [1] has been proposed as solvents with claimed good thermal properties for use in high power dye lasers. However as can be seen from figure 5 at these concentrations there is a significant increase in the dn/dT compared with water with consequent degradation of thermal properties.

ii) Water / Urea series.

Viktorova et al (1983) [13] reports an observed increase in fluorescence efficiency from ~ 0.4 in water to ~ 0.7 on addition of 40% by mass of urea, while still retaining the good thermo-optical properties of water. Figure 6 shows the measured effect on dn/dT of the addition of 10% and 30% urea, compared with pure water. As can been seen from Fig. 6 the effect of adding 30% urea to water is substantial. This mixture has a dn/dT approaching that of organic solvents, hence rendering it poor thermo-optically. An empirical expression for the refractive index of the solution is,

$$n_m = n_{water} + \beta.P \qquad (4.9)$$

where P is the proportion by weight of urea, and β, which is a function of temperature is given by, $\beta=0.1308 - (5.084 \times 10^{-4}.T)$ for the range 0–30°C, where T is the temperature in °C. While no density/temperature measurements were made for the water plus urea solution it is strongly suspected that the effect is similar to the addition of ammonyx LO to water as described in the previous section.

c) Solvent Mixtures.

In this class are mixtures of water based solvents, mixtures of organic solvents, or mixtures of water based and organic solvents. In section (a) the solvents benzyl alcohol and propylene carbonate were combined in equal proportions to observe the resultant dn/dT. This experiment shows that, to a good approximation, the index properties (n, dn/dT) of mixtures are given by an average of the index properties of the parent solvents weighted in proportion to their percentages in the mixture. It has been claimed [1] that by adding 25% ethylene glycol to an ammonyx LO solution that the desired flat spot in the dn/dT of water may be preserved, although shifted to higher temperatures (10°C). However, since a non zero dn/dT had been observed in ammonyx LO, and a larger dn/dT in ethylene glycol it was not expected that a zero dn/dT should occur for any combination of ammonyx LO/ethylene glycol. The results of this experiment are shown on Figure 4(b) for the bulk indices (20°C) and Figure 7 for dn/dT's, and as with other solvent mixtures, show that the bulk index and the dn/dT for a particular solvent mix is simply inherited from the parent solvents in proportion to their percentages in the mixture.

This combined with the evidence of the water/ammonyx LO series allows the conclusion that, with the two exceptions noted below, the effect of mixing two or more liquids is simply to add proportionally their bulk indices and dn/dT's.

The two exceptions to the proportional addition of the bulk refractive indices observed occurred when either ethanol or methanol was mixed with water. Figure 8 shows the variation of refractive index as a function of proportion, by volume, of methanol in a methanol/water mix. Due to the nonlinear packing of the water and methanol molecules simple proportioning does not apply in this case. In addition to experimentally obtained values those from CRC Handbook [8] are also shown.

4.7 Conclusion.

Using the technique described the refractive indices of most commonly used dye laser solvents have been measured. The results of these measurements are tabulated in tables 1 and 2. From these it can be seen that dn/dT for water is smaller than organic solvents, and furthermore that dyes dissolved in water which is cooled to 4°C represents the best obtainable solvent (dn/dT is zero at this temperature) in terms of thermo-optical properties. It has been recognized (Schafer [10]) that organic additives generally improve the quantum efficiency of dyes dissolved in water. The effect of these additives on dn/dT and hence the thermo-optical properties is reported here for the first time and, contrary to previous claims, it is found that an additive superimposes an additional dn/dT on that of water. For liquid mixtures the resultant dn/dT is simply the proportional average of the parent dn/dT's. For the temperature range of interest the molecular polarizability of liquid molecules is seen to be constant hence indicating that the changes in refractive indices reported are derived from density change with temperature. Thus if density/temperature measurements are available, dn/dT, and hence the thermo-optical suitability, may be inferred. Since water is unique in its $d\rho/dT=0$ at around 4°C it still remains the best solvent thermo-optically, despite attempts to engineer superior ones.

Solvent	n (20°C) (5-25°C)	dn/dT ($-1x10^{-5}$ K^{-1})
Methanol	(1.327)	46.8 (1.1)
Ethanol	(1.360)	43.8 (0.4)
Ethylene Glycol	(1.431)	30.6 (0.3)
Benzyl Alcohol	(1.540)	42.0 (0.4)
Propylene Carbonate	(1.421)	38.0 (0.4)
50/50 BA/PC	(1.471)	42.0 (0.5)

Table 1. Measured values of dn/dT (over range 5°C - 25°C) for organic solvents. For convenience refractive index data for the individual solvents is given in brackets, and is taken from CRC [8] tabulated values.

Temperature °C	Refractive index
26.0	1.3793
24.0	1.3796
22.0	1.3800
20.0	1.3803
18.0	1.3806
16.0	1.3809
14.0	1.3812
12.0	1.3816
10.0	1.3819
8.2	1.3822

Table 2 Measured refractive index n versus temperature for ammonyx LO.

Substance	Mol Weight	Ref Index	Density (g/cc)	A (from eqn 5)
Water	18.0	1.333	0.98	3.71
Ammonyx LO	24.9	1.380	0.96	6.00
Lauryl Amine Oxide	229.0	----	----	74.10

Table 3. Measured molar refractivity for mixtures of water and ammonyx LO.

References Chapter IV

[1] I.A.McIntyre, M.E. Lusty, and M.H. Dunn: J Mod.Optics **35**, 3, 325(1988).

[2] T.F.Johnston, Jr., R.H.Brady, and W.Proffitt: Appl. Opt. **21**, 2307-2316, (1982).

[3] B.Wellegehausen, L.Laepple, and H.Welling: Appl. Phys. **6**, 335-340, (1975).

[4] R.B.Andreev, S.S.Galidov, A.G.Kalintsev, D.I.Staselo, and V.L.Strigin: Opt. Spectrosc. (USSR) **54**, (2), 206-209, (1983).

[5] H.Schroder, H.Welling, and B.Wellegehausen: Appl. Phys. **1**, 343-348, (1973).

[6] M.E. Lusty and M.H. Dunn: Appl. Phys B **44**, 193-198, (1987).

[7] I.A.McIntyre and M.H.Dunn: J.Phys.E, **18**, 19-20, (1985).

[8] M.Born and E.Wolf, *Principles of Optics* Pergamon Press London (1959), pp86-87

[8] CRC, *Handbook of Chemistry and Physics*, 57th edition (1976).

[9] L.A.Lee and R.A.Robb: IEEE J.Quantum Electron.,QE-**16**, 777-784 (1980).

[10] P.Schafer (ed), *Dye Lasers*, Springer Verlag, Berlin (1973).

[11] R.R.Alfano, S.L.Sharpiro, and W.Yu: Opt. Commun, **7**, 191-192, (1975).

[12] O.G.Peterson, S.A.Tuccio, and B.B.Snavely: Appl.Phys.Letters, **17**, 245-247, (1970).

[13] A.A.Viktorova, A.Savikin, and V.B.Tsaregradskii: Sov.J.Quant.Electron., **13**(8), 1140-1142, (1983).

[14] J.Y.Allain: Appl.Optics **18**, 287, 289, (1979).

[15] P.Anliker, H.R. Luthi, W.Seelig, J.Steiner, H.Weber, S.Leutwyler, E. Schumacher, and L.Wost: IEEE J. Quantum Electron (Lett), QE-**13**, 547-548, (1977).

[16] F. Bos: Appl. Optics **20**, 1886-1890, (1981).

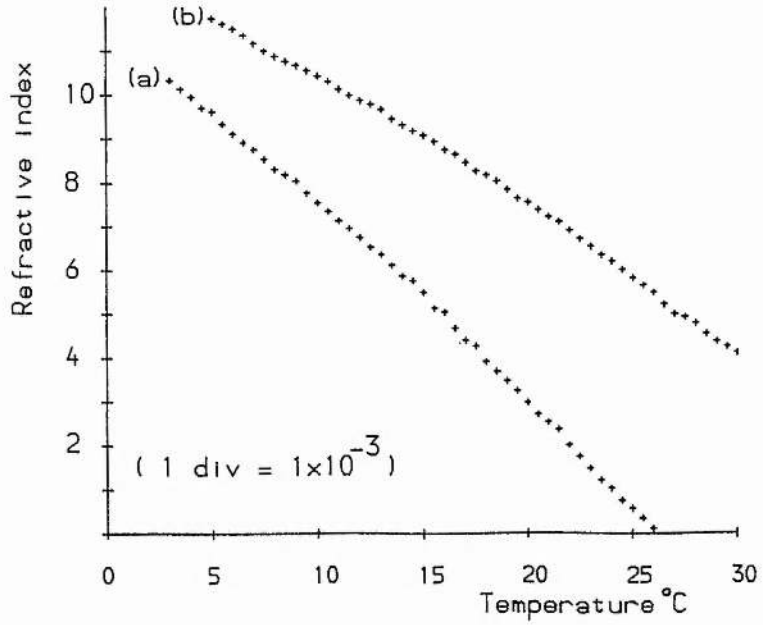

Figure 1. Refractive index against temperature of (a) methanol, and (b) ethylene glycol. Vertical axis divisions correspond to a change in refractive index of $1x10^{-3}$. Methanol had the largest dn/dT of any of the solvents measured.

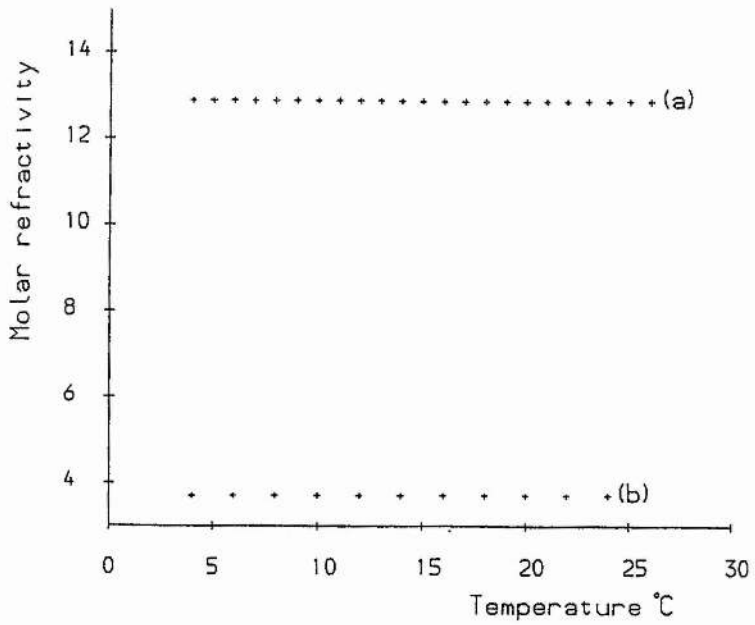

Figure 2. Molar refractivity against temperature for (a) ethanol, and (b) water. In both cases the refractivity is constant to 1 part in 10^{+4}.

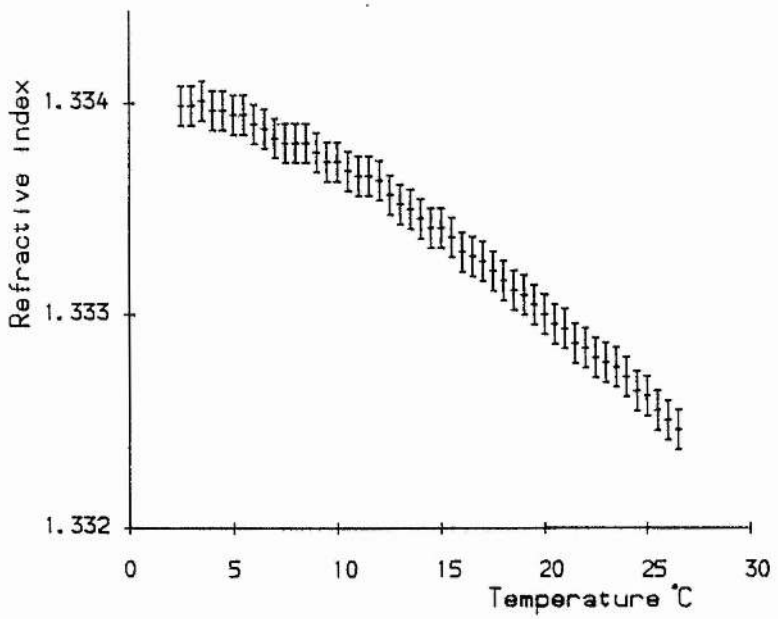

Figure 3. Refractive index against temperature of pure water. Vertical axis divisions correspond to a change in refractive index of 1×10^{-3}. Around 4°C refractive index is constant i.e. dn/dT=0.

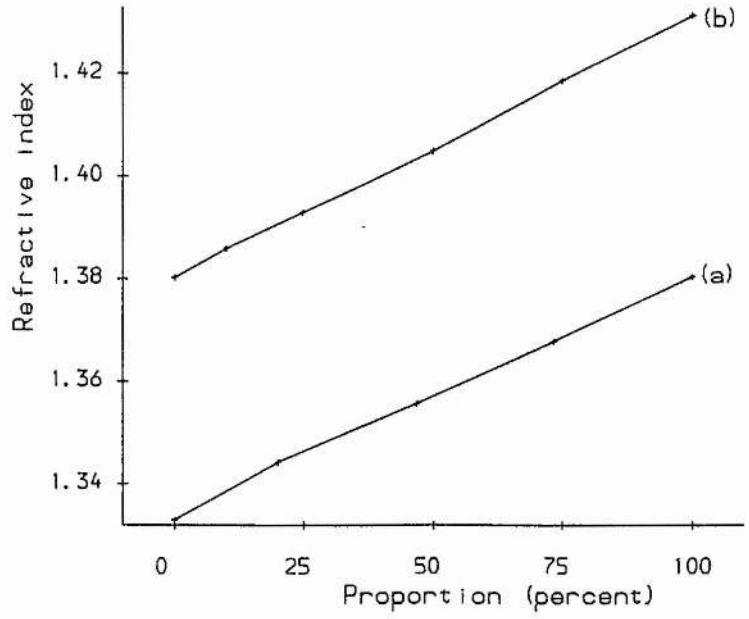

Figure 4. Refractive Indices for (a) water/ammonyx LO series, and (b) ammonyx LO/ethylene glycol series. 0% represents pure water in (a), and 100% ammonyx LO in (b) respectively.

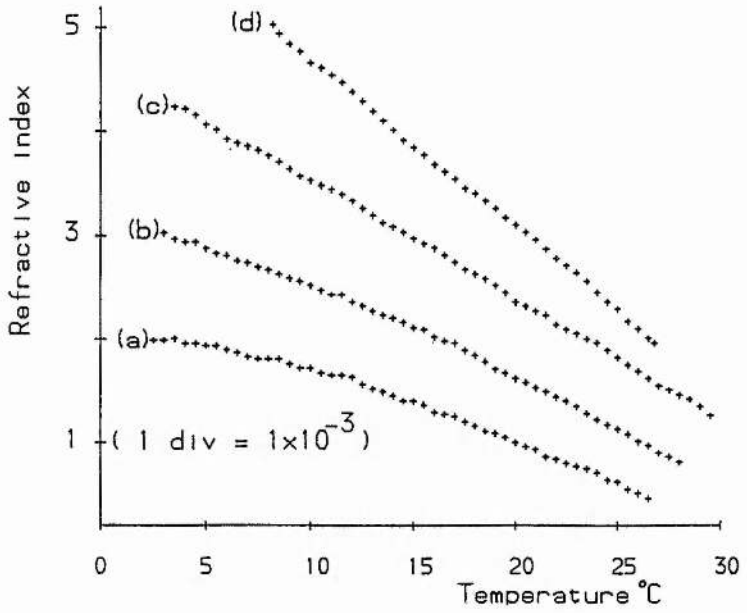

Figure 5. Refractive index against temperature of (a) pure water, (b) 75% water 25% ammonyx LO, (c) 50% water 50% ammonyx LO, (d) 100% ammonyx LO. Vertical axis divisions correspond to a change in refractive index of $1x10^{-3}$. As ammonyx LO is added the dn/dT of the solvent is increased in proportion to the amount added.

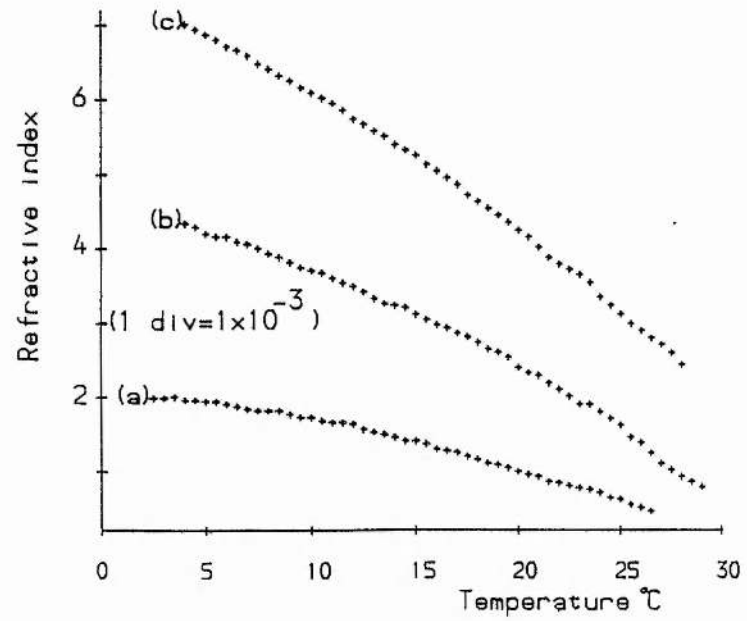

Figure 6. Refractive index against temperature of (a) pure water, (b) water with 10%, by mass, urea, and (c) water with 30%, by mass, urea. Vertical axis divisions correspond to a change in refractive index of $1x10^{-3}$.

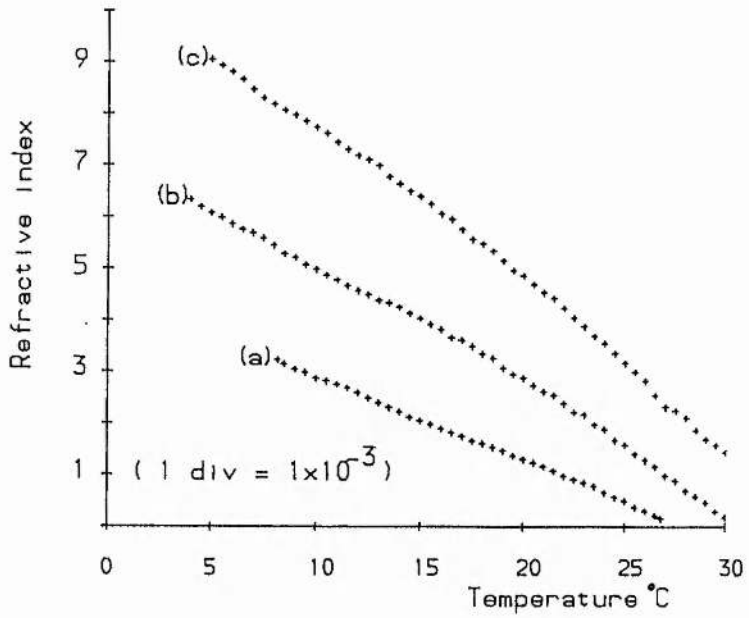

Figure 7. Refractive index against temperature of (a) ammonyx LO, (b) 75% ammonyx LO 25% ethylene glycol, and (c) 100% ethylene glycol. Vertical axis divisions correspond to a change in refractive index of $1x10^{-3}$. As expected the mixtures of these two solvents have index properties (n, dn/dT) inherited from the parent solvents.

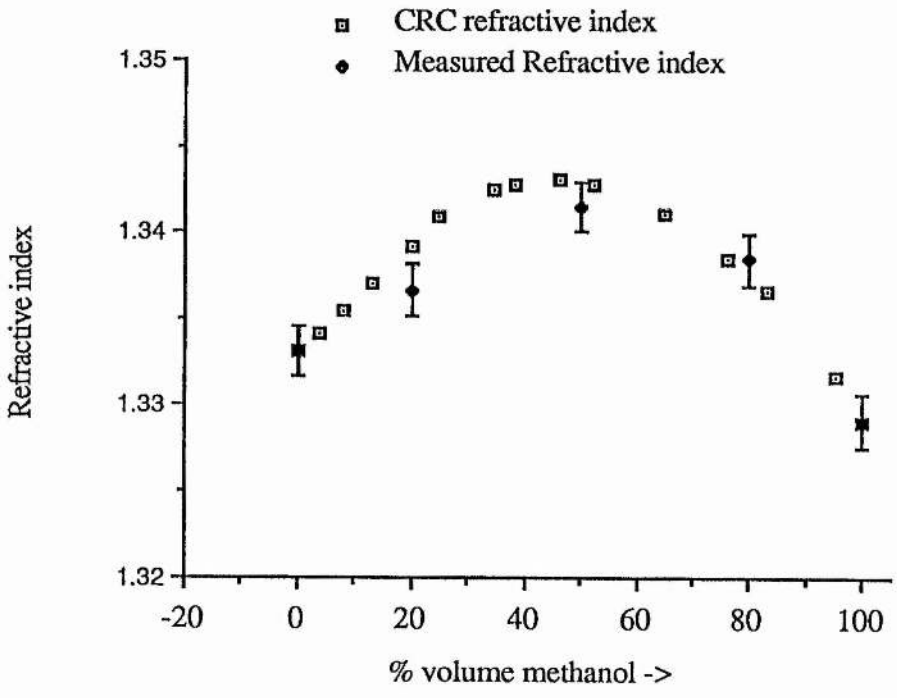

Figure 8. Refractive index against percentage volume for a water/methanol mix. CRC Handbook [8] values are plotted in addition to those obtained experimentally.

Chapter V–DFDL rate equation analysis.

5.1 Introduction.

This chapter contains an account of how rate equations, describing the temporal evolution of the population inversion and the photon density inside the DFDL active region, can be used to predict the operation of the laser. The rate equations are common to any laser with only one exception. In a Fabry-Perot cavity laser the cavity decay time is a constant, depending mainly on mirror reflectivity. In contrast however, the decay time of a distributed feedback laser is a function of the modulation providing feedback. Since, as will be shown later, the cavity decay time is proportional to the square of the laser gain, the cavity decay time is time dependent. Rate equations in DFDL analysis were first used by Bor [1,2] to explain the pulsing behaviour of a nitrogen pumped DFDL. In section 2 the rate equations themselves are developed. Section 3 describes the numerical solution of the equations and in section 4 various solutions are presented outside the near threshold region described by Bor to show how the rate equations can predict smooth pulsing.

5.2 Rate equation model.

In the rate equation model to be developed, the laser is assumed to be an ideal homogeneously broadened four level laser. A schematic representation of the energy levels of a dye molecule with important transistions labelled maybe found in Chapter I. In describing the evolution of N_1 – the population of the S_1 band, the rate of change of N_1 is given by,

$$\frac{dN_1}{dt} = R - W_i N_1 - \frac{N_1}{\tau_f} \qquad (5.1)$$

where,

R is the pumping rate per unit volume ($m^{-3}\ s^{-1}$),

W_i the induced transition rate (s^{-1}) and,

τ_f is the fluorescence lifetime of the S_1 to S_0 transition (s).

The second and third terms on the r.h.s. side of equation (1) describe the competing processes of stimulated and spontaneous emission which deplete the inversion. A similar type of equation can also describe the evolution of the intra-cavity photon density, q, as,

$$\frac{dq}{dt} = B\,N_1\,q - \frac{q}{\tau_c} + \frac{\Omega N_1}{\tau_f} \tag{5.2}$$

where,

B is the induced decay rate, defined by $W_i = Bq\ (s^{-1})$ and,

Ω is a geometric constant defining the fraction of spontaneous emission falling inside the angular and spectral range of the DFDL beam.

The first and third terms on the r.h.s. side of equation (2) describe stimulated and spontaneous emission while the second term describes the loss of the cavity. These first-order nonlinear differential equations therefore describe the interplay between the population inversion and the cavity photon density. The equations are coupled i.e., the solution of (1) depends on the solution of (2) and vice versa. Equations (1) and (2) are general and can be made more specific to dye lasers by rewriting terms such as W_i in terms of cross sections, since these are the more commonly used parameters. The pumping rate R, determining the growth of population in the S_1 state is given by the product of the pump rate I_p, the absorption cross section σ_p and the population in the S_0 state, (N_0-N_1), i.e. $R=I_p\sigma_e(N_0-N_1)$. Stimulated emission, the product of W_i and q can be written in terms of the stimulated emission cross section, σ_e, and refractive index, η, as,

$$W_i\,q = \frac{\sigma_e c}{\eta} N_1 q. \tag{5.3}$$

B in equation (2) can be replaced with,

$$B = \frac{(\sigma_e - \sigma_a)}{\eta} \tag{5.4}$$

and thus equations (1) and (2) may be rewritten as,

$$\frac{dN_1}{dt} = I_p(t)\,\sigma_e(N_0-N_1) - \frac{\sigma_e c}{\eta} N_1 q - \frac{N_1}{\tau_f} \tag{5.5}$$

$$\frac{dq}{dt} = \frac{(\sigma_e-\sigma_a)}{\eta} N_1 q - \frac{q}{\tau_c} + \frac{\Omega\,N_1}{\tau_f} \tag{5.6}$$

As described above, Ω is the factor determining the proportion of spontaneous emission which propagates into the angular and spectral range of the DFDL beam and is given by,

$$\Omega = \frac{b}{\pi N \sigma_p L^2 S} \tag{5.7}$$

where L is the length of the DFDL, a and b are the width and height respectively of the excited volume, and S is the spectral factor determining the fraction of spontaneous emission which falls inside the DFDL linewidth. In the solution of the rate equations to follow it is seen that the exact value of Ω is insignificant because it represents the noise of the system from which the laser oscillation starts. If this term is not present then, by (2), at t=0, if q=0, q would always remain zero. This noise term is often neglected in related literature, since once oscillation occurs it becomes insignificant, but the term is vital in a numerical solution. In equations (5) and (6) the pump photon density, the density of molecules in the S_1 state and the density of DFDL photons are written as the time dependent variables, $I_p(t)$, $N_1(t)$ and $q(t)$ respectively. For the purpose of modelling $I_p(t)$ is assumed to have a Gaussian form,

$$I_p(t) = I_{max} \exp(-\beta t^2) \tag{5.8}$$

with β chosen to give the appropriate Gaussian halfwidth. The default value of β for a 10 ns (FWHM) pulse is $\beta = 2.77 \times 10^{16}$ (s^{-2}).

Equations (5) and (6) are common to any type of dye laser but an important distinction exists in the cavity decay time τ_c of a DFDL. A conventional Fabry–Perot cavity laser has a fixed cavity decay time whereas, as will be seen below, the cavity decay time of a DFDL is variable. In a cavity laser the cavity decay time is $\tau_c = 2L/Bc$, where B is the fractional intensity loss per pass. Neglecting diffraction effects and other losses τ_c may be written as,

$$\tau_c = \frac{2L}{c(1-R)} \tag{5.9}$$

where R is the mirror reflectivity. Inside the excited length of the DFDL Kogelnik and Shank [3] considered the laser field as being composed of two counter propagating waves, R and S, each strongly reflected by Bragg reflection from the induced grating. Using this analysis Chinn [4] recognized that the (1-R) term of (9) can be expressed as the ratio of power emitted by the DFDL divided by its intracavity power and hence obtained an expression for the cavity lifetime. Using the notation used above, τ_c is written as,

$$\tau_c(t) = \frac{\eta L^3}{2c\pi^2}\left[\left(\frac{\pi}{\lambda_o}\eta_1(t)\right)^2+\left(\frac{1}{2}\alpha_1(t)\right)^2\right] \qquad (5.10)$$

Using the notation of Kogelnik and Shank, η_1 and α_1 are the amplitudes of the spatial modulation of the refractive index and gain respectively. As can be seen in equation (10) τ_c is now a time dependent variable, which, in a Fabry-Perot cavity laser, would be equivalent to having a time dependent mirror reflectivity, or some time dependent loss in the cavity, such as might be provided by an electro-optic modulator although, unlike an e–o modulator, the behaviour of the decay time is a function of the laser parameters and cannot be controlled externally. Bor [1] rewrites the modulation of refractive index η_1 as,

$$\eta_1(t) = \frac{dn}{dT}\Delta T(t) \qquad (5.11)$$

but an appendix to the paper claims that the effect is negligible. Comparing the magnitudes of the gain and refractive index feedback mechanisms it is indeed found that the feedback due to gain modulation exceeds that of refractive index modulation by several orders of magnitude. We are therefore in agreement with Bor [1] in that within the constraints of this analysis, the term may be neglected. The modulation of gain, $\alpha_1(t)$, may be written in terms of stimulated emission cross section, σ_e, S_1 state population N_1, and visibility of fringes V as,

$$\alpha_1(t) = (\sigma_e-\sigma_a)\, N_1 V \qquad (5.12)$$

Using (11) the expression for cavity decay time used in the analysis is written as,

$$\tau_c(t) = \frac{\eta L^3}{2c\pi^2}\left[N_1(t)\,(\sigma_e-\sigma_a)V\right]^2 \qquad (5.13)$$

Thus in a DFDL the time dependent cavity decay time is proportional to the square of the excited state population N_1.

The power emerging from both ends of the DFDL is given by the cavity photon density, q, divided by the cavity decay time τ_c. Multiplying this by the photon energy hc/λ and knowing the active volume of the DFDL, (Lab), the output power emerging from one end of the DFDL is,

$$P_{out}(t) = \frac{1}{2}\frac{hc}{\lambda}\,\text{Lab}\frac{q}{\tau_c} \quad \text{(Watts)} \qquad (5.14)$$

A useful parameter for subsequent analysis is that of steady state excited population threshold, N_{th}, obtained by setting $\frac{dq}{dt} = 0$ in equation (6) and hence,

$$\frac{dq}{dt} = \frac{(\sigma_e - \sigma_a)}{\eta} N_{th}\, q - \frac{q}{\tau_c} = 0$$

Thus,

$$N_{th} = \frac{2}{(\sigma_e - \sigma_a)L} \left(\frac{\pi}{V}\right)^{\frac{2}{3}} \qquad (5.15)$$

5.3 Numerical Solution of Rate Equations.

5.3.1 The Fourth Order Runge–Kutta Method.

The coupled nonlinear rate equations developed above describe the time evolution of population inversion and photon density. The numerical solution of these equations as a function of time allows these and other parameters, such as cavity decay time to be plotted, hence providing a useful insight into the behaviour of the DFDL. Reviews of numerical methods for the solution of differential equations may be found in applied mathematics textbooks such those of [5] and [6]. The simplest method for numerical solution of this type of differential equation is the first order forward difference method, known as Euler's method. Considering, for example, the simple first order ordinary differential equation,

$$\dot{y} = f(x,y) \qquad (5.16)$$

Euler's method may be written as,

$$y_{n+1} = y_n + h\, f\,(x_n, y_n), \qquad n = 0, 1, 2, \ldots \quad (5.17)$$

The algorithm therefore involves multiplying both sides of equation (16) by the small time interval dt (denoted as the step size, h, above), and obtaining the change in y i.e. dy after that time interval. The value of dy is then added to y and thus a new value for y is obtained for the time t = t + dt. This process is repeated many times, each time substituting the newly obtained values of y into the equation. The program developed uses a common extension of this method known as the classical, or fourth order, Runge-Kutta method which, written in the style of (17), is,

$$y_{n+1} = y_n + \frac{h}{6}[k_1 + 2k_2 + 2k_3 + k_4], \qquad (5.18)$$

where,

$$k_1 = f(x_n, y_n),$$

$$k_2 = f(x_n + \tfrac{1}{2}h,\ y_n + \tfrac{1}{2}h\,k_1),$$

$$k_3 = f(x_n + \tfrac{1}{2}h,\ y_n + \tfrac{1}{2}h\,k_2),$$

$$k_4 = f(x_n,\ y_n + h\,k_3).$$

This method is used to give a weighted average over four points and, for a given step size h, is generally more accurate. A slight variation of this Runge-Kutta method was used by Bor [1,2] to compute the dynamic behaviour of his DFDL. For modelling of the DFDL the one variable method outlined above was extended to the two variables, population inversion, N_1, and photon flux, q. Since changes in N_1 and q occur on a sub-nanosecond basis so the step size h must be much less than the fastest changes that may occur. In the program developed, a step size of 10 picoseconds was found to give reliable results. Step sizes of more than 40 ps lead to the program going unstable. Smaller step sizes yielded no noticeable difference in the program output but simply used more computational time. The Euler method was also used but it required a step size of around 5 ps, rendering it a less accurate and less efficient routine. Further details of the FORTRAN program used, including a program listing can be found in appendix III.

Since the algorithm loop typically needed to be performed around 4000 times, computation seems the obvious method of solution but interestingly Schmitt and Schafer [7] successfully modelled cavity dye laser operation using an analogue computer.

5.3.2 Model Parameters.

The values used in the modelling to follow are now presented. Where possible these parameters were chosen to fit the laser's normal experimental mode of operation. To this end the pump pulse energy was taken to be 2 mJ and the laser dye molarity 3×10^{-4} M. These represent typical operating values. Values for σ_e, σ_a, and σ_p, were obtained from [8], τ_f and S were obtained from [2]. Unless otherwise stated 2 mJ pumping, 3×10^{-4} M solution and FWHM= 10 ns are the default parameters for all modelling performed. Table 1 lists the values of all the default parameters. Figure 1 shows the temporal form of the 10 ns FWHM pulse used in most of the modelling to follow. So as to overcome numerical

instabilities in the program, modelling was started at t = - 20 ns from the centre of the pump pulse maximum. Thus at four Gaussian halfwidths, the initial value of I_p was less than 1000 times that of the peak value for pumping I_{max}. Unlike Bor [2], no initial values of N_1 and q were necessary, these being zero at time t = -20 ns.

In the analysis to follow, reference will be made to the inversion value, N_{th}, an expression for which is given by equation (15). Using this equation and the parameters above a value for N_{th} is obtained as,

$$N_{th} = \frac{2}{(\sigma_e - \sigma_a)L}\left(\frac{\pi}{V}\right)^{\frac{2}{3}} \qquad = N_{th} = \frac{2}{(2.0 \times 10^{-20} - 1.0 \times 10^{-20})\ 0.02}\pi^{\frac{2}{3}}$$

$$= 2.15 \times 10^{22}\ m^{-3}.$$

5.4 Rate Equation Solutions.

This section considers the rate equation model and how it can be used to predict two quite different types of solution. It will be seen that the model predicts that, near threshold, self Q-switching leads to the production of pulses of much shorter duration than those of the pump pulse. However, in conditions equivalent to operation at levels substantially above threshold the model predicts that the DFDL produces pulses which are temporally similar to those of the pump laser. Thus, to a first approximation the type of operation predicted is dependent on the level of pumping. As will be seen in the next chapter both such types of operation have been observed experimentally. In addition to the effect of different levels of pumping, considerations of the effect of dye concentration, grating visibility etc. were also investigated.

5.4.1 Picosecond pulse regime.

As will be shown, in this region single and multiple pulses which have durations typically two or three orders of magnitude less than those of the pump laser are predicted. Such operation occurs when the laser is operated near to its threshold. To illustrate the dynamics of laser action consider figures 2 (a) and (b) which show the temporal evolution of the population inversion (obtained from equation 5) and the output power (obtained from equation 14) for the case where pumping is at the 0.1 mJ level. All of the other equation parameters are given by the default values of table (1). As can be seen from the

figures, a number of pulses of picosecond duration are predicted while pumping at this level. Such pulses are caused by the interplay between the circulating cavity radiation field and the atomic inversion. A similar type of action is observed in Fabry–Perot cavity lasers in conditions leading to the formation of relaxation oscillations (see for example [9,10]). Although such an analogy is not strictly applicable because of the time dependence of feedback, it will be seen shortly that a useful comparison with relaxation oscillations can be made.

In the early part of the pump pulse the population inversion increases towards its threshold value which, using the default parameters equals 2.15×10^{22} m^{-3} (see equation 14). As pumping continues the inversion approaches and surpasses that of threshold for laser action. When this occurs the laser gain exceeds the cavity loss and the intracavity field increases. However, initially there are insufficient photons in the laser 'cavity' to provide depletion of the inversion through the process of stimulated emission. The only photons that experience gain are those contained in the Ω term (that fraction of spontaneous emission falling inside the spectral and angular range of the feedback region). The net effect is therefore that the inversion continues to increase as the pumping rate exceeds the depletion rate. In doing so the cavity Q is also increasing. This situation describes the rising edge of the DFDL pulse when laser action is quickly established. However, this action sweeps out a substantial portion of the inversion through stimulated emission causing the inversion to fall below its threshold value and hence switching the cavity Q from a high to low value. Thus a single pulse is emitted as the cavity Q switches from a low to high Q to establish oscillation before returning to a low Q state in the latter half of the pulse. The description above applies to the situation where the laser is operating just above threshold. If the pumping is sufficiently strong then the medium has sufficient time to recover, the inversion can again exceed the threshold value and another short pulse is emitted.

Such behaviour is in good agreement with experiment. It has further been observed experimentally that increased pumping causes the number of short pulses to increase and the separation between then decrease. The role of pumping is now examined where it will be seen that this helps in the formation of a link to another type of regime which is

observed experimentally i.e. where the laser generates pulses which mimic the temporal behaviour of the input pulse.

5.4.2 The role of pumping.

To explore the effect which pumping has on the DFDL the pump rate, I_p, was assigned a constant value. This is equivalent to providing a step input from zero to a constant value. Figures 3 (a) and (b) show the predicted output for a constant pump power of (a) 20 kW and, (b) 40 kW respectively. On inspection of the figures some general conclusions may be made namely:

i) at higher levels of pumping the time between the pulses decreases and,

ii) a higher degree of damping is superimposed on the secondary pulses.

Similar observations have been made in considerations of relaxation oscillations in Fabry–Perot cavity lasers. By considering small perturbations from the equilibrium state (i.e. $dN_1/dt = dq/dt = 0$) Yariv [9] obtained an equation of motion describing a damped harmonic oscillator. Defining the pumping factor r as $r = RB\tau_c\tau$, (R,B,τ_c, and τ are as defined in section 5.2) the equation of motion is written as,

$$\frac{d^2q}{dt^2} + \frac{r}{\tau}\frac{dq}{dt} + \frac{1}{\tau\,\tau_c}(r-1)\,q = 0 \qquad (5.19)$$

hence obtaining the damping rate α and the oscillation frequency ω_m as,

$$\alpha = \frac{r}{2\tau} \qquad (5.20)$$

$$\omega_m = \sqrt{\frac{1}{\tau\,\tau_c}(r-1) - \left(\frac{r}{2\tau}\right)^2} \qquad (5.21)$$

Although this analysis is not valid for strong modulation, and in the case of the DFDL τ_c is not a constant but proportional to the square of the inversion, the analysis is in reasonable agreement with those predictions made about the effect of pump power on the DFDL. Extending this argument to high levels of pumping which are considered next, leads to an understanding of the mechanisms causing longer pulse production.

5.4.3 Nanosecond pulse regime.

In the two previous sections the input parameters of the rate equation analysis were equivalent to near threshold pumping of the DFDL. Under these conditions the predicted output consists of one or more picosecond pulses. This section now considers the predictions of the model under conditions of high levels of pumping. Previously this regime has not been considered in DFDL analysis and, as will be seen in later chapters, the predictions are in good agreement with experimental results.

To extend the model to high levels of pumping the pump pulse parameter was increased to be equivalent to a pump pulse energy of 10 mJ. All of the other equation parameters are as given in table (1). Figures 4 (a) and (b) show the effect of this change on the predicted temporal forms of the inversion and DFDL output. The dynamics of operation are now explained. In the initial portion of the pulse self Q-switching leads to the formation of short pulses. Unlike the previous section, where the laser is operating near threshold, in this instance pumping is sufficiently strong to quickly dampen the initial pulse modulation. The pulses effectively merge together as the population inversion approaches a quasi steady state level, near to that the inversion threshold. As can be seen from figure 4(a) the inversion reaches this value before the establishment of the long pulse which it precedes. After reaching this value, the inversion remains nearly constant (to within 1%) while the pumping term increases to out and beyond its maximum (at t = 20 ns). The effect of this inversion clamping (which also clamps the laser gain) on the intracavity photon flux may be considered with reference to equation (5). Since, for the reasons which have been described above, the inversion may be considered as constant and hence $dN/dt = 0$ then if $I_p(t)$ is increasing then the second term on the r.h.s. of (5) (which describes the stimulated emission) must increase in magnitude to compensate for an increase in I_p. The photon flux must therefore increase in direct proportion with the temporal form of the input, $I_p(t)$. Recalling that the cavity decay time is proportional to square of the population inversion and, since the output power is proportional to the photon flux divided by the cavity decay time, the output pulse also follows the temporal form of the input pulse. Thus, as can be seen from figure 4 (b), for the majority of the predicted DFDL output the pulse follows that of the Gaussian form of the pump pulse.

Consideration of equation (6) i.e. the equation describing the rate of change of photon flux, suggests that the above explanation is an over-simplification. Neglecting the spontaneous emission term equation (6) may be written as,

$$\frac{dq}{dt} = q\left[\frac{(\sigma_e-\sigma_a)}{\eta} N_1 - \frac{1}{\tau_c}\right] \qquad (5.22)$$

Since q has been observed to follow the pump pulse increasing to a maximum before decaying in the latter portion of the output pulse, there must be three solutions of equation (22) namely,

$$\text{i)}\ \frac{dq}{dt} + \text{ve} = \frac{(\sigma_e-\sigma_a)}{\eta} N_1 > \frac{1}{\tau_c}$$

$$\text{ii)}\ \frac{dq}{dt} = 0 = \frac{(\sigma_e-\sigma_a)}{\eta} N_1 = \frac{1}{\tau_c}$$

$$\text{iii)}\ \frac{dq}{dt} \text{-ve} = \frac{(\sigma_e-\sigma_a)}{\eta} N_1 < \frac{1}{\tau_c} \qquad (5.23).$$

Since σ_e, σ_a and η are constants this implies that at least a small change in N_1 is occurring causing the growth and decay of the intracavity photon flux. Furthermore, it should be remembered that solution (ii) of equation (23) defines the threshold (i.e. where gain = loss, dq/dt = 0) and therefore regions (i), (ii) and (iii) defines regions above threshold, at threshold and below threshold operation respectively. Figure (5) shows an expanded view of the time dependence of the population inversion around the centre region of the output pulse. As can be seen from the figure the inversion is indeed decaying slowly, passing below threshold at t = 20 ns. Figure (6) is a plot of dq/dt in this region as a function of time. As expected this is positive for times less than t = 20 ns (neglecting the initial pulse modulation), zero at t = 20 ns and negative for times greater than t = 20 ns.

It should be noted that the modulation on the leading edge of the pulse has an amplitude of less than 10% of the peak output and that the integrated power contained in these pulses accounts for only a very small fraction (less than 1%) of the total output power.

In summary therefore, a new operating regime, where the output pulse follows that of the temporal form of the input, has been identified using the rate equation analysis. As will be seen in later chapters, such behaviour is often observed experimentally and hence the theory is in good agreement with experiment.

5.4.4 Equation constants.

In order to explore different output regimes, parameters such as pump pulse rate, molarity of dye solution and the visibility of fringes were varied and it was found that relatively minor alterations in these parameters could cause major effects on the form of the predicted output. These are now investigated.

i) Molarity.

The effect of molarity of a dye solution on the output of the DFDL was modelled by using two concentrations of dye other than the $3x10^{-4}$ M solution normally used. Solutions of $1x10^{-4}$ M and $5x10^{-4}$ M were used to investigate the effects of weakening and strengthening the dye concentration. The results of this analysis are displayed in figures (7) and (8). Considering the case, as illustrated in figure 7, it is seen that compared to higher concentrations the $1x10^{-4}$ M solution shows a large modulation on the leading edge of the output pulse. By increasing the molarity to $5x10^{-4}$ M the modulation on the leading edge of the pulse has an amplitude of less than 15% of the peak output. Note also that the integrated power contained in these pulses accounts for only a small fraction of the total output power.

ii) Fringe Visibility.

From equation (13) it is seen that the cavity decay time is proportional to the square of the visibility of fringes. Figures 9 (a) and (b) show the effect of reducing the fringe visibility from the default value of 1 to 0.1. As can be seen from the figure, the effect is to produce a pulse strongly modulated on its rising edge. Again it is found that equations (20) and (21) can provide an insight into why this occurs. For a given pump rate R, the pumping factor r is reduced since $r = R\ B\ \tau_c\ \tau$, (τ_c being proportional to V^2). Recalling equation (20), the damping constant α is given by, $\alpha = r/2\tau$, so it is to be expected that a reduction of r should cause α to be reduced. Inspection of the figures shows that there is less damping present when $V = 0.1$ than in the default case when $V = 1$.

5.5 Summary.

In this chapter the rate equations describing the evolution of the population inversion and cavity photon flux were described and are seen to provide an insight into the operation of the DFDL. Considering the simplicity of the rate equations model, the analysis proves useful in both the picosecond pulse regime and in the production of longer pulses. Self Q-switching is cited as the mechanism for the production of short pulses, caused by the interplay between photon flux and inversion. It is a new feature that damping of this switching causes the inversion to settle into a quasi-steady state level and, thereafter, when the laser gain is practically constant, the output follows the temporal form of the input. The model has therefore been extended into a new regime, namely that of operation where the output of the DFDL output follows the temporal form of the pump laser.

In conclusion it is seen that the rate equation model can provide a good description of both types of operation which are observed experimentally. Experimental observations of the temporal behaviour of the DFDL are presented in the Chapter VI and the relation between these and the rate equation analysis considered in Chapter VII.

Parameter	Symbol	Value	[Unit]
Fluorscence lifetime	τ_f	$5x10^{-9}$	[s]
S_0 - absorption cross section	σ_p	$2.5x10^{-20}$	[m^2]
Stimulated emission cross section	σ_e	$2.0x10^{-20}$	[m^2]
S_1 - S_2 absorption cross section	σ_a	$1.0x10^{20}$	[m^2]
Ground state population	N_0	$1.806x10^{23}$	[m^{-3}]
DFDL active length	L	0.02	[m]
DFDL depth	a	$1/N_0\sigma_p = 220$	[μm]
DFDL height	b	250	[μm]
Spectral fraction	S	$1x10^4$	
Refractive index	η	1.44	
Gaussian constant	β	$2.77x10^{16}$	[s^{-2}]

Table 1. Default values for all parameters used in rate equation analysis, obtained from references [1], [2], and [8].

References Chapter V

[1] Z.Bor: "Tunable picosecond pulse generation by a N_2 laser pumped self Q switched DFDL" IEEE J Quantum Electron. QE-16, 517 (1980).

[2] Z.Bor, A.Muller, B.Racz and F.Schafer: "Ultrashort pulse generation by DFDLs" Appl. Phys B **27**, 9 (1987).

[3] H.Kogelnik and C.V.Shank: "Coupled Wave Theory of Distributed Feedback Lasers" J. Appl. Phys **43**,5,p2327 (1972).

[4] S.R. Chinn: Optics Comm., 19, 208, (1976).

[5] G.M. Phillips and P.J. Taylor: *Theory and Applications of Numerical Analysis* (1973 Academic Press, London).

[6] R. Burden, J. Faires, A.C. Reynolds: *Numerical Analysis* (1981 Prindle, Weber and Schmitt, Boston, USA).

[7] W. Schmitt and F.P. Schafer: Z. Naturforsch 22(a), 1563, (1967).

[8] E. Sahar and D. Treves: IEEE J. QE-13, No 12, 962, (1977).

[9] A. Yariv : *Optical Electronics* Third Edition (1985, Holt - Sanders, Japan).

[10] A.E. Sigeman: *Lasers* (1986, University Science Books, California, USA).

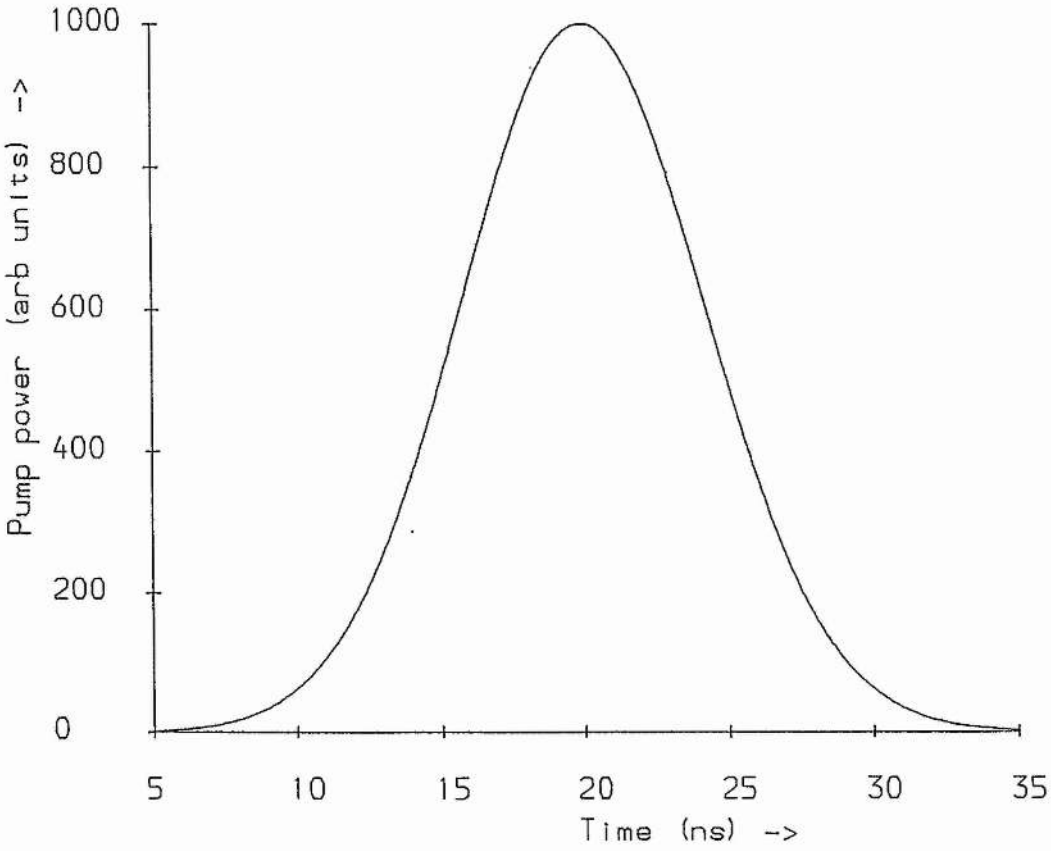

Figure 1. Temporal form of the Gaussian pump pulse ($I_p(t) = I_{max} \exp(-\beta t^2)$) used in modelling. For a 10 ns (FWHM) pulse $\beta=2.77\times10^{16}$.

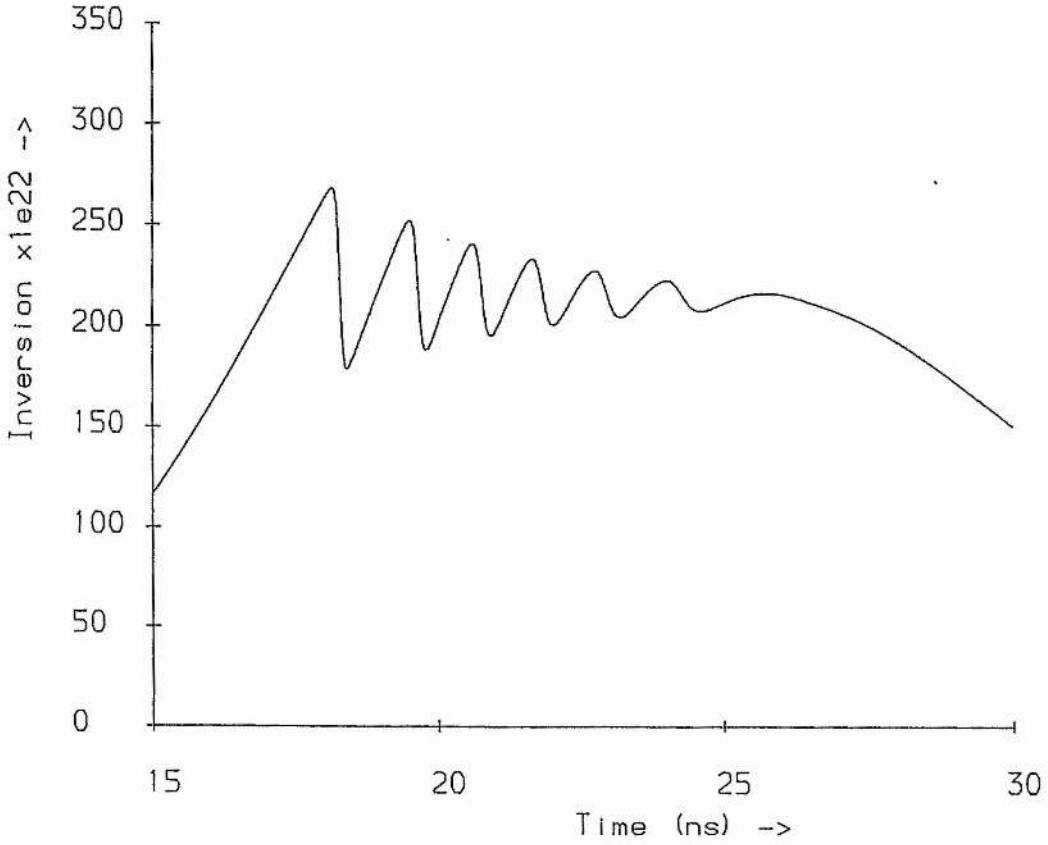

Figure 2. Temporal form of (a) population inversion and (b) output power of a DFDL with 0.1 mJ pumping (all other parameters are the default values – see table 1). Picosecond pulses are present in this case when the laser is operating just above threshold.

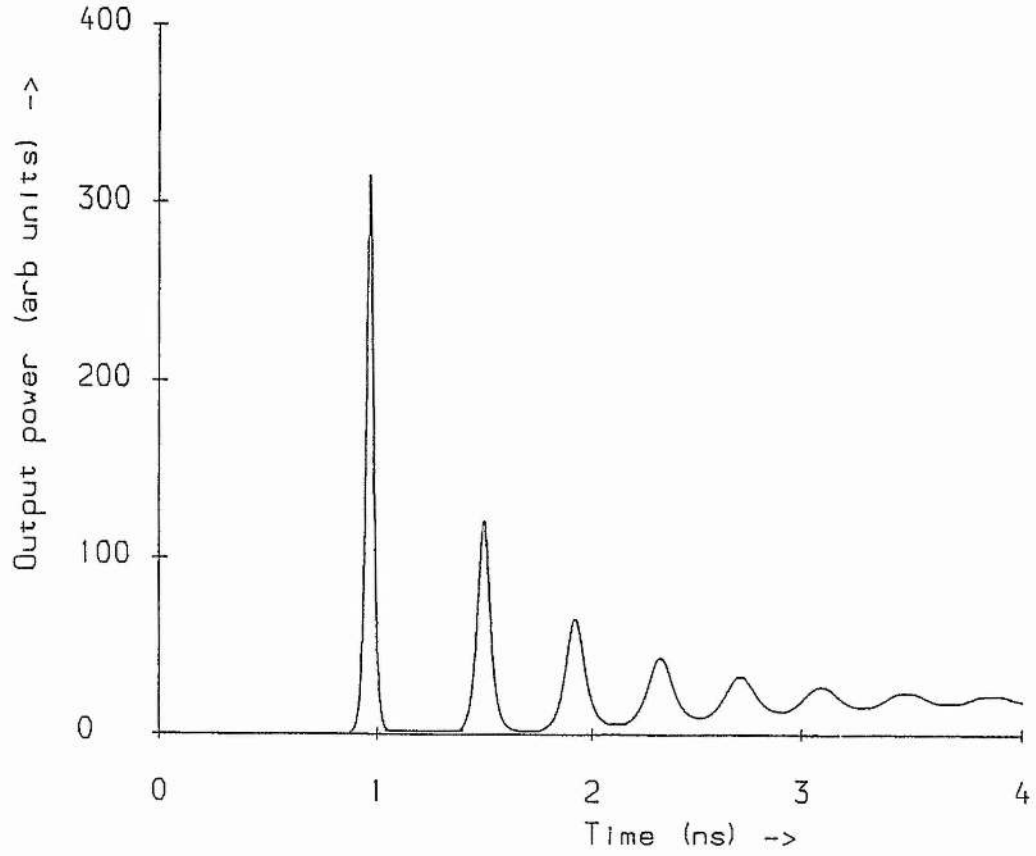

Figure 3. Time evolution of DFDL output power for constant pumping at a level of (a) 20 kW and (b) 40 kW. Increased pumping increases both the damping rate and the oscillation frequency.

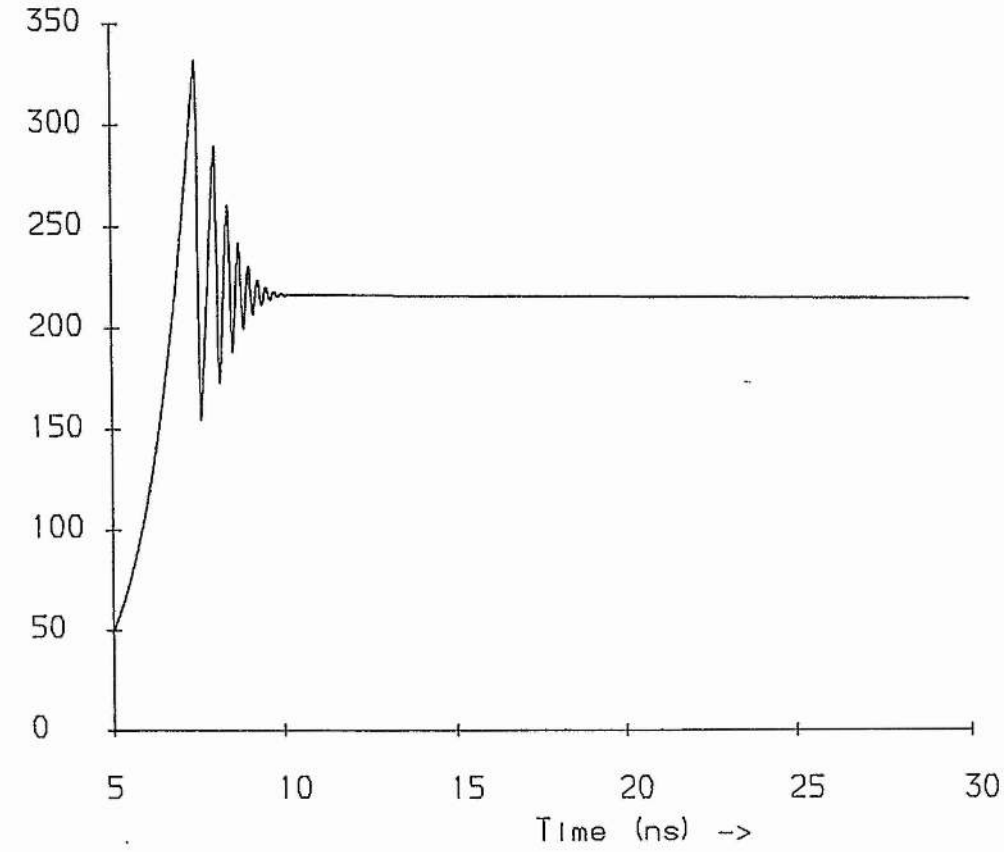

Figure 4. Time evolution of (a) population inversion and (b) DFDL output power at the 10 mJ pumping level. Note initial modulation in the population inversion until damping causes it to reach a quasi-steady state value (around the inversion threshold value (see equation 14) is in this case 2.15 x 10^{22} m^{-3}). Thereafter output follows the form of the pump pulse.

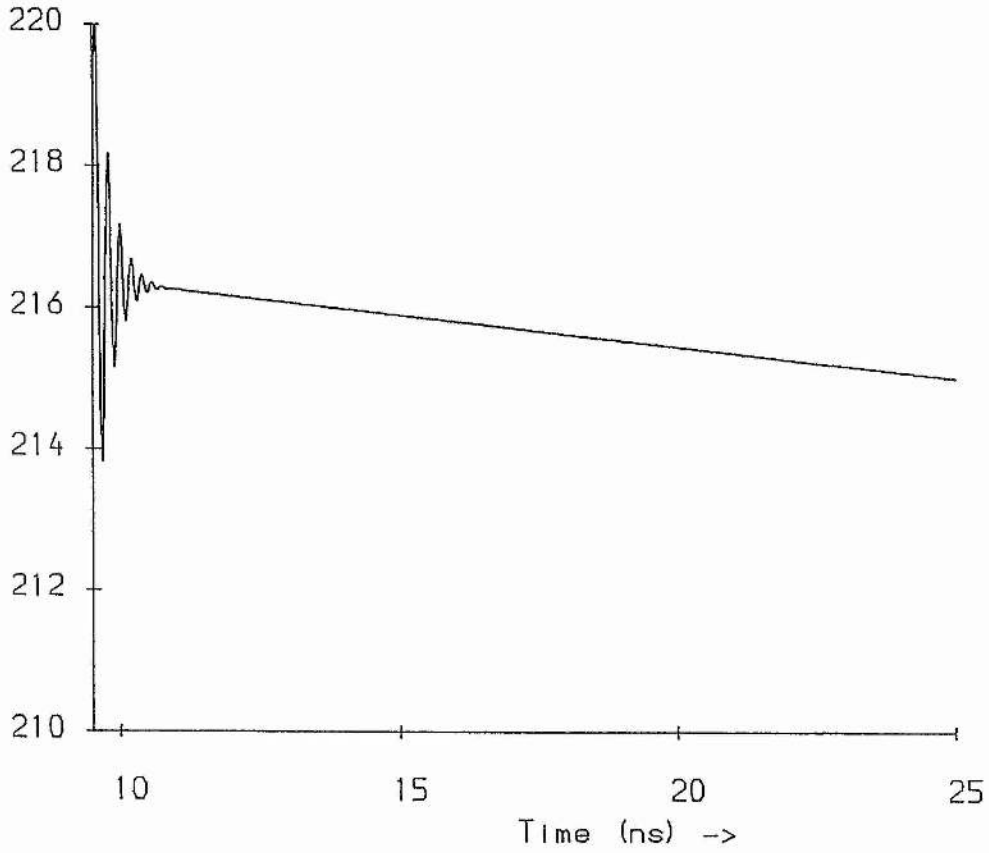

Figure 5. Expanded view of the population inversion around the centre portion of the DFDL pulse for the case of 10 mJ pumping. For a significant portion of the pulse it can be seen that the population inversion is within 1% of that of the threshold inversion.

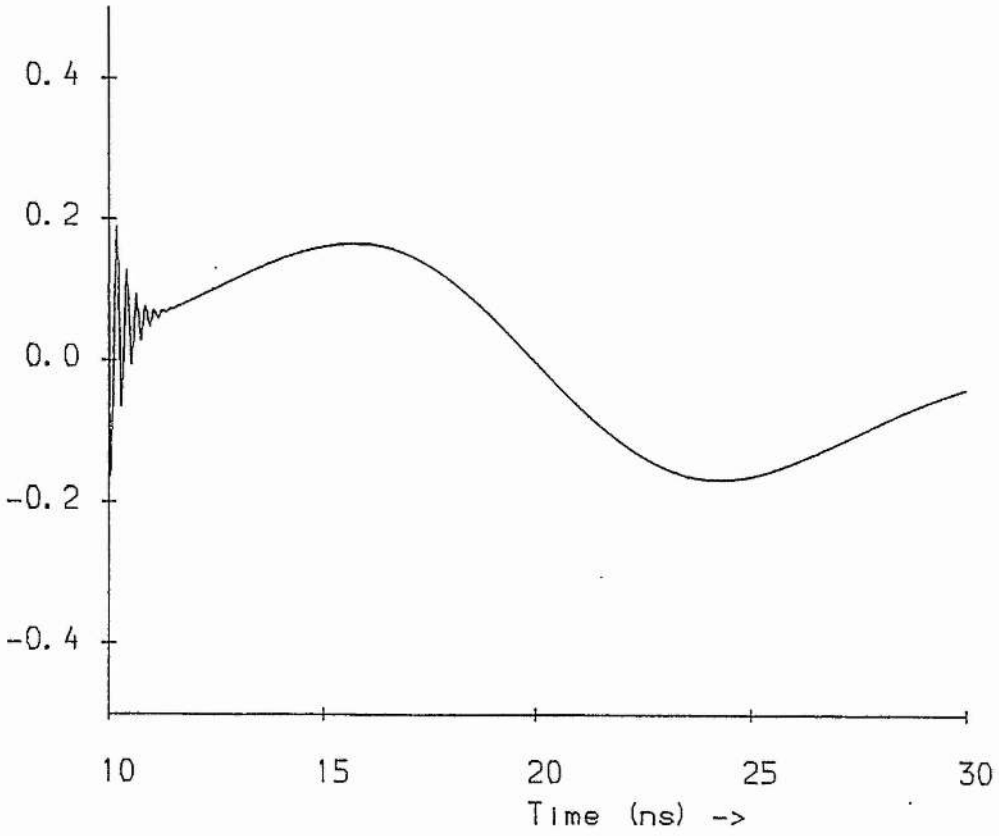

Figure 6. Plot of the change in intracavity photon flux q with respect to time (dq/dt) in regions around the centre portion of the DFDL pulse for the case of 10 mJ pumping. On the rising edge of the pulse i.e. those times below t = 20 ns the gain exceeds loss, whereas, in the falling edge of the pulse (t>20 ns) the gain is less than the loss.

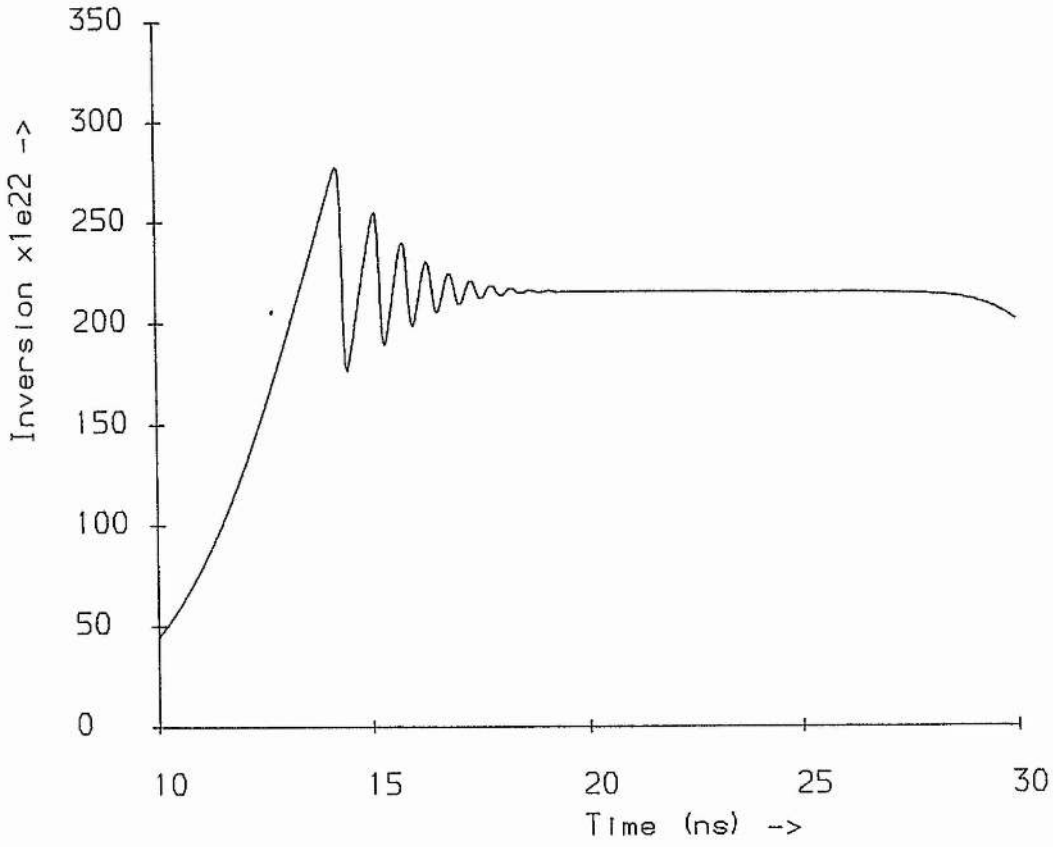

Figure 7. Time evolution of (a) population inversion and (b) DFDL output power with a dye of molarity = 1×10^{-4} M.

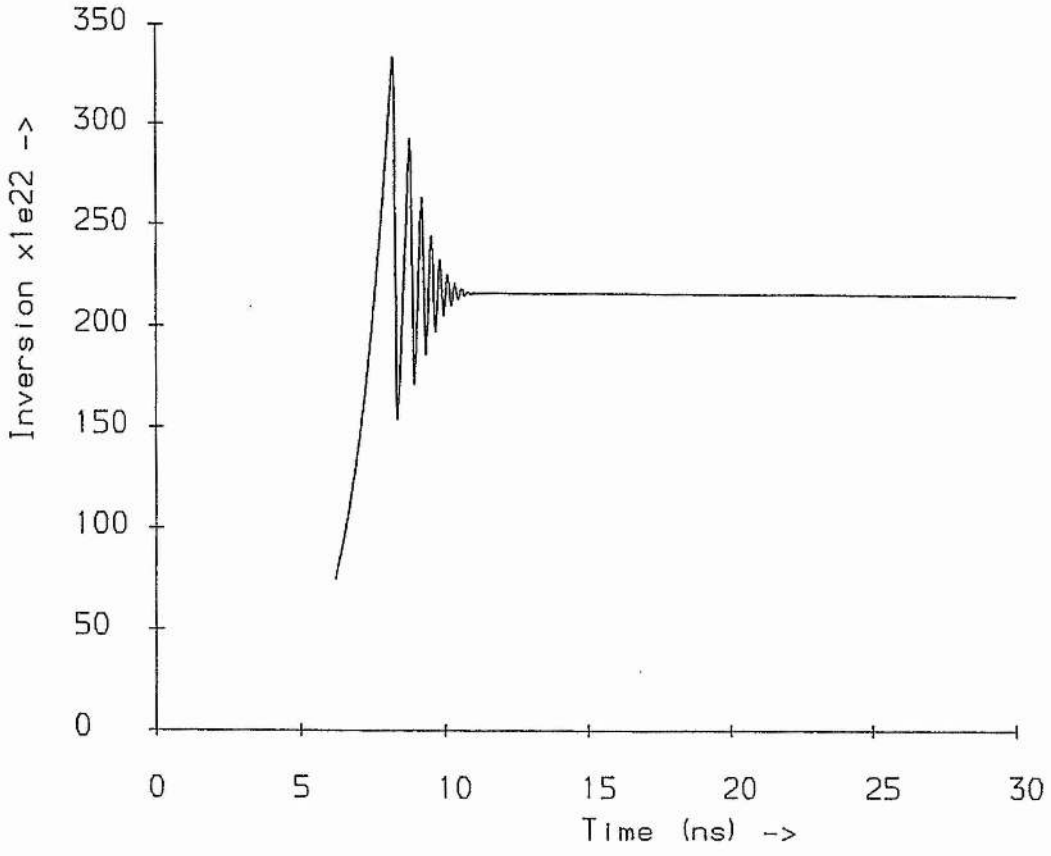

Figure 8. Time evolution of (a) population inversion and (b) DFDL output power with a dye of molarity = 5×10^{-4} M.

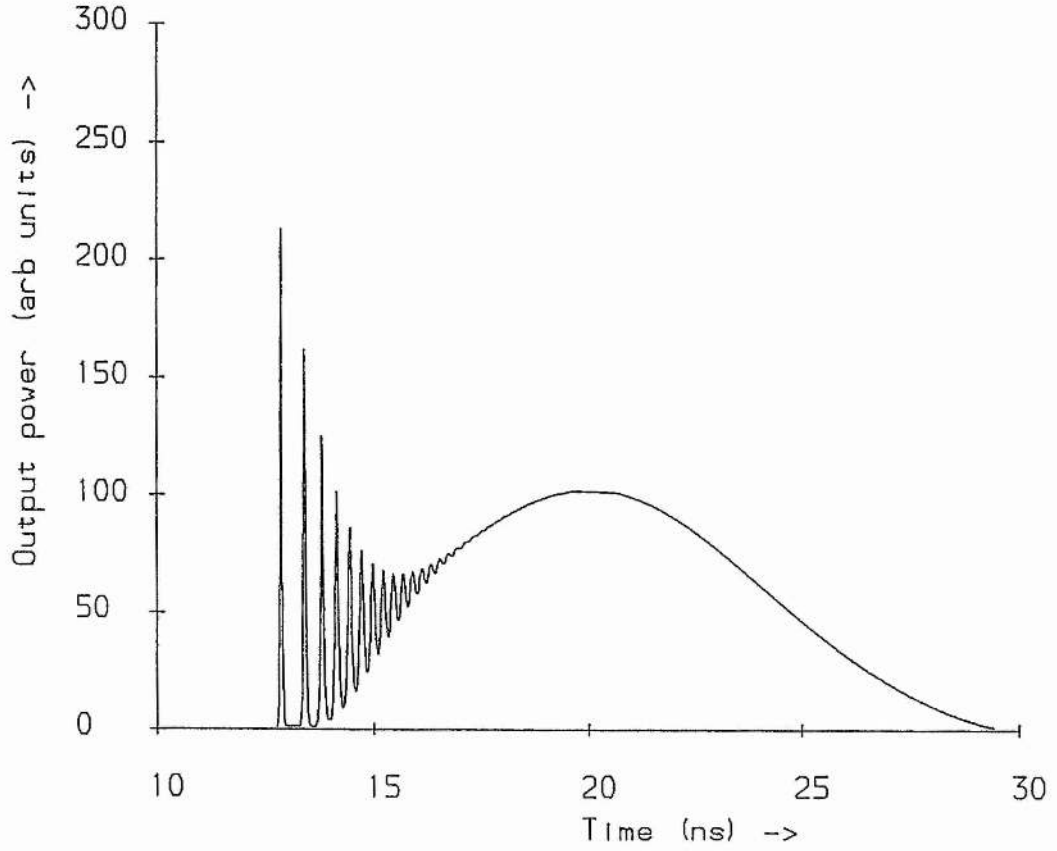

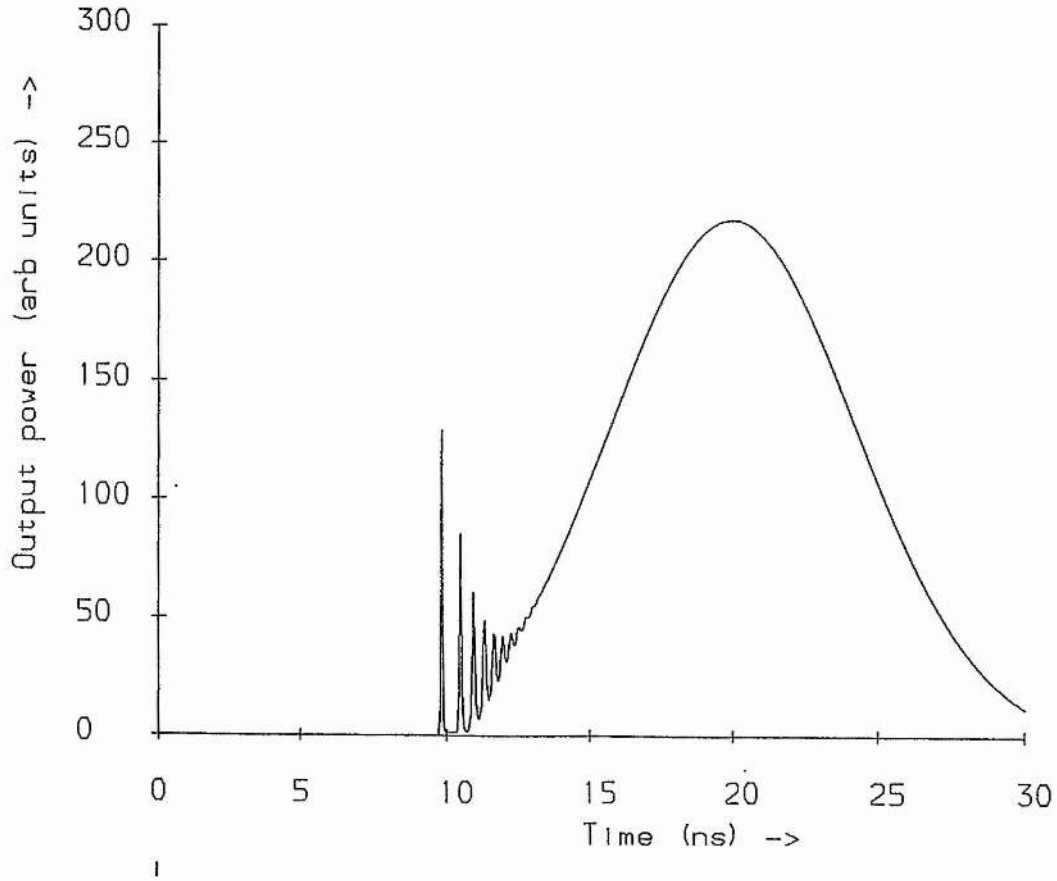

Figure 9. Time evolution of DFDL with (a) visibility of fringes = 0.1 and (b) the default value of 1.0. Note large modulation on the leading edge of the pulse which, as a result of reduced fringe visibility, is less damped.

Chapter VI–Experimental results.

6.1 Introduction and Background.

In the first chapter of this thesis the processes affecting linewidth and temporal behaviour of the DFDL are reviewed. We have identified that previous DFDL reports fall into one of two categories depending upon the laser's temporal behaviour. These are:

(1) a single, or multiple, picosecond pulsing regime and,

(2) a 'smooth' pulsing regime where the DFDL output follows the course of the pump pulse.

The most significant feature of the DFDL operation in the picosecond pulse regime (1) is that the laser is operated close to threshold. Operating near threshold, self Q-switching can lead to the production of single picosecond pulses. In the pursuit of single ultrashort pulses three criteria must be satisfied:

(i) the laser is operated very close to its threshold (i.e. is pumped at less than twice threshold pumping power,

(ii) the grating length of the laser is very small (less than ~ 100 μm), and

(iii) the pump pulse duration must be minimised (see for example [1] and [2]).

Operating at slightly increased pump powers (less than five times threshold) leads to multiple pulsing, the number of pulses increasing and their separation decreasing with increased pumping. This temporal behaviour can be modelled using a pair of coupled rate equations which describe the interplay between the cavity radiation field and the atomic inversion. This rate equation model has been developed further in Chapter V.

Operating at an increased level of pumping identifies a second regime where the DFDL output follows the temporal form of the pump laser pulse. In Chapter V the rate equation model of the DFDL is extended to consider the effect of higher pump powers. This has added our understanding of the dynamics of this second region. Its findings are now briefly summarised. The initial pulsing, as the laser passes through threshold, is quickly damped as the gain of the medium (and hence cavity feedback) becomes clamped at a constant level. Clamping of the gain and cavity feedback means that the output pulse can only follow the temporal profile of the input. When compared with short pulse DFDLs those lasers operating in this second regime are characterized by:

(i) increased levels of pumping (greater than ~ 10 times threshold),

(ii) grating lengths typically greater than two orders of magnitude more than those of short pulse DFDLs, and

(iii) longer pump pulse durations.

In this second regime the processes contributing to the linewidth of the laser were attributed to:

i) properties of the pump laser and,

ii) the level of pumping of the DFDL.

The properties of the pump laser (effect i) mainly contribute to the linewidth by affecting the properties of the induced grating and, as such, DFDL linewidth has also been shown to scale with the pump laser linewidth and divergence and furthermore to be a function of the spatial coherence of the incident wavefront (see for example [3] and[4]). The power dependent linewidth effects (effect ii) are derived from thermally and dispersively induced changes of refractive index during the course of the pump pulse. To a first approximation (avoiding linewidth saturation at high pump powers, see § 2.2. of Chapter I) the linewidth scales directly with the level of pumping employed. Further considerations of the origin of thermal and dispersive effects reveals that thermal effects depend upon the efficiency of the dye and solvent dn/dT, and that dispersive effects show a wavelength dependence.

Of the two regimes it is the smooth pulse regime which is of particular interest to this thesis which places an emphasis on the production of a narrow linewidth source. With regard to the linewidth determining processes a strategy for developing a narrow linewidth DFDL is to:

(i) reduce pump laser effects to a minimum by employing a narrow linewidth, highly coherent, low divergence pump laser,

(ii) operate the laser at reduced pump powers and also minimizing, where possible, thermal effects by the use of low dn/dT solvents and operating the laser in wavelength regions of low dispersion.

However, in following these guide-lines for narrow linewidth operation the pump laser cannot be reduced to a level where the laser is operated near threshold since picosecond pulsing, a consequence of which is to broaden the linewidth, can result.

With these considerations in mind the need for a two tiered experimental investigation becomes apparent, the first investigating the temporal behaviour of the DFDL in order to establish the conditions leading to short pulse production, the second investigating the linewidth behaviour in the smooth pulsing regime. Experiments along those lines were performed and are now described.

In the first experiment to be described, temporal resolution down to approximately 10 picoseconds was provided by using a streak camera. This resolution was obtained over a one nanosecond window. The full pulse duration of approximately 10 ns was monitored with a temporal resolution of ~ 1.3 ns using a 275 MHz bandwidth oscilloscope and fast photodiode. In order to give a more complete characterization of the DFDL the frequency behaviour of the laser was measured simultaneously with a interferometer of 1.5 GHz free spectral range .

Having established that a narrow linewidth regime exists for the DFDL, the second part of this experimental investigation examines the linewidth behaviour more closely. In this investigation the linewidth was measured interferometically using the CAIN system and the effect of different solvents, solvent dn/dT and the wavelength dependence of linewidth are investigated using a number of different dyes and solvents.

A full description of these experiments and the results obtained now follows.

6.2 Experimental Details.

Although the results from the experiments investigating the temporal and linewidth behaviour of the DFDL in the two regimes are presented in two separate sections, much of the apparatus used in the experiments was common to both. Details of the apparatus used now follows with specific details on their incorporation into the particular experiment left until each experiment is considered. The equipment consists of four main subsystems:

1) the Nd:YAG pump laser,

2) the DFDL apparatus,

3) temporal diagnostic equipment and,

4) linewidth diagnostic equipment.

1) The Nd:YAG pump laser.

The modified Quantel YG480 Nd:YAG pump laser has been described previously in Chapter II. For the purpose of this investigation it should be assumed that the laser was operated in the 'TEM_{00}' geometry in order to maximize the spatial coherence and minimise the divergence of the output beam. The laser could be operated multimode using the normal (active) Q-switch, or on a single longitudinal mode (SLM) using the slow Q-switch. SLM linewidth was at or near to the transform limit of ~ 50 MHz for the 12 ns pulse. The pump pulse energy was generally in the region of 0.5–1.0 mJ at the second harmonic wavelength of 532 nm.

2) The DFDL apparatus.

The DFDL apparatus has also been described in Chapter II to which the reader is referred for further details. Both the Shank and the Bor style geometries were employed. It was found that, at the ≤ 1.0 mJ level of pumping, flowing of the dye was unnecessary hence enabling the removal of the dye circulator system, leaving only the dye cell in place. Since the volume of the dye cell is only 15 ml it was easy to make accurate changes of the laser dye and/or solvents used.

3) Temporal diagnostic equipment .

Two methods of investigation were used used in the time domain analysis of the DFDL: (a) photodiode and oscilloscope, and, (b) a streak camera. These are now considered, highlighting the advantages and disadvantages of each.

(a) Photodiode and oscilloscope

This is the more conventional method of recording the temporal profile of an optical pulse. The optical signal is converted into an electrical current using the photodiode. An oscilloscope is then being used to display voltage as a function of time. The oscilloscope used was a Hewlett Packard 1725A which has a bandwidth of 275 MHz. Two photodiodes were used, a Telefunken BPW 28 avalanche photodiode which has a risetime 200 ps, and an ITL vacuum photodiode which has a risetime of 100 ps. The overall resolution of the system is now considered.

The lower limit of resolution of any transient measuring system is determined by the risetime of the system. The risetime is defined as the time taken for a signal to go from 10% to 90% of the final value value. The risetime T_r of an oscilloscope, is related to its bandwidth by the formula,

$$T_r = \frac{0.35}{\text{Bandwidth}} \tag{6.1}$$

The overall risetime of a measurement system comprising of two elements is given by the square root of the sum of the squares of the individual risetimes and hence for an oscilloscope and photodiode combination the overall risetime is given by,

$$T^2_{r(\text{overall})} = T^2_{r(\text{oscilloscope})} + T^2_{r(\text{photodiode})} \tag{6.2}$$

In evaluating (2), for either of the two photodiodes used, it can be seen that the risetime of the system of the system is limited by the bandwidth of the oscilloscope to approximately 1.3 ns. The system was tested by using femtosecond pulses from a colliding pulse mode locked (CPM) ring dye laser. Since these pulses had a duration which were very much less than the risetime of the oscilloscope and photodiode combination the risetime of the system could be measured. To this end the pulses from the CPM dye laser were incident onto the BPW 28 photodiode. Figure (1) shows the oscilloscope trace produced and, as can be seen from the trace the risetime is that which is predicted.

It is interesting to predict how such a system, with its nanosecond response time, would respond to a pulse with picosecond modulation of the type modelled in Chapter V. To properly achieve this one must convolve the impulse response G(t) of the measuring system (as measured from figure 1) with the time varying input $V_i(t)$ as given by,

$$V_o(t) = \int_{-\infty}^{t} V_i(t')\, G(t-t')\, dt' \tag{6.3}$$

This is equivalent in the Fourier domain to multiplying the F.T of the input signal with the bandwidth response of the detector and oscilloscope.

However, for reasons which will become apparent shortly, it was decided to approximate the detector and oscilloscope response to that of an RC circuit i.e. one with

an exponential rise and decay. In this case the time dependent output signal $V_o(t)$ is determined by,

$$\frac{dV_0(t)}{dt} = \frac{V_i(t)}{\tau} - \frac{V_0(t)}{\tau} \qquad (6.4)$$

where $V_i(t)$ is the time dependent input signal. In the case of an RC circuit the time constant τ is the product of R and C i.e. $\tau = RC$. In modelling the detector and oscilloscope τ is given in terms of the detector risetime by,

$$\tau = -\frac{\text{risetime}}{ln\,(0.1)} = 0.55 \text{ ns} \qquad (6.5)$$

Figure (2) shows the response of such a system to a square pulse of duration 5 ns.

Since the output is now described in terms of a first order differential equation it was straightforward to include the term described by (4) in the numerical solution of the similar equations in the rate equation analysis presented in Chapter V. The existing Runge–Kutta method provides a general solution to the differential equations describing the population inversion N and the photon flux q of the DFDL laser. The model was extended to include the additional term for V_o and was therefore of the form,

$$\frac{dN_1}{dt} = I_p(t)\,\sigma_e(N_0-N_1) - \frac{\sigma_e c}{\eta} N_1 q - \frac{N_1}{\tau_f}$$

$$\frac{dq}{dt} = \frac{(\sigma_e-\sigma_a)}{\eta} N_1 q - \frac{q}{\tau_c} + \frac{\Omega\, N_1}{\tau_f}$$

$$\frac{dV_0(t)}{dt} = \frac{V_i(t)}{\tau} - \frac{V_0(t)}{\tau} \qquad (6.6)$$

where V_i is related to N and q by the equation determining the output power of the DFDL namely,

$$V_i = \text{Output power} = \frac{1}{2}\frac{hc}{\lambda} \text{Lab} \frac{q}{\tau_c} \qquad \text{(see Chapter V, equation 13)}$$

and the detector risetime is obtained from (5) above. As can be seen from figure (4) where $V_i(t)$ and the response of the detector response to this signal are drawn, it is seen that a highly modulated DFDL pulse shape, typical of those predicted by rate equations analysis, an instrument with a risetime of 1.3 ns would not properly resolve the sub-nanosecond structure.

In order to resolve such structure a streak camera was used which is described in the next section. This oscilloscope and photodiode measurements did however, allow viewing the full temporal (~ 10 ns) width of the DFDL pulse. Resolution down to approximately 10 picoseconds was made available by the use of a streak camera which is now considered.

(b) The streak camera.

The streak camera is a useful device for the temporal measurement of optical pulses on a picosecond timescale. The mode of operation of a streak camera is somewhat similar to that of an oscilloscope. Light from a source is incident on a slit, and imaged onto a photocathode where the optical pulse is converted into a pulse of electrons. These electrons are in turn imaged on the centre of a phosphor of the streak tube forming the output. By deflecting the slit across the phosphor, temporal information is converted into spatial information. Since the photoelectron current in the streak tube is kept small to avoid defocussing the light output of the phosphor is low. A high gain image intensifier is then used to intensify the output signal forming the output. The end product is therefore a streak of light across a phosphor screen. Since the deflection across the streak occurs as a linear function of time, then the intensity of the streak as a function of position is the intensity of the input pulse as a function of time.

Operation of the streak camera.

The streak camera used in the analysis of pulses emitted from the DFDL was a variation of a Photochron Mk 3 modified for use as a framing camera. Details of this camera may be found in references [5] and [6]. This camera may be used in single shot mode if the electrical potential difference applied to the camera deflection plates overlaps temporally with an optical pulse arriving at the photocathode. To this end the deflection plate voltage, obtained through the use of an avalanche transistor chain switches a 6 kV potential in 2 nanoseconds. The camera static sensitivity was of the order of 2.5 cm/kV. The streak produced by the camera was approximately 4 cm long. From the above information an approximation to the streak time may be obtained by determining the streak velocity and hence time taken to write the 4 cm streak. The calculation is as follows:

From the above:

Switching time = 6 kV in 2 ns (50 Ω impedance) = 3 kV ns^{-1}

Static sensitivity = 2.5 cm kV^{-1}

Streak size = 4 cm

the streak velocity is therefore obtained from the product of switching time and sensitivity i.e.,

Streak velocity = Switching time x Static sensitivity

$$= 3 \text{ kV ns}^{-1} \text{ x } 2.5 \text{ cm kV}^{-1}$$

$$= 7.5 \text{ cm ns}^{-1} \tag{6.7}$$

The time taken for the streak sweep is therefore,

$$\frac{\text{Streak size}}{\text{Streak velocity}} \sim 0.5 \text{ ns} \tag{6.8}$$

However, the above calculation is only an approximation since it assumes that the impedance of the camera deflection plates is 50 Ω, and furthermore that this impedance has no frequency dependence. As such the camera requires calibration [8]. Under the conditions reported above the camera was previous calibrated as having a streak time of approximately 1 ns [9].

Timing is initiated by triggering from an external event, in this case a 30 V pulse from a photodiode. Since there are inherent delays in the system, e.g. ~ 10 ns in the switching circuit, ~ 5 ns transit time of electrons from the photocathode to the phosphor, then an optical delay must be introduced between the optical pulse incident onto the photodiode and the optical pulse incident onto the streak camera photocathode. The photodiode used for time t = 0 was placed after the first dichroic mirror i.e. in that position where the Nd:YAG fundamental wavelength is normally dumped. As will become apparent later the shot to shot fluctuation of the output significantly effects which portion of the pulse is observed.

When the timing of the voltage switching of the streak camera deflection plates and the arrival of the optical pulse on the input slit must coincide to within a nanosecond care must be taken to account for the electrical and optical delays which occur. The optical delays are now considered. These account for the time difference in the optical pulse

reaching the trigger photodiode and the the DFDL pulse arriving at the camera input slit and are as follows,

i) The three pass optical delay line normally used (2.88 m/pass) was reduced to two round trips i.e a total of 5.76 m,

ii) one metre each from the delay line to the DFDL laser, and

iii) one metre from the DFDL laser to the streak camera.

Addition of (i), (ii) and (iii) total to a path difference of 7.76 m which corresponds to a time delay of approx 26 ns.

These delays must be compensated for by electrical delays. Delays in the trigger circuit account for approximately 15 ns. Additional delays could be introduced by incorporation of BNC 50 Ω (delay 5 ns/m) cable. Two metres of cable were introduced to provide an additional delay of 10ns which, together with the circuit delays outlined above resulted in an electrical delay of 25 ns. These delays enabled suitable streaks to be obtained. Fine tuning was achieved by either increasing or decreasing the length of BNC cable. However, because of jitter in the trigger signal, caused by intensity variations in the Nd:YAG laser, for any given streak it was difficult to estimate which nanosecond section of the DFDL pulse was being observed.

The image intensified output was coupled with a lens to a CCD camera and video framestore. The CCD camera, video framestore and computer system, described elsewhere in this thesis, proved to be useful for capturing and displaying the streak camera image since, the framestore could be reliably triggered from the Nd:YAG laser Q-switch. After being grabbed the image was displayed as a video picture on a monitor, and read into the computer for measurement. Specific details of the implementation of the image store and measurement system are presented in section 6.3.2.

4) Linewidth diagnostic equipment.

Most of the linewidth measurements which are reported in this chapter were recorded using the computer aided interferometry (CAIN) system which was specifically constructed for this experiment. The system is described fully in Chapter III. Briefly summarised again, the fringes from a 1.5 GHz non-degenerate confocal interferometer are

projected onto a CCD camera the output of which is then digitised and stored by a video framestore. Thereafter the fringes are analysed by computer. The diverging output from one end of the DFDL was allowed to travel a distance of approx 30 cm before it formed the input into the interferometer. At this separation the DFDL beam filled most of the 1 cm diameter interferometer mirror, hence providing full illumination of the interference fringes produced.

Wavelength measurements were made using a Monospek 1000 high resolution monochromator.

The two experimental investigations are now presented.

6.3 Picosecond pulse regime: Time and frequency domain measurements.

6.3.1 Introduction.

In this section the results of an experimental investigation into the temporal behaviour and the linewidth properties of the DFDL are presented. Using the streak camera and the interferometer, which are described in the previous section, a temporal resolution down to ~ 10 picoseconds and a frequency resolution of around 100 MHz was available for the investigation. The emphasis of this section is to report on the conditions leading to picosecond pulsing.

6.3.2 Experimental Details.

The apparatus used in this experiment has been described in § 6.2 of this chapter. The Nd:YAG laser was operated in the TEM_{00} configuration using either the normal Q-switch to provide multimode operation or, the slow Q-switch which provided SLM operation. The Shank style geometry was employed. The laser dye chosen for this investigation was rhodamine B using either water or methanol as the dye solvent. Rhodamine B was chosen since this dye had been used extensively both in previous investigations performed in the laboratory, and also for the results in the smooth pulse regime which are presented in the next section. In the results to follow, the alignment of the DFDL is seen to play an important role in determining its behaviour. As is described in Chapter II, alignment of the DFDL is mostly a matter of the degree of overlap between the two pump beams. For the purpose of this investigation this degree of overlap was varied by rotation of the

cylindrical lens which, in effect, reduces the length of interaction of the two beams. A schematic diagram of how the streak camera and interferometer were incorporated in the experiment is illustrated on figure (4). The essential elements of the streak camera and the interferometer have been previously described. Acquision of the images produced by each of the instruments was made possible by employing two CCD cameras and two framestores. Considering the streak camera first, the image intensified streak containing the relevant information was coupled with a lens to the first CCD camera. The output from the camera was grabbed and read into the computer for analysis. The interference fringes were projected onto a second CCD camera and thereafter grabbed by and stored in the second framestore. For the purposes of this experiment the computer was therefore dedicated to the framestore used in conjunction with the streak camera. Recording of the stored image of the interference fringes was made by photographing the monitor image with an oscilloscope camera. Similar to the operation of the CAIN system, the timing sequence for the framestores was obtained from the Nd:YAG Q-switch control.

6.3.3 Streak camera and interferometer results.

In the experiment two parameters were varied and the effect on the temporal and linewidth behaviour recorded. The first was to observe the effect of different pump laser parameters on the DFDL. To this end the Nd:YAG laser was operated in three different modes: (i) slow Q-switched with SLM operation, (ii) slow Q-switched with two modes oscillating, and (iii) normal Q-switching causing the Nd:YAG laser to run multimode. The second parameter to be varied was the alignment of the DFDL. By rotation of either the beam steering mirrors or the cylindrical lens the degree of overlap between the two pump beams could be reduced. The results can be grouped into four categories which are based upon the pump laser and DFDL alignment. Each of the four cases is now considered in turn.

Case (a).

In this case the slow Q-switched Nd:YAG laser was tuned, using its intracavity etalon, to achieve stable SLM operation. The DFDL was carefully aligned, paying particular attention to ensure that: (i) the optical paths of the two pump beams were nearly identical,

(ii) the cylindrical lens was near normal incidence to the incident pump beam, (iii) the beam steering mirrors and cylindrical lens were rotated to ensure maximum overlap, in both the horizontal and vertical directions, of the two pump beams. This alignment was made much easier by being able to use the CAIN system to monitor the linewidth of the DFDL in real-time.

Figure (5) shows a photograph of the interference fringes produced by the interferometer and the streak obtained from the camera to give an example of the DFDL output while operating in these circumstances. As can be seen from the figure the laser is operating with a narrow linewidth. The fringes are probably finesse limited (finesse limited resolution ~ 100 MHz) and hence the laser linewidth is estimated to be at a level with approaches its transform limit ~ 100 MHz. With regard to the temporal information obtained using the streak camera it is seen that no sub-nanosecond pulsing of the laser exists for the one nanosecond sweep recorded. The position of the 1 ns window inside the DFDL pulse was varied by using different lengths of coaxial cable between the trigger signal and the streak camera. No pulsing was observed in any part of the output pulse.

Case (b).

In this case the slow Q-switched Nd:YAG laser was allowed to run with two longitudinal mode oscillating. The DFDL was carefully aligned, in a fashion similar to case (a). By observation with the interferometer and streak camera it was seen that there were two separate narrow linewidth components in the DFDL interferogram. These are caused by the formation of two gratings inside the DFDL as a result of the oscillation of two modes of the Nd:YAG laser. It is estimated that the frequency separation of such DFDL 'modes' would be nearly equal to the intermode spacing of the pump laser, which for the ~ 1 m cavity length is 150 MHz. On observation of such type of operation, the spacing of the fringes produced in observing the DFDL varied in a similar fashion to that of the Nd:YAG laser. This indicates that additional modes which oscillate in the pump laser may not always be the adjacent longitudinal mode. The temporal mode beating of from two, adjacent, modes with 150 MHz frequency separation would have a period of

approximately 6.5 ns. As such, over the streak time of ~ 1 ns, no temporal detail is expected for the streak trace, and indeed no such structure was observed.

Case (c).

In this case the Nd:YAG pump laser was slow Q-switched to produce SLM pulses. The DFDL alignment was however slightly reduced by a reduction of the beam overlap in the vertical direction. The effect of this on the DFDL can be considered with reference to figure (6). As can be seen from the figure there is a broadening of the DFDL linewidth. The trace obtained from the streak camera shows that the DFDL is modulated on a picosecond timescale. This modulation takes the form of pulses of average duration around 60 ps. Considering that the transform limited linewidth of a 50 ps pulse is almost 10 GHz it may seem surprising that interference fringes are present (considering that the time bandwidth product should be of the order of 1). This behaviour may be explained by considering another example obtained under similar conditions. This second example is shown in figure (7) where it can be seen that a broadening of linewidth occurs over that of case (a). The trace obtained from the streak camera again shows that the laser is pulsing with pulses of duration of the order of 50 ps. The pulses are seen to sit on top of a 'dc' bias i.e. the pulse modulation is less than 100%. The dc bias represents the nanosecond time variation of the DFDL as it follows that of of the pump pulse. As a nanosecond pulse it has an associated linewidth in the 100's of MHz region. The modulation of the pulse which is occurring on picosecond time-scales has an associated linewidth in the region of 10's of GHz. As such the effect of these pulses, when passing through an interferometer, illuminate all output angles, hence providing a dc bias on the interferometer trace. The interferometer and streak camera results therefore complement each other i.e. what appears as a dc bias in one domain appears as resolved structure in the other.

In conclusion, case (c) represents a regime of SLM pumping with reduced alignment of the DFDL pump beams. The pulse is seen to consist of two components, a ~ 50 ps modulation superimposed on a 10 ns pulse envelope.

Case (d).

In this case the DFDL alignment was good, as in case (a). The pump laser was operated multimode by using the lasers standard Q-switch. Strong temporal mode beating was observed when the laser was used in this fashion. The results obtained from the DFDL were somewhat erratic, as would be expected considering the shot-to-shot instability of the pump laser. Figures (8) and (9) are representative of the traces obtained in the experiment. As can be seen from the figures the interference fringes were nearly, or completely washed out in these conditions, thus indicating that the linewidth was greater than 1.5 GHz. The streak camera results show that pulses of approximately 180 ps duration were present. If transform limited, such pulses would have a linewidth of approximately 3 GHz.

6.3.4 Summary.

In the experiment reported in this section the DFDL has been analysed temporally using a streak camera and spectrally using an interferometer. Measurements in both domains were made on a single shot basis, the results presented representing samples typical of those regularly observed.

Under the range of operating conditions investigated four operating regimes have been identified, the operation of the DFDL depending on the alignment of the grating (which determines the active grating length) and on the operation of the Nd:YAG pump laser. A summary of each of the four operating regimes appears in table (1). Both picosecond and smooth pulse operation of the DFDL was observed, the length of the grating being the determining factor as to its operation.

When considering the properties of the laser in the frequency domain, it was seen that only when the laser was producing smooth, nanosecond duration, pulses were sharp fringes observed, indicating that the laser was operating with a narrow linewidth. When picosecond pulses were produced and observed on the streak camera the linewidth was greater, as expected, than those produced when nanosecond pulses were produced. The increase was not however, as large as would be expected if the pulses had a 100% modulation. The streak camera measurements indeed confirmed that the modulation was

less than 100% when it was seen that the picosecond modulation was superimposed upon a pulse of much longer (nanosecond) duration.

An investigation into the linewidth properties of the DFDL while adopting the strategy for producing narrow linewidths now follows.

6.4 Smooth pulse regime: Time and frequency domain measurements.

6.4.1 Introduction.

In this section the results of the experimental investigation into the temporal and linewidth behaviour of the DFDL are presented. The temporal behaviour is described first where it will be shown that the DFDL pulse follows the course of the pump pulse to the extent that modulations in the Nd:YAG laser are followed by the DFDL. The linewidth behaviour of the DFDL is then presented. Three main parameters are investigated. The first two are for the case of the dye rhodamine B and are: (i) the wavelength dependence of linewidth and, (ii) the effect of varying the dye solvent. Linewidth measurements using a variety of different laser dyes forms the last section of the linewidth investigation. The results are summarized at the end of the section.

6.4.2 Background and experimental details.

The apparatus used in this experiment has been described in § 6.2 of this chapter. The Nd:YAG laser was operated in the TEM_{00} configuration together with the slow Q-switch to produce a single longitudinal mode. In Chapter I it was shown that the linewidth of the DFDL is dependent upon the linewidth of the pump laser (see Chapter I, equation 18). Operating with a SLM pump laser reduces this effect to a minimum.

Previously it has been shown that at a high level of pumping the properties of the laser dye used as the active medium for the DFDL contribute directly to the lasers linewidth. The mechanism cited for this, which is described fully in Chapter I, is a refractive index change during the course of the laser pulse. This is attributed to two effects: (i) a heating of the solvent and (ii) dispersion associated with optical gain and absorption. Thermal changes in refractive index occur because of two heating mechanisms inherent in the absorption and emission of optical radiation. The first is due to non-radiative relaxation within the excited or S_1 state, the second is non-radiative decay from the S_1 to the S_0

state. The figure of merit of the later process is the fluorescence efficiency, sometimes referred to as the quantum yield, which gives the fraction of photons which decay radiatively. The fluorescence efficiency can vary between 40% for rhodamine B in methanol to 100% for rhodamine 101 [7] in the same solvent. The gain dispersive changes in refractive index, occurring as the electronic population of the dye molecule changes, may be reduced by operating the laser at gain line-centre. However if the Stokes shift is sufficiently small then absorption may result in a contribution to refractive index changes. It can therefore be seen that through these processes the linewidth of the DFDL can be expected to be dependent upon the laser dye used. The aim of this experiment was to investigate the effect on DFDL laser linewidth at reduced pump power levels (<1 mJ) when using a range of different laser dyes. As will be seen below, where each dye is considered in turn, all of the dyes were observed to lase with sub-GHz level linewidths.

For the majority of the experiments described, the DFDL was operated in the Shank style geometry, although the Bor style geometry was used and is considered in relation to the laser's shot to shot frequency stability. Since the emphasis of this experiment was in the production of narrow linewidth pulses the overlap of the two pump beams was maximized (see § 6.3).

The 580–680 nm wavelength range investigated was covered efficiently using five laser dyes. These were rhodamine 6G (560–600), rhodamine B (580–630), sulforhodamine B (600–640), rhodamine 101 (590–640) and laser dye DCM (600–680). The figures in brackets represent typical tuning ranges of the dyes. With the exception of laser dye DCM, water, methanol or ethanol (or a combination of these solvents) was used as the dye solvent. Laser dye DCM used a combination of propylene carbonate, ammonyx LO and water.

Temporal measurements were made using the photodiode and oscilloscope and, linewidth measurements made using the CAIN system.

6.4.3 Results.

(i) Temporal investigation.

Using the photodiode and oscilloscope temporal measurements with a resolution of 1.3 ns were made. Both temporal profiles of the DFDL and the pump laser were recorded. As an example of the traces obtained consider figures 10 (a and b). Since the oscilloscope has only a single beam each input was separated temporally by introducing an electrical time delay between the photodiode used for detecting the DFDL pulse and the oscilloscope. By operating the oscilloscope in 'A+B' mode both signals could then be displayed. The two signals were separated by approximately 20 ns. In the figure the pump pulse is therefore located on the left of the oscilloscope trace. Figure 10(a) is an example of a smooth (i.e. near SLM) Nd:YAG pulse, whereas the pump pulse of figure 10(b) shows a modulation caused by mode beating of the pump laser. As can be seen in the figures in both cases the DFDL output pulse follows that of the pump laser. In all the experiments performed with this apparatus, this following of the temporal form of the pump pulse by the DFDL was observed.

(ii) Linewidth investigation.

Since rhodamine B formed the majority of the previous work done in the laboratory (see § 6.3 for results from a simultaneous streak camera and interferometer measurements using the dye) it was the obvious choice for an investigation under the new pumping conditions of narrow linewidth and reduced pump power. To this end two experiments were carried out using rhodamine B investigating:

(i) the wavelength dependence of linewidth and,

(ii) the effect of solvent dn/dT on linewidth.

The results of these two experiments are now presented and are followed by a summary of results obtained using four other laser dyes.

(i) The wavelength dependence of linewidth.

In this experiment the dye was used with water as its solvent, at a concentration of 3×10^{-4} M. The laser was tuned over its entire tuning range which, using water as the solvent and approximately 1 mJ pump pulse energy, was found to be between 596.8 and

634.5 nm. Narrow linewidth operation of the DFDL was observed over all of this wavelength range. Figure (11) is an example of such operation obtained when the laser was operated at a wavelength of $\lambda = 615.7$ nm. This figure was obtained using the CAIN five line average algorithm. Except for close to 600 nm, this figure was typical of the trace obtained for the wavelength range investigated. As discussed in Chapter III, around 600 nm the ratio of absorption to transmission of the interferometer is at a maximum and therefore its throughput is at a minimum. Figure (12) shows the effect of reduced transmission when operation at a wavelength of $\lambda = 596.8$ nm. As can be seen from the figure the intensity falling onto the CCD array is reduced at $\lambda = 596.8$ nm when compared with $\lambda = 634.5$ nm.

(ii) The effect of solvent dn/dT on linewidth.

The DFDL's linewidth dependence on solvent dn/dT was also investigated using the dye rhodamine B. Since methanol and ethanol had the highest dn/dT's of any solvents surveyed (see Chapter IV) these were the solvents chosen for this experiment. The proportion, by volume, of the methanol or ethanol was varied from 0 to 100% in steps of 10% by mixing with water. It was found that under similar pumping conditions that narrow linewidths were produced for all solvent combinations. As an example consider figures (11), (13) and (14). These represent CAIN five line averages using 100% water, 50% methanol/50% water and 100% methanol respectively. The dn/dT's of the solvents at room temperature are 8, 24, and 40 ($x10^{-5}$) K^{-1} respectively. As can be seen from the figures all represent linewidths which are approaching the transform limit for the DFDL. The ethanol/water mixtures yielded approximately similar results. Figure (15) shows a comparable five line scan obtained using 100% ethanol, which, similar to using the dye in water, shows that the linewidth of the laser when using this dye was in the 100 MHz region.

Although rhodamine B formed the majority of the DFDL investigations (see previous sections for simultaneous interferometric and streak camera measurements) other dyes were investigated. These are now considered in turn.

Rhodamine 6G typically lases over the wavelength range of 560–600 nm. When used in the DFDL with water as the dye solvent laser action was observed at the higher end of this range. Since the transmission of the interferometer was low around this wavelength region no CAIN measurements are available. Observation of interferometer fringes was made by eye using a microscope focussed between the interferometer mirrors. Since the free spectral range of the interferometer was 1.5 GHz the observation of fringes gives an upper estimate of the laser linewidth as around 500 MHz. Under all conditions, fringes were observed, from which it can be inferred that the linewidth was always less than 500 MHz.

Sulforhodamine B typically lases between 600 and 640 nm. The dye was dissolved in both water and ethanol and operated at a wavelength of around 620 nm. Figures (16) and (17) represent CAIN five line averages obtained using the dye dissolved in water and ethanol respectively. As can be seen from the figures, the finesse limited linewidths of ~ 100 MHz were measured using this dye were independent of solvent used.

Rhodamine 101 typically lases over the wavelength range of 590–640 nm. It as a dye with a very high fluorescence efficiency. The dye was operated using ethanol as its solvent. Figures (18) and (19) represent examples of CAIN outputs using the dye using five line scan and elliptical averages respectively. As can be seen from the figures R101 is another dye for which the DFDL exhibits a linewidth at or near its transform limit (~ 100 MHz).

Laser dye DCM is a relatively recent addition to commercially available laser dyes. The observed tuning range of the DFDL with the dye was 612–687 nm whilst using a solvent mix containing 85% water, 6.5% propylene carbonate and 6.5% ammonyx LO. We have previously reported that near transform limited operation has been observed around line centre (~ 650 nm) using this dye. In addition sub-GHz operation was observed over all of DCM's tuning range.

6.4.4 Summary.

In this section the results from the experiments performed into the linewidth behaviour of the DFDL have been reported. The two fold strategy presented for the reduction of the

DFDL linewidth involving the reduction of linewidth effects from pump laser and the DFDL power dependent linewidth effects yielded successful results. As was seen in the section, operation with a SLM pump laser with a pump pulse energy of between 0.5 and 1.0 mJ resulted in narrow linewidth operation (<500 MHz) over the entire tuning range investigated (580–680 nm).

6.5 DFDL stability.

6.5.1 Introduction.

When operating the DFDL with linewidths of less than approximately 500 MHz a shot to shot instability in the operating wavelength became apparent. A description of and the results from an experiment into the magnitude of the effect is now described. The section concludes with a discussion as to the origins of the instability.

6.5.2 Stability measurements.

In the experiments performed to investigate the shot to shot variation in the DFDL wavelength the laser was operated with a narrow linewidth (~ 100 MHz). At this level of linewidth sharp fringes were produced and monitored in real time on the CAIN (1.5 GHz free spectral range). The wavelength variation between successive shots was observed as an instability in the fringe position of the 1.5 GHz interferometer. These instabilities were present using both the Shank and the Bor style geometries. Over the time taken for 10 pulses (1 second at 10 Hz) it is estimated that the maximum variation in the wavelength was of the order of one half of the interferometer's free spectral range. When fringe movement of this order is recorded it is important to establish if the movement is within a free spectral range of the interferometer. In order to make an unambiguous interpretation of such movements it is necessary to compare fringe movements on interferometers with different free spectral ranges. To this end the DFDL output was analysed using a plane parallel interferometer with a plate separation of 1 cm. A lower estimate of the finesse of the interferometer is around 10. Since no instabilities in the fringe position were visible using the plane parallel interferometer then it may be concluded that the shot to shot instability was contained with one free spectral range of the interferometer i.e. over the period of 1 second better than 750 MHz.

The probable origins of the shot to shot wavelength instability are now considered.

6.5.3 Origin of shot to shot instability.

Recalling the basic equation which describes the wavelength of operation of the DFDL in terms of $n_s \lambda_p$, and θ ie,

$$\lambda_d = \frac{n_s \lambda_p}{\text{Sin } \theta}$$

the effect on λ_d, of shot to shot instabilities in either of the three variables on the right hand side of the equation can be estimated in a similar fashion to that used in predicting their effect on the DFDL linewidth. These effects have been discussed in the Chapter I and the effect of a variation in n_s, λ_p and θ are described in equations (18), (12) and (14) of that Chapter. Choosing, for example, the effect on the shot to shot instability in the pump laser linewidth $\Delta\lambda_{p(ss)}$ has the same form as (1.12) and is given by,

$$\Delta\lambda_{d(ss)} = \frac{n_s}{\text{Sin } \theta} \Delta\lambda_{p(ss)} \qquad (6.9)$$

As can be seen therefore from (9) the shot to shot stability of the DFDL is dependent upon that of the pump laser. In a similar fashion the shot to shot variations of n_s and θ must be controlled according to the wavelength stability required. These factors therefore place a large emphasis on both the positional and wavelength stability of the pump laser when DFDL is optomised for narrow linewidth operation. At high levels of pumping these effects are masked by the increased dynamic linewidth of the device. However, it should be recalled that the Bor geometry effectively de-couples the DFDL wavelength from the latter two parameters i.e. pumping wavelength and angle of intersection of the two pump beams. In the experiment described above both the Shank and the Bor geometries were employed and it was found that the shot to shot stability was of similar magnitude in both cases. It is therefore thought that shot to shot changes in the solvent refractive index causes the wavelength instability. The refractive index stability Δn required to produce a wavelength stability $\Delta\lambda$ can be obtained using the formula,

$$\frac{\Delta\lambda_d}{\lambda_d} = \frac{\Delta n}{n} \qquad (6.10)$$

The effect of a change in temperature ΔT of the dye solvent on the DFDL wavelength can be obtained by rewriting (5) in terms of dn/dT, the equation therefore becomes,

$$\Delta T = \frac{n\,\Delta\lambda_d}{\lambda_d}\left(\frac{dn}{dT}\right)^{-1} \qquad (6.11)$$

If a solvent such as methanol is used ($dn/dT \sim -4\times10^{-4}\ K^{-1}$) then evaluation of (6) shows that the temperature of the solvent must vary by less than 0.5 mK over the entire length of the solvent if a 100 MHz stability is required.

6.6 Summary and conclusion.

Previous investigations into the properties of the DFDL have concentrated on describing the laser's behaviour in either the time or frequency domain with experimenters concentrating in the production of a DFDL producing either ultrashort pulses or experiments investigating the DFDL linewidth. In this study, the laser has been characterized in both domains and in doing so both picosecond pulse and narrow linewidth operation have been observed.

While pumping the laser with the SLM slow Q-switch Nd:YAG with a pump pulse energy of between 0.5 and 1.0 mJ and creating a DFDL active grating length of approximately 2 cm, the DFDL operated with a linewidth at or near the transform limit of ~ 100 MHz for the 5–10 ns pulses produced. Linewidths were measured on a single shot basis using the CAIN system. A shot to shot instability in the operating wavelength of the DFDL was observed which is estimated to be around 750 MHz over the period of one second (10 shots with the laser operating at 10 Hz). Temporally the DFDL pulse followed that of the Nd:YAG laser, even when this was highly modulated by mode beating in the pump laser. When operated in this fashion no picosecond pulsing was observed, even when using a streak camera with a temporal resolution of ~ 10 picoseconds. The narrow linewidth operation was obtainable for all of the tuning range investigated (580–680 nm) while employing a variety of laser dyes and solvents.

By degrading the overlap between the two pump beams, hence reducing the grating length (while all other features remained constant), a train of picosecond pulses was observed. These had a pulse duration down to approximately 50 picoseconds. As has

been previously considered (see Chapter V) the appearance of a pulse train, rather than a single pulse, suggested that the laser was operating well above its threshold.

Often the laser operated on what is probably best described as a combination of the above two regimes i.e. a picosecond modulation was present on top that of nanosecond duration. In this circumstance a broadening of fringes could be observed using the CAIN 1.5 GHz FSR interferometer. Using the streak camera, a picosecond modulation was seen to sit on top of the nanosecond pulse envelope.

The results presented have therefore characterised the DFDL in a new operating regime and, as has been seen in this investigation, both picosecond and smooth pulse operation have been observed. These are now drawn together in a summary of the thesis.

Case	Nd:YAG	DFDL alignment	Linewidth	Temporal behaviour 10ps – resolution – 1 ns	
(a)	slow Q-switched (SLM)	high	transform limited ~ 100 MHz	smooth streak	follows pump pulse
(b)	slow Q-switched (two mode)	high	two separate ~ 100 MHz components	smooth streak	follows pump pulse
(c)	slow Q-switched (SLM)	reduced pump beam overlap	linewidth in 0.5–1 GHz range	30–60 ps pulsing on d.c. offset	follows pump pulse normally SLM
(d)	normal Q-switched (multimode)	high	> 750 MHz	150 ps pulses	follows pump pulse

Table (1). Summary of results of temporal and frequency investigation of DFDL.

References Chapter VI

[1] Zs Bor: "Tunable picosecond pulse generation by a N_2 laser pumped self Q–switched DFDL" IEEE J QE-**16**, 517, (1980).

[2] S.Szatmari and B Racz: "Generation of 320 fs pulses with a DFDL" Appl. Phys. B, **43**, 93 (1987).

[3] I.A. Mc Intyre: Ph.D.Thesis "Dye lasers with induced Bragg gratings" University of St Andrews 1984.

[4] I.A. Mc Intyre, M.E. Lusty and M.H. Dunn:"Linewidth determining processes in DFDL's" J.Mod Optics **35**, 325 (1988).

[5] D.J. Bradley, B Liddy and W.E. Sleat: Opt. Commun. **2**, 391, (1971).

[6] S.F. Byrant: Ph.D. Thesis Imperial College London (1978).

[7] F. Schafer (ed): *Dye lasers,* Topics Appl. Phys. 1, Springer Verlag, Berlin (1973).

[8] Andrew Finch: University of St. Andrews, private communication (1988).

[9] A. Walker: University of St. Andrews, private communication (1988).

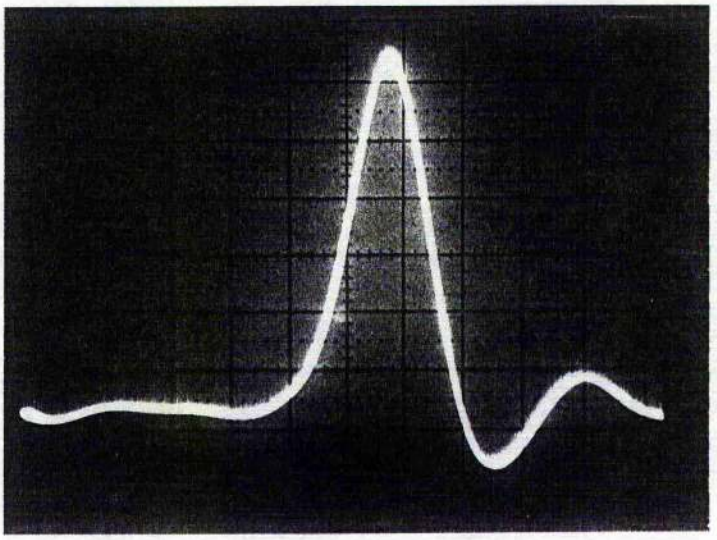

Figure 1. The overall risetime of the temporal measurement system containing the Hewlett Packard 1725 Å oscilloscope and the Telefunken BPW 28 photodiode. Risetime is of the order 1.3 ns.

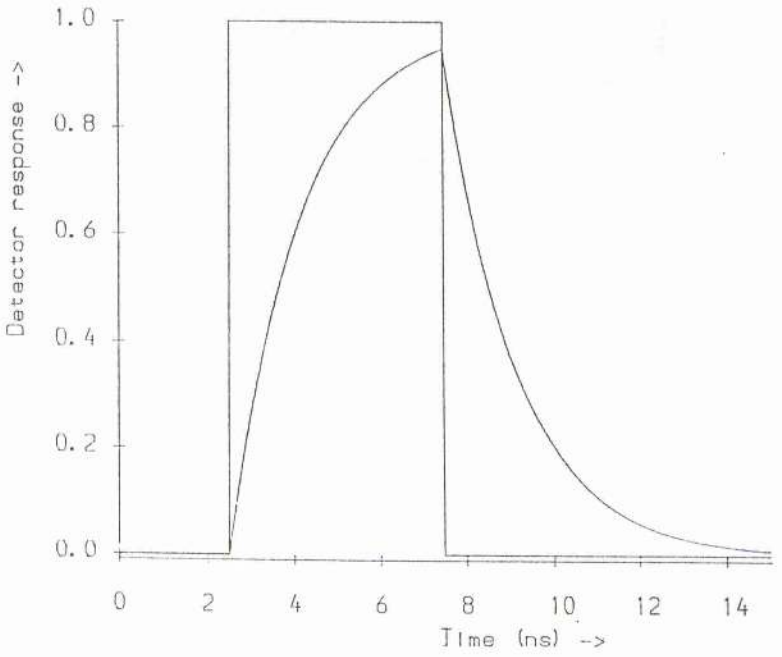

Figure 2. Exponential rise and decay of a 'RC' damped system when subjected to a square wave input.

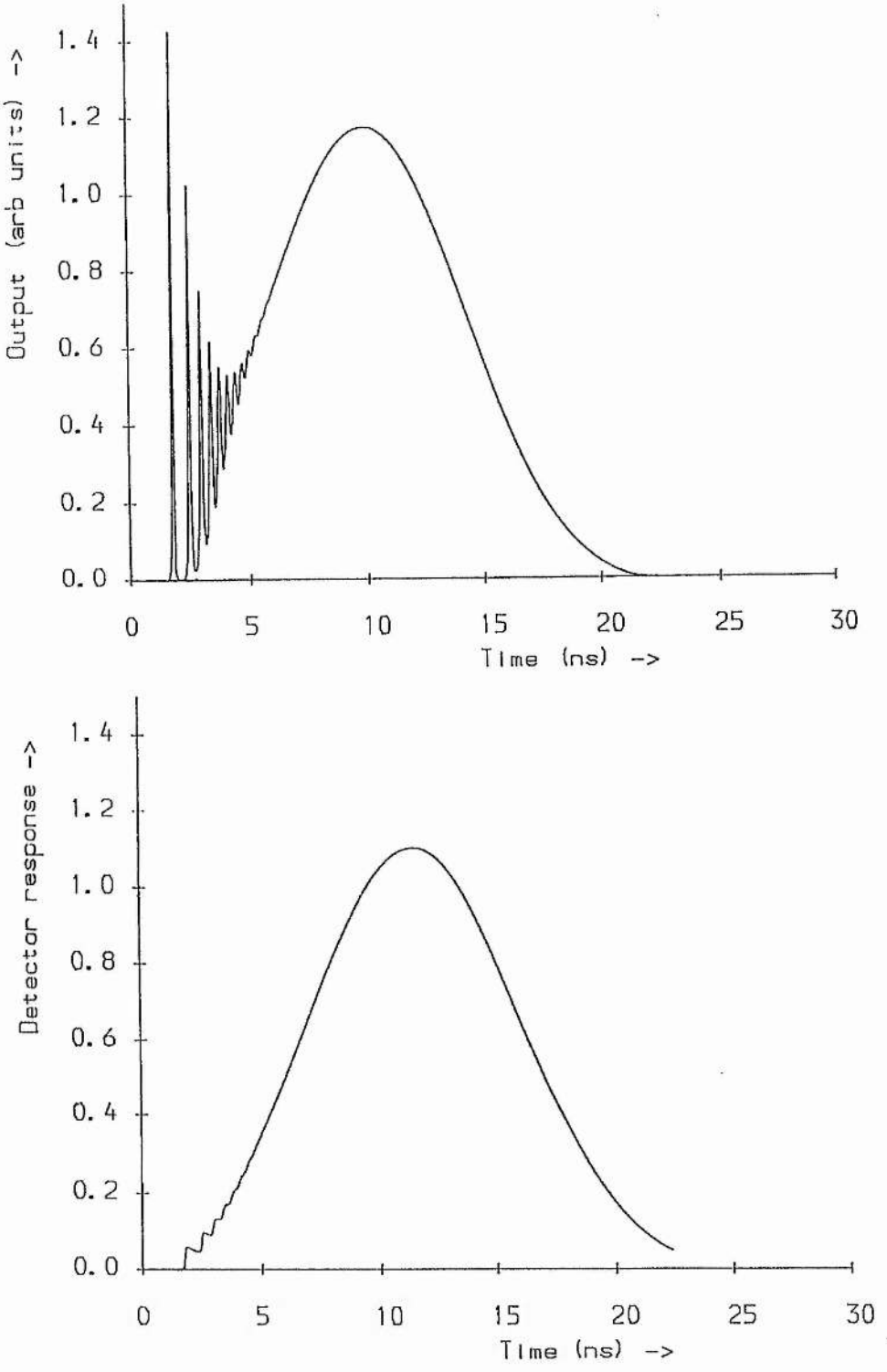

Figure 3. (a) DFDL output power as predicted by laser rate equations, with 1 mJ Nd:YAG pumping. (b) Resolved signal using a detector with a bandwidth of 275 MHz. This trace was obtained by solving numerically the differential rate equation,

$$\frac{dV_o}{dt} = \frac{V_i}{\tau} - \frac{V_o}{\tau}$$

where V_o and V_i are the output and input signals respectively. The time constant τ is given in terms of the detector risetime by $\tau = -\frac{\text{risetime}}{\ln 0.1}$.

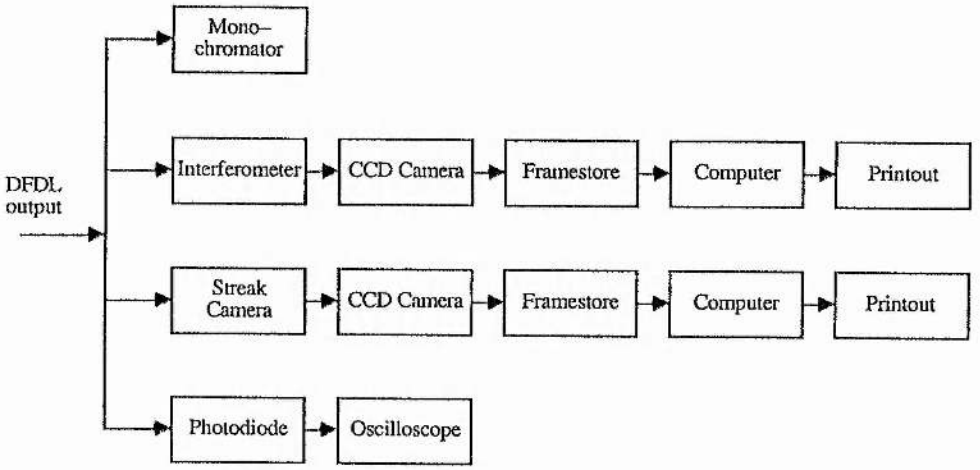

Figure 4. Schematic diagram of the experimental apparatus used in the temporal and frequency investigation of the DFDL. Temporal information was obtained using a streak camera, providing a resolution down to around 10 picoseconds, and a photodiode and 275 MHz oscilloscope which provided a resolution of approximately 1.3 nanoseconds. Linewidth information was obtained using the 1.5 GHz CAIN system.

Measurand	Apparatus	Resolution
Wavelength (λ)	Monospek 1000 monochromator	~ 0.02 nm
Linewidth ($\Delta\nu$)	CAIN system	~ 100 MHz
Pulse duration ($\Delta\tau$)	Streak camera	~ 30 ps
Pulse dulation ($\Delta\tau$)	ITL photodiode and oscilloscope	~ 1.3 ns

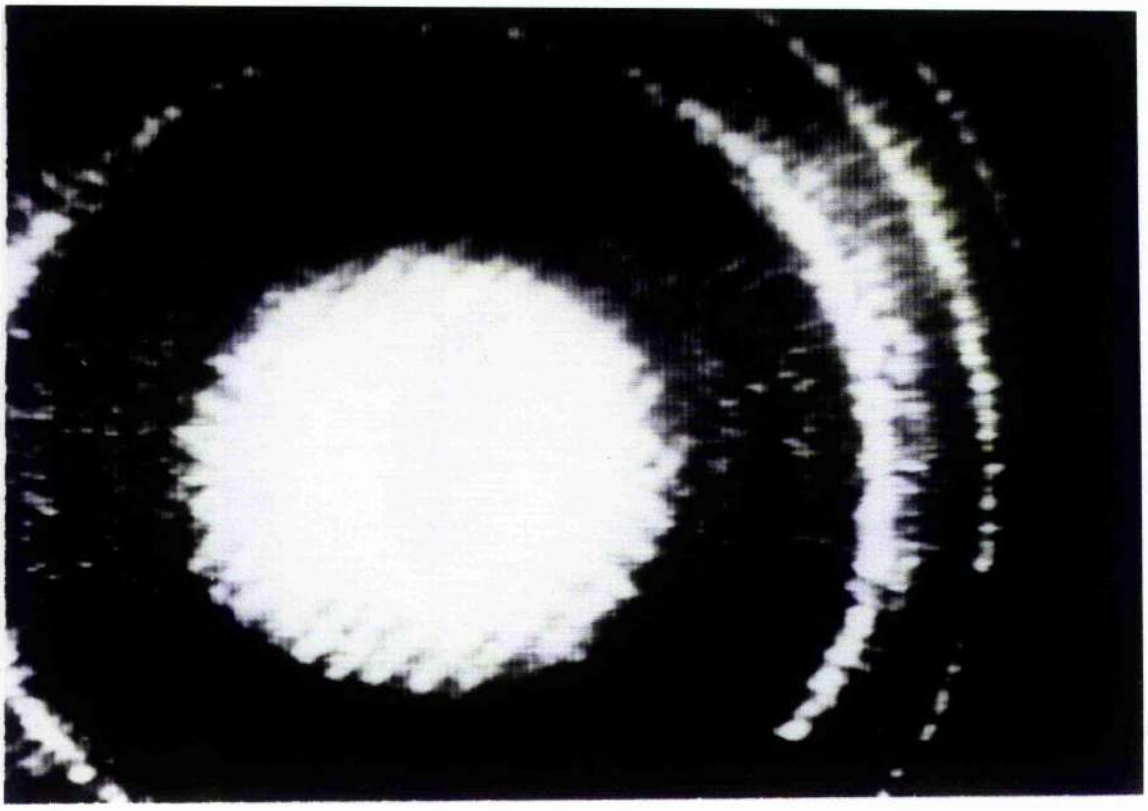

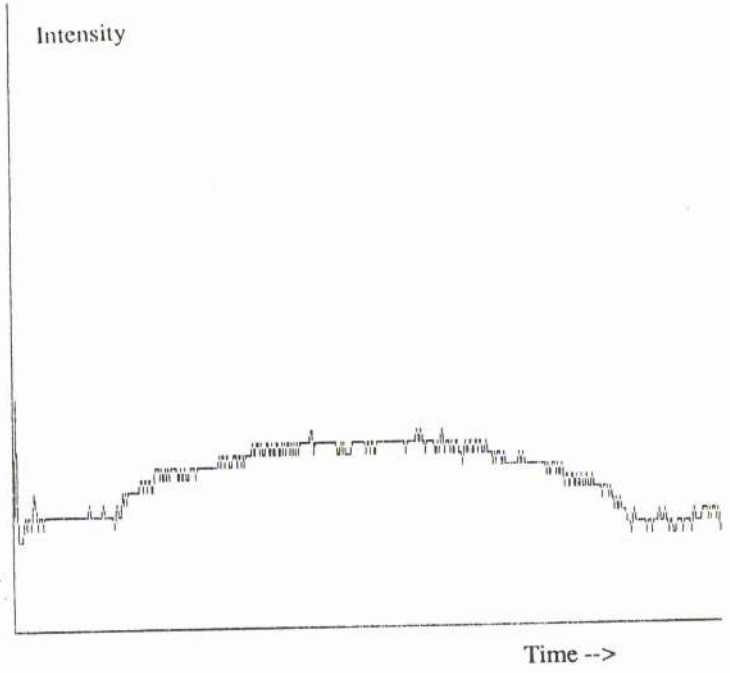

Figure 5. Photograph of the interferogram and streak camera trace obtained from the an analysis of the DFDL output. For this type of result the DFDL was operated with a high degree of overlap of the two pump beams. The Nd:YAG pump laser was operated on a single longitudinal mode. The recorded linewidth is of the order of 100 MHz. The smooth streak indicates that no sub–nanosecond pulsing was present in the output.

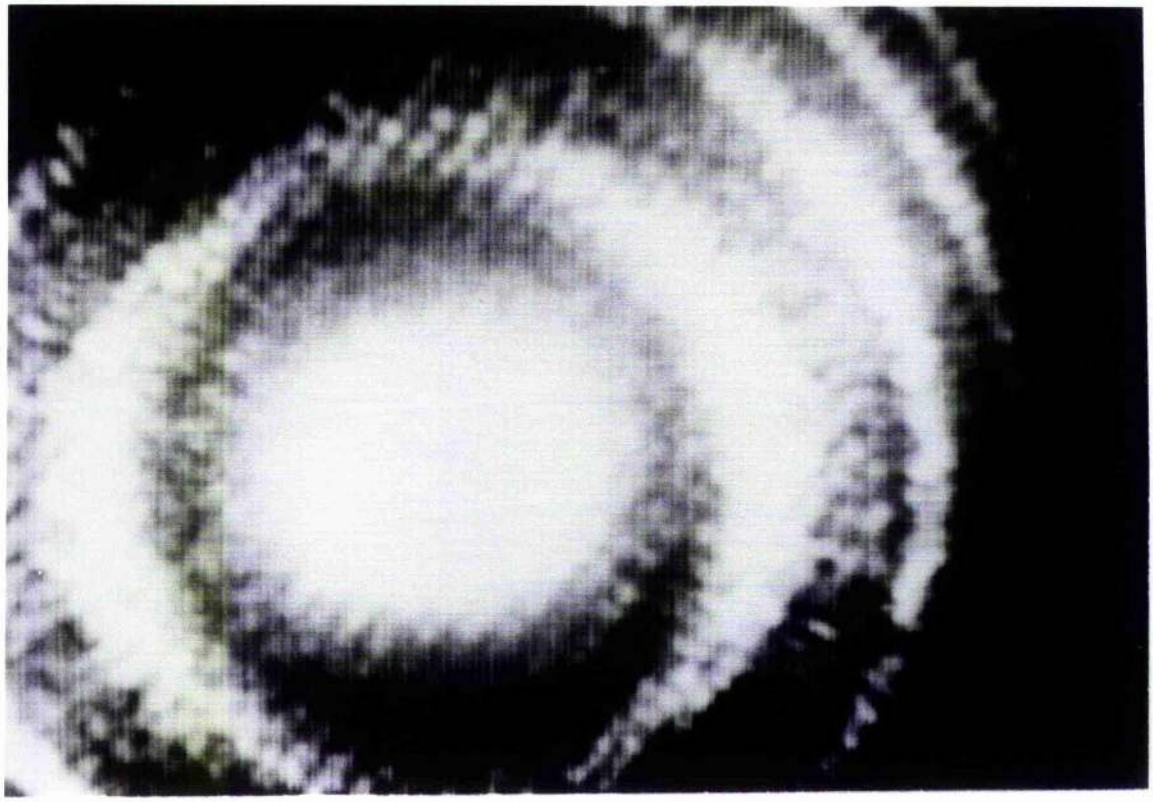

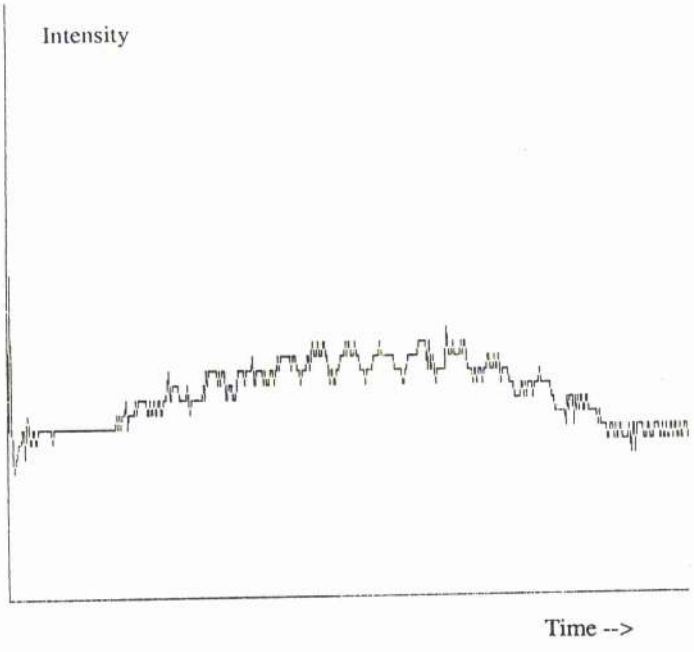

Figure 6. Photograph of the interferogram and streak camera trace obtained from the DFDL. Similar to the previous figure the Nd:YAG pump laser was operated on a single longitudinal mode. The overlap of the two pump laser beams was reduced by rotation of the cylindrical focussing lens. As can be seen from the figure the effect was to produce modulation pulses, of duration ~50 ps, superimposed onto a pulse of longer duration.

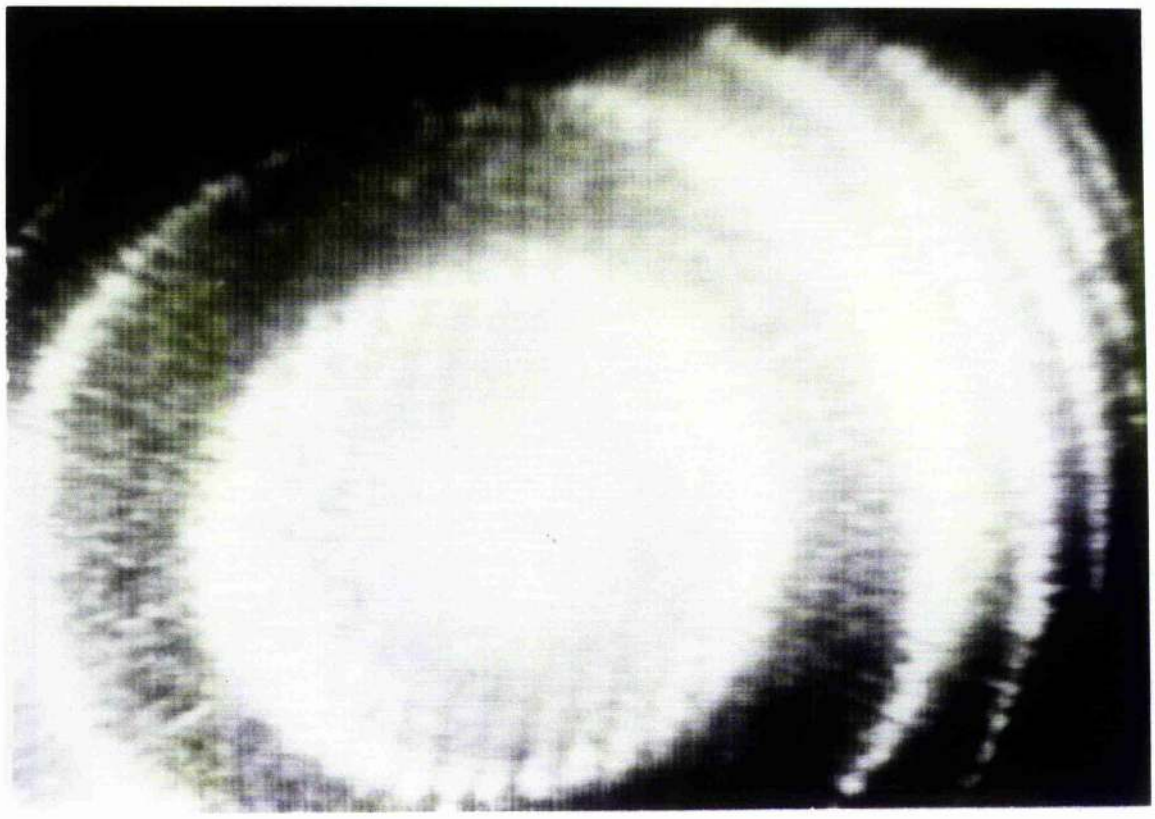

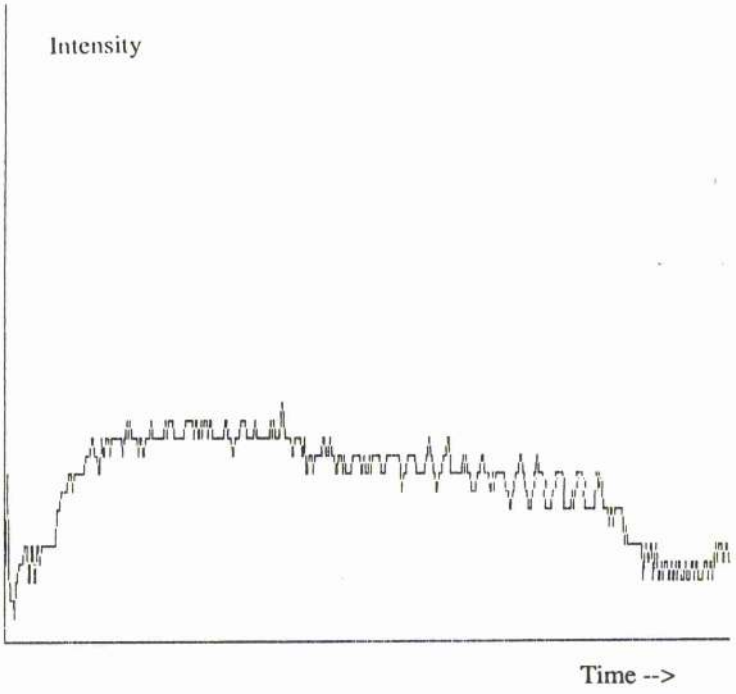

Figure 7. These traces were recorded under similar operating conditions as those of the previous figure. The 'dc' offset of the picosecond modulation is more marked in the streak camera trace of this example.

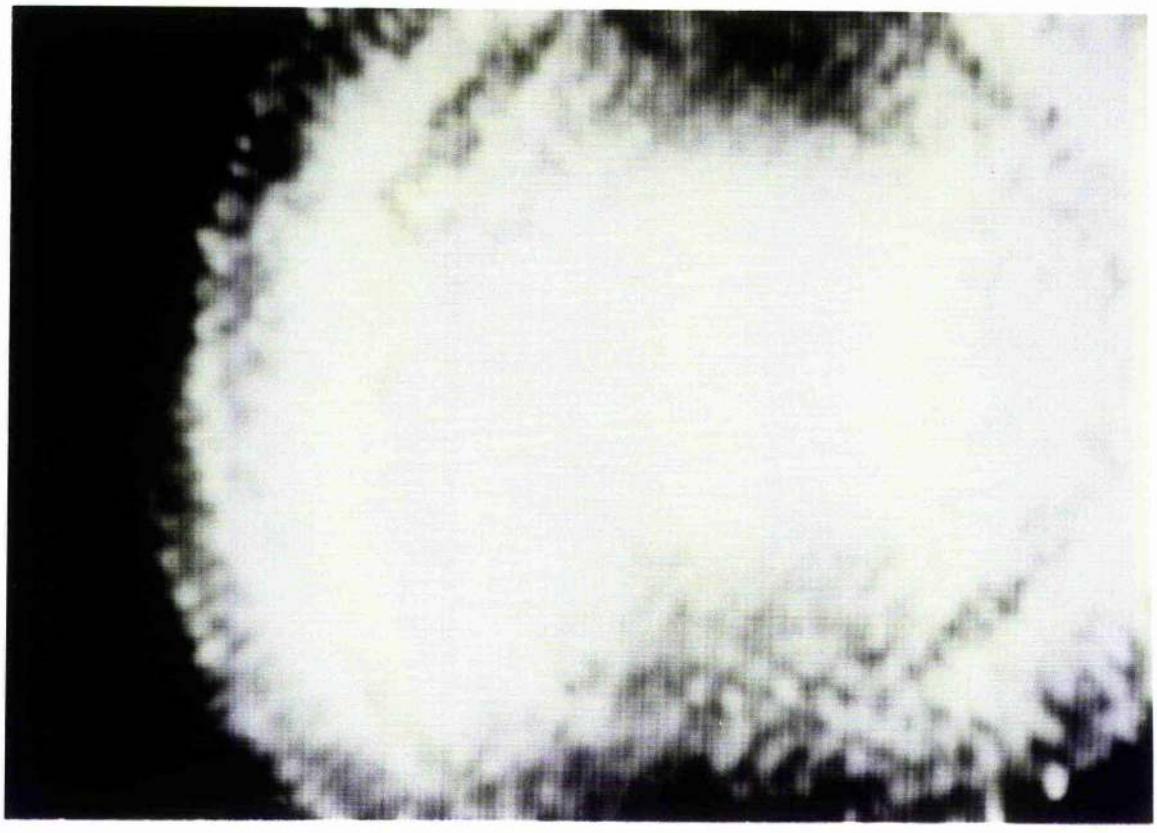

Figure 8. Photograph of the interference fringes and streak camera trace obtained from the DFDL. The DFDL was in good alignment. In contrast to the previous three figures the Nd:YAG pump laser was operated multimode. The effect on the DFDL was to produce a pulse modulation of the order of 150 ps. As can be seen from the intererogram the linewidth is greater than the free spectral range of the interferometer (1.5 GHz).

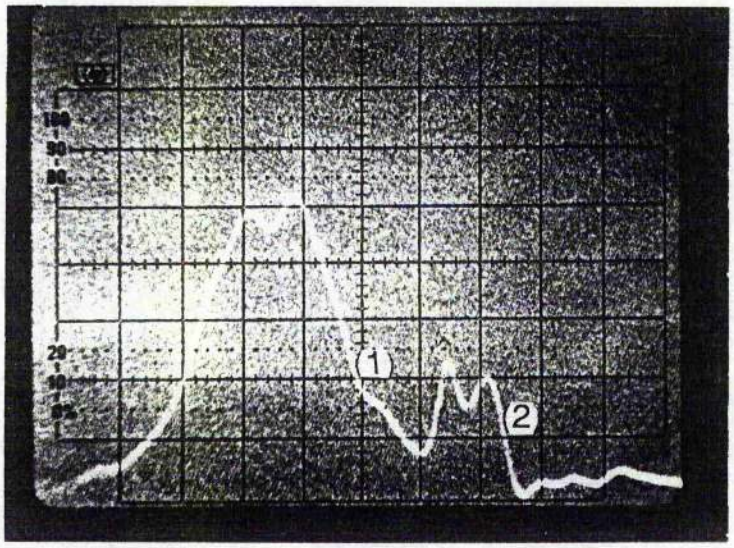

1 div = 5 ns

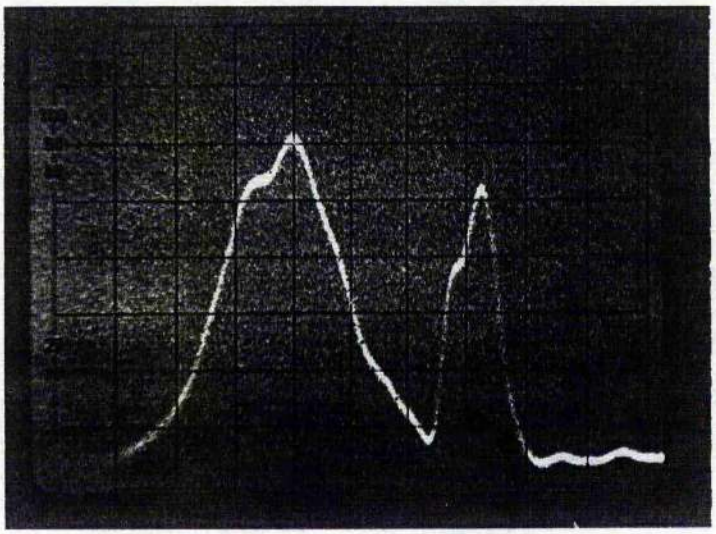

Figure 10. Temporal pulse shapes of the Nd:YAG pump laser (left) and DFDL (right). Two figures are shown, representing typical of the operation of the laser. In both cases the DFDL follows the temporal form of the input.

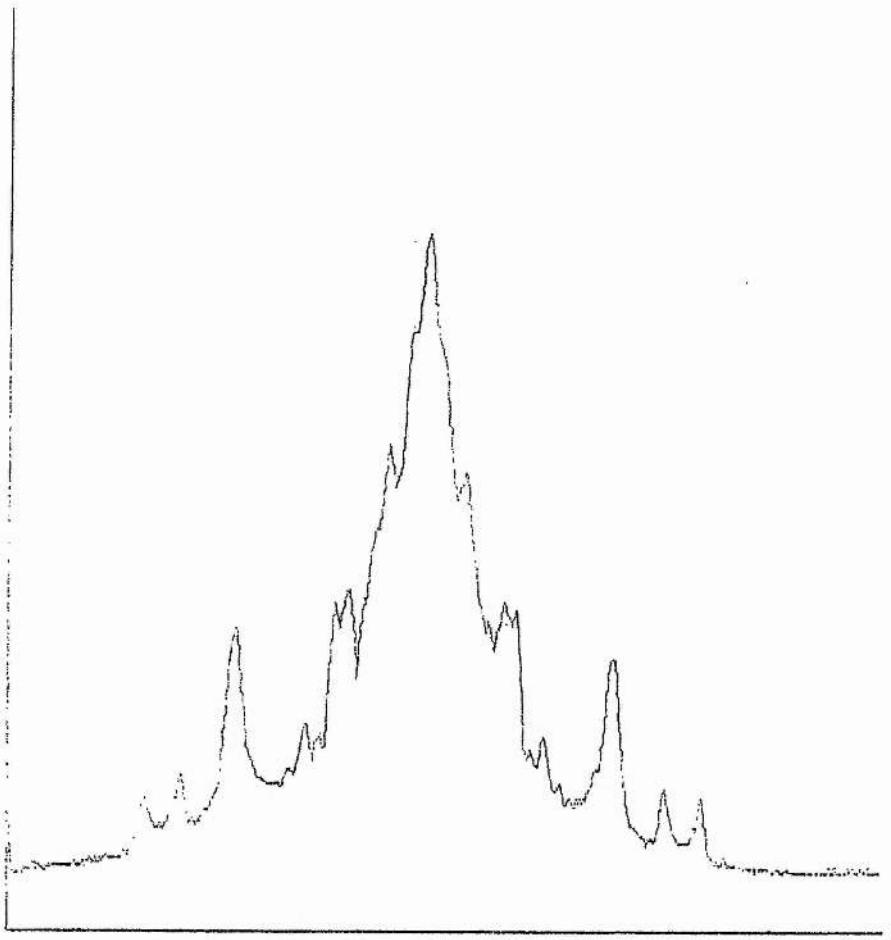

Figure 11. CAIN five line average interferogram of the DFDL output. In this case the laser used the dye Rhodamine B and 100% water as the dye solvent. The laser output wavelength for this scan was $\lambda = 615.7$ nm.

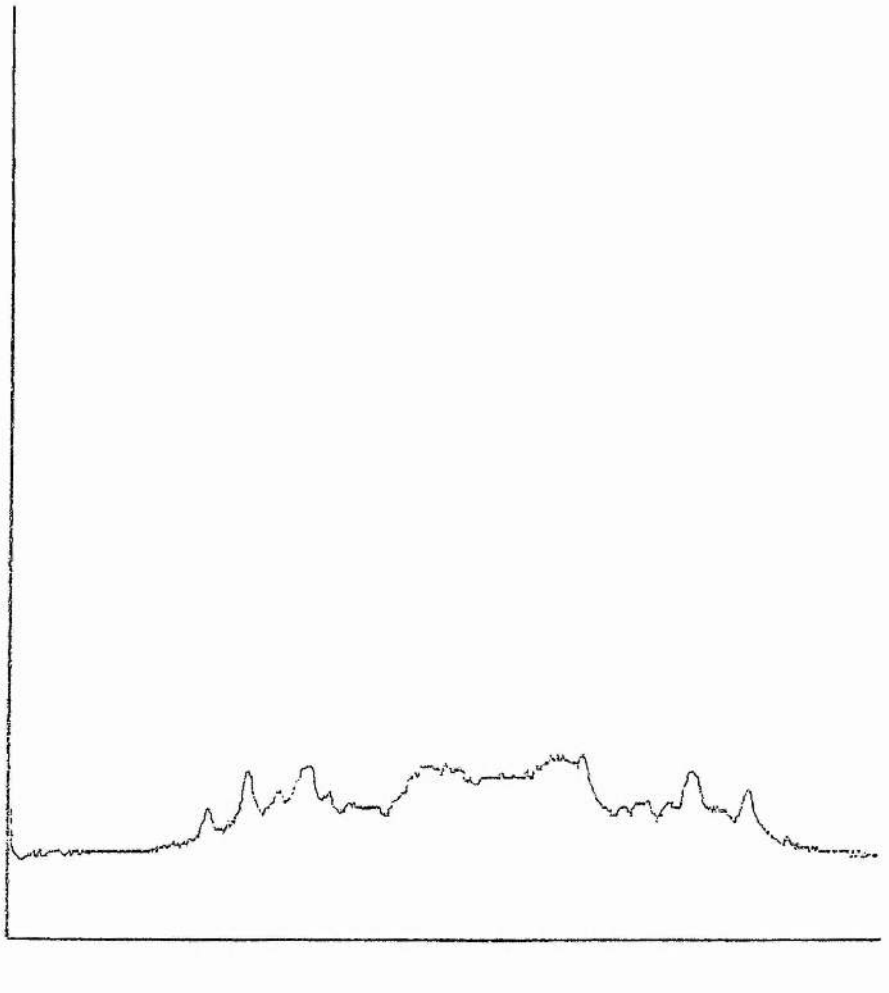

Figure 12. CAIN five line average interferogram of the DFDL output. In this case the laser used the dye Rhodamine B and 100% water as the dye solvent. The laser output wavelength for this scan was λ = 596.8 nm. The interferometer transmission for this wavelength is reduced for wavelengths in the region of 600 nm.

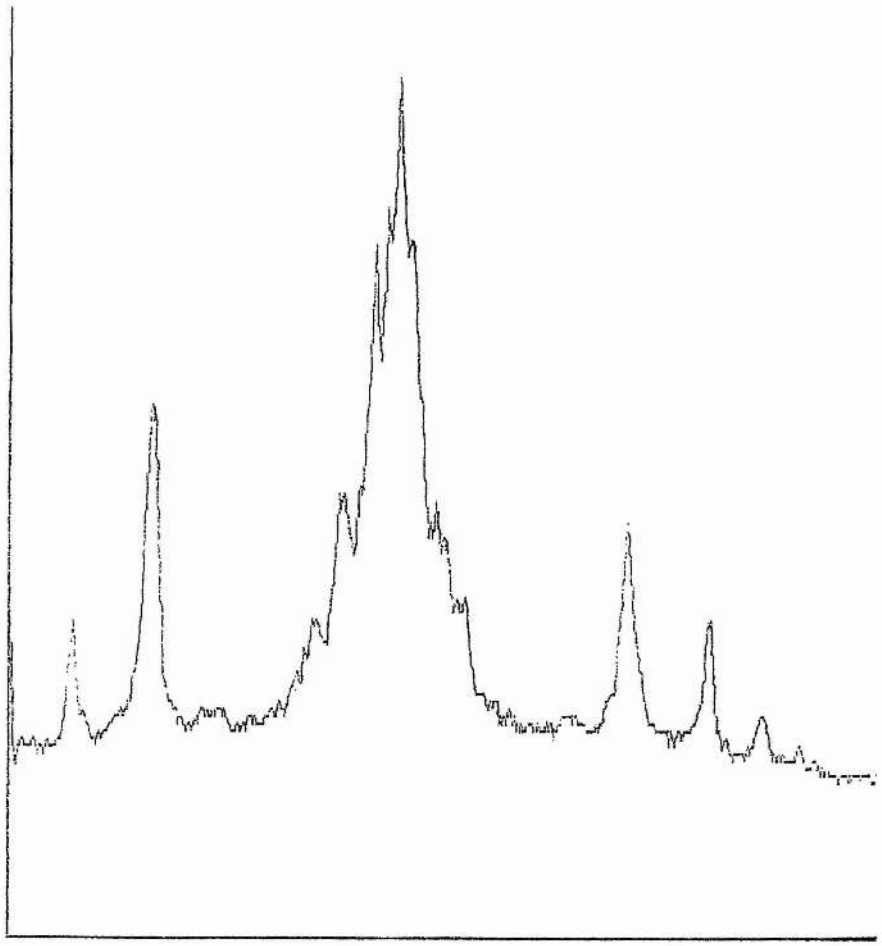

Figure 13. CAIN five line average interferogram of the DFDL output. In this case the laser used the dye Rhodamine B with 50% water and 50%, by volume, methanol as the dye solvent. The laser output wavelength for this scan was $\lambda = 616$ nm.

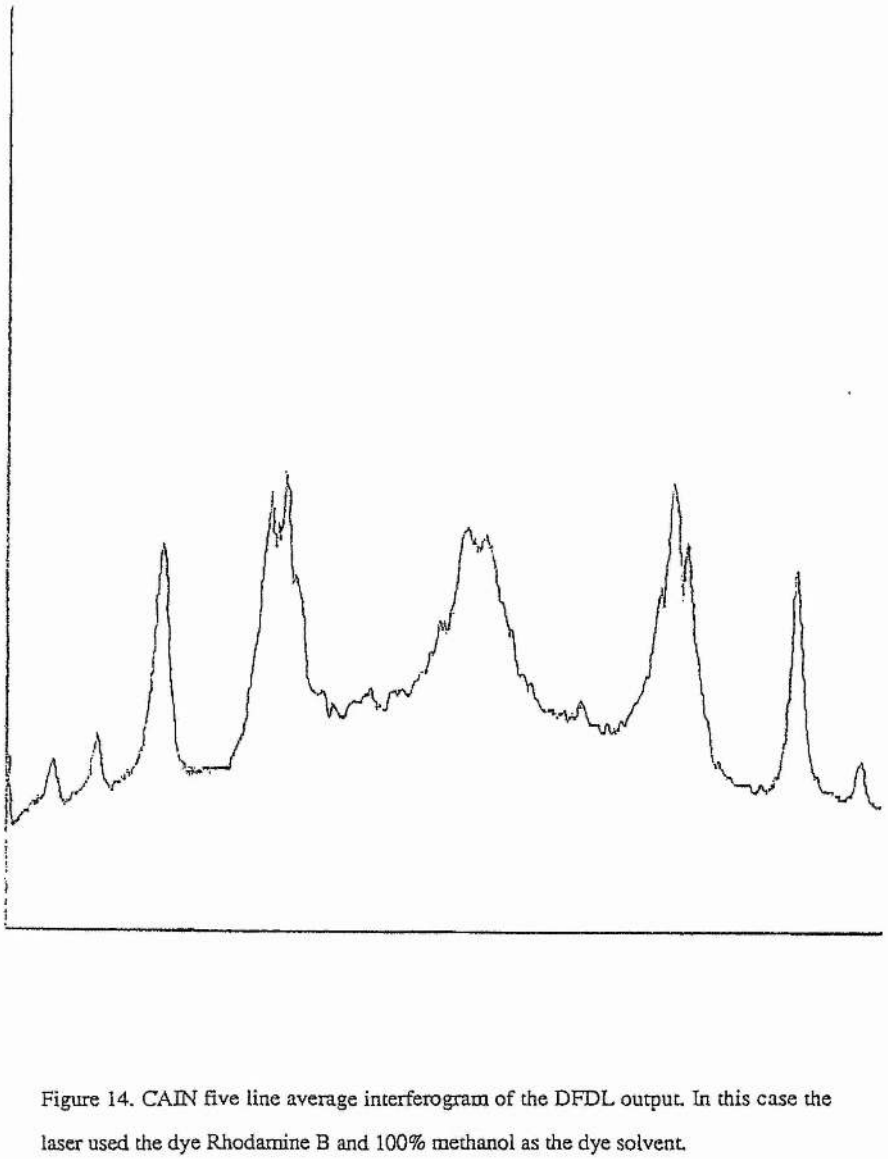

Figure 14. CAIN five line average interferogram of the DFDL output. In this case the laser used the dye Rhodamine B and 100% methanol as the dye solvent.

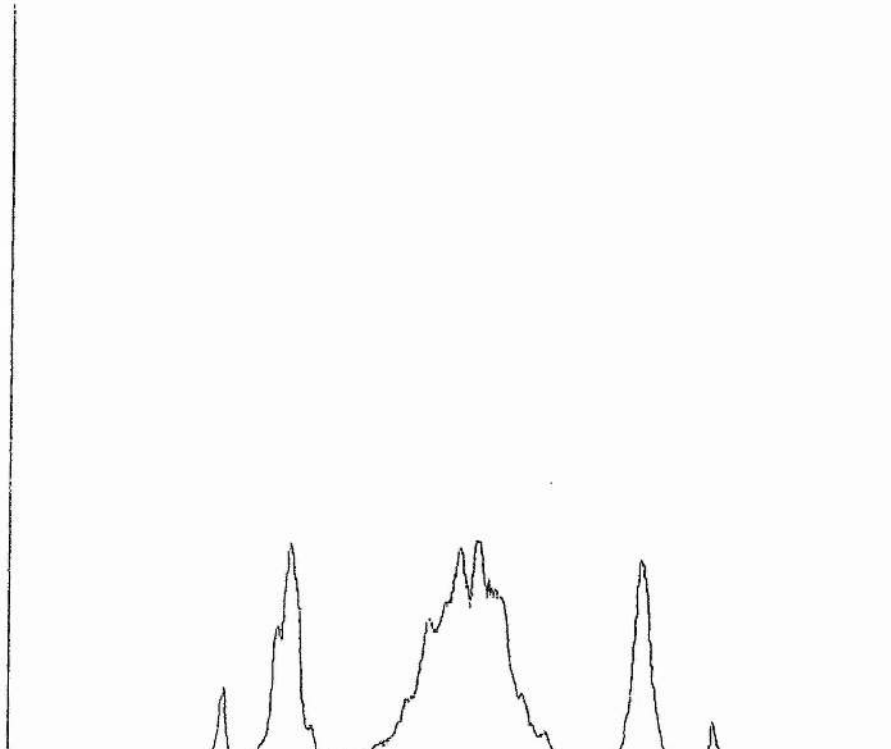

Figure 15. CAIN five line average interferogram of the DFDL output. In this case the laser used the dye Rhodamine B and 100% ethanol as the dye solvent. The laser output wavelength for this scan was $\lambda = 624.3$ nm.

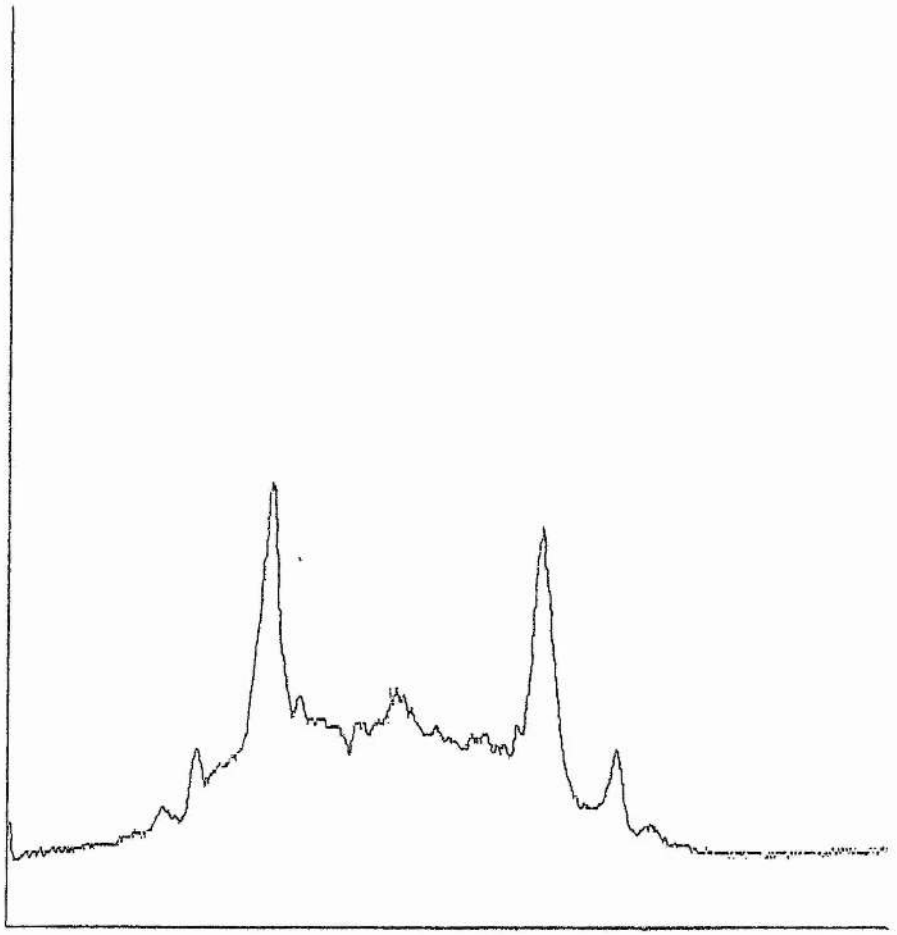

Figure 16. CAIN five line average interferogram of the DFDL output. In this case the laser used the dye Sulforhodamine B and 100% water as the dye solvent.

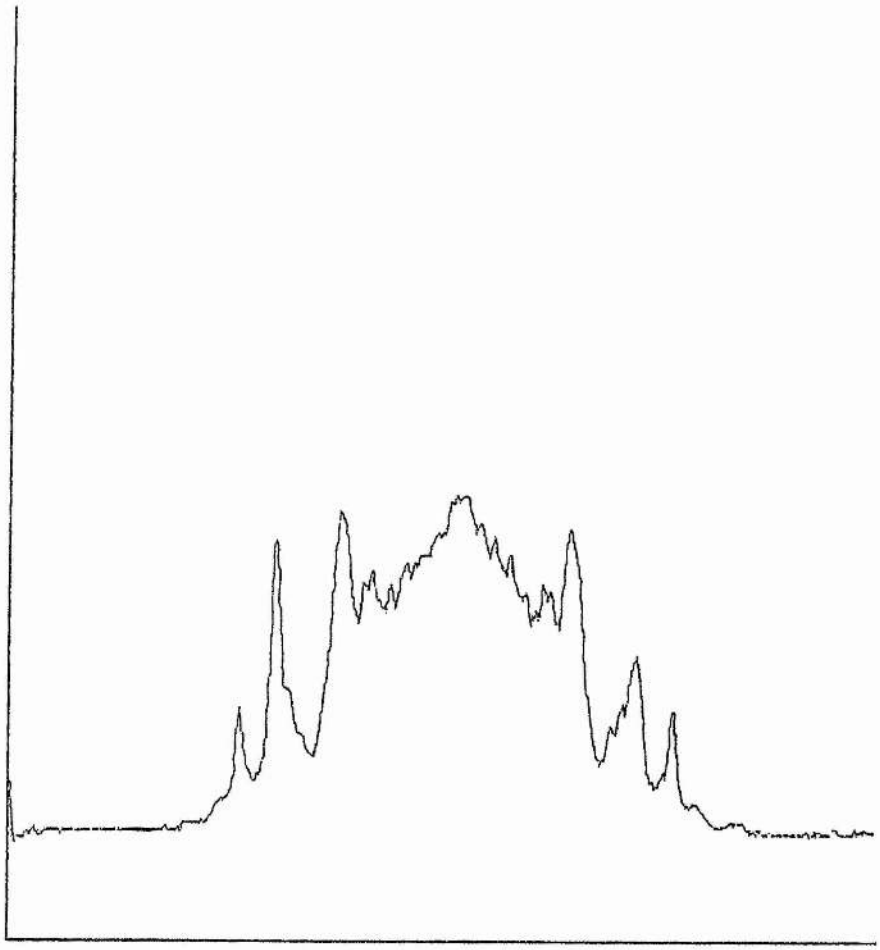

Figure 17. CAIN five line average interferogram of the DFDL output. In this case the laser used the dye Sulforhodamine B and 100% methanol as the dye solvent.

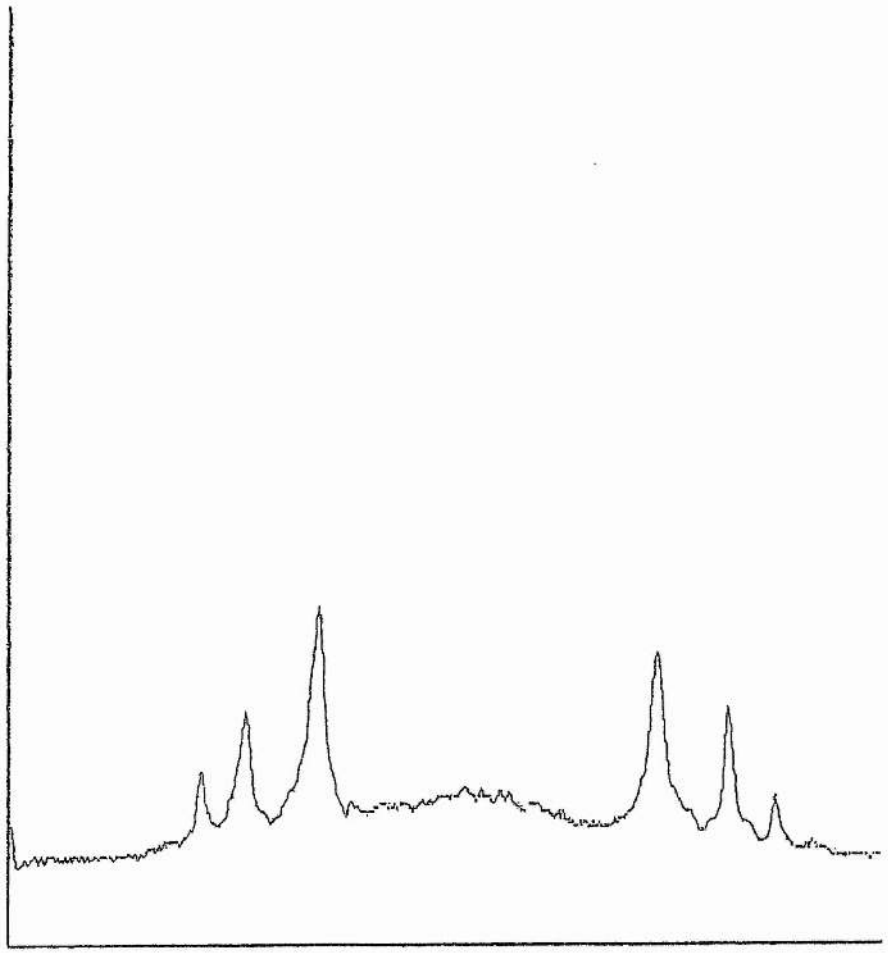

Figure 18. CAIN five line average interferogram of the DFDL output. In this case the laser used the dye Rhodamine 101 and 100% ethanol as the dye solvent. The laser output wavelength for this scan was $\lambda = 633.3$ nm.

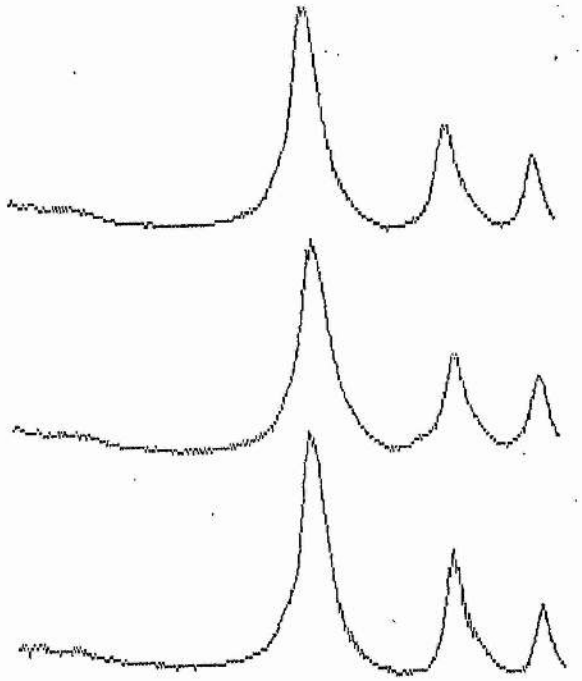

Figure 19. CAIN elliptical average interferogram of the DFDL output. Similar to Figure 18, the laser used the dye Rhodamine 101 and 100% ethanol as the dye solvent.

Chapter VII–Conclusion.

7.1 Introduction.

In Chapter I a review of previously reported DFDL experiments and theories has been presented. The review identifies two, seemingly distinct, operating regimes. In the first regime, where the laser operates around threshold, the DFDL produces pulses which typically have durations two or three orders of magnitude smaller than those of the pump source. In the second regime the laser produces pulses which temporally match those of the pump source. In this second regime the laser linewidth is determined by the power (through thermal and dispersive changes induced in the refractive index of the dye medium) and the characteristics of the pump laser. It has been the aim of this thesis to present details of new investigations into these two operating regimes hence gaining a new understanding of the laser's behaviour. A summary of results, the connection between these and previously reported results and the relevance of the rate equation model is presented in this concluding chapter. In the light of these considerations, a new model of DFDL behaviour is now proposed, which links the operation of the laser in the seemingly distinct regimes.

7.2 Summary of results.

By following the strategy presented in Chapter I for linewidth reduction, the DFDL linewidth has been reduced to near transform limited levels. Implementing the strategy involved employing a SLM pump laser and the reduction of pump powers to around the 1 mJ level. At the 100 MHz level of linewidth obtained, the DFDL is comparable with other tunable pulsed narrow linewidth lasers of more complicated construction. In Chapter VI, where the range of operating conditions for narrow linewidth was explored, it was seen that such narrow linewidth operation occurred over all of the wavelength range investigated (580–680 nm). Since dynamic linewidth effects had been reduced to a minimum in this region, it was possible to explore effects such as increased pump laser linewidth, offsetting the DFDL alignment etc. Chapter VI presents the results of a systematic investigation into how such parameters affect the operation of the laser. One of the most significant result from this investigation was the discovery that, by offsetting the DFDL alignment, thereby reducing the overlap of the interfering pump beams, narrow

linewidth operation was suppressed as the laser switched from a smooth pulsed operation to a regime where the output consisted of picosecond pulses contained within the nanosecond pump pulse envelope. These results, combined with those previously reported, are drawn together in a later section (§ 7.5) where a new model describing the general behaviour of the DFDL is presented. The relation between the new results reported in this thesis and those previously reported are also examined. Before doing so the relevance of the rate equation analysis is discussed.

7.3 The rate equation analysis: Its fit with experiment.

Despite its simplicity, the rate equation analysis has been successful in predicting how the temporal form of the laser varies with pump power. In brief its findings are now summarized. For pumping just above threshold, self Q-switching causes the production of a single pulse of considerably shorter duration than that of the pump laser. At increased levels of pumping the gain medium has sufficient time to recover to allow the production of one or more secondary pulses. It was previously known that the time between such multiple pulses decreases with increased pumping. Previously the analysis had not, however, been extended to the next logical step i.e., to moderate and high pump powers. This, new regime, is examined in Chapter V where it is seen that the pulses merge together eventually leading to the formation of a pulse of similar duration to that of the pump laser. the model can therefore describe all of the types of temporal behaviour which have been observed experimentally.

It is only fair, however, to point out that the model does not convey any frequency information and, as such, cannot be used to predict the laser's linewidth. Conclusions about the laser's linewidth may only be drawn if the linewidth is transform limited. If such is the case, the thermal and dispersive contributions to linewidth, which have been seen to dominate linewidth in many circumstances, must be eliminated.

There are discrepancies between the predictions of the rate equation analysis and the experimental behaviour. The rate equation analysis shows that for the output pulse to temporally follow the pump pulse the laser gain must be clamped (to within 1%) at a constant value. This type of operation is indeed observed experimentally at high levels of

pumping where the linewidth and amplified spontaneous emission (ASE) are observed to saturate. However, at intermediate pumping levels, where linewidths and ASE are observed to scale with the pump power (i.e. the gain is not clamped), it as observed that the temporal form of the DFDL output follows that of the pump laser. Thus the predictions of the model are not consistent with the experimental behaviour throughout the full range of pump powers.

As will be seen below the behaviour is strongly dependent on grating length and although the rate equation analysis fails to account for this it is thought that it still provides a useful insight into the dynamics of DFDL laser action.

7.4 Consideration of DFDL grating length.

Previously the importance of the length of the DFDL's induced grating has largely been neglected in theoretical and experimental investigations of the laser. The importance of the grating length in determining the laser's temporal and linewidth properties is now discussed.

The length of the DFDL grating is not discussed fully by Bor and co-workers when they observe that the minimum pulse length ($\Delta\tau$) obtainable is of the order of the transit time of the DFDL length ($c\Delta T \leq \eta L$). However, it is perhaps to be expected that the number of fringes along the active grating, causing feedback, would determine its frequency resolution. Thus the induced grating might be compared to a diffraction grating where the resolution is determined by the total number of lines. Since the induced grating has its period determined by the output wavelength of the laser the length of the grating determines the number of 'lines' and hence its resolution. A diffraction grating with a grating length L, has spectral resolution $\lambda/\Delta\lambda$ given by;

$$\frac{\lambda}{\Delta\lambda} = mN = m\frac{L}{\Lambda} \qquad (7.1)$$

where m is the diffraction order and N is the total number of lines. The total number of lines induced in the DFDL is given by the length L divided by the grating period Λ, so for m=1 (1) may be written as

$$\Delta\nu = \frac{c}{2L\eta} \qquad (7.2)$$

Applying such an estimate to our DFDL with a grating length L of around 2 cm in a medium of refractive index η equal to 1.5 then the resolution of the grating ($\Delta\nu$) would be in order of 5 GHz. Since this value of $\Delta\nu$ is that obtained for a single pass it is to be expected that these type of calculations give an upper limit on spectral bandwidth. For the 10 ns pulse times of our DFDL which has a grating length of around 2 cm the counter propagating waves experience around 25 round through the frequency selective region. Similar calculations for Fabry Perot cavity lasers employing diffraction gratings as an integral part of their laser cavity feedback, such as were first described by Soffer and McFarland and later improved by Hansch, show that laser linewidths can be reduced many times below that of the resolution of the grating. Thus it may be expected that as the DFDL cavity length increases there is a corresponding linewidth reduction.

A similar calculation may be employed when considering the minimum expected pulse obtained from a DFDL configured to produce ultrashort pulses. For the production of 320 femtosecond pulses Szatmari and Racz state empirically that the length of the DFDL must be less than 100 μm. Consideration of (2) shows that for a grating length of 100 μm, $\Delta\nu$ the spectral resolution is approx 1000 GHz. Assuming a transform limited pulse with a Gaussian profile, this bandwidth yields a pulse duration of around 400 fs, in good agreement with the pulse duration observed experimentally. It is therefore thought that the resolution of the grating limits the pulse width in the short pulse DFDL's.

Such a theory is confirmed by the experimental findings of Chapter VI where it is seen that by offsetting the overlap of the two pump beams thereby creating a shorter grating the laser switches from nanosecond to picosecond operation.

These and other findings are now collated into a new model which describes the temporal and frequency characteristics of distributed feedback dye lasers. The model is now presented.

7.5 A general model of DFDL behaviour.

7.5.1 General model.

In the light of the above considerations a new model which provides a general description of DFDL behaviour has been created and is now presented.

The model is summarized in graphical form in figures (1) and (2). In figure (1) the linewidth of the laser is plotted as a function of the pulse power of the pump laser. In the second figure the laser pulse duration is plotted against the pulse power of the pump laser. Although the axes have arbitrary units, the x axis is common to both figures, hence allowing the relation between linewidth and pulse duration to be seen. The three operating areas labelled represent operation in:

(a) picosecond pulsed,

(b) smooth pulsed (linewidth scales with pump power), and

(c) smooth pulsed (constant linewidth) modes.

The operation of the laser in each of these areas is now considered in relation to the model.

(a) Near threshold, short pulsed operation.

Just above threshold the laser operates with a single pulse of much shorter duration than that of the pump laser pulse. This type of operation is presently an active area of research in the pursuit of single ultrashort pulses (typically in the 100's of femtosecond region). The mechanism for the production of such ultrashort pulses has been attributed to a self Q–switching action. The action has been simply and accurately modelled using a set of coupled rate equations which describe the time dependent interplay between the population inversion and the cavity photon flux. As the population inversion exceeds the inversion threshold value, gain exceeds loss and the photon flux builds up rapidly, hence establishing the DFDL pulse. In doing so however, stimulated emission sweeps out the inversion hence causing the rapid termination of the pulse. The consequence of this short pulse production is that the linewidth is broadened over that of the transform limited nanosecond pulses of region (b) to be considered shortly.

Increasing the pump pulse energy from that necessary to produce a single pulse, leads to multiple pulse generation. Multiple pulsing occurs because, in this instance, the gain medium has sufficient time to recover (while pumping continues) to allow the gain to again exceed loss, hence generating another laser pulse. Such multiple pulsing is predicted by the rate equation analysis, where it is seen that, by increasing the level of pumping, the time between pulses decreases.

Continuing the sequence to higher levels of pumping the rate equation model has shown that the pulses eventually merge together to form a single pulse. This is the second region of DFDL operation and is now considered.

(b) Smooth pulsed (linewidth scales with pump power).

In this region it has been shown that, to a good first approximation, the linewidth scales directly with the power of the pump laser pulse. The pump power dependence is due to time dependent thermal and dispersive changes in refractive index, which sweep (or chirp) the wavelength of the laser throughout the course of the output pulse. When integrated over the whole pulse, this sweeping is interpreted as a linewidth. Thermal effects are predominantly determined by the efficiency of the dye and the thermo-optical properties of the dye solvent. When considering the thermo-optical properties, the quantity dn/dT is of particular importance in assessing the suitability of a solvent. Chapter IV presents a full investigation of the thermo-optical properties of commonly used solvents. Thermal effects have also been related to the fluorescence efficiency of the dye, which can vary considerably (even within the rhodamine series of dyes the fluorescence efficiency can vary between 40 and 100%). Dispersive changes in refractive index are a consequence of changes in the electronic distribution of the dye molecules. Time resolved studies of refractive index changes have shown that a distinction exists in the temporal evolution of thermal and dispersive chirps. In the dispersive chirp, the medium has a virtually instantaneous response to changes in pump power and hence the chirp sweeps out to a maximum and decays, following the temporal evolution of the gain. In contrast however, the thermal chirp is unidirectional as, on the nanosecond timescales involved, the thermal energy cannot escape into the surroundings. The temperature change is positive which leads to a negative wavelength chirp during the pulse (all solvents have a negative dn/dT). The dispersive chirp is strongly wavelength dependent, in magnitude and direction, and, (neglecting absorption dispersion) can be zero at gain line centre.

The factors outlined above (operating wavelength, type of dye and dye solvent) determine the gradient of the linewidth / pump power curve. The lower limit to this regime is dependent upon properties of the induced grating providing feedback. Similar to a

diffraction grating the length of the induced grating determines its resolution, hence a larger grating provides higher resolution and thus lower DFDL linewidth). Considering the effect of grating length in the temporal domain, it has been shown above that the shortest DFDL pulse lengths are attainable by minimising the grating length. Thus two lines are drawn on the linewidth / pump power and pulse duration/pump power graphs of figures (1) and (2). The lines represent two different grating lengths, L_1 and L_2 where $L_1 > L_2$. Thus considering the extremes of operation thus far reported for DFDL operation, 320 fs pulses were obtained in a laser with 100 μm length, whereas our results show that narrow linewidth (100 MHz) operation was obtainable with a 2 cm grating length.

It has also been shown that properties of the pump laser determine the lower limit to the DFDL linewidth as these e.g. linewidth, divergence etc. determine the spectral selection of the induced grating. In the laser system as described, linewidths (down to ~100 MHz) have been reported which compare favourably with other, often more elaborate, dye laser systems.

Increased pumping leads to the saturation of linewidth i.e. the linewidth remains independent of pumping power. This region is now considered.

(c) Smooth pulsed (saturated linewidth).

At high levels of pumping the DFDL linewidth is observed to remain constant as pumping increases.An explanation of this is the following. As the gain is clamped for an increasing portion of the pulse the average dispersive contribution to the time averaged linewidth is reduced. However, with increasing pump power, the thermal contribution to the time–averaged linewidth continues to increase, so that the overall effect is that the observed linewidth remains independent of pump power. The onset of saturation is dependent upon a variety of parameters e.g. concentration of dye, operating wavelength, etc.

Having described a general model of DFDL behaviour the model is now discussed with particular reference to specific measurements made with the laboratory DFDL system.

7.5.2 Specific considerations of the laboratories' DFDL system.

For the experimental laser system used in the investigations described the particular details may be found in the main text of the thesis (see Chapters I, II and VI). As should now be apparent, the minimum expected linewidth of the DFDL is mainly dependent upon the properties of its feedback grating (length, visibility etc) which are determined by the properties of the Nd:YAG pump laser. In order to minimize linewidth, the strategy which was presented in Chapter I was followed. This involved reducing the pulse power of the pump laser, and optimising its performance, to produce a high visibility monochromatic grating. To this end the laser was operated at around 1 mJ pulse energy with a SLM linewidth of ~ 50 MHz (using a modified slow Q–switch). For the majority of investigations the induced grating length was around 20 mm and the laser was operated in the region of 580–680 nm using a variety of dyes (typically one of the rhodamine dyes).

Under such conditions the DFDL would operate around the theoretical linewidth minimum of figure (1). By altering the various parameters of the induced grating, the DFDL was operated in a range of different conditions. These are fully considered in chapter six where it is seen that the laser could operate in either of the modes described above. So as to provide an illustrated guide to the operation of the model presented, figures (1) and (2) are redrawn, this time labeling the figures with data obtained from our specific system. This data is presented on figures (3) and (4).

Under the conditions described above, the DFDL would reliably operate with linewidths in the 100 MHz region. This represents the first report of such operation for such a wide wavelength range. The pulse durations for such operation where typically of the same order as that of the pump laser (between 5 and 10 nanoseconds), the slight decrease in pulse length to below that of the pump pulse being due to operating at reduced levels of pumping.

Offsetting the overlap between the two pump beams, and hence reducing the effective grating length, leads to the production of much shorter duration pulses (measured down to 30 picoseconds) and a corresponding increase in linewidth (measured as greater than 1.5 GHz). This causes the laser to jump to line L_2, which encourages short pulse production, hence causing a degradation of linewidth.

The linewidth saturated operating regime is also labelled on the diagram. In our laser system this typically occurs at pump energies of around 20 mJ.

7.6 Conclusion.

New investigations into the temporal and frequency behaviour of the DFDL have lead to the development of a simple model which accounts for the experimental behaviour of the laser. The model links together the operation of the laser in what have, until now, been considered as two separate operating regimes. The model is in good agreement with previously reported operation. The dynamics of laser action have been further investigated by the extension of a coupled rate equation analysis. It is hoped that the model will aid the understanding of the distributed feedback dye laser which has proven to be a simple and versatile device.

Both experimental and theoretical areas of work are suggested for future consideration. As yet, no theory exists which can predict the temporal and linewidth behaviour of the distributed feedback dye laser. Any such theory would have to explain the modes of DFDL operation which have been described in this thesis.

Experimentally, it would be interesting to observe the effect of higher pump powers while still retaining a SLM laser. Using our Nd:YAG laser with the slow Q-switch we have been forced into operating at reduced pump powers to achieve SLM operation. It is thought that if SLM operation were possible at higher pump powers then such an experiment would be worthy of investigation. Recent advances in injecting seeding of high power Q–switched lasers with diode pumped Nd:YAG lasers may provide such a possibility.

The results presented here have shown that the DFDL can operate with transform limited linewidths (~ 100 MHz for the ~ 10 ns DFDL pulses). If a narrower linewidth is required then longer pulse durations are necessary and hence it is suggested that a some method of pulse stretching is employed to reduce the DFDL linewidth still further.

Frequency jitter in the output is presently one of the disadvantages of the DFDL (or any dye laser where the active volume is of similar size to that of the cavity). It has been already been stated that to achieve better than the 100 MHz shot to shot stability the

temperature must be stabilized to better than 0.5 mK. Although it is not presently considered practicable to stabilize the dye solvent to such a level, it is thought that this point must be addressed before the laser stability can be increased.

In conclusion, by operating at a reduced level of pumping with a line narrowed pump laser the DFDL linewidth was reduced to ~ 100 MHz. For the nanosecond pulse durations involved this represents near transform limited operation. Such operation was achieved over the entire tuning range investigated (580–680 nm) in a variety of laser dyes and solvents. A degradation in the linewidth was observed if any of the operating parameters where offset from those producing transform limited operation. Such a degradation was characterised by a shortening of the pulse duration with a corresponding increase in linewidth.

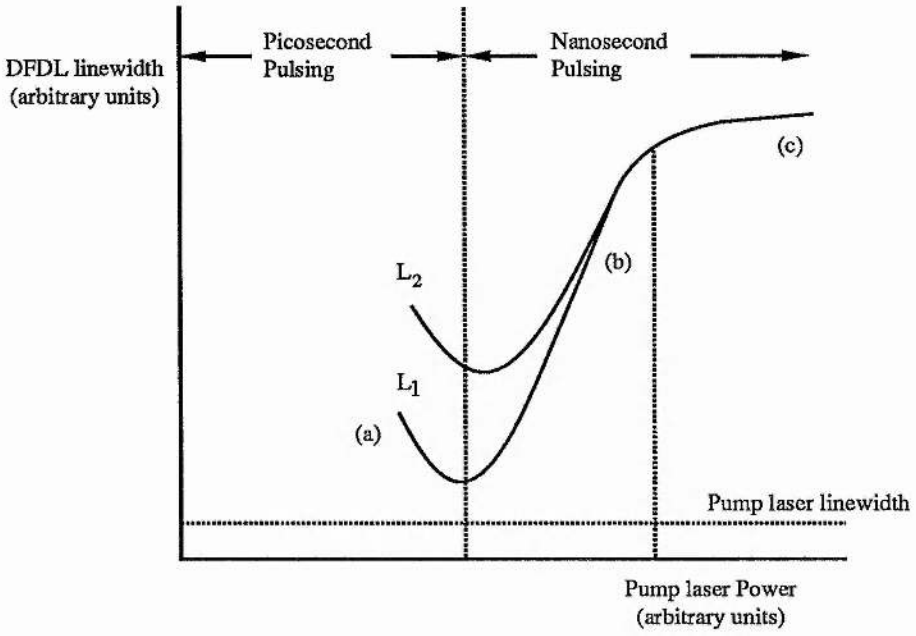

Figure 1. General illustration of how DFDL linewidth behaves as a function of pump power and induced grating length.

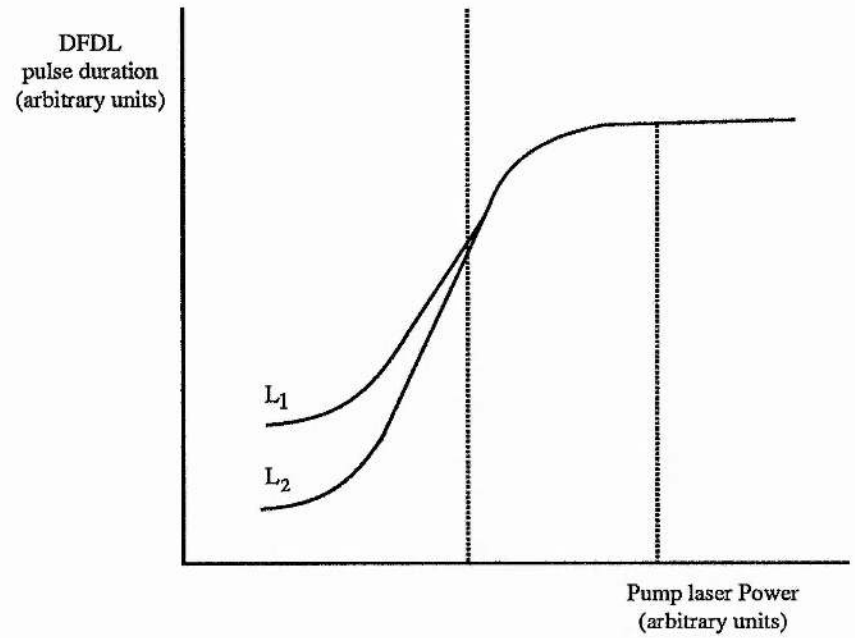

Figure 2. General illustration of how DFDL pulse duration behaves as a function of pump power and induced grating length.

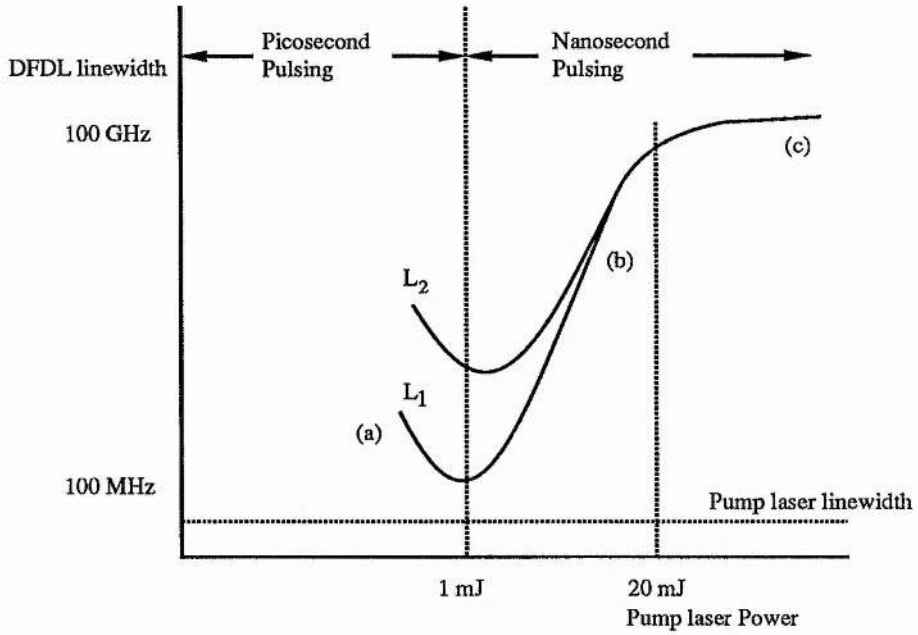

Figure 3. An extension of the general DFDL linewidth behaviour including specific areas observed in our DFDL.

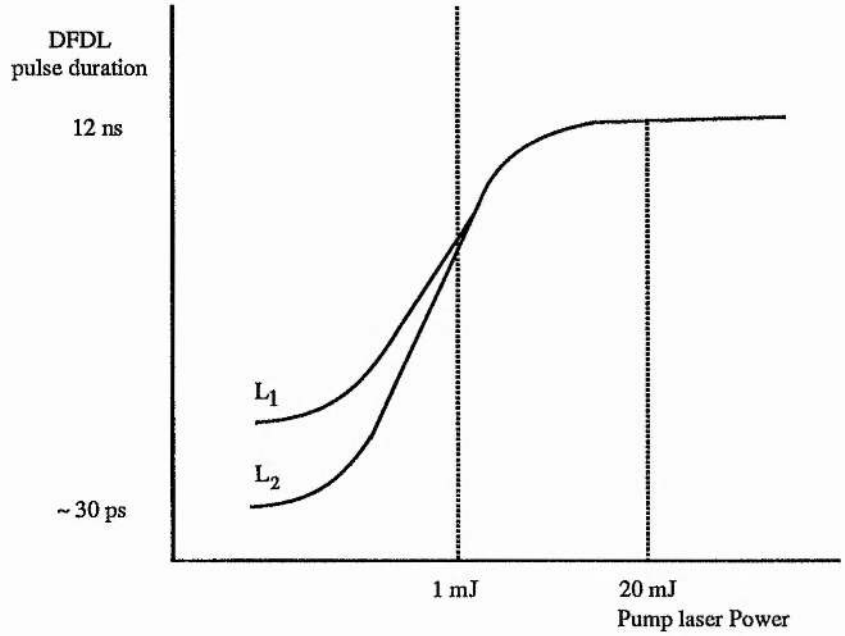

Figure 4. An extension of the general dependence of DFDL pulse duration on pump power and induced grating length to include regions observed experimentally.

Plates

Plate 1. Photograph of the DFDL apparatus configured in the Shank style geometry.

Plate 2. Photograph of the DFDL and the diagnostic equipment used in our investigations. Located to the left of the DFDL are the streak camera, the vacuum photodiode and the 275 MHz oscilloscope. To the right hand side of the DFDL is the CAIN apparatus showing the interferometer, the relay lens and the CCD camera. The computer and framestore are located in the top right hand corner of the photograph.

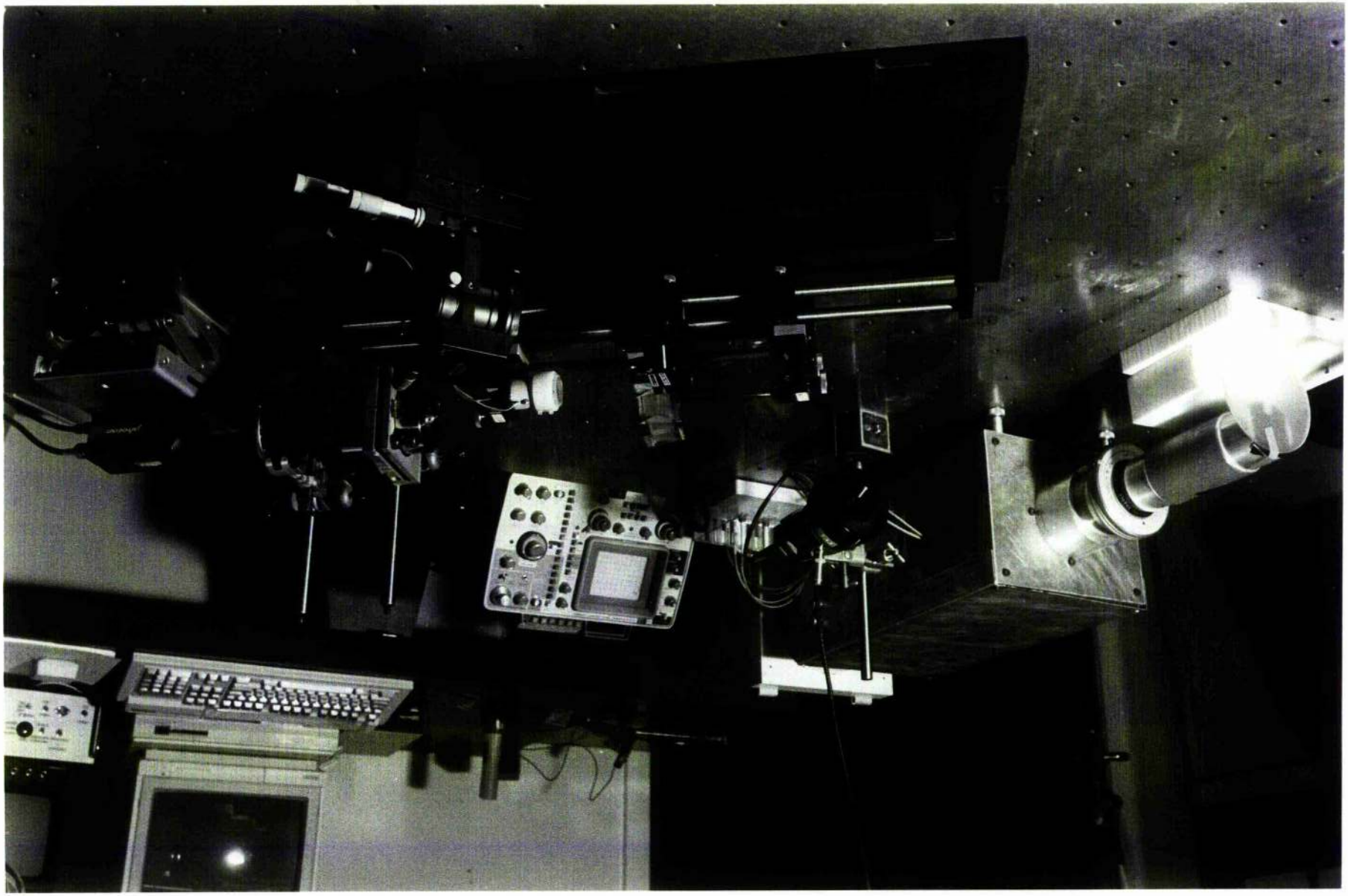

Plate 3. Photographic reproduction of two examples of the false colour images produced when the using the CCD camera, framestore and computer in conjunction with the streak camera. The streak time is of the order of one nanosecond. The top figure is a smooth streak indicating that no sub-nanosecond structure was present in the DFDL pulse. In contrast the lower photograph clearly shows that the laser was producing picosecond pulses.

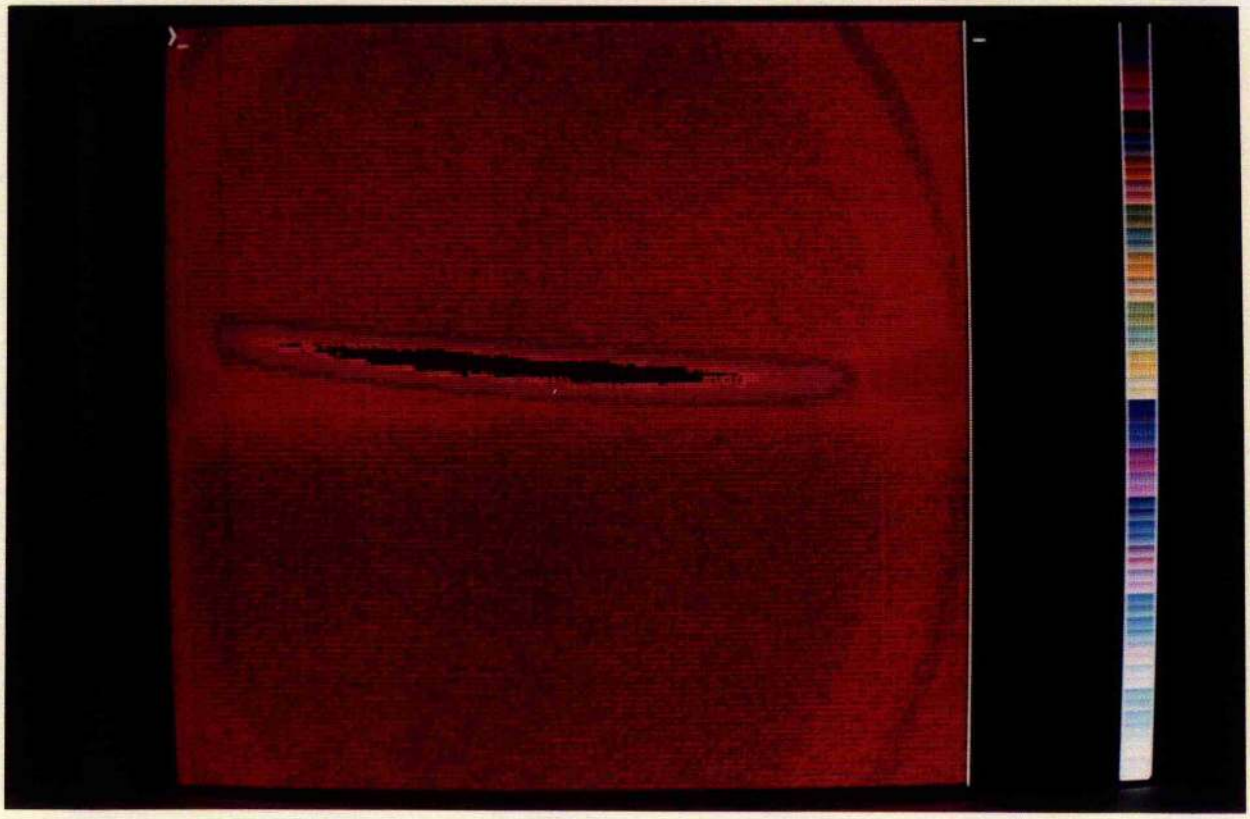

Appendices I–IV

JOURNAL OF MODERN OPTICS, 1988, VOL. 35, NO. 3, 325–343

Linewidth-determining processes in distributed feedback dye lasers

I. A. McINTYRE†, M. E. LUSTY and M. H. DUNN
Department of Physics, University of St Andrews,
St Andrews, Fife KY16 9SS, Scotland

Abstract. Processes determining the linewidths of distributed feedback dye lasers (DFDL) have been investigated. Time resolution of the frequency of the output pulse shows that the linewidth, averaged over a pulse, arises predominantly from a dynamic sweeping of the laser frequency during the course of the pulse. This sweeping results from refractive-index changes in the dye over the duration of the pumping pulse; either through thermal effects or dispersion associated with the saturated gain. Thermal effects may be minimized by suitable choice of solvent but the dispersive sweep is inherent in this type of laser. The magnitude of the dispersive sweep changes across the tuning range of the laser. By judicious choice of dye solvent and dye parameters we have developed a narrow linewidth DFDL of 140 MHz for $\tau = 3{\cdot}2$ ns pulses, which is close to the transform limit.

1. Introduction

Although distributed feedback dye lasers have been investigated since 1971, when the first practical system was developed by Kogelnik and Shank [1], there has been no systematic evaluation of the processes determining the linewidths in such lasers. Linewidths reported in the literature vary widely, depending on the details of the laser configuration, the type of pump laser used and on the degree of pumping above laser threshold [2–7].

In previous studies of linewidths in DFDLs, the linewidth has been shown to depend on the level of pumping of the DFDL. Shank [2] found that the linewidth of his device was very small at threshold, about 0·01 Å (0·03 cm^{-1}), but this increased to 0·5 Å when the pump power was five to fourteen times the threshold power. This was confirmed by Bakos [3] who found that the linewidth increased from 0·13 Å to 4 Å at high pump powers. The linewidth has also been shown to depend on the visibility of the grating. Both of the above investigators used Q-switched ruby lasers of good spatial and temporal coherence as the pump lasers, hence producing gratings in the dye active medium of high visibility. The use of a broadband laser (such as a nitrogen laser) as the pump has been shown to increase the linewidth. For example Bor *et al.* reported a linewidth of 2·5 Å when pumping a DFDL in a Chandra type configuration [4] with a nitrogen laser [5]. Bakos found that using a ruby laser of poor spatial coherence increased the linewidth of the DFDL by a factor of seven over that obtained using a beam of high spatial coherence [6]. An increase in the divergence of the pump beam has also been shown to increase the linewidth. Vashchuk used highly divergent beams in a Bakos type DFDL [3] and obtained a linewidth of 7 Å pumping only six times above threshold [7]. It is interesting to note that, in all the above

† Present address: Department of Physics, University of Illinois at Chicago, Chicago, Illinois 60680, U.S.A.

studies, the characteristic mode structure predicted by the coupled-wave analysis of Kogelnik and Shank [1] has never been unambiguously observed. This is perhaps due to the lack of sharp boundaries between the regions with and without the induced grating.

In the present paper we demonstrate that after the dependence on pump-beam divergence and pump-laser linewidth has been minimized, refractive-index changes in the dye caused by solvent heating during the course of the pumping pulse produce a frequency chirping in the output pulse from the dye laser, which, on time averaging over the pulse, is interpreted as a contribution to the linewidth. Correct choice of dye solvents enables this effect to be minimized. A further process is shown to then limit the ultimate linewidth achievable in DFDLs, which is the changing dispersion of the active medium during the course of the pumping pulse due to the saturation of the gain. A model of this process is used to predict correctly the temporal behaviour of the central laser frequency during the course of the pumping pulse, and also to predict how the magnitude of the effect changes with tuning of the dye laser across the spectral profile of the dye.

In the light of these findings we have been able to develop a DFDL which has a linewidth approaching the transform limited linewidth for a pulse of 3·2 ns, namely 140 MHz. This is discussed in § 5.

2. The experimental system

The distributed feedback dye laser employed the Shank-type geometry and is illustrated in figure 1. This laser was optically pumped with a frequency-doubled, Nd : YAG laser, which could be either actively or passively Q-switched. Since the pump laser employed an unstable resonator, the output beam, after frequency doubling, was propagated along a 9 m delay line to improve the spatial quality of the output wavefront. The resulting output beam had a diameter of 14 mm, a divergence of 0·5 mrad (half angle), and a Gaussian intensity profile. The coherence of the wavefront was assessed using a two-beam shearing interferometer. The fringe visibility observed with this interferometer when the beams were sheared so that

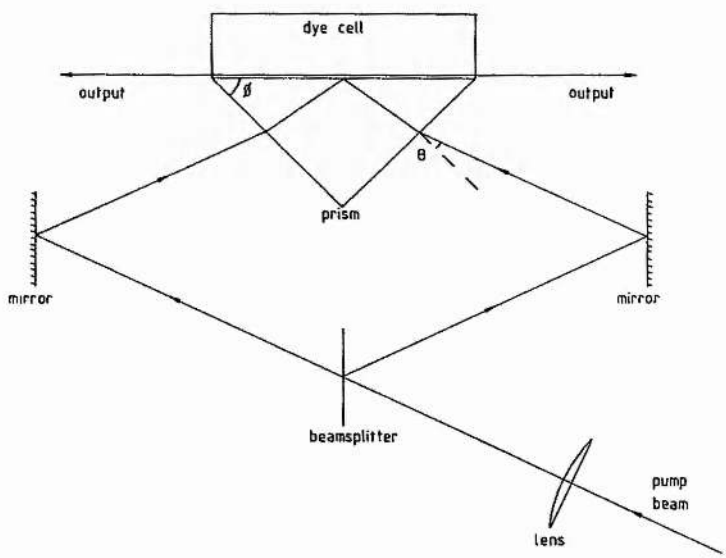

Figure 1. Distributed feedback dye laser of Shank-type geometry, showing the angle of incidence on the prism θ and the prism angle ϕ.

only their opposite edges overlapped was found to be reduced to about one-third of that when the two beams were in complete register. When the laser was operated in active Q-switched mode together with a line-narrowing etalon in the cavity (4 GHz free spectral range), the output pulse was of 10 ns duration (full width at half maximum), was of linewidth 0·04 Å measured at the frequency-doubled wavelength of 532 nm, and was of maximum energy up to 110 mJ when the laser was operated at 10 Hz. In order to obtain a temporally smooth pulse for the time-resolved measurements across the pulse profile (to be described later), the laser was either passively Q-switched using an intracavity saturable absorber or slow Q-switched [8, 9] to produce in both cases single axial mode oscillation. Smooth reproducible output pulses were obtained with a transform-limited linewidth of about 50 MHz and a pulse duration of 10 ns. Peak pulse energy was, however, limited to about 5 mJ.

With the exception of the results discussed in § 5, the distributed feedback dye laser was operated at wavelengths of around 600 nm using the dye rhodamine B in aqueous solution with added detergent to avoid dimerization (3×10^{-4} M solution in a 98% water, 2% Decon-90 mix, giving a 200 μm absorption length for the pump light). In order to couple the pump light at 532 nm into the dye cell at an appropriate angle for distributed feedback to occur at around 600 nm in the dye, a 90° coupling prism was affixed to the front face of the dye cell using index-matching fluid. Because of the oblique angles of incidence involved in the arrangement, the 14 mm diameter pump beam resulted in a 20 mm length of dye being optically pumped. The dye flowed through the cell at a rate of about 2 l min^{-1}. The pump beam was focused down into the dye cell using an optimum form cylindrical focusing lens of focal length 30 cm placed before the beam splitter as shown in figure 1. With such an arrangement it was possible to produce a pumped region in the dye cell with a width of 30 μm for an input beam divergence of 0·5 mrad. In practice, the dye laser was operated with the pump beam defocused so that this width was increased to 100–200 μm to avoid optical damage.

3. Basic properties of the distributed feedback dye laser

We first report on the basic characteristics of the distributed feedback dye laser as operated. The threshold for distributed feedback lasing required a pump energy of about 0·1 mJ (10 kW). The variation of output power with pump power when operating above threshold is shown in figure 2. For a pump power of 10 mJ the efficiency of the distributed feedback dye laser, taking into account the power emitted at both ends of the structure, was 18%. At higher pumping levels the efficiency decreases, for example at 50 mJ pumping, it was down to 14%. This is probably due to the device being under-coupled at this pump level, when internal losses play an increased role [7]. The measured beam divergence of the output beam from the dye laser was 11 mrad by 17 mrad, the latter figure being the divergence measured out of the plane of figure 1. These divergences are greater than the diffraction limits implied by the cross-sectional area of the pumped volume in the dye (approximately 100 μm by 100 μm), and correspond to geometrical limitations. The beam showed a smooth 'Gaussian-like' intensity profile in both dimensions. The output pulse was observed to closely follow the pumping pulse in time, when monitored with a temporal resolution of 1 ns. There was no evidence for the presence of pulsing of the type reported by Bor [10].

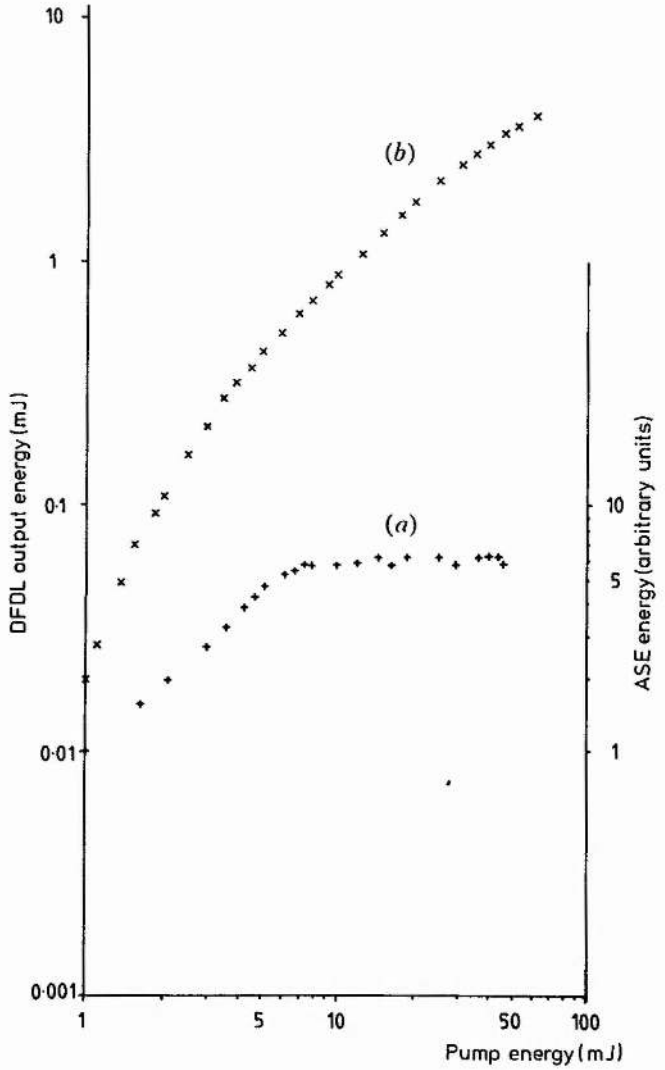

Figure 2. Energy (arbitrary units) of amplified spontaneous emission in the presence of DFB action (curve *a*) and energy (mJ) of the line-narrowed output (one end) due to DFB action (curve *b*) as a function of pumping energy (mJ), for the case of Shank-type geometry.

Using rhodamine B the device could be tuned over a range 580–630 nm. It was found possible to tune over some 10 nm by rotation of the beam-steering mirrors only, but outwith this range it was found necessary also to translate the mirrors.

The amplified spontaneous emission (ASE) present in the output was also monitored. The spectrum of the ASE is shown in figure 3, and the dependence of the ASE on pump power is also shown in figure 2. When the laser was tuned to 587 nm, close to the centre of the ASE spectrum at 589 nm, the total power in the ASE output at a pump power of 5 mJ was around 2% of the tuned output at this pump power. The ASE content did increase above this level if the laser was tuned towards the edges of the ASE spectrum. Again the ASE was observed to follow closely the pump pulse in its temporal behaviour. The behaviour of the ASE power with pump power, especially the way in which the ASE power saturates with pump powers above about 20 mJ, is of particular importance in relation to the linewidth studies discussed in § 4, and is discussed there.

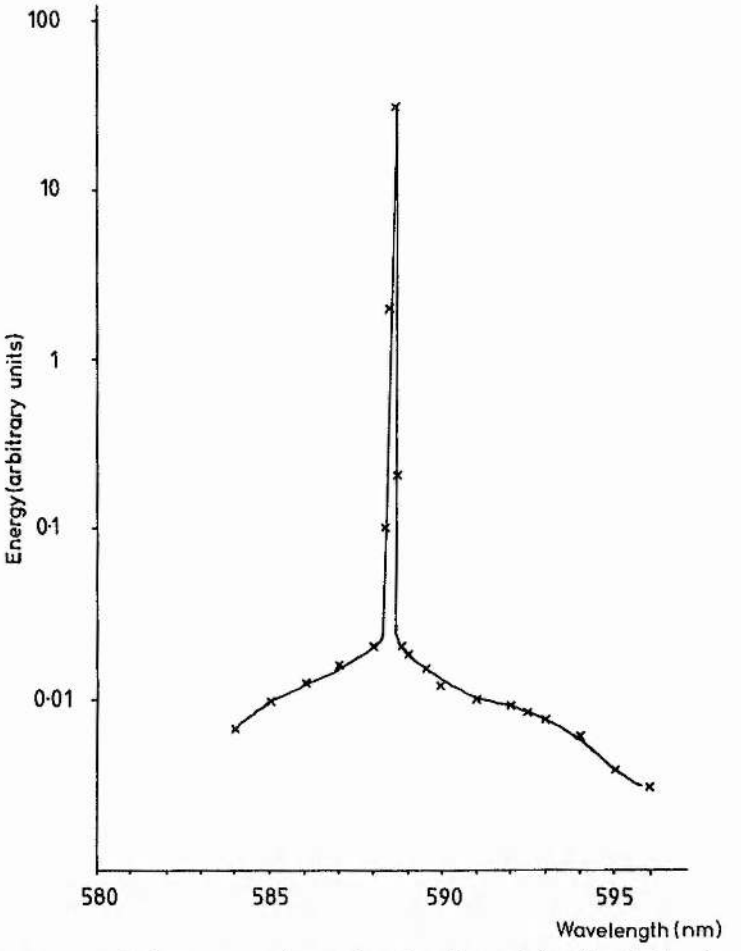

Figure 3. Spectrum of the output from the distributed feedback dye laser for a pumping energy of 1·5 mJ.

4. Linewidths in distributed feedback dye lasers

We have carried out a systematic investigation of the processes determining the linewidths observed in practical DFB dye lasers. In addition to the ultimate limit to the linewidth as discussed by Kogelnik and Shank [1], and which we will consider later, we investigate possible additional effects, namely:

(1) the linewidth of the pump laser radiation,
(2) the divergence of the pump laser radiation,
(3) a time-dependent refractive index for the solvent arising from thermal effects, and
(4) a time-dependent contribution to the refractive index of the active medium arising from the dispersion associated with the optical gain.

Although the first three effects may be minimized by judicious choice of parameters (as we will show), the fourth effect is inherent in the laser active medium and constitutes a fundamental practical limit to the minimum linewidth achievable in a DFB dye laser. Although we regard the latter two effects as determining linewidth, this is only strictly the case when the linewidth averaged over the duration of the output pulse is being considered. As we shall see shortly, these latter effects are really associated with frequency sweeping or chirping occurring during the time duration of the output pulse from the dye laser.

Linewidths averaged over the duration of the output pulse were measured either using a grating spectrometer with a linear photodiode array to record the spectrum when the linewidth was in excess of 0·2 Å [11], or a plane-parallel Fabry–Perot interferometer of variable free spectral range when the linewidth was below this limit. Linewidth resolution with the latter was down to 0·01 Å. Techniques for monitoring the laser wavelength variation during the course of the pulse will be discussed later.

In table 1, we summarize linewidths of the DFDL measured at different operating wavelengths and for different dye-solvent temperatures. In figure 4 we show the measured linewidths of the DFDL as a function of pumping energy for two different temperatures of the water-based dye solvent. The saturation in the linewidth as a function of pump power for pump powers above 15–20 mJ should be noted; this is a similar behaviour to that shown by the ASE output (see figure 2). These functional dependences will be fully discussed shortly.

4.1. *Linewidth of pump radiation*

The standard relation between the wavelength of the distributed feedback output λ_d (free space), pump wavelength λ_p (free space), and refractive index of solvent n_s is

$$\lambda_d = \frac{n_s \lambda_p}{n_p \sin\{\phi + \sin^{-1}[(\sin\theta)/n_p]\}}, \tag{1}$$

Table 1. Linewidth of the distributed feedback dye laser at different operating wavelengths and for two solvent temperatures (1·5 mJ pumping, water/Decon solvent).

λ_d (nm)	Linewidth at 5°C (Å)	Linewidth at 22°C (Å)
580	0·15	0·22
590	0·22	0·32
600	0·4	0·6

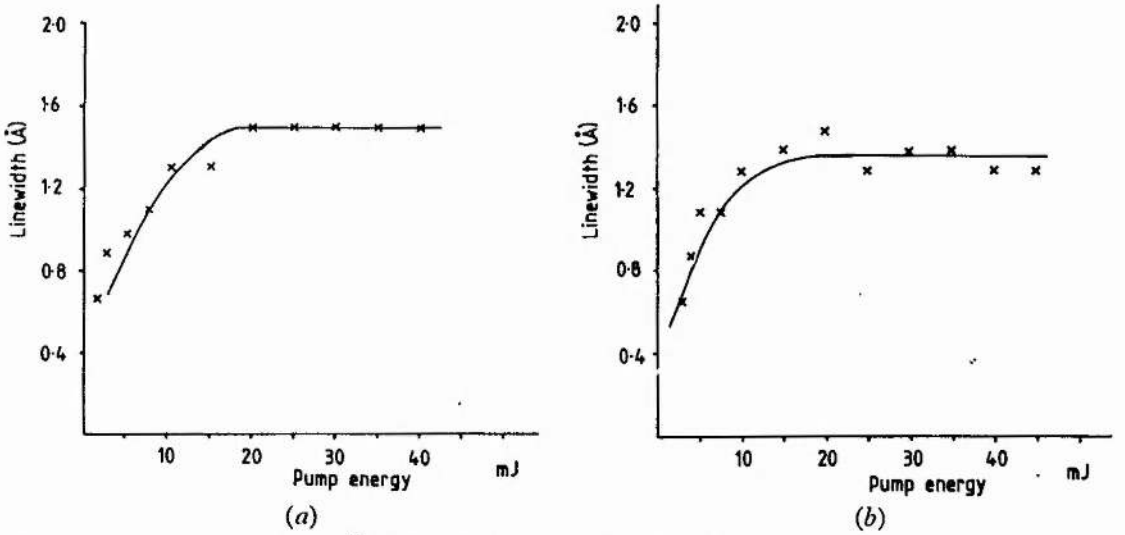

Figure 4. (*a*) Linewidth (Å) of the distributed feedback dye laser as a function of the pumping energy (mJ) with the dye solvent at 30°C. (*b*) Same as (*a*) but with solvent at 4°C. Conditions: DFB selected wavelength 587 nm, pump-beam divergence 0·5 mrad, 98% water/2% Decon-90 solvent, 3×10^{-4} M solution of rhodamine B.

where n_p and ϕ are the refractive index and angle respectively of the coupling prism, and θ is the angle of incidence of the pump beams on the prism faces. From this it may be seen that the linewidth of the DFDL output due to a finite pump linewidth is

$$\Delta\lambda_d = \frac{n_s \Delta\lambda_p}{n_p \sin\{\phi + \sin^{-1}[(\sin\theta)/n_p]\}}, \tag{2}$$

For the present configuration, with $\theta = 15°$, $n_p = 1{\cdot}55$ and $n_s = 1{\cdot}33$, the expected value of $\Delta\lambda_d$ is $\Delta\lambda_d = 1{\cdot}05\Delta\lambda_p$. For the case when the pump-light linewidth is 0·04 Å (active Q-switched) $\Delta\lambda_p$ is 0·05 Å, while a transform-limited linewidth is to be expected for the case of SLM operation of the pump laser. For the present configuration even the former expected linewidth is small compared to observed linewidths and, further, no change in the DFDL linewidth was observed on switching from one form of pumping to the other at similar pulse energies. We hence conclude that, in the present configuration, there is no significant contribution to the DFDL linewidth from the finite linewidth of the pump radiation. However, when other more dominant linewidth effects, to be discussed shortly, are minimized, the effects arising from pump linewidth become apparent. This is further discussed with reference to narrow linewidth DFDLs in § 5.

4.2. *Pump-beam divergence*

The influence of pump-beam divergence on the DFDL linewidth may be estimated by differentiating equation (1) with respect to θ to obtain

$$\Delta\lambda_d = \frac{-\lambda_d \cos\theta}{\tan\{\phi + \sin^{-1}[(\sin\theta)/n_p]\}(n_p^2 - \sin^2\theta)^{1/2}} \Delta\theta, \tag{3}$$

where $\Delta\theta$ is the pump-beam divergence. For the present case of a beam divergence of 0·5 mrad, the expected linewidth is around 0·9 Å, which is a significant effect in relation to observed linewidths. However, a rather more careful analysis shows that equation (3) overestimates the effect of beam divergence. In fact, as figure 5 shows, the effect of beam divergence is not to alter the grating spacing, but rather to skew the axis of the grating relative to the axis of the gain medium at each end of the medium. Hence, although a detrimental effect arising from divergence is to be expected, the linewidth predicted by equation (3) should be regarded as an overestimate.

An experiment was performed in order to examine the effect of divergence on the linewidth. The beam from the pump laser was passed through two 20 cm (nominal) focal-length lenses which were separated by approximately 40 cm (see figure 6). The

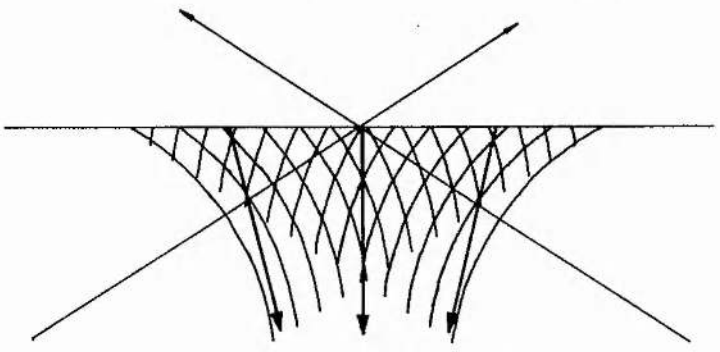

Figure 5. Illustration of the manner in which beam divergence results in the grating orientation becoming skewed through the active medium.

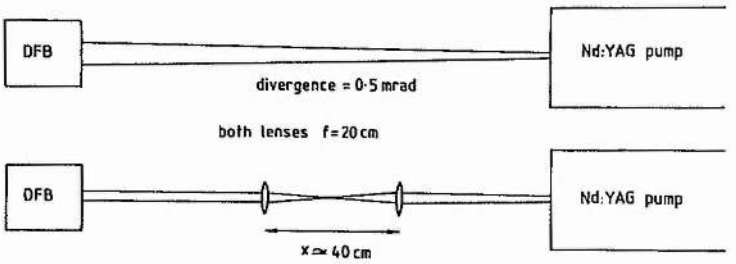

Figure 6. The arrangement used to vary the divergence of the pump beam of the distributed feedback dye laser.

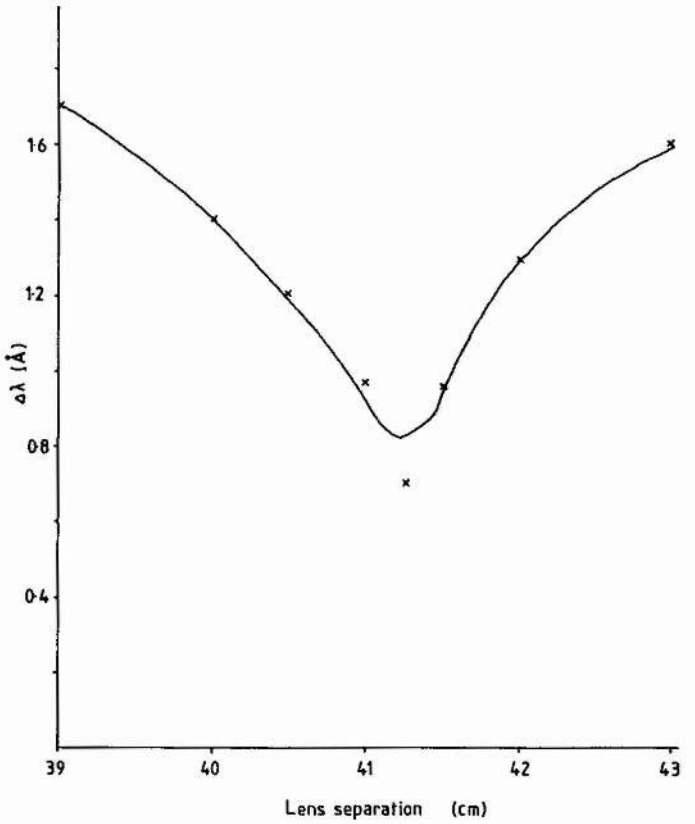

Figure 7. The dependence of the linewidth of the distributed feedback dye laser on lens separation, and hence on divergence of the pump beam.

lenses were situated in the delay line and, in order to prevent clipping of a passing beam, the pump beam made only one complete traverse in this case rather than three. Consequently, the pumped region in the dye cell was shorter, which increased the linewidth of the DFDL to 0·9 Å when pumped with 5 mJ and for a beam divergence of 0·5 mrad.

The object of the experiment was to determine the dependence of the DFDL linewidth on the divergence of the beam. The divergence was altered by moving one of the lenses with respect to the other and the resulting linewidth was then measured (figure 7). This experiment showed that the linewidth of the DFDL is dependent on the divergence, coming to a minimum for a separation between the lenses (41·2 cm) corresponding to the beam waist formed by the lens combination falling in the dye cell when, of course, the divergence of the pump beams in the cell is a minimum.

Although the DFDL demonstrates a dependence of linewidths on pump-beam divergence, the effect of divergence cannot account for the wavelength dependence of the linewidth or its power dependence. Therefore, it must be concluded that the divergence of the pump beam is not a limiting factor but can contribute to the linewidth under certain circumstances. In all subsequent experiments, the divergence of the pump beam was 0·5 mrad.

We now consider the last two effects (3) and (4), both of which are due to changes in the refractive index n_s of the dye solution. From equation (1), it may readily be seen that if the refractive index changes by an amount Δn_s during the course of the pumping pulse, there is an associated shift in the wavelength of the DFDL given by

$$\Delta\lambda_d/\lambda_d = \Delta n_s/n_s. \tag{4}$$

Although this effect is a dynamic sweeping of the wavelength during the course of the pulse, it is interpreted as a contribution to the linewidth on averaging over the time duration of the pulse.

We now consider the thermal and dispersive contributions to the linewidth separately, and present experimental data that allow us to differentiate between their relative contributions.

4.3. *Thermal effects in dye solvent*

The refractive-index change in the pumped region of the dye, of volume V, arising from heating is given by

$$\Delta n_s = \frac{AE}{\rho V s}\left(\frac{\delta n_s}{\delta T}\right), \tag{5}$$

where E is the pumping energy (per pulse) and A is the fraction of the pumping energy converted into heat (approximately 50%). The other parameters are properties of the solvent used; ρ is the density, s is the specific heat capacity and $\delta n_s/\delta T$ is the rate of change of refractive index with temperature. Expression (5) assumes that the active medium is uniformly pumped and that thermal diffusion can be ignored for the time scales involved (10 ns).

The mechanism by which thermal effects contribute to the linewidth is that, during a pumping pulse, the temperature of the active volume increases, thus reducing the refractive index (for negative $\delta n_s/\delta T$) with a consequent reduction in the DFDL wavelength. On integrating over the whole pulse, this sweep in DFDL wavelength is seen as a contribution to the linewidth, given by

$$\Delta\lambda_d = \frac{\lambda_d AE}{\rho V s n_s}\left(\frac{\delta n_s}{\delta T}\right). \tag{6}$$

The solvent parameters for methanol and water are given in table 2, from which it is obvious that water is expected to be superior to methanol (i.e. to give the lower

Table 2. Thermal properties of dye solvents (at 20°C).

Property	Methanol	Water
Density ($kg\,m^{-3}$)	740	1000
Specific heat capacity ($J\,kg^{-1}\,K^{-1}$)	2500	4200
$\partial n_s/\partial T$ ($10^{-4}\,K^{-1}$)	−4	−1

linewidth). For example, for a 5 mJ pump pulse the expected refractive index change in a methanol solution is $\Delta n_s = -9{\cdot}6 \times 10^{-4}$, with an associated change in wavelength of about -4 Å, whereas using water at room temperature reduces the refractive-index change to $\Delta n_s = -1{\cdot}04 \times 10^{-4}$, with a consequent reduction in wavelength sweep to $-0{\cdot}5$ Å. However, we have shown elsewhere that $(\delta n_s/\delta T)$ for water is temperature dependent, falling from $-1 \times 10^{-4}\,\mathrm{K}^{-1}$ at room temperature to zero at 4°C [12, 13], thus making it an even more attractive solvent when cooled.

The dependence of the DFDL linewidth on the solution temperature when using water as the solvent (see table 1 and figure 4) clearly shows that thermal effects do contribute to the linewidth and that this contribution is reduced by having the solvent close to the condition $\delta n_s/\delta T = 0$. However, equation (6) predicts that the thermal contribution to the linewidth is zero if the dye solution is cooled to 4°C and the experiments show that the observed linewidth at this temperature is still significant. The linewidth would also be expected to continue to increase proportionally with increasing pump energy. This is not observed to be the case; the linewidth reaches a maximum value at about 15 mJ of pumping and becomes independent of pump energy above this (see figure 4). Moreover, the wavelength-dependent nature of the linewidth (see table 1) cannot be explained by heating of the pumped volume, and so it must be concluded that, although thermal effects do contribute to the linewidth, there is another, dominant broadening mechanism present. We now consider this other mechanism before discussing time-resolved measurements of the wavelength of the DFDL output, when it will be seen that such measurements also provide further evidence of thermal effects.

4.4. *Gain-induced dispersion*

The refractive index of a medium varies rapidly with frequency for frequencies close to an atomic or molecular resonance of the medium. More particularly, if a resonance has a Lorentzian profile, with a half-width $\Delta\nu$, the dispersion resulting from the resonance has the functional dependence on frequency

$$n(\nu) = 1 + \frac{c(\nu - \nu_0)a(\nu)}{2\pi\nu\Delta\nu}, \tag{7}$$

where c is the speed of light, ν_0 is the resonant frequency and $a(\nu)$ is the frequency-dependent gain of the medium, and depends on the relative populations in the upper and lower states of the resonance and also the transition cross-section (if a is negative then the medium exhibits absorption and the more usual condition of anomalous dispersion applies).

A consequence of this dispersion is that the refractive index of the active medium is dependent on the upper- and lower-state populations, and also on wavelength. In the case of a DFDL this can result in an oscillation frequency which is dependent on the intracavity laser radiation intensity. Moreover, since this intensity changes during the course of a pulse, i.e. increases and then decreases, it is to be expected that the oscillation frequency will also undergo an 'excursion' during the pulse, and if the output is integrated over the length of the pulse, this excursion will be interpreted as a linewidth.

Dispersion in a dye laser active medium is more complicated than implied above; for instead of having a single Lorentzian gain profile, the (fluorescent) emission resonance is Stokes-shifted with respect to the absorption resonance (see figure 8 for

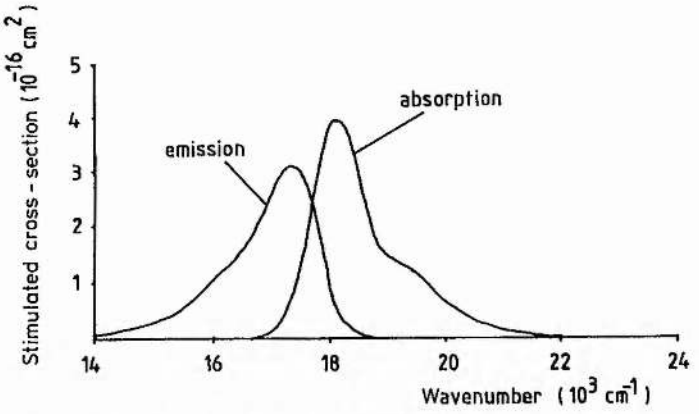

Figure 8. Absorption and fluorescence spectra of rhodamine B.

the emission and absorption spectra of rhodamine B), and so the resulting dispersion curve has two frequency-dependent components, one arising from absorption and the other from emission. In addition, the absorption and emission spectra do not have Lorentzian profiles and so the exact form of the dispersion relation given in equation (7) does not hold; numerical methods now being necessary to determine dispersion curves. However, certain general conclusions regarding the form of the dispersion profile may be deduced from the absorption/gain profile using the Kramers–Kronig relations without knowing the exact gain profile [14]; namely that the dispersion is always zero where the frequency derivative of the gain or absorption is zero and that the dispersion reaches a peak when the gain or absorption is changing fastest with frequency. Since these general relations exist between gain/absorption and dispersion, it is appropriate to represent the absorption and emission spectra of the dye molecule by a reasonable analytic approximation (e.g. Lorentzian) and expect the resulting dispersion curve to show the correct general behaviour. Such an approximation allows the functional dependence of the dye dispersion to be examined with respect to relative populations and DFDL wavelength without recourse to an extensive numerical solution to the Kramers–Kronig relations, but gives only an estimate of the magnitude of such effects.

Using this Lorentzian approximation, the refractive index of a dye solution may be written as the sum of refractive indices

$$n(\nu)=n_s-\frac{c(\nu_e-\nu)N_1\sigma_e(\nu)}{2\pi\nu\Delta\nu_e}+\frac{c(\nu_a-\nu)(N-N_1)\sigma_a(\nu)}{2\pi\nu\Delta\nu_a}, \tag{8}$$

where n_s is the bulk refractive index of the solvent, ν_e is the frequency of the fluorescent-emission peak, $\Delta\nu_e$ is the half-width of fluorescent emission, ν_a is the frequency of maximum absorption, and $\Delta\nu_a$ is the half-width of absorption. The density of dye molecules is N and the population in the upper state S_1 is N_1. The frequency-dependent emission and absorption cross-sections are σ_e and σ_a respectively. These are approximated here by Lorentzian profiles with the above half-widths and appropriate magnitudes (see figure 8). The second term on the right-hand side of (8) represents dispersion due to gain and the third term represents dispersion due to ground-state absorption. Dispersion due to triplet absorption has been ignored because the 10 ns pulse is too short to allow the growth of a significant triplet-state population.

As can be seen from equation (8), the dispersive contributions to the refractive index are dependent on the excited-state population N_1 and also on the frequency of the DFDL radiation.

The mechanism through which the dispersion affects the linewidth of the DFDL is that, during a pumping pulse, the upper-level population N_1 grows from zero to a maximum and then falls back to zero again, while the ground-state population N_0 undergoes a dip during the pulse. As this happens, the refractive index of the medium given by equation (8) undergoes an excursion, the instantaneous refractive index being determined by N_1 and N_0. Any change in the refractive index of the DFDL results in a change in the oscillating wavelength, and so the time-averaged linewidth appears to be broadened.

This incorporation of a dispersive contribution in the DFDL linewidth can explain the dependence of the linewidth on both pump energy and laser wavelength. Firstly, let us consider the behaviour of the linewidth with an increasing level of pumping. Figure 4 shows that when the pump energy is increased from threshold to 50 mJ per pulse, the linewidth initially increases for energies up to 20 mJ and thereafter is constant. The dependence of the ASE on pump power (figure 2) shows a similar turn-over at about 20 mJ. The ASE is a measure of the saturated gain, and so this behaviour suggests that the saturated gain above 20 mJ is independent of pumping energy, i.e. the maximum upper-state population N_1 is independent of pumping energy. Below 20 mJ, the saturated gain (as shown by the ASE behaviour) increases with pumping power, implying that the maximum value of N_1 also increases with increased pumping. Thus, since N_1 behaves in this manner, so must the dispersive component increase with pumping energy up to about 20 mJ and then remain constant. As a result, the laser is expected to sweep during an increasingly shorter fraction of the pulse duration for energies above 20 mJ, i.e. the laser frequency is constant at a frequency corresponding to the saturated gain for an increasingly longer fraction of the pulse. For a time-averaged spectrum, this is interpreted as a decrease in the contribution to the linewidth arising from dispersion. Since thermal effects continue to contribute increasingly with pumping power the two effects now offset one another. The observed independence of linewidth on pump power for pump powers above 20 mJ (see figure 4) is consistent with this behaviour.

Secondly, let us consider the wavelength dependence of the linewidth. Equation (8) is obviously wavelength dependent, and this is more clearly seen in figure 10 which shows the dispersive contribution to the refractive index as a function of relative excitation (N_1/N_0) for various wavelengths. This figure indicates a maximum contribution by dispersion to the time-averaged linewidth at around 600 mm, and this is exactly what is observed (see table 1). Interestingly, around 558 nm the dispersive contribution to the refractive index is zero, i.e. the refractive index is decoupled from (N_1/N_0). This occurs when the dispersive contribution from emission is equal and opposite to that of absorption, the linewidth then being determined only by the three previously mentioned processes. Unfortunately at this wavelength for this dye absorption exceeds emission and so laser oscillation cannot occur.

Thus the dispersive model of line broadening can be used to explain the observed dependence of linewidth on both pump power and operating wavelength. Moreover, as we shall see, it successfully predicts the temporal behaviour of the DFDL wavelength during the course of a pumping pulse.

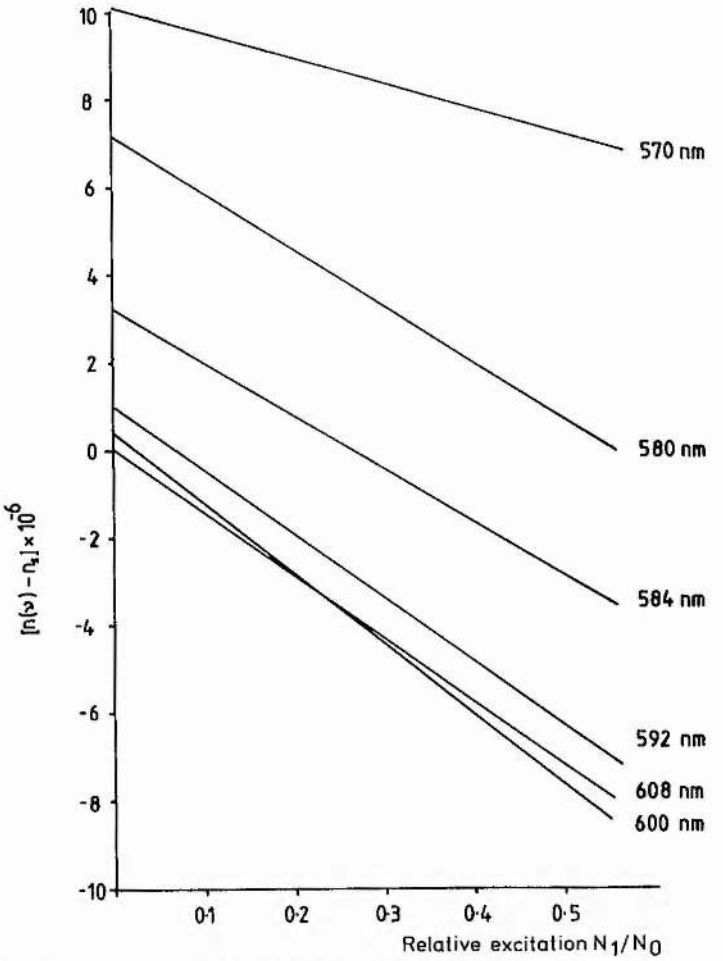

Figure 9. Dispersive contribution to the refractive index calculated using equation (8), for the case where $N=8\times10^{15}$ cm^{-3}. Parameters for rhodamine B are obtained from figure 8 and [19].

4.5. *Transient behaviour of the DFDL wavelength*

In the §§ 4.3 and 4.4 we have proposed that the wavelength of the DFDL changes during the course of the pumping pulse; either because of thermal effects, in which case it monotonically sweeps (i.e. chirps) towards shorter wavelengths with time, or because of dispersion associated with gain, in which case it decreases initially to a minimum value at the peak of the pumping pulse before returning to its original value in the latter half of the pulse. The former effect can be minimized by suitable choice of solvent temperature, while the latter effect depends on the oscillation wavelength, and is greater at 600 nm than at 580 nm. We now describe an experiment to observe this temporal behaviour of the DFDL wavelength.

The radiation from the DFDL was passed through a Fabry–Perot interferometer (FSR = 0·7 cm^{-1}, finesse ~ 30), which could be piezoelectrically scanned. The centre fringe was detected using a 100 μm pin-hole in the focal plane of an imaging lens ($f=20$ cm) followed by a fast rise-time photodiode (rise-time = 100 ps). The response time of the optical detection system was 1·3 ns, limited by the storage oscilloscope used. By altering the voltage on the piezoelectric element, different frequency components of the emitted pulses could be monitored, and their relative times of arrival hence determined. This is more clearly understood by referring to

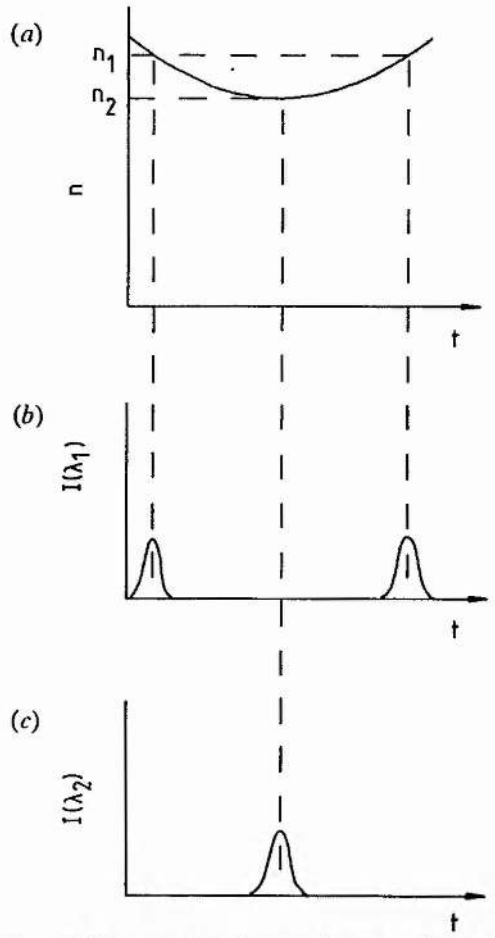

Figure 10. Explanation of time-resolved experiments. The medium refractive index dips during a pulse, (*a*). If the interferometer is set to detect radiation at a wavelength λ_1 (corresponding to $n=n_1$), then two pulses are observed, (*b*). If the interferometer is tuned to detect a wavelength corresponding to the peak of the excursion in refractive index ($n=n_2$), only one pulse is detected, (*c*).

figure 10 in which a schematic diagram of the expected temporal behaviour of the wavelength arising from gain-related dispersion is shown. Detection of radiation at longer wavelengths is expected to demonstrate the double-pulsing behaviour, whereas the shortest wavelength emitted is expected to produce only a single pulse.

To be able to monitor temporal behaviour within a pulse, the pump laser was run on a single longitudinal mode (reducing the maximum energy to 1·5 mJ per pulse at 532 nm) thus ensuring that successive pulses from the DFDL had the same smooth Gaussian-like temporal profile. A small portion of the pump beam was used to trigger the oscilloscope at the same point in successive pulses.

It was found, as predicted by the dispersion model, that the behaviour of the DFDL at 590 nm differed from that at 600 nm; see figure 11.

With a cooled dye and the DFDL tuned to 580 nm, it can be seen that the output showed little excursive behaviour, as evidenced by the small double pulse at the longest wavelength that could be monitored. This is to be expected since dispersion effects are less at this wavelength. A residual thermal component caused the slight one-way shift of the pulse with time, shown by the straight line through the peaks. The wavelength sweep at 580 nm was measured to be around 0·025 Å when pumped by 1 mJ.

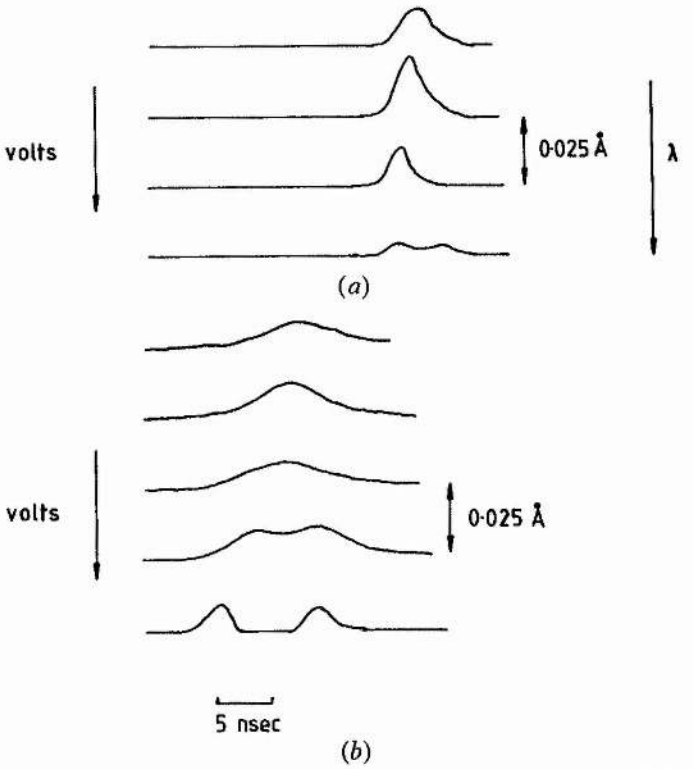

Figure 11. Results from the time-resolved experiments for the DFDL tuned to two wavelengths ((*a*) 580 and (*b*) 600 nm) using a dye solvent cooled to 6°C. The larger voltage offset required to observe the separated peaks at 600 nm indicates greater dispersive broadening at this wavelength.

At 600 nm the behaviour of the DFDL was markedly different from that at 580 nm. The residual thermal component was still present, but this time the wavelength excursions arising from gain dispersion were larger than before, and led to the clearly resolved peaks at the now-increased longest wavelength emitted. This is a result of the greater dispersion at 600 nm leading to the greater wavelength sweep of about 0·075 Å, also at 1 mJ of pumping.

From equation (4) and the dispersion curves (figure 9), the measured wavelength sweeps suggest a relative excitation in the medium (N_1/N_0), of around 0·1. This is a reasonable value; for example, using standard rate equations, we calculate the relative excitation at threshold (0·1 mJ pumping energy) to be around 0·04, rising to 0·4 (unsaturated) for pumping energy of 1 mJ.

Figure 12 shows the case where the DFDL is operating at 22°C, so that ($\delta n_s/\delta T$) is no longer zero. It shows that the sweep from long to short wavelength throughout the duration of the pumping pulse is larger than that obtained with the cooled solution. The gain-related dispersive excursion is still present. The frequency sweep resulting from the thermal effects is measured to be around 0·1 Å, close to the value of 0·14 Å predicted using equation (6) for the case of a 1·5 mJ pumping pulse.

It is interesting to compare the observed sweeps in frequency with the 'unsaturated' linewidth predicted by the threshold analysis of Kogelnik and Shank [1], where the linewidth is assumed to be that width from the selected wavelength over which the distributed feedback coupling falls by a factor of two. It is hence given by

$$\Delta\lambda/\lambda = a/\kappa, \tag{9}$$

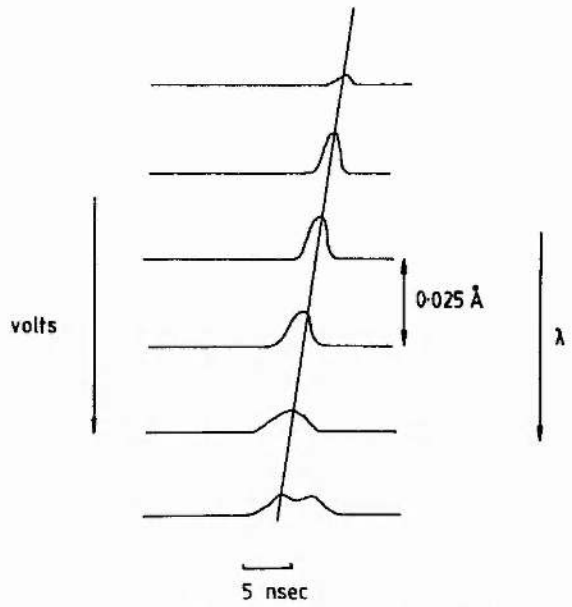

Figure 12. Time-resolved spectrum for a room-temperature dye solution (22°C) with the DFDL tuned to 580 nm. The larger unidirectional sweep observed arises from enhancement of the thermal decrease in refractive index at this temperature.

where a is the gain per unit length in the medium and κ is the propagation constant. For operation at around 600 nm and a threshold gain of about 1 cm^{-1} [1], (9) predicts a linewidth of order 0·04 Å. This analysis of course does not predict the dynamic sweeping reported above.

5. Development of a transform-limited DFDL

Four processes have been identified which contribute to the linewidth of the DFDL (see §4). By minimizing each of these in turn, we have developed a DFDL which has a linewidth approaching the transform limit; we now discuss the procedures for doing this. Pump-laser linewidth (effect 1) is reduced to a minimum by using a single longitudinal-mode pump laser. Divergence (effect 2) is kept to a minimum by producing a beam-waist incident at the dye cell. Changes in the refractive index during the course of the output have been shown to limit the minimum linewidth achievable, although the thermal effect (effect 3) can be removed by using a low $\delta n_s/\delta T$ solvent, ideally water cooled to 4°C. The frequency-dependent dispersion (effect 4) is always non-zero over the tuning range of rhodamine B (see §4.4). This is due to the relatively small Stoke's shift of 22 nm for rhodamine B. However laser-dye DCM has a large Stoke's shift of 163 nm and thus one can operate the laser far removed from absorption dispersion. Under these conditions, dispersion is zero at gain centre. Although DCM is not water-soluble we have been able to produce a low $\delta n_s/\delta T$ solvent using a solvent mix which contains 85% water, 7·5% propylene carbonate and 7·5% ammonyx LO†. Mixtures of solvents have been shown [16] to inherit the refractive-index properties (n, $\delta n_s/\delta T$) from their parent solvents in proportion to the quantity, by volume, of each in the mix. Since the solvent mixture is mostly water it has a relatively low $\delta n_s/\delta T$ in comparison to the organic solvents, such as propylene carbonate, with which DCM is normally used. Since there is some residual $\delta n_s/\delta T$, and for frequencies other than line centre there is gain

† Ammonyx LO is a proprietary surfactant obtainable from Croda Surfactants Ltd, Goole.

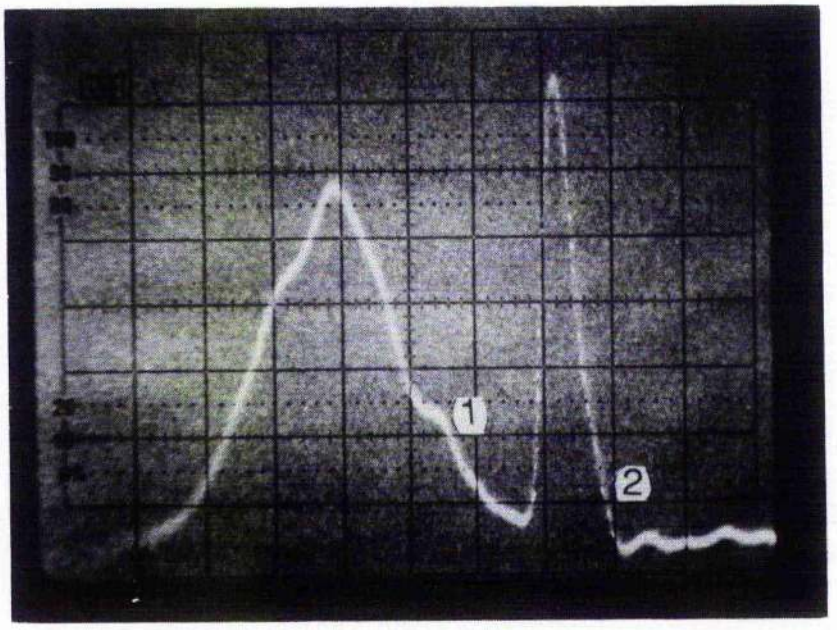

Figure 13. Temporal form of (1) Nd:YAG pulse and (2) DFDL pulse. One division represents 5 ns. DFDL pulse is shorter than the pump pulse since the DFDL is operating close to threshold.

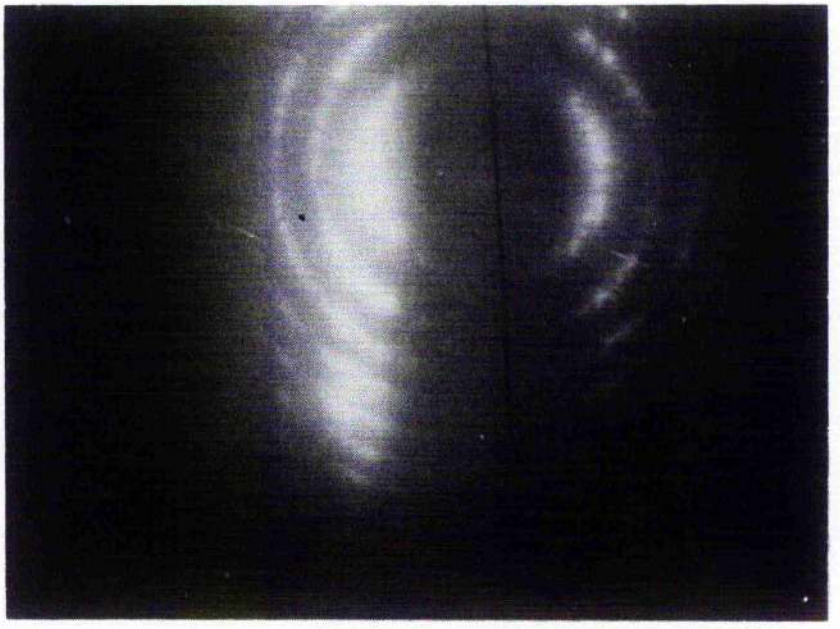

Figure 14. Interferogram of the pulse shown on figure 13. FSR of the interferometer is 1·5 GHz. Blooming, corresponding to saturation of the CCD sensor can be seen on the upper left-hand side of the photograph.

dispersion, the intensity of the pump laser was reduced from 1·5 to 0·5 mJ. Using DCM we have obtained narrow linewidth (i.e. sub-GHz operation, $<0{\cdot}014$ Å) over the tuning range of the dye (612–687 nm). The linewidth measurements were obtained using a non-degenerate confocal interferometer [15] with FSR = 1·5 GHz. Fringes from the interferometer were projected onto a CCD camera. Figure 13 shows the temporal profile of the 3·2 ns pulse and figure 14 is the corresponding

interferogram obtained from the CCD camera with the laser operating around line centre (650 nm). For a Gaussian pulse profile the transform-limited time bandwidth product is $\Delta\nu\Delta\tau = 0{\cdot}441$. Thus for $\Delta\tau = 3{\cdot}2$ ns, the transform limit $\Delta\nu$ is 140 MHz. As can be seen from figure 14 the linewidth is at or near the transform limit. These linewidths compare well with those from recently reported conventional narrow-linewidth dye lasers [17, 18], and, to our knowledge, are the narrowest linewidths yet reported for DFDLs.

6. Conclusions

We have shown that the linewidth of a distributed feedback dye laser where the grating is produced through interference between pump beams, is mainly determined by refractive-index changes associated with the dye laser medium itself. These may either be of a thermal character, when they can be minimized by judicious choice of dye solvent, or are associated with changes in the saturated gain of the dye through the course of the pumping pulse. These conclusions are broadly in keeping with earlier suggestions of Bor [5] regarding linewidths of distributed feedback dye lasers, although the experimental evidence of frequency shifting during the course of the pumping pulse was not advanced.

Using rhodamine B, the minimum linewidth obtained with the distributed feedback dye laser operating under reproducible conditions from pulse to pulse was 0·15 Å at 580 nm using a cooled water-based dye solution and pumping with 1·5 mJ. Using DCM, dispersive changes in refractive index may be reduced to a minimum and have allowed narrow-linewidth operation around the 140 MHz level. Relaxation of any of the above conditions will tend to increase the linewidth. For such circumstances we have previously reported how the application of frequency selective feedback, employing a mirror and etalon, may be used to reduce the linewidth of the emitted radiation from a DFDL laser by a factor of up to twenty [18].

The dispersive process limiting the DFDL linewidth is not restricted to this type of laser alone; any pulsed dye laser is subject to an inversion-dependent dispersion which produces mode pulling and pushing. The problem for conventional lasers is not as severe as in the DFDL, where the 'cavity' and active lengths are the same, because now the active medium forms only a small fraction of the cavity length (typically about 1/20th in a Hansch or grazing-incidence design), and so dispersion sweeps in mode frequency are proportionately reduced.

Even in the case of a single-mode pulsed dye laser with an active medium filling 1/20th of the cavity length and pumped by 1 mJ, it can be calculated, as above, that the mode pulling and pushing would only amount to about 50 MHz, approximately the transform limit for a 10 ns pulse. So dispersive effects may not limit the operation of a conventional pulsed dye laser pumped close to threshold. They may, however, contribute to the linewidths of a more strongly pumped system, and to our knowledge this has not been considered previously.

Acknowledgments

The investigation was supported by a Science and Engineering Research Council grant, and we are grateful to Barr and Stroud plc, Glasgow for support for one of us (I.A.M) through the CASE Scheme, and to the Department of Education, Northern Ireland for grant support of M. E. Lusty.

References

[1] KOGELNIK, H., and SHANK, C. V., 1972, *J. appl. Phys.*, **43**, 2327–2335.
[2] SHANK, C. V., BJORKHOLM, J. E., and KOGELNIK, H., 1971, *Appl. Phys. Lett.*, **18**, 395–396.
[3] BAKOS, J. S., FÜZESSY, Z., SORLEI, Zs., and SZIGETI, J., 1974, *Phys. Lett.* A, **50**, 227–228.
[4] CHANDRA, S., TAKEUCHI, N., and HARTMANN, S. R., 1972, *Appl. Phys. Lett.*, **21**, 144–146.
[5] BOR, ZS, RACZ, B., KOZMA, L., RUBINOV, A. N., and EFENDIEV, T. SH., 1978, *Optics Commun.*, **24**, 265–267.
[6] BAKOS, J. S., and SORLEI, ZS., 1977, *Optics Commun.*, **22**, 258–260.
[7] VASHCHUK, V. I., GOROT, K. F., MALYKHINA, N. N., and TIKHONOV, E. A., 1979, *Soviet Jl. quant. Electron.*, **9**, 626–28.
[8] BERRY, A., HANNA, D., and SAWYERS, C., 1981, *Optics Commun.*, **40**, 54–58.
[9] PARK, I., and BYER, R., 1981, *Optics Commun.*, **37**, 411–416.
[10] BOR, ZS, 1980, *IEEE Jl. quant. Electron.*, **16**, 517–24.
[11] MCINTYRE, I. A., and DUNN, M. H., 1984, *J. Phys. E.*, **17**, 274–6.
[12] MCINTYRE, I. A., and DUNN, M. H., 1985, *J. Phys. E.*, **18**, 19–20.
[13] LUSTY, M. E., and DUNN, M. H., 1987, *Appl. Phys.* B, **44**, 193.
[14] LOUDON, R., 1973, *The Quantum Theory of Light* (Oxford University Press).
[15] HERCHER, M., 1968, *Appl. Optics*, **7**, 951–966.
[16] LITTMAN, M., 1984, *Appl. Optics*, **23**, 4465–4468.
[17] BOLLEN, G., KLUGE, H.-J., and WALLMEROTH, K., 1987, *J. opt. Soc. Am. B*, **4**, 329–336.
[18] MCINTYRE, I. A., and DUNN, M. H., 1985, *Optics Commun.*, **55**, 45–48.
[19] PETERSON, O. G., WEBB, J. P., MCCOLGIN, W. C., and EBERLY, J. H., 1971, *J. appl. Phys.*, **42**, 1917–28.

Appl. Phys. B 44, 193–198 (1987)

Applied Physics B Photophysics and Laser Chemistry

Refractive Indices and Thermo-Optical Properties of Dye Laser Solvents

M. E. Lusty and M. H. Dunn

University of St. Andrews, Department of Physics, St. Andrews, Fife, KY16 9SS, U.K.

Received April 1987/Accepted 9 June 1987

Abstract. By measuring the wavelength tuning of a distributed feedback dye laser, solvent refractive-index changes as small as 0.0002 may be determined. This technique hence allows precise measurement of refractive-index dependence on temperature (dn/dT) and therefore enables the thermo-optical properties of solvents used in dye lasers to be assessed. In addition to single component solvents, the thermo-optical properties of solvent mixtures and additives are reported here. The refractive-index change with temperature (dn/dT) is related to solvent density change with temperature ($d\varrho/dT$) through molecular polarizability.

PACS: 42.55.Mx, 42.65.Jx.

A major limitation on achieving high-power, spectrally narrow and spatially coherent radiation from dye lasers lies in the formation of refractive-index gradients due to non-uniform heating by the pump radiation in the region of optical gain. Pump radiation is converted into heat in the dye solution by two processes; radiationless deactivation of molecules in excited states, the proportion of which determines the dyes fluorescence efficiency, and through the Stokes shift since the emitted photons are less energetic than the absorbed photons. Typically about 25% of incident light is converted into heat, within a confined area. In high-power cw and pulsed dye lasers the formation of such refractive-index gradients acts as a thermal lens with severe consequences for output power [1], cavity stability [2], spatial coherence [3], and minimum linewidth obtainable [4]. Further, the effect has been shown to be a major limiting factor in narrow linewidth operation of distributed feedback dye lasers (DFDL) [5]. The quantity dn/dT, the rate at which solvent refractive-index changes with temperature, is a most useful parameter in assessing a solvent thermo-optically. Accurate values of dn/dT for a wide range of dye laser solvents, solvent mixtures and solvents with additives are reported here for the first time.

1. Experimental Method

The DFDL, originally reported by Shank (1971), is a simple device for producing tunable dye laser radiation. The two pump beams, obtained from the sam laser, are caused to intersect in the cell containing t dye solution. An interference pattern is produc along the axis of the dye cell, the period of which dependent only on the free-space wavelength of t pump laser, λ_p, and the angle of intersection, θ. Th interference causes Bragg backscattering of radiati with a wavelength in the solvent equal to twice t grating period, thus providing frequency selecti feedback. As a result the free-space wavelength which the dye laser oscillates is given by

$$\lambda_d = \frac{n\lambda_p}{\sin\theta}, \qquad (1)$$

where n is the solvent refractive index at waveleng λ_d. As can be seen from (1), this wavelength can tuned by altering n, λ_p, and θ. The pump laser used w a frequency-doubled Nd:YAG laser (Quantel YG48 which was slow Q-switched to produce narro linewidth (single longitudinal mode) pulses of durati 12 ns and energy 1 mJ at a wavelength of $\lambda_p = 532$ n In order to determine dn/dT for a solvent the change lasing wavelength λ_d was measured, using a hig resolution monochromator (Rank Hilger Monosp 1000) giving resolution down to 0.01 nm, as the d solvent temperature was changed by using a r frigerator unit in the circulator system. Equation (was then used to deduce the associated change refractive index. The DFDL wavelength was normal

around 600 nm. DFDL linewidth, and shot to shot fluctuation of DFDL wavelength were less than the resolution limit set by the monochromator. This technique was first demonstrated by McIntyre and Dunn [6]. In the tables of results to follow, where a numerical value of dn/dT is quoted for a particular temperature this represents a least squares fit over the range $\pm 2\,^{\circ}C$ around that temperature. Since n is recorded every 0.5 °C each fit utilizes nine data points. Errors quoted in brackets are the standard deviation of the fit to the data. Values of dn/dT are quoted for 20 and 5 °C representing room-temperature and cooled dye-laser operation, respectively.

2. Background

The Lorentz-Lorenz formula [7] relates the mean polarizability α to the refractive index n and the number of molecules per unit volume N by

$$\alpha = \frac{3}{4\pi N}\frac{n^2-1}{n^2+2}. \tag{2}$$

Using the molar refractivity A, which is essentially the total polarizability of a mole, (2) may be written as

$$\frac{n^2-1}{n^2+2} = \frac{A}{W}\varrho, \tag{3}$$

where W is the molecular weight, and ϱ the density. For a mixture of liquids, the refractive index of the mixture is given by

$$\frac{n_m^2-1}{n_m^2+2} = \left(\frac{A_1}{W_1}f_1 + \frac{A_2}{W_2}f_2\right)\varrho_m = \left[\frac{A}{W}\right]_m \varrho_m, \tag{4}$$

where n_m and ϱ_m represent the refractive index and density, respectively, of the mixture. A_1, A_2 and W_1, W_2 represent the molar refractivities and molecular weights of molecules type 1 and 2. f_1 and f_2 are the fractions, by mass, of molecules of type 1 and 2. Refractive index and density are functions of temperature (T), but molar refractivity is expected to be independent of temperature, so that we have

$$\frac{n_m^2(T)-1}{n_m^2(T)+2} = \left[\frac{A}{W}\right]_m \varrho_m(T). \tag{5}$$

Hence assuming that the refractivity of a liquid is constant, dn/dT may be estimated from the density, refractive index and $d\varrho/dT$, by differentiating (5) with respect to temperature to find

$$\frac{dn_m}{dT} = \left[\frac{A}{W}\right]_m \frac{(n_m^2+2)^2}{6n_m}\frac{d\varrho_m}{dT}. \tag{6}$$

However, since

$$\left[\frac{A}{W}\right]_m = \frac{1}{\varrho_m}\frac{n_m^2-1}{n_m^2+2},$$

(6) may be expressed in terms of the macroscop properties of density and refractive index.

3. Results

Solvents for dissolving organic dyes may be divid into three main categories: a) Simple organic solven e.g., methanol, ethanol, ethylene glycol, and mixtu of them; b) Water based solvents, e.g., pure water water based solutions such as ammonyx LO. Using and b) together yields a third class of dye laser solve i.e., c) Mixtures of water based solvents and orga solvents, e.g., ethylene glycol/ammonyx LO. The ne for this class of solvent, as will become appare shortly, is to combine good solubility of the laser d with good thermo-optical characteristics.

3.1. Organic Solvents

The most commonly used dye-laser solvents are co tained in this class, e.g., methanol, ethanol, ethyle glycol, benzyl alcohol and propylene carbona Figure 1 shows the variation of refractive index w temperature for ethylene glycol and methanol whi are typical of this group. Since the dn/dT's of the organic solvents are, to within 10% independent temperature, results are quoted as a straight line over the temperature range of 5–25 °C. Results of the organic solvents we measured are found listed Table 1, and show that the dn/dT's of these orga solvents are much higher than that of water. The liquids, unlike water, have a normal density/tempe ture behaviour, i.e., their density decreases linearly,

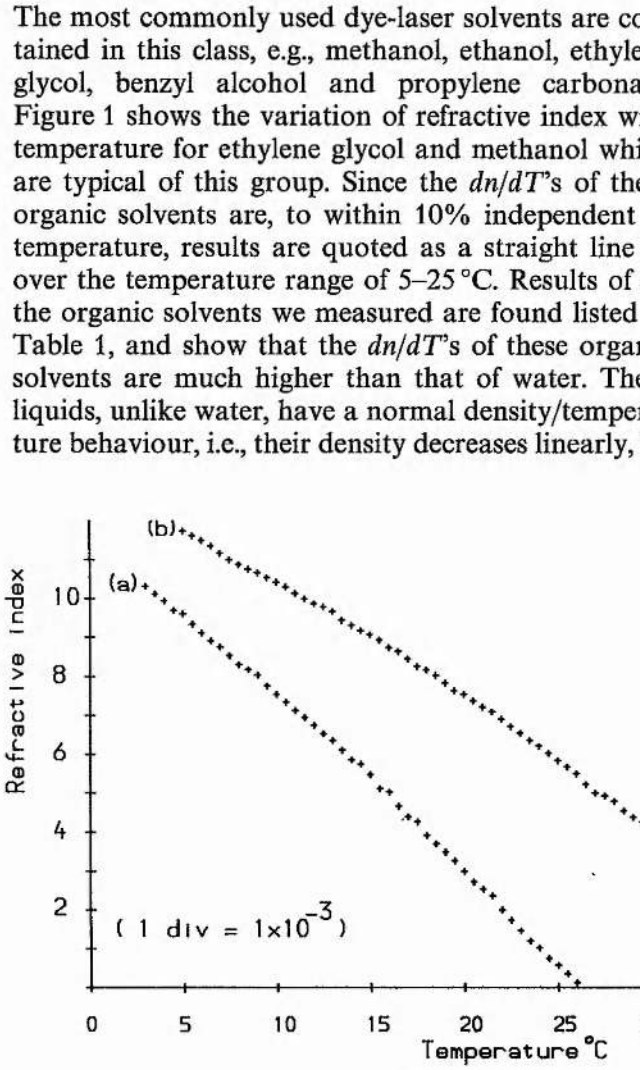

Fig. 1. Refractive index against temperature of *a* methanol, an ethylene glycol. Vertical axis divisions correspond to a change refractive index of 1×10^{-3} Methanol had the largest dn/dT any of the solvents measured

Table 1. Measured values of dn/dT (over range 5–25 °C) for organic solvents. For convenience refractive index data for the individual solvents is given in brackets, and is taken from CRC [8] tabulated values

Solvent	n(20 °C)	dn/dT [$-1 \times 10^{-5}\,K^{-1}$] (5–25 °C)
Methanol	(1.327)	46.8(1.1)
Ethanol	(1.360)	43.8(0.4)
Ethylene glycol	(1.431)	30.6(0.3)
Benzyl alcohol	(1.540)	42.0(0.4)
Propylene carbonate	(1.421)	38.0(0.4)
50/50 BA/PC	(1.471)	42.0(0.5)

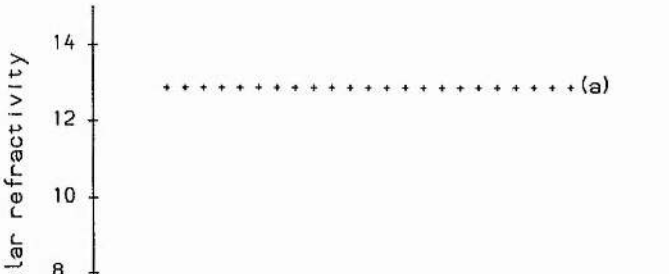

Fig. 2. Molar refractivity against temperature for *a* ethanol, and *b* water. In both cases the refractivity is constant to 1 part in 10^{+4}

expansion, with increasing temperature. In order to verify that the temperature dependence of refractive index is due solely to the temperature dependence of density, as implied by (5), we have plotted in Fig. 2a, A as a function of temperature deduced from our measured values of $n(T)$ and CRC tabulated values of density [8] for ethanol. The constancy of A with temperature verifies this assumption. Its value of 12.9 is close to that expected from the addition of generally accepted atomic refractivities [8], which gives 13.2.

3.2. *Water Based Dyes*

Water-based solvents are generally regarded as superior in their thermo-optical properties since $d\varrho/dT$ and hence from (6) dn/dT is small in comparison with other liquids. Furthermore the density of water increases until 4 °C, the temperature at which the density

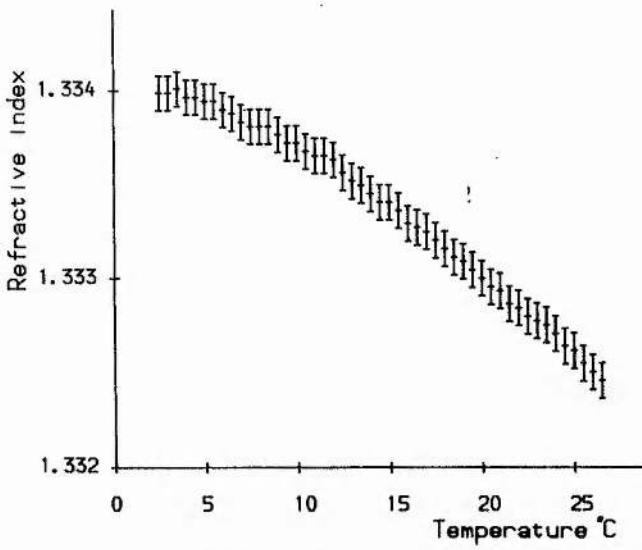

Fig. 3. Refractive index against temperature of pure wa
Vertical axis divisions correspond to a change in refractive in
of 1×10^{-3}. Around 4 °C refractive index is constant i.e. dn/dT

is at a maximum, i.e. $d\varrho/dT$ equals zero. Thus for sm
changes in temperature around 4 °C, dn/dT may
expected to be zero, although there is some dou
about the exact temperature at which this occurs [9]
is this particular property, exhibited only by wat
that makes it the best solvent thermo-optical
Figure 3 shows the measured refractive index vers
temperature profile for water and it can be seen th
around 4 °C there is no detectable change in refract
index with temperature. The molar refractivity A
water is plotted as a function of temperature on Fig.
using our measured values of refractive index and CR
[8] values for density. As is the case of ethanol, t
refractivity is constant, with $A = 3.71$. This compa
very well with the tabulated values of 3.72 [7,
However dye lasers based on aqueous solutions exhi
low efficiencies. This is due to the association of c
molecules to produce dimers, whose absorption sp
tra lie in the absorption region of the lasing monom
and also frequently overlap their fluorescence ba
hence reducing the fluorescence efficiency. In orga
solutions dimerization is slight and hence the efficien
is much improved. It is possible however to suppr
this process of dimerization by the addition of orga
compounds to water [10–13]. This class includes t
two soaps ammonyx LO (lauryl dimethylamine oxi
[10, 11], Triton-X100 [12], and the much simp
compound urea $CO(NH_2)_2$ [13], and indeed in c
DFDL we have observed an increase in efficiency usi
these products. What has been misunderstood ho
ever is their effect on the temperature dependence
refractive index. To this end we have characterized t
effects of the addition of both ammonyx LO and ur

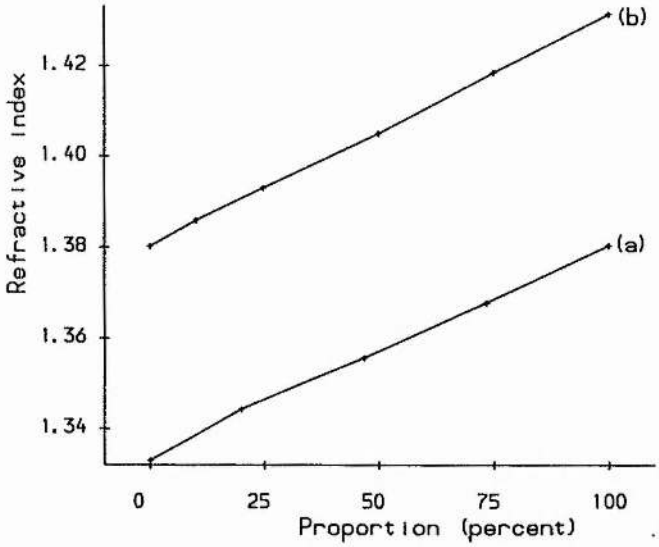

Fig. 4. Refractive indices for *a* water/ammonyx LO series, and *b* ammonyx LO/ethylene glycol series. 0% represents pure water in *a*, and pure ammonyx LO in *b*

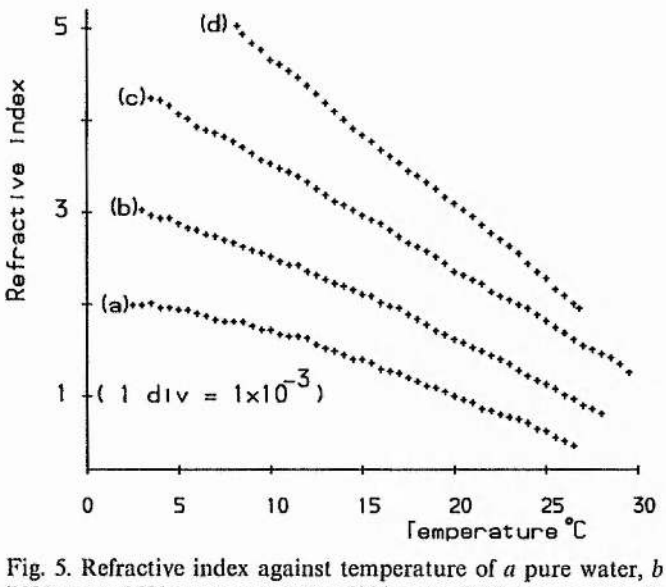

Fig. 5. Refractive index against temperature of *a* pure water, *b* 75% water 25% ammonyx LO, *c* 50% water 50% ammonyx LO, *d* 100% ammonyx LO. Vertical axis divisions correspond to a change in refractive index of 1×10^{-3}. As ammonyx LO is added the dn/dT of the solvent is increased in proportion to the amount added

i) Ammonyx LO/Water Series. The ratio of liquid ammonyx LO [30%, by mass lauryl dimethylamine oxide

$(CH_3(CH_2)_{10}-CH_2-N(CH_3)_2 \rightarrow O)$,

70% water] to water was varied in this experiment from 0 to 100% by volume and two features of refractive index measured, namely: a) bulk index (the refractive index at 20 °C) for different proportions of ammonyx LO and water; and b) temperature de-

Table 2. Measured refractive index n versus temperature for ammonyx LO

Temperature [°C]	Refractive index
26.0	1.3793
24.0	1.3796
22.0	1.3800
20.0	1.3803
18.0	1.3806
16.0	1.3809
14.0	1.3812
12.0	1.3816
10.0	1.3819
8.2	1.3822

Table 3. Measured molar refractivity for mixtures of water a ammonyx LO

Substance	Mol.-wt.	Refractive index	Density [g/cc]	A from (
Water	18.0	1.333	0.98	3.71
Ammonyx LO	24.9	1.380	0.96	6.00
Lauryl amine oxide	229.0	–	–	74.10

pendence of refractive index dn/dT for particul mixes. Results to part (a) are given in Fig. 4a. The show that the measured bulk index is equal to the rat by volume of ammonyx LO times its refractive ind ($n(20\,°C)=1.380$) plus the ratio by volume of wat times its refractive index ($n(20\,°C)=1.333$), as is to anticipated on the basis of simple proportionalit Note that we were unable to cool the solution to le than 8.2 °C due to its high viscosity. Results to part (are given in Fig. 3, for pure water, and Fig. 5 f varying proportions of ammonyx LO. Since ammony LO is a commonly used solvent the refractive index temperature relation is listed more fully in Table The effect of the addition of lauryl dimethylamin oxide to water may be explained using (4). To dete mine the molar refractivity of the ammonyx LO acti ingredient (lauryl dimethylamine oxide) Eq. (4) solved using the following values: $n_m=1.380$, W $=18$ g, $W_2=229$ g, $f_1=0.7$, $f_2=0.3$, $\varrho_m=0.96$ g cc and $A_1=3.71$ to give A_2, the molar refractivity of t lauryl dimethylamine oxide molecule, as 74.1. This la figure may be checked by the usual procedure of t addition of the refractivities of the constituent aton [7, 8], which gives $A=72.63$, in good agreement wi our experimentally obtained value. Results are show fully in Table 3. The molar refractivity A versu temperature was obtained using refractive index an

density values which were experimentally obtained as a function of temperature for the mixture of 1:1 by volume of ammonyx LO: water. The density/-temperature measurement for this mix showed that $d\varrho/dT$ was always non zero. As was observed previously with ethanol and water, the molar refractivity of the mixture was independent of temperature, to greater than 1 part in 10^{+4} showing that the refractive-index behaviour is due solely to the change in the density with temperature, the addition of ammonyx LO acting to suppress the agglomeration of water molecules which normally leads to a density minimum. Since the dn/dT of pure ammonyx LO is similar to that of a normal liquid (Fig. 5d), i.e. no flat portion in dn/dT, the addition of ammonyx LO will degrade the thermal properties of water in proportion to the amount added. On the basis of these results, the commonly used proportions of 1.5 to 4% ammonyx LO [11, 14] produce only a slight degradation in the thermal properties.

The use of ammonyx LO at much higher concentrations has been reported, e.g. 18% [15] or 20% [16] have been used, and indeed 100% ammonyx LO [1] has been proposed as solvents with claimed good thermal properties for use in high-power dye lasers. However, as can be seen from Fig. 5, at these concentrations there is a significant increase in the dn/dT compared with water with consequent degradation of thermal properties.

ii) Water/Urea Series. Viktorova et al. [13] reported an observed increase in fluorescence efficiency from ~0.4 in water to ~0.7 on addition of 40% by mass of urea, while still retaining the good thermo-optical properties of water. Figure 6 shows the measured effect on dn/dT of the addition of 10% and 30% urea, compared with pure water. As can been seen from Fig. 6 the effect of adding 30% urea to water is substantial. This mixture has a dn/dT approaching that of organic solvents, hence rendering it poor thermo-optically. An empirical expression for the refractive index of the solution is;

$$n_m = n_{\text{water}} + \beta P, \tag{7}$$

where P is the proportion by weight of urea, and β, which is a function of temperature is given by

$$\beta = 0.1308 - (5.084 \times 10^{-4}\, T)$$

for the range 0–30 °C, where T is the temperature in °C. While no density/temperature measurements were made for the water plus urea solution we strongly suspect that the effect is similar to the addition of ammonyx LO to water as described in the previous subsection.

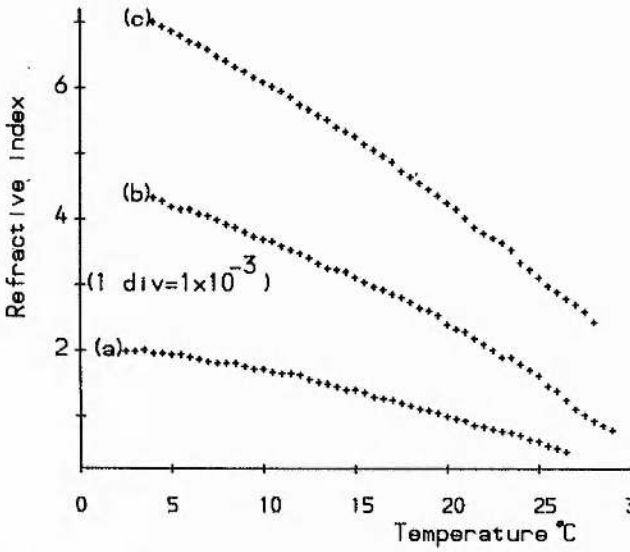

Fig. 6. Refractive index against temperature of *a* pure wate water with 10%, by mass, urea, and *c* water with 30%, by m urea. Vertical axis divisions correspond to a change in refract index of 1×10^{-3}

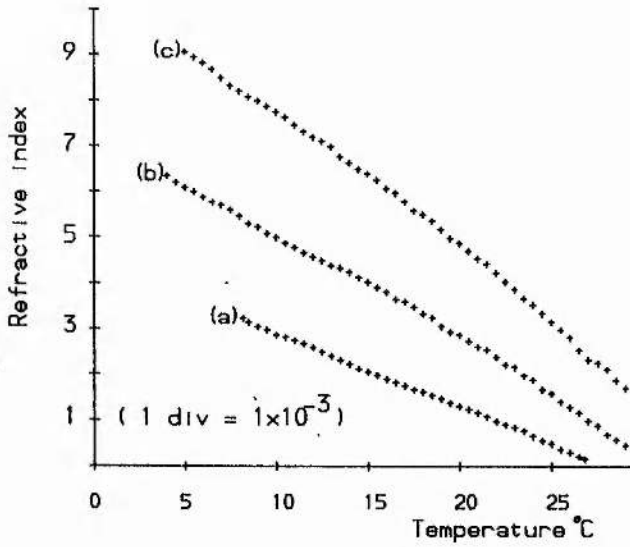

Fig. 7. Refractive index against temperature of *a* ammonyx LO 75% ammonyx LO 25% ethylene glycol, and *c* 100% ethyl glycol. Vertical axis divisions correspond to a change in refract index of 1×10^{-3}. As expected the mixtures of these two solve have index properties (n, dn/dT) inherited from the par solvents

3.3. Solvent Mixtures

In this class are mixtures of water based solver mixtures of organic solvents, or mixtures of wa based and organic solvents. In Sect. 3.1 the solve benzyl alcohol and propylene carbonate were co bined in equal proportions to observe the result dn/dT. This experiment shows that, to a good app ximation, the index properties (n, dn/dT) of mixtu are given by an average of the index properties of

parent solvents weighted in proportion to their percentages in the mixture. It has been claimed [1] that by adding 25% ethylene glycol to an ammonyx LO solution that the desired flat spot in the dn/dT of water may be preserved, although shifted to higher temperatures (10 °C). However, since we had observed a non-zero dn/dT in ammonyx LO, and a larger dn/dT in ethylene glycol we did not expect a zero dn/dT for any combination of ammonyx LO/ethylene glycol. The results of this experiment are shown on Fig. 4b for the bulk indices (20 °C) and Fig. 7 for dn/dT's, and as with other solvent mixtures, show that the bulk index and the dn/dT for a particular solvent mix is simply inherited from the parent solvents in proportion to their percentages in the mixture. This combined with the evidence of the water/ammonyx LO series allows us to conclude that the effect of mixing two or more liquids is simply to add proportionally their bulk indices and dn/dT's.

4. Conclusion

We have measured, using the technique first described by McIntyre and Dunn [6], the refractive indices of most commonly used dye laser solvents. The results of these measurements are tabulated in Tables 1 and 2. From these it can be seen that dn/dT is smaller for water than for organic solvents, and furthermore that dyes dissolved in water which is cooled to 4 °C represents the best obtainable solvent, since dn/dT is zero at this temperature, in terms of thermo-optical properties. It has been recognized [10] that organic additives generally improve the quantum efficiency of dyes dissolved in water. The effect of these additives on dn/dT and hence the thermo-optical properties is reported here for the first time and, contrary to previous claims, it is found that an additive superimposes an additional dn/dT on that of water. For liquid mixtures the resultant dn/dT is simply the proportional average of the parent dn/dT's. For the temperature range of interest the molecular polarizability of liquid molecules is seen to be constant hen indicating that the changes in refractive indices r ported are derived from density change with temper ture. Thus if density/temperature measurements a available, dn/dT, and hence the thermo-optical suit bility, may be inferred. Since water is unique in $d\varrho/dT=0$ at around 4 °C it still remains the be solvent thermo-optically, despite attempts to engine superior ones.

Acknowledgements. This work was supported by SERC (UI Michael Lusty gratefully acknowledges financial support fr the Department of Education, Northern Ireland.

References

1. T.F. Johnston, Jr., R.H. Brady, W. Proffitt: Appl. Opt. 2307–2316 (1982)
2. B. Wellegehausen, L. Laepple, H. Welling: Appl. Phys. 335–340 (1975)
3. R.B. Andreev, S.S. Galidov, A.G. Kalintsev, D.I. Staselo, V Strigin: Opt. Spektrosk. (USSR) **54**, 206–209 (1983)
4. H.W. Schroder, H. Welling, B. Wellegehausen: Appl. Phys. 343–348 (1973)
5. I.A. McIntyre, M.H. Dunn: CLEO (1984), Anaheim US Digest, FW2, P264
6. I.A. McIntyre, M.H. Dunn: J. Phys. E **18**, 19–20 (1985)
7. M. Born, E. Wolf: *Principles of Optics* (Pergamon, Lond 1959) pp. 86–87
8. *CRC Handbook of Chemistry and Physics* 57th ed. (19 p. E209, F3
9. L.A. Lee, R.A. Robb: IEEE J, QE-**16**, 777–784 (1980)
10. P. Schafer (ed.): *Dye Lasers*, Topics Appl. Phys. **1** (Spring Berlin, Heidelberg 1973)
11. R.R. Alfano, S.L. Sharpiro, W. Yu: Opt. Commun. **7**, 191–1 (1975)
12. O.G. Peterson, S.A. Tuccio, B.B. Snavely: Appl. Phys. Le **17**, 245–247 (1970)
13. A.A. Viktorova, A. Savikin, V.B. Tsaregaradskii: Sov. Quant. Electron. **13**, 1140–1142 (1983)
14. J.Y. Allain: Appl. Opt. **18**, 287–289 (1979)
15. P. Anliker, H.R. Luthi, W. Seelig, J. Steiner, H. Weber, Leutwyler, E. Schumacher, L. Woste: IEEE J. QE- 547–548 (1977)
16. F. Bos: Appl. Opt. **20**, 1886–1890 (1981)

Responsible for Advertisements: E. Lückermann, G. Probst, Heidelberger Platz 3, D-1000 Berlin 33, Tel. (030) 8207-0, Telex 01-85411
Responsible for the Text: H. K. V. Lotsch, Tiergartenstrasse 17, D-6900 Heidelberg. Printers: Brühlsche Universitätsdruckerei, Giessen

Springer-Verlag GmbH & Co. KG, D-1000 Berlin 33

Appendix 3: Computer aided interferometer - Software description

The computer program used in the CAIN system is described and listed in thi appendix.

The program presented is written in a combination of BBC BASIC and machine cod and was run on an Acorn Archimedes computer. The function of the program was t control the operation of the framestore and to obtain results from the CAIN apparatus When used in conjunction with the CAIN system the program sampled the framestor which contained the relevant information from the interference fringes produced by th interferometer i.e. the linewidth of the laser was obtained from the intensity of the fringe as a function of position. The computer program then allowed the used to sample and plo sections of the stored picture (such as was used in the five line scan). A more advance algorithm was employed to exploit the elliptical symmetry of the fringes produced henc allowing the averaging of the majority of the fringe pattern produced (hence increasing th signal to noise ratio of the signal obtained). The program is menu driven via the 1 function keys provided on the machine. Each function key activates a task which normall comprises of one or more procedures. These tasks are summarized in tabular form wher each is described together with a list of the appropriate procedures used.

A listing of the computer program used is given at the end of the appendix.

Function key	Task description	Associated procedures
F1	Resets framestore to capture next triggered frame (trigger normally obtained from Nd:YAG laser)	———
F2	Samples current stored frame	SETRD,RESET, SCALE FS to CPU, LINE, code% UNBLANK
F3	Draws intensity/position of current picture	INTDRAW, RDRAW
F4	Draws histogram of the frequency of occurrence of intensity for current picture (to help obtain maximum dynamic range of camera/framestore)	STATS
F5	Saves the current picture to floppy disk (requires 160 kB memory)	FILESAVE
F6	Loads a picture from disk and displays on screen	FILELOAD
F7	Positions and samples intensity/position from 5 adjacent lines on screen	LSCAN, INVERT, SAMPLE, DISPLAY, UNINVERT
F8	Converts current colour picture to 16 level black and white picture with linear grey scale	GREY
F9	Displays ellipse on screen in order to allow user to find centre and equation of elliptical fringes produced by CAIN	ECONST, EDRAW
F10	Similar to F3 (except for expansion of y axis)	DISPLAY2,DISPLAY
F11	Activates elliptical averaging routine	SCREEN
F12	Activates screen–dump of current screen	———

An understanding into the operating sequence is probably best described by considering two examples. In the first a single frame of video is captured, read into the computer, and a simple scan of intensity verses position of a segment of the picture is displayed and then printed on an Epson printer. In the second example the procedure for obtaining an elliptical scan is described.

Example 1 – Steps to obtain a 5 line average

i) Reset framestore (F1)

ii) Sample picture (F2)

iii) Perform linescan (F7)

iv) Display linescan result (F3 or F10)

v) Screen dump of result (F12)

vi) Reset framestore (F1)

Example 2 – Steps to obtain an elliptical average of intensity/position

i) Reset framestore (F1)

ii) Sample picture (F2)

iii) Convert to black and white picture (F8)

iv) Position ellipse to obtain ellipse equation (F9)

v) Resample picture (F2)

vi) Execute elliptical averaging

vii) Display elliptical scan results (F3 of F10)

viii) Screen dump of result (F12)

ix) Sample picture (F20

x) Save picture to disk (F5)

xi) Reset framestore (F1)

```
>LIST
    2 REM Computer Aided Interferometer Algorithm
    4 REM
    6 REM                          MICHAEL LUSTY + JAMES WADE
   10 ON ERROR PRINT TAB(0,0)"ERROR       RETYPE":GOTO 130
   20 MODE15:COLOUR 3
   30 DIM L%(511):start%=&1FD8000:finish%=&1FFFFFF:B%=4:O%=0
   40 CP%=&FF:R%=0:CK%=1:LS%=2:FSEL%=4:FS%=8:BLNK%=&20:WR%=&80
   50 PROCSETRD:PROCRESET:PROCUNBLANK
   60 DIM code%2000
   70 PROCassemble
   80 CLS:VDU28,65,31,75,0:CLS
   90 CALL scale
  100 LINE 1028,0,1028,1024:LINE1236,0,1236,1024:LINE1278,0,1278,1024
  110 REM Main programe loop START
  120 PRINT TAB(0,0) " READY     "
  130 IF INKEY(-114)=TRUE:SYS 6,147,&F1,&EF:WAIT:WAIT:SYS 6,147,&F1,&FF
  140 IF INKEY(-115)=TRUE:PROCSETRD:PROCRESET:CALL scale:CALL FStoCPU:
PROCLINE:PROCUNBLANK
  150 IF INKEY(-116)=TRUE:PROCINTDRAW
  160 IF INKEY(-21)=TRUE:PROCSTSTS
  170 IF INKEY(-117)=TRUE:PROCfilesave
  180 IF INKEY(-118)=TRUE:PROCfileload
  190 IF INKEY(-23)=TRUE:PROCLSCAN
  200 IF INKEY(-119)=TRUE:CALL GREY
  210 IF INKEY(-120)=TRUE:PROCECONST
  220 IF INKEY(-31)=TRUE:PROCDISPLAY2
  230 IF INKEY(-29)=TRUE:PROCSCREEN
  240 IF INKEY(-30)=TRUE: *HARDCOPYRX
  250 IF INKEY(-113)=TRUE:END
  251 *FX15
  260 GOTO 130:REM Main program loop END
  270 CLS:MOVE1024,0:DRAW1024,1024:MOVE1278,0:DRAW1278,1024:MOVE1236,0:
DRAW1236,1024
  280PROCSETRD:PROCRESET
  290 CALL code%
  300 PROCLINE:PROCUNBLANK
  310 REM*SAVE"PictureW/S" 1FD8000 1FFFFFF
  320 CALL GREY
  330 END
  331
  340 DEFPROCSETRD
  350  CP%=&FF-BLNK%:SYS "OS_Byte",147,&F1,CP%
  360  time%=TIME:REPEAT UNTIL TIME>time%+25
  370 ENDPROC
  371
  380 DEFPROCSETWR
  390  CP%=&FF-BLNK%-WR%:SYS "OS_Byte",147,&F1,CP%
  400  time%=TIME:REPEAT UNTIL TIME>time%+25
  410 ENDPROC
  411
  420 DEFPROCUNBLANK
  430  CP%=&FF-BLNK%:SYS "OS_Byte",147,&F1,CP%
  440  time%=TIME:REPEAT UNTIL TIME>time+25
  450  CP%=&FF:SYS "OS_Byte",147,&F1,CP%
  460 ENDPROC
  461
  470 DEFPROCCLOCK
  480  SYS 6,147,&F1,CP%-CK%:SYS 6,147,&F1,CP%
  490 ENDPROC
  491
  500 DEFPROCLINE
  510  SYS "OS_Byte",147,&F1,CP%-LS%:SYS "OS_Byte",147,&F1,CP%
```

```
  520 ENDPROC
  521
  530 DEFPROCRESET
  540  SYS "OS_Byte",147,&F1,CP%-FS%:SYS "OS_Byte",147,&F1,CP%
  550  FOR N%=1 TO 30 :PROCLINE:NEXT
  560 ENDPROC
  561
  570 DEF PROCfilesave
  571  *FX15
  580  INPUT"File Save"''"Please"'"Enter"'"Filename"'FILE$
  590  CLS:OSCLI "SAVE" "+FILE$+" "+STR$~start%+" "+STR$~finish%
  600 ENDPROC
  601
  610 DEF PROCfileload
  620  INPUT"File Load"''"Please"'"Enter"'"Filename"'FILE$
  630  CLS:OSCLI "LOAD "+FILE$+" "+STR$~start%
  640 ENDPROC
  641
  650 DEF PROCassemble
  660  FOR pass%=0 TO 3 STEP 3:P%=code%
  670
  680  [ OPT pass%
  690 .scale STMFD R13!,{R0-R12,R14}
  700  MOV R4,&&1000000:ADD R4,R4,&&FD0000:ADD R4,R4,&&8000
  710  MOV R6,&20:MOV R7,&256:MOV R8,&640
  720 .loop MUL R3,R7,R8:ADD R3,R3,R4:SUB R3,R3,&2:SUB R7,R7,&1
  730 .loop2 STRB R7,[R3]:SUB R3,R3,&1:SUB R6,R6,&1:CMP R6,&0:BNE loop2:MOV
R6,&20:CMP R7,&0:BNE loop:LDMFD R13!,{R0-R12,PC}
  740 .FStoCPU STMFD R13!,{R0-R12,R14}:MOV R7,&&FF:MOV R4,&&1000000:ADD
R4,R4,&&FD0000:ADD R4,R4,&&8000
  750 .line MOV R0,&147:MOV R1,&&F1:MOV R2,&&DD:SWI 6:MOV R2,&&DF:SWI 6
  760  MOV R6,&&200:ADD R6,R6,&1:CMP R7,&0:BEQ line4:SUB R7,R7,&1
  770 .line2 SUB R6,R6,&1:CMP R6,&0:BEQ line3
  780  MOV R0,&146:MOV R1,&&F1:MOV R2,&0:SWI 6:STRB R2,[R4]
  790  MOV R0,&147:MOV R1,&&F1:MOV R2,&&DE:SWI 6
  800  ADD R4,R4,&1
  810  MOV R0,&147:MOV R1,&&F1:MOV R2,&&DF:SWI 6:B line2
  820 .line3 ADD R4,R4,&&80:B line
  830 .line4 LDMFD R13!,{R0-R12,PC}
  840;
  850 .GREY STMFD R13!,{R0-R12,R14}
  860  MOV R4,&&1F00000:ADD R4,R4,&&D8000:MOV R5,&&2000000
  870 .GREY2 LDRB R0,[R4]:MOV R0,R0,ROR &4:AND R2,R0,&&C
  880  CMP R2,&4:ADDEQ R0,R0,&40
  890  CMP R2,&8:ADDEQ R0,R0,&200
  900  CMP R2,&12:ADDEQ R0,R0,&240
  910  STRB R0,[R4]
  920  ADD R4,R4,&1:CMP R4,R5:BNE GREY2
  930  LDMFD R13!,{R0-R12,PC}
  940  ]:NEXT pass%
  950 ENDPROC
  960
  970 DEF PROCECONST
  980  REM This procedure is called ELLIPSE1 since in B+W it finds the
ellipse
  990  REM constants
 1000  M%=293:RATIO=1.42379148:H%=519:U%=457
 1010  PRINT TAB(0,0)"ELLIPSE1"
 1020  PROCEDRAW:REPEAT:PROCEDRAW:MOUSE H%,U%,BUTTON%:PROCEDRAW
 1030  IF BUTTON%=1:PROCEDRAW:M%=M%+1:PROCEDRAW
 1040  IF BUTTON%=2:PROCEDRAW;M%=M%-1:PROCEDRAW
 1050  IF INKEY(-26):PROCEDRAW:RATIO=RATIO/1.005:PRINT TAB(0,0) RATIO:
PROCEDRAW
```

```
 1060  IF INKEY(-122):PROCEDRAW:RATIO=RATIO*1.005:PRINT TAB(0,0) RATIO:
PROCEDRAW
 1070  UNTIL INKEY(-74):PROCEDRAW:PRINT H%;",";U%
 1080  REM ellipse centred at graphic co-ordinates H% and U%
 1090  REM the values to be returned to MAIN PROG
 1100  REM are H%,U%,M%,RATIO
 1110 ENDPROC
 1120
 1130 DEF PROCEDRAW
 1140  REM this draws an ellipse using the ELLIPSE command
 1150  GCOL 4,0:ELLIPSE H%,U%,M%,RATIO*M%
 1160  MOVE H%-100,U%:PLOT 6,H%+100,U%:MOVE H%,U%-100:PLOT 6,H%,U%+100
 1170 ENDPROC
 1180
 1190 DEF PROCINTDRAW
 1200  MODE15:VDU 28,65,31,75,0:LOCAL V%(),W%(),S%:DIM V%(1000),W%(1000)
 1210  PRINT TAB(O,O)"INTDRAW":S%=0:A%=M%:FILE=OPENIN "TESTDATA"
 1220  REPEAT
 1230  INPUT£ FILE,V%(A%),W%(A%):A%=A%+1
 1240  UNTIL EOF£ FILE:CLOSE£ FILE
 1250  PROCRDRAW
 1260  REPEAT
 1270  IF INKEY(-122)CLG::S%=S%+1:PROCRDRAW:PRINT TAB(0,0)S%
 1280  IF INKEY(-26)CLG:S%=S%-1:PROCRDRAW:PRINT TAB(0,0)S%
 1290  UNTIL INKEY(-99):PRINT TAB(0,0)" READY   "
 1300 ENDPROC
 1310
 1320 DEF PROCSTATS
 1330  PRINT "STATISTICS"
 1340  LOCAL ST%(),FMAX%:DIM ST%(255):FMAX%=0
 1350  FOR I%=&1FD8000TO&1FFFFFF:ST%(?I%)=ST%(?I%)+1:NEXT
 1360  FOR I%=2TO255STEP2:IF ST%(I%)>FMAX% FMAX%=ST%(I%):M%=I%
 1370  NEXT:MODE15:MOVE 1020,100:DRAW 0,100:DRAW 0,600:MOVE 8,100:GCOL 0,14
 1380  COLOUR 100:FOR I%=2TO255STEP2:DRAW I%*4,100+ST%(I%)*500/FMAX%:NEXT
 1390  PRINT TAB(0,30) "0":PRINT TAB(42,30)"Intensity --->     255"
 1400  PRINT TAB(0,12)"Frequency":VDU28,65,31,75,0
 1410 ENDPROC
 1420
 1430 DEF PROCLSCAN
 1440  PRINT TAB(0,0) "LINESCAN":IF Y%<10 Y%=128
 1450  PROCINVERT
 1460  REPEAT
 1470  IF INKEY(-42) PROCUNINVERT:Y%=Y%+1:PROCINVERT
 1480  IF INKEY(-58) PROCUNINVERT:Y%=Y%-1:PROCINVERT
 1490  UNTIL INKEY(-99)
 1500  PROCUNINVERT
 1510  PROCSAMPLE
 1520  PROCDISPLAY
 1530  REPEAT UNTIL INKEY(-99)
 1540  PROCDISPLAY:PRINT TAB(0,0) " READY  "
 1550 ENDPROC
 1560
 1570 DEF PROCUNINVERT
 1580  S%=Y%*640+&1FD8000
 1590  FOR N%=0TO511:?(N%+S%)=?(N%+S%)-100:NEXT
 1600 ENDPROC
 1610
 1620 DEF PROCDISPLAY
 1621  PRINT TAB(0,0)"MAGN = ";B%/4
 1630  MOVE 0,L%(0):FOR N%=0TO511:PLOT 6,N%*2,B%*L%(N%)+O%:NEXT
 1640 ENDPROC
 1650
 1660 DEF PROCDISPLAY2
```

```
1670  CLG:GCOL 25:MOVE 1024,0:DRAW 0,0:DRAW 0,1024:GCOL 50:PROCDISPLAY
1680  REPEAT:IF INKEY(-58) PROCDISPLAY:B%=B%+1:PROCDISPLAY
1681  IF INKEY(-42) PROCDISPLAY:B%=B%-1:PROCDISPLAY
1682  IF INKEY(-122) PROCDISPLAY:O%=O%+50:PROCDISPLAY
1683  IF INKEY(-26) PROCDISPLAY:O%=O%-50:PROCDISPLAY
1684  UNTIL INKEY(-99)
1690 ENDPROC
1700
1710 DEF PROCINVERT
1720  S%=Y%*640+&1FD8000
1730  FOR N%=0TO511:?(N%+S%)=?(N%+S%)+100:NEXT
1740 ENDPROC
1750
1760 DEF PROCSAMPLE
1770  LOCAL C%:FOR N%=0TO511:L%(N%)=0:NEXT:FOR C%=Y%TOY%+4
1780  S%=C%*640+&1FD8000
1790  FOR N%=0TO511:L%(N%)=L%(N%)+?(N%+S%):NEXT:NEXT
1800  FOR N%=0TO511:L%(N%)=L%(N%)*0.2:NEXT
1810 ENDPROC
1820
1830 DEF PROCSCREEN
1840  REM ELLIPSE 1 passes the variables H%,U%,M%,RATIO
1850  REM X%,Y% starting co-ords, M% the minor axes length,RATIO
1860  LOCAL V%(),W%(),NV%(),NW%(),MAJ,MIN,SX%,SY%
1870  DIM V%(1000),W%(1000),NV%(1000),NW%(1000)
1880  SX%=H%*0.5:SY%=255.75-U%*0.25
1890  FOR R%=20TOM%
1900  MIN=R%*0.5:MAJ=MIN*RATIO*0.5
1910  FOR X%=SX%TOSX%+MIN
1920  S%=MAJ*SQR(1-((X%-SX%)/MIN)^2)
1930  Y%=SY%+S%:IF ?(&1FD8000+640*Y%+X%)=255 GOTO 1990
1940  V%(R%)=?(&1FD8000+640*Y%+X%)+V%(R%):NV%(R%)=NV%(R%)+1
1950  ?(&1FD8000+640*Y%+X%)=255
1960  Y%=SY%-S%:IF ?(&1FD8000+640*Y%+X%)=255 GOTO 1990
1970  W%(R%)=?(&1FD8000+640*Y%+X%)+W%(R%):NW%(R%)=NW%(R%)+1
1980  ?(&1FD8000+640*Y%+X%)=255
1990  NEXT:NEXT
2000  FILE=OPENOUT "TESTDATA"
2010  FOR I%=10TOM%
2020  IF NV%(I%)=0 GOTO 2050
2030  IF NW%(I%)=0 GOTO 2050
2040  PRINT£ FILE, V%(I%)/NV%(I%),W%(I%)/NW%(I%)
2050  NEXT
2060  CLOSE£ FILE
2070 ENDPROC
2080
2090 DEF PROCRDRAW
2100  MOVE 2*M%,4*V%(M%):FOR I%=M%TOA%:DRAW 2*I%,4*V%(I%):NEXT
2110  MOVE 2*M%,4*W%(M%+S%):FOR I%=M%TOA%:DRAW 2*I%,4*W%(I%+S%)+200:NEXT
2120  MOVE 2*M%,2*(V%(M%)+W%(M%+S%))+400
2130  FOR I%=M%TOA%:DRAW 2*I%,2*(V%(I%)+W%(I%+S%))+400:NEXT
2140 ENDPROC
>
```

Appendix 4: Numerical solution of coupled DFDL rate equations

This appendix gives a description and a listing of the FORTRAN program used for the numerical solution of the coupled rate equations. As was seen in Chapter V, the equations were successfully used to predict the temporal behaviour of the DFDL.

In Chapter V, where the model is considered fully, it is seen that the model describes the interplay between the population inversion, N_1 and the cavity photon flux q. The two differential equations which describe and couple the two parameters are, retaining the notation of chapter 5, given by,

$$\frac{dN_1}{dt} = I_p(t)\,\sigma_e\,(N_0-N_1) - \frac{\sigma_e c}{\eta} N_1 q. - \frac{N_1}{\tau_f} \qquad \text{(A4.1)}$$

$$\frac{dq}{dt} = \frac{(\sigma_e-\sigma_a)}{\eta} N_1 q - \frac{q}{\tau_c} + \frac{\Omega\, N_1}{\tau_f} \qquad \text{(A4.2)}$$

Chapter 5 also gives details of the fourth order Runge–Kutta method of solution of the equations. This commonly used method basically involves the forward integration of both (A4.1) and (A4.2), each time substituting the new values of N_1 and q into the equations. Each integration step is evaluated over a weighted average of four points; k1, k2, k3, k4.

Specific details of the program are now considered.

The program is written in standard FORTRAN 77 and was executed on a Digital Equipment Corporation (DEC) VAX 11/785, one of the University's mainframe computers.

The program may be divided into two sections:

In the first variables are declared and values assigned to constants. It is thought that the variable names have a sufficient similarity to those used in the equations that they are self-explanatory (e.g. SIGE = σ_e, RI = η (refractive index), EN = Energy of laser pulse, etc.). The variables K1–K4 are assigned to N_1, while C1–C4 are assigned to q.

The main section of the algorithm is the forward integration contained with a DO loop. In the program as shown, the program runs from 0 to 30 nanoseconds with a step size (H) of 10 picoseconds i.e. the loop is executed 3000 times. Output is written to two formatted data files which, in this case, represent the output power (see chapter 5, equation 13) and the population inversion. The graphical displays of chapter 5 where drawn using a program written using the GHOST–80 graphics package.

Excution of the program was achieved by running a command proceedure which is tabulated overleaf along with a program listing.

```
$!
$ GOTO OK
$! As an example default parameters should be the following
$ run rkdfb
2E-20 ! Emission cross section
1.0E-20 ! Absorption cross section
3E-4 ! molarity
1 ! Visibility
2 ! Pump pulse energy
0.02 !DFDL length
4E-12 !STEP SIZE
$ run reduce
output
$  run reduce
inversion
$ ren inversion.dat idef.dat
$ ren output.dat odef.dat
$ del inversion.dat;*
$ del output.dat;*
$ OK:
$ WRITE SYS$OUTPUT " **  RUNNING RKDFB FORTRAN PROGRAM  **"
$ !
$ run rkdfb
2E-20 ! Emission cross section
1.0E-20 ! Absorption cross section
5E-4 ! molarity
1 ! Visibility
2 ! Pump pulse energy
0.02 !DFDL length
4E-12 ! STEP SIZE
$ run reduce
inversion
$ ren inversion.dat I5M.dat
$ del inversion.dat;*
$ del output.dat;*
$ exit
```

```
C     This is an Runge-Kutta method of solving dfb rate equations
C
C     parameters are for Rhodamine B (SI units)
      IMPLICIT NONE
C
C     These are the FORTRAN formats of all variables used
C
      REAL*8 IMAX,SIGA,SIGP,NO,C1,C2,C3,C4,N,Q,TF,TC,FWHM,NTH
      REAL*8 RI,PO,L,C,SIGE,WA,A,B,PL,H,LP,PI,QF,EN,M
      REAL*8 OP,T,BETA,OM,S,CC1,CC2,CC3,K1,K2,K3,K4,V
C
C     These are the equation constants
C
      DATA TF/5E-9/,SIGP/2.5E-20/,B/2.5E-4/,FWHM/1E-8/,M/3E-4/,
     !PI/3.142/,C/3E8/,RI/1.44/,H/1E-11/,SIGE/2E-20/,L/0.02/,SIGA/1E-20/
     !  PL/6.63E-34/,WA/600E-9/,S/1E4/,LP/532E-9/,V/1.0/,EN/2E-3/
C
C     Now some constants used in the routine
C
      BETA=0.693/(FWHM*0.5)**2
      CC1=SIGE*C/RI
      CC2=(SIGE-SIGA)*C/RI
      CC3=V*(SIGE-SIGA)*SQRT(RI*L**3/(80*C))
      NO=6.02E26*M
      A=1/(NO*SIGP)
      QF=1/TF
      OM=B/(PI*NO*SIGP*L*L*S)
      IMAX=EN*LP/(FWHM*L*A*C*PL)
C
      NTH=2*((PI/V)**0.6667)/((SIGE-SIGA)*L)
      PRINT*,'Inversion threshold = ',NTH
C
      OPEN(UNIT=2,FILE='INVERSION',STATUS='NEW')
      OPEN(UNIT=3,FILE='OUTPUT',STATUS='NEW')
C
C     Now do calculation
C
      DO 10, T=0,3E-8,H
      K1=IMAX*EXP(-BETA*(T-2.0E-8)**2)*SIGP*(NO-N)-CC1*N*Q-N*QF
      K2=IMAX*EXP(-BETA*(T-2.0E-8+0.5*H)**2)*SIGP*(NO-(N+0.5*H*K1))-
     !    (CC1*(N+0.5*H*K1)*Q) -((N+0.5*H*K1)*QF)
      K3=IMAX*EXP(-BETA*(T-2.0E-8+0.5*H)**2)*SIGP*(NO-(N+0.5*H*K2))-
     !    (CC1*(N+0.5*H*K2)*Q) -((N+0.5*H*K2)*QF)
      K4=IMAX*EXP(-BETA*(T-2.0E-8+H)**2)*SIGP*(NO-(N+H*K3)) -
     !   (CC1*(N+H*K3)*Q) - (N+H*K3)*QF
      N=N+H*(K1+2*K2+2*K3+K4)/6
      TC=N*CC3*N*CC3
      IF(TC.LE.1E-13) TC=1E-13
      C1=CC2*H*Q-(Q/TC)+OM*QF*N
      C2=CC2*N*(Q+0.5*H*C1)-((Q+0.5*H*C1)/TC)+OM*QF*N
      C3=CC2*N*(Q+0.5*H*C2)-((Q+0.5*H*C2)/TC)+OM*QF*N
      C4=CC2*N*(Q+H*C3)-((Q+H*C3)/TC)+OM*QF*N
      Q=Q+H*(C1+2*C2+2*C3+C4)/6
      IF(Q.LE.0)Q=0
      PO=1E-4*PL*C*Q*A*B/(2*WA*TC)
C     1E-4 IN LINE ABOVE IS A SCALING FACTOR
      IF(PO.GT.1)    WRITE(UNIT=3,FMT=20) T*1E9,PO
      IF(N.GT.NO/20) WRITE(UNIT=2,FMT=20) T*1E9,N*1E-20
   10 CONTINUE
C     end of routine
   20 FORMAT(2E11.4)
      CLOSE (UNIT=2)
      CLOSE (UNIT=3)
      PRINT*,CHAR(7)
      STOP
      END
```